Durham E-Theses

Cosmological redshift surveys, big data and semi-analytical galaxy formation models

GIORGIO MANZONI

How to cite:

MANZONI, GIORGIO (2022) Cosmological redshift surveys, big data and semi-analytical galaxy formation models. Doctoral thesis, Durham University.

Use policy

Cosmological redshift surveys, big data and semi-analytical galaxy formation models

Giorgio Manzoni

A thesis presented for the degree of

Doctor of Philosophy
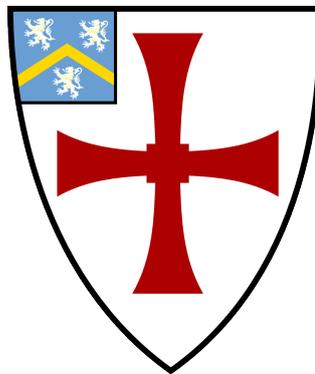
Institute for Computational Cosmology (ICC)

Centre for Extragalactic Astronomy (CEA)

Institute for Data Science (IDAS)

The University of Durham

United Kingdom

March 2022

Cosmological redshift surveys, big data and semi-analytical galaxy formation models

Giorgio Manzoni

Abstract

The focus of this thesis is to connect observations from different galaxy redshift surveys to physically motivated models of galaxy formation. The Physics of the Accelerating Universe Survey (PAUS) and the VIMOS Public Extragalactic Redshift Survey (VIPERS) are the two major surveys used in this thesis. For both I use the semi-analytical model `GALFORM` to create a physically motivated scenario and explore the evolution of some observational galaxy properties starting from an epoch when the Universe was approximately half of the current age. In particular, for PAUS, we used GALFORM implemented in the Planck Millennium N-body simulation, to build a mock PAUS galaxy catalogue on an observer's past lightcone. The increased mass resolution and the higher frequency of simulation outputs allows us to make improved galaxy property predictions. We compared the mock catalogue predictions with the observed number counts, redshift distributions and the redshift evolution of the observer frame colours. The red and blue population of the model galaxies are roughly in agreement with the observed ones.

The interest in galaxy colours and the relation to their star formation histories lead us to exploit VIPERS for a galaxy evolution study. In particular we analysed the evolution of the rest frame colour-magnitude relation tracking the evolution of the bright edge with the aim of deriving constraints on the quenching of star formation activity in galaxies in $0.5 < z < 1.1$. Through the modelling of parametrised star formation histories (SFHs) we estimated the average time-scale of the suppression of the star formation. We showed that modelling a fast suppression of the star formation activity in galaxies, we are able to reproduce better the observational data. We created a physically motivated mock with `GALFORM` and we obtained a similar qualitative trend.

We tested that AGN feedback, as the main quenching process in `GALFORM`, is crucial in reproducing the trend of the bright-edge.

As part of the Centre for Doctoral Training (CDT), I developed data-analysis techniques, during an internship with Procter & Gamble (P&G) and with the National Health Service (NHS), in two projects described in this thesis. In the P&G project the aim was to model the density of the laundry powder in order to understand the chemical ingredients that mostly contribute to the density and hence changing the industrial process accordingly. In the NHS project, we aimed at establishing new normative ranges for vital signs of newborn babies. The results of this project have the potential of helping doctors in making critical decision for the treatment that can save the life of babies in critical conditions.

Supervisors: Prof. Peder Norberg and Prof. Carlton Baugh

Declaration

The work in this thesis is based on research carried out at the Institute for computational cosmology (ICC), Centre for Extragalactic Astronomy (CEA) and Institute for Data Science (IDAS), in the Department of Physics, Durham University, England. No part of this thesis has been submitted elsewhere for any other degree or qualification, and it is the sole work of Giorgio Manzoni unless referenced to the contrary in the text.

Part of the results on the study of the colour-magnitude in Chapter 5 have been investigated during my master at INAF-IASF Milano under the supervision of the VIPERS team. As part of my PhD I have complemented the observational results on the colour-magnitude with physical motivated models of galaxy formation. This further analysis made possible the publication of Manzoni et al. (2021) which is reported verbatim in Chapter 5.

Finally, Section 6.2 presents the results of Loganathan et al. 2021 as submitted to the *Pediatric Research* journal. Minor changes have been made to the text and the layout to make it more easily understandable to an astronomy audience. The abstract of this manuscript was presented as electronic poster at REASON conference, UK, 2021.

Contents

Introduction

In this chapter, I introduce the main cosmological concepts that are needed to understand the rest of the thesis. Starting from the cosmological model for our universe that is largely accepted, the ΛCDM model, to the definition of the main observational quantities like fluxes, luminosities and magnitudes. All this knowledge can be found in any cosmology book, for some derivations here we follow the approach adopted by Ryden (2003).

1.1 Theoretical framework

Cosmology is the study of the Universe as a whole and it relies on the *cosmological principle*. The cosmological principle states that there is nothing special about our location in the Universe. More specifically the cosmological principle is the assumption that the Universe is *homogeneous* and *isotropic* on large scales. Homogeneous means that if we measure some properties of the Universe in a specific location, the same properties will be be found at any other location. Isotropy instead means that if we look at any direction of the sky we are going to observe the same average pattern, or in other words, there is no preferred direction. This approximation only applies on very large scales, i.e. distances greater than 100 Mpc, as on smaller scales the Universe is dominated by structures such as groups and clusters of galaxies that are strongly anisotropic.

With the assumption of homogeneity and isotropy, we can model the entire Universe with simple equations. Specifically, we can define a metric that describes space-time. In a Euclidean universe the Minkowski metric is used:

$$\mathrm{d}s^2 = -c^2\,\mathrm{d}t^2 + \mathrm{d}x^2 + \mathrm{d}y^2 + \mathrm{d}z^2, \tag{1.1}$$

which becomes more convenient when expressed in spherical coordinates (r, θ, ϕ):

$$\mathrm{d}s^2 = -c^2\,\mathrm{d}t^2 + \mathrm{d}r^2 + r^2\left[\mathrm{d}\theta^2 + \sin^2\theta\,\mathrm{d}\phi^2\right], \tag{1.2}$$

and even more compact if we define the angular part as $\mathrm{d}\Omega^2 \equiv \mathrm{d}\theta^2 + \sin^2\theta\,\mathrm{d}\phi^2$:

$$\mathrm{d}s^2 = -c^2\,\mathrm{d}t^2 + \mathrm{d}r^2 + r^2\mathrm{d}\Omega^2. \tag{1.3}$$

The Minkowski metric applies to a static universe with a Euclidean geometry, which means that if we draw a triangle using three random points in the universe, then the sum of its internal angles is 180 degrees. This is the geometry we experience in everyday life but there is no reason to assume that this is the geometry of the entire universe. So the first extension that we need to apply to our metric to describe a universe in a more general way is to allow for a spatial curvature. The spatial curvature can be described by including a factor $S_k(r)$ in the angular part of the metric, $\mathrm{d}\Omega$. This factor assumes different forms in case of positive ($k = 1$), negative ($k = -1$) or zero curvature ($k = 0$):

$$S_k(r) = \begin{cases} R\,\sin(r/R) & (k = 1) \\ r & (k = 0) \\ R\,\sinh(r/R) & (k = -1), \end{cases} \tag{1.4}$$

where R is the curvature radius ($R \to \infty$ for a Euclidean or flat Universe). The second extension we need to apply to the metric is to allow for the expansion of the Universe, as first observed by Hubble in the early 1900's. To do this, we introduce a scale factor $a(t)$ which takes into account the expansion (or potentially the contraction) of the spatial components of the metric. We set this parameter

to be 1 at the current epoch t_0 and to 0 at the beginning of the universe, at the epoch of Big Bang, when all distances shrinks to 0 thanks to the scale factor

$$a(t) = \begin{cases} 0 & (t = 0 = \text{Big Bang}) \\ 1 & (t = t_0 = \text{today}). \end{cases} \tag{1.5}$$

With the addition of curvature and expansion, the Minkowski metric becomes the Robertson-Walker metric:

$$\mathrm{d}s^2 = -c^2\,\mathrm{d}t^2 + a(t)^2 \left[\mathrm{d}r^2 + S_k(r)^2\mathrm{d}\Omega^2\right]. \tag{1.6}$$

Applying the Einstein equation of general relativity to this metric, instead of the Minkowski one, results in the first of the Friedman equations which describe the expansion of the universe:

$$\left(\frac{\dot{a}}{a}\right)^2 = \frac{8\pi G}{3c^2}\varepsilon(t) - \frac{kc^2}{R_0^2}\cdot\frac{1}{a^2}, \tag{1.7}$$

where ε is the energy density of all the components of the universe, namely matter, radiation, and the cosmological constant ($\varepsilon = \varepsilon_{\mathrm{mat}}+\varepsilon_{\mathrm{rad}}+\varepsilon_\Lambda$), G is the gravitational constant, c is the speed of light, k controls the curvature as described before, R_0 is the curvature radius and $a(t)$ is the scale factor.

If we rearrange the above equation by normalising the energy densities to the critical energy density for which the Universe would be flat today, and making explicit their dependence on the scale factor we obtain:

$$\frac{H^2(t)}{H_0^2} = \frac{\Omega_{\mathrm{rad},0}}{a^4(t)} + \frac{\Omega_{\mathrm{mat},0}}{a^3(t)} + \Omega_\Lambda + \frac{1 - \Omega_{\mathrm{tot},0}}{a^2(t)}, \tag{1.8}$$

where the Hubble parameter controls the speed of the expansion as it is related to the scale factor by $H(t) = \dot{a}(t)/a(t)$, and the Hubble constant is its value in the current era $H_0 = H(t_0)$, the density parameters Ω are the energy densities normalised to the critical energy density for a flat Universe today, i.e. $\Omega_{\mathrm{rad},0} = \varepsilon_{\mathrm{rad},0}/\varepsilon_{\mathrm{c},0}$, $\Omega_{\mathrm{mat},0} = \varepsilon_{\mathrm{mat},0}/\varepsilon_{\mathrm{c},0}$ and $\Omega_{\Lambda,0} = \varepsilon_\Lambda/\varepsilon_{\mathrm{c},0}$ with $\varepsilon_{\mathrm{c},0} = 3c^2H_0^2/8\pi G$. $\Omega_{\mathrm{tot},0}$ is the total density parameter today and is made up of the sum of the individual component density parameters: $\Omega_{\mathrm{tot},0} = \Omega_{\mathrm{rad},0}+\Omega_{\mathrm{mat},0}+\Omega_\Lambda$. The first three terms

of Eq. (1.8) represent the evolution of the different components of the Universe with the appropriate power of the scale factor. As expected we can see that in an expanding Universe, the densities of matter and radiation decrease, but at different rates. For the matter density we have the three spatial dimension which dilute the energy density as the universe expands. For the radiation, we have an additional contribution from the wavelength of photons increasing with the scale factor, hence the expansion factor appears to the fourth power. The unexpected behaviour comes from the energy density of the cosmological constant which does not show any dependence on the scale factor. Since the density of the cosmological constant does not change to keep the density constant, the energy needs to increase as a^3, to counteract the increase in volume. The last term of Eq. (1.8) is related to the curvature. Some observations point toward a Universe in which $\Omega_{\mathrm{tot},0} = 1$ making the Universe flat, which means it has an Euclidean geometry (see for example Planck Collaboration et al. 2014). For this reason we can neglect the last term of Eq. (1.8) and focus on the first three terms.

The first three terms on the right hand side of Eq. (1.8) imply that the expansion of the universe has been dominated by different components during different epochs. Radiation dominated during the first stages of the universe (the radiation dominated era). Next the matter started to dominate the dynamics of the universe because its energy density decreases more slowly than that of the radiation (matter dominated era). Since the energy density of the cosmological constant does not decrease, it is inevitable that the final era of cosmic expansion is the one dominated by the cosmological constant; we are currently in this era. The fact that we only recently (about 4 billion years ago) entered the dark energy dominated era, made people suspect that the the dark energy is not actually a cosmological constant but may be a dynamical component that evolves with time. This is related to the fine tuning problem, as it is very unlikely that we are in a special era like the transition between a matter dominated Universe and a dark energy dominated Universe. However the main model of the Universe, which we also assume in this

thesis is the ΛCDM, where the Λ represents the cosmological constant while CDM stands for cold dark matter, which is the theory that assumes that the majority of the matter in the universe is in form of dark matter and this dark matter is made of non relativistic particles, i.e. with velocities considerably lower than the speed of light.

The Friedman equation (Eq. 1.8), describes the evolution of the Universe as a whole, from the Big Bang to today. It relies on the hypothesis of homogeneity and isotropy as described above. However, this hypothesis holds on large scales but when we study smaller scales than ~ 100Mpc, the Universe is highly inhomogeneous and non-isotropic. This is because it is dominated by small structures such as galaxies and cluster of galaxies. These are the visible components of our Universe and can be observed with galaxy surveys like the Physiscs of the Accelerating Universe Survey (PAUS; Eriksen et al. 2019) or the VIMOS Public Extragalctic Redshift Survey (VIPERS; Guzzo et al. 2014; Scodeggio et al. 2018) which are able to collect a large number of galaxies for a wide range of redshifts. With a large number of galaxy redshifts, it is possible to better constrain the cosmological parameters that appear in Eq. (1.8), which are $\Omega_{rad,0}$, $\Omega_{mat,0}$, Ω_Λ and the Hubble parameter H_0. The estimate of parameters through the statistic of galaxy clustering is not the only aim of galaxy surveys. Measuring galaxy spectra, emission lines and colours can give us insight into the processes that regulate star formation. This thesis will focus mainly on the latter direction.

1.2 Redshifts and related distances

When observing a galaxy, it is of primary importance to estimate its distance. For example, without an estimate of the distance, it would be impossible to estimate the intrinsic luminosity of a galaxy as two identical galaxies would appear different if they are at different distances. However, the concept of distance in a Universe that is currently expanding is not straightforward. We have seen in Sect. 1.1,

that the scale factor $a(t)$ takes into account the expansion at any cosmological time t, from $t = 0$ at the instant of the Big Bang to $t = t_0$ at the present day. However, the scale factor is related to the cosmological model we are using and in the case of the ΛCDM model, it depends on the cosmological parameters $\Omega_{\mathrm{rad},0}$, $\Omega_{\mathrm{mat},0}$, Ω_Λ and H_0. However, one observable that has always been associated with distances, since the early 1900's, is redshift. When looking at a galaxy spectrum, it is common to observe emission or absorption lines of specific elements shifted from the wavelength that we would normally observe in a laboratory. This shift is usually towards redder wavelengths, hence the name redshift. This shift is easy to measure when the spectrum of a galaxy is available. Knowing the wavelength of the emission line that we would observe in a laboratory, λ_{em}, we can measure the wavelength at which we observe that specific emission line for the galaxy considered, λ_{ob}. We can then define the redshift as:

$$z = (\lambda_{\mathrm{ob}} - \lambda_{\mathrm{em}})/\lambda_{\mathrm{em}}. \tag{1.9}$$

This quantity comes straightforwardly from observation and it is model independent. However, inferring distances from the redshift is model dependent.

Using local galaxies, Hubble was the first to try and connect redshift to distance, in the famous Hubble law first published in Hubble (1929) (see Fig. 1.1). We note that for a few galaxies the redshift has negative values. These galaxies are blueshifted. The galaxies belong to the local group and they are gravitationally bound to us, so that the expansion of the universe is negligible compared to the gravitational attraction that makes them fall toward us. However, apart few examples of blueshift for very nearby galaxies, all the other galaxies are redshifted as expected in an expanding Universe.

Given the cosmological model in use, it is possible to connect redshift with distance. The first step is to connect the redshift to the scale factor $a(t)$. If we consider the path of a photon from a distant galaxy to us, the photon will follow a null geodesic (i.e. $\mathrm{d}s = 0$ and $\mathrm{d}\Omega = 0$) in the space-time metric. Using the
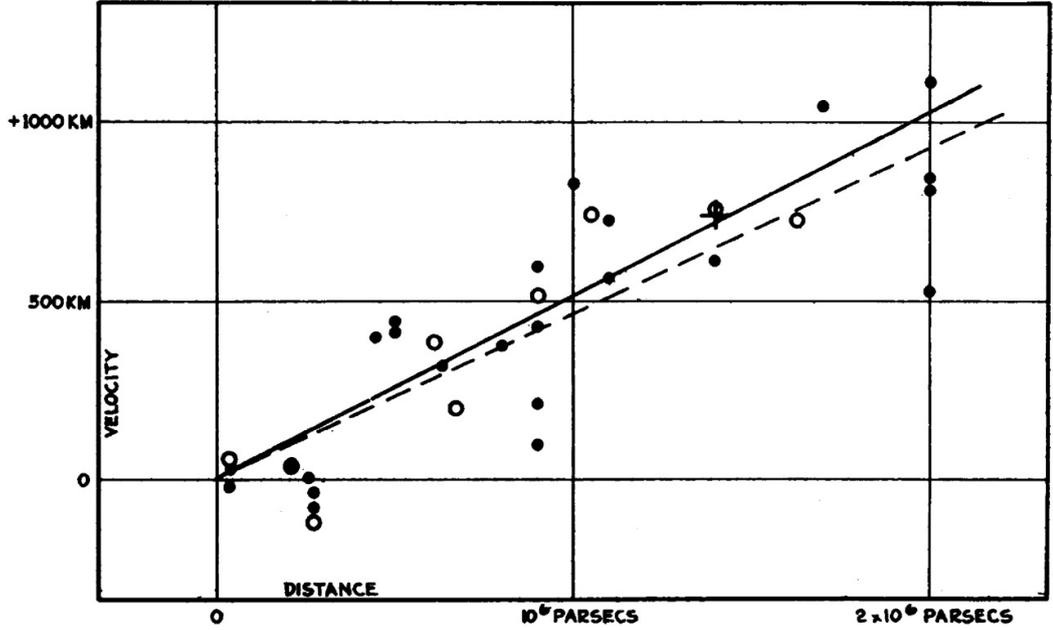
Figure 1.1: The original Hubble plot for the relation between redshift, plotted on the *y*-axis as $cz[\mathrm{km}/s]$ versus an independent estimate of distances on the *x*-axis for very local galaxies. More recent estimates of distances shows that Hubble underestimated distances finding a much higher value for the Hubble parameter than the currently accepted value. Plot reproduced from `https://www.pnas.org /content/15/3/168`.

Robertson-walker metric in Eq. 1.6, we find:

$$c\frac{\mathrm{d}t}{a(t)} = \mathrm{d}r. \tag{1.10}$$

Considering a photon that starts travelling from a distant galaxy at the time t_e with wavelength λ_e, and reaches us at t_0 with wavelength λ_0, we can integrate this expression to find:

$$\frac{\lambda_e}{a(t_e)} = \frac{\lambda_0}{a(t_0)}, \tag{1.11}$$

and considering the definition of redshift in eq. 1.9 we can rearrange this in a more convenient way:

$$1 + z = \frac{a(t_0)}{a(t_e)} = \frac{1}{a(t_e)}. \tag{1.12}$$

The important thing we learn is that the redshift is not affected by what happens to the universe between t_e and t_0 but only by the value of the scale factor at these specific moments.

Thanks to Eq. (1.12), we can use redshift as an observable to estimate the scale factor, $a(t)$. The scale factor give us the rate of the expansion of the universe at the cosmological time t. However, if we want to estimate the distance to a galaxy, we need first to define a distance. In an expanding universe, the distance between two astronomical objects (e.g. the Earth and the galaxy) is expanding with time. To measure a proper distance we should hypothetically be able to stop the expansion at a precise time t and measure the distance at that time. Although not physically possible, we can define the *proper distance* as the spatial geodesic between two astronomical objects when the scale factor $a(t)$ is considered a constant (or equivalently the time interval $dt = 0$). From the Robertson-Walker metric, imposing $dt = d\Omega = 0$ in Eq. (1.6), we find $ds = a(t)dr$ and integrating over the radial comoving coordinate r we find the proper distance to be:

$$d_p(t) = a(t)\, r, \tag{1.13}$$

where we define r to be the comoving distance, i.e. a distance that does not change with the expansion of the universe, as the latter is purely described by the factor $a(t)$.

Even if the proper distance is arguably the most intuitive definition of distance in an expanding universe, it is not directly measurable. In fact, even if we use the redshift to estimate the scale factor, the comoving distance r is not measurable itself. In the attempt to define a distance that is directly related to observables, astronomers introduced the *luminosity distance*. The luminosity distance is based on the concept of standard candles. Standard candles are a class of objects that have a fixed intrinsic luminosity L. This means that the flux f that we receive in Earth is directly related to the distance, which we call *luminosity distance*, as the intrinsic luminosity is always the same. The luminosity distance is defined as:

$$d_L \equiv \sqrt{\frac{L}{4\pi\, f}}\,. \tag{1.14}$$

In a flat expanding universe, the luminosity distance can also be related to the

proper distance and the comoving distance by the following*:

$$d_L = r\,(1+z) = d_p(t_0)\,(1+z).\qquad(1.15)$$

The luminosity distance is not the only definition of distance that can be directly related to observables. If instead of standard candles, we use standard rulers, defined as object with a fix length l, we can define the *angular-diameter distance* as:

$$d_A \equiv \frac{l}{\delta\theta},\qquad(1.16)$$

where $\delta\theta$ is the subtended angle by the two ends of the ruler assuming the ruler is perpendicular to the line of sight. We also assume that $\delta\theta \ll 1$ so that we can use the small angle approximation. Like the luminosity distance, the angular-diameter distance can also be related to the comoving and proper distance:

$$d_A = \frac{r}{(1+z)} = \frac{d_p(t_0)}{(1+z)},\qquad(1.17)$$

and combining Eq. (1.15) and Eq. (1.17) we can also find a relation between luminosity distance and angular diameter distance:

$$d_A = \frac{d_L}{(1+z)^2}\,.\qquad(1.18)$$

These are the main definitions of distance used in cosmology and they can each be used in different applications. The luminosity and the angular diameter distances in particular are needed to connect observations to the theoretical framework of the ΛCDM model and can be used to estimate the cosmological parameters.

1.3   Fluxes and Magnitudes

The concept of magnitudes comes from ancient Greece, marking the attempt to classify stars in brightness. The system of magnitudes comes naturally in a logarithmic scale as the sensitivity of the human eye is also logarithmic. When measuring

---

*In a curved Universe, instead of using the comoving distance r, $S_k(r)$ should be used, as defined in Eq. (1.4).

the amount of light we receive from a distant galaxy, however, it is convenient to count the number of photons on a linear scale rather than a logarithmic one. Using charge-coupled devices (CCDs) we can measure the number of photons received (defined as the *flux*) and, if the distance to the object is known, it is possible to determine the number of photons that have been emitted by the source (defined as *luminosity*). Flux and Luminosity, on the original logarithmic scale are defined as *apparent magnitude* (m) and *absolute magnitude* (M) respectively.

$$m - m_{\text{ref}} = -2.5 \log_{10}\left(\frac{f}{f_{\text{ref}}}\right) \qquad M - M_{\text{ref}} = -2.5 \log_{10}\left(\frac{L}{L_{\text{ref}}}\right), \qquad (1.19)$$

where fluxes and luminosities are related by:

$$f = \frac{L}{4\pi d_L^2} \qquad (d_L = \text{Luminosity Distance})^* \qquad (1.20)$$

and the reference quantities depend on the band in which we are observing. Specifically, when considering monochromatic fluxes and luminosities, which means only looking at photons of a fixed frequency ν, the energy can be expressed as:

$$d\varepsilon_\nu = \varepsilon_\nu \, d\nu = \frac{d\varepsilon}{d\nu} d\nu. \qquad (1.21)$$

We can also express the energy in terms of the number of monochromatic photons, given that the energy of a single photon of constant frequency ν is $h\nu$:

$$\varepsilon_\nu = \frac{d\varepsilon}{d\nu} = \frac{dn}{d\nu} h\nu. \qquad (1.22)$$

We know that monochromatic luminosity is the power emitted at a certain frequency $d\nu$ so that using previous relations we have:

$$L_\nu = \frac{dL}{d\nu} = \frac{d\varepsilon}{d\nu \, dt} = \frac{dn}{d\nu \, dt} h\nu \qquad (1.23)$$

If we assume that a source emits isotropically over the entire solid angle of 4π steradians, the number of photons that reach an observer are those contained in a solid angle $d\Omega$ that represent the telescope. The solid angle is defined as the

---

*See the discussion about the luminosity distance in Sect. 1.2 and its definition in Eq. 1.14.

surface that intercepts the photons divided by the square distance from the source:

$$d\Omega = \frac{ds}{r^2}, \tag{1.24}$$

where r is the comoving distance. To determine the flux we receive, we need to estimate how many photons will hit the comoving surface ds. If the total number of photons is conserved, the number of observed photons n_0 is related to the number of emitted photons n by:

$$dn_0 = \frac{dn}{4\pi} d\Omega = \frac{dn}{4\pi} \frac{ds}{r^2}. \tag{1.25}$$

Eq 1.25 shows that the number of observed photons decreases with the square of the comoving distance. The expansion of the universe also has an effect on the frequencies of the photons that we receive, which depends on the scale factor as:

$$d\nu_0 \, a(t_0) = d\nu \, a(t) \Rightarrow d\nu_0 = \frac{d\nu}{1+z}, \tag{1.26}$$

where we use the subscript 0 for observed quantities. Then the observed monochromatic flux is:

$$f_{\nu_0} = \left. \frac{df}{d\nu} \right|_{t=t_0} = \frac{d\varepsilon_0}{d\nu_0 \, dt_0 \, ds} = \frac{L_\nu}{4\pi r^2 (1+z)}, \tag{1.27}$$

Using the relation in Eq. (1.15), we can express the monochromatic flux in terms of luminosity distance:

$$f_{\nu_0} = \frac{L_\nu}{4\pi d_L^2}(1+z). \tag{1.28}$$

Since redshift has the effect of changing the frequencies of photons towards redder frequencies, the observed luminosity L_{ν_0} is also different from the emitted luminosity L_ν. We can introduce explicitly L_{ν_0}:

$$f_{\nu_0} = \frac{L_\nu}{4\pi d_L^2}(1+z) \frac{L_{\nu_0}}{L_{\nu_0}} = \frac{L_{\nu_0}}{4\pi d_L^2} \left[\frac{L_\nu}{L_{\nu_0}}(1+z) \right], \tag{1.29}$$

where we can define the $K(z)$-*correction* as the term in square brackets:

$$K(z) = \frac{L_\nu}{L_{\nu_0}}(1+z), \tag{1.30}$$

so that Eq. (1.29) becomes:

$$f_{\nu_0} = \left(\frac{L_{\nu_0}}{4\pi d_L^2} \right) K(z).$$

(1.31)

The K-correction is a key element when converting luminosity from the rest frame of the object to the observer frame. Eq. (1.30) shows that in order to estimate the K-correction we need to know the spectrum of the object in order to calculate the change in luminosity from ν_0 to ν. This process is usually accomplished by using stellar population synthesis models that provide spectra for galaxies of a specific type or an observed template spectrum.

It is common practice to convert Eq. (1.31) into the magnitude system. For this we can use the definitions of absolute and apparent magnitude in Eq. (1.19). We obtain:

$$M - M_{\text{ref}} = -2.5 \log_{10} \left(\frac{f_{\nu_0} \cdot 4\pi \, d_L^2}{f_{\text{ref}} \cdot 4\pi \, (10 \, \text{pc})^2} \cdot \frac{1}{K(z)} \right),$$

(1.32)

where we have used the fact that the reference luminosity is related to the reference flux by $L_{\text{ref}} = f_{\text{ref}} \cdot 4\pi \, (10 \, \text{pc})^2$. We can also redefine the k-correction to be:

$$\mathsf{K}(z) := -2.5 \log_{10} K(z)$$

(1.33)

we can finally obtain the relation that describe the transition between rest frame and observed frame in the magnitude system[*]:

$$M - M_{\text{ref}} = m - m_{\text{ref}} - 5 \log_{10} \left(\frac{d_L}{1 \, \text{pc}} \right) + 5 - \mathsf{K}(z)$$

(1.34)

1.4 Motivation for galaxy surveys

The objective of galaxy redshift surveys is to collect a large number of galaxy redshifts to address various science goals. Because of the limited time available at the telescope, a choice must be made regarding the galaxies to be targetted. Keeping the number of observed objects constant, these objects can be spread over

---

[*]Note that in this definition the luminosity distance needs to be expressed in parsec.

a small solid angle and go deep in redshift, or alternatively cover a wide solid angle but for smaller values of redshift. These two different choices are motivated by different scientific objectives. For example, going deep in redshift (with a small solid angle) aims to probe the earliest stages of the Universe understanding the key processes behind galaxy evolution. For example the dramatic change in the global star formation rate and the downsizing of star formation activity from the most massive galaxies at higher redshifts to lower mass galaxies at the present day are best probed in surveys that span a wide baseline in redshift. However, narrow beam high redshift surveys may struggle to understand environmental processes, for example how isolated galaxies behave differently from cluster galaxies. Another main reason for choosing wide or shallow surveys is the statistics that can be used to estimate cosmological parameters. Two powerful cosmological probes are the baryonic acoustic oscillations (BAO) and the redshift space distortions (RSD), both measured from the galaxy correlation function. The first is a measure of an overdensity of galaxies at the specific distance that should reflect the cycle of compression and expansion, due to pressure and gravity, of the baryon-photon fluid when radiation and matter where still coupled together. The BAO scale is the maximum distance that can be travelled by a sound wave up to matter-radiation decoupling, the sound horizon scale. Redshift space distortions are a phenomenum due to the peculiar velocities of galaxies. In particular, the doppler effect due to the peculiar motion of galaxies is added to the cosmological redshift, creating an elongated distribution of galaxies in the redshift space along the line of sight (*fingers of God*), and coherent bulk flows of galaxies towards overdensities on larger scales. Measuring BAO and RSD from shallow wide surveys makes possible the estimation of cosmological parameters in the ΛCDM framework. The first two surveys of this kind to measure these statistical estimator are the Sloan Digital Sky Survey (SDSS; York et al. 2000) and the 2dF Galaxy Redshift Survey (2dFGRS; Colless et al. 2003). For this last survey, Fig. 1.2 shows the observed distribution of galaxies in the plane of right-ascension (RA) versus redshift (for a thin slice of declination,
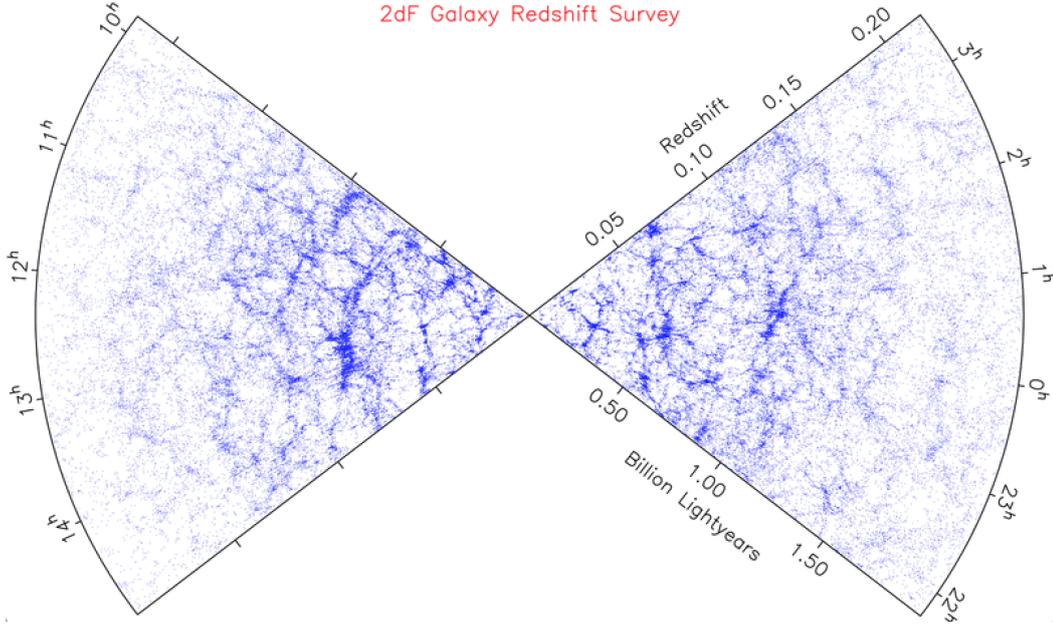
Figure 1.2: Redshift vs RA lightcone for the 2dFGRS survey (Colless et al., 2003).

DEC). It can be seen how such a wide angle combined with a large number of objects (245 591) allows us to probe the large scale distribution of galaxies, with filaments and clusters being apparent spread over the cosmic web. The 2dFGRS survey is limited in the optical to $b_{\mathrm{J}} < 19.45$, resulting in a distribution of redshifts which peaks at $z \sim 0.1$ (see Fig. 1.3). In contrast to such a wide angle survey as 2dFGRS, VIPERS instead is much narrower and deeper in redshift. It covers a solid angle of about $23.5\,\mathrm{deg}^2$ over two fields (W1 and W4). Fig. 1.4 shows the distribution of galaxies in the RA vs redshift space. Galaxies can be classified according to their intrinsic colours as red (for galaxies belonging to the red sequence), blue (for galaxies belonging to the blue cloud) and green (for galaxies belonging to the green valley, which is intermediate between the red sequence and blue cloud). It can be seen how red galaxies are more common in clusters rather than in filaments, in agreement with the suppression of star formation for satellite galaxies falling in the potential well of the centrals, and the shutdown of gas cooling in massive halos due to heating by active galactic nuclei. VIPERS collected redshifts for nearly 90 000 galaxies, targetting only galaxies above redshift $z \gtrsim 0.5$ using an empirical colour-colour pre-selection. The fainter magnitude limit used in VIPERS, coupled with
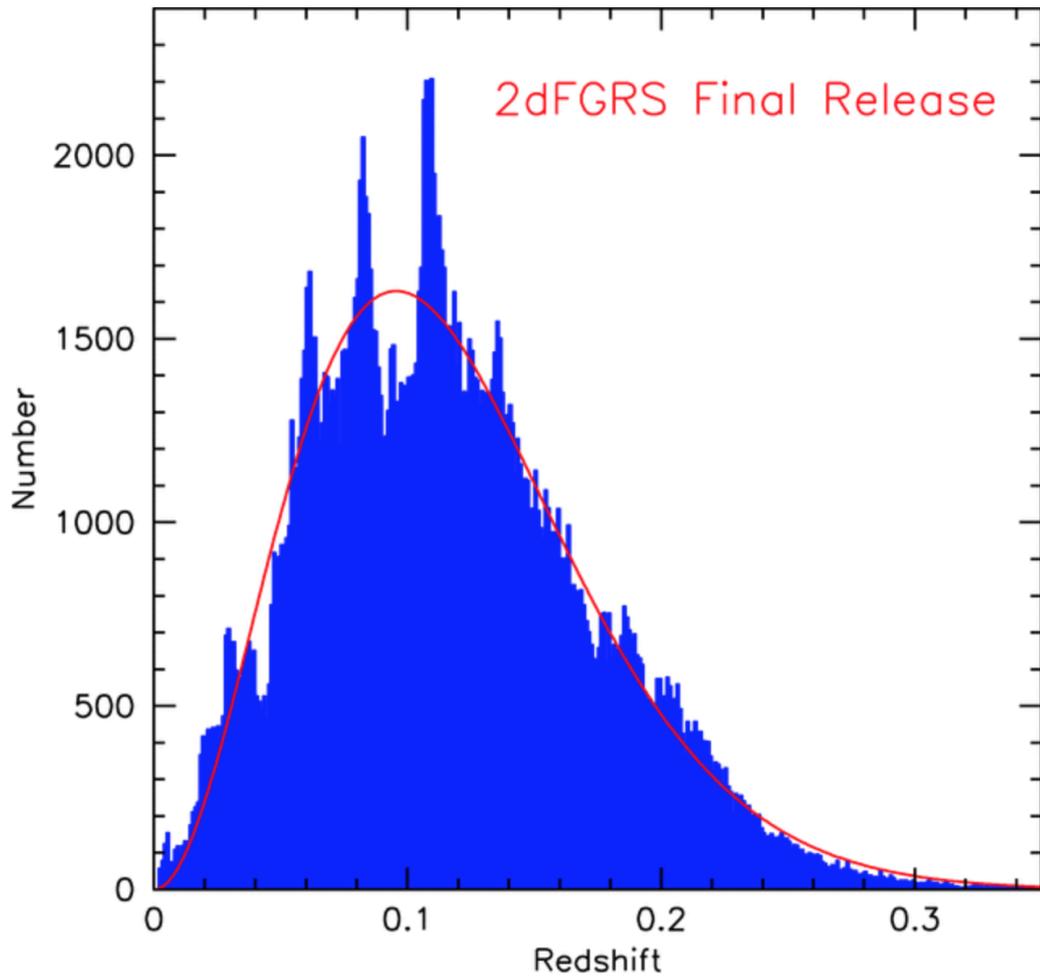
Figure 1.3: Redshift distribution for the 2dFGRS survey (Colless et al., 2003).
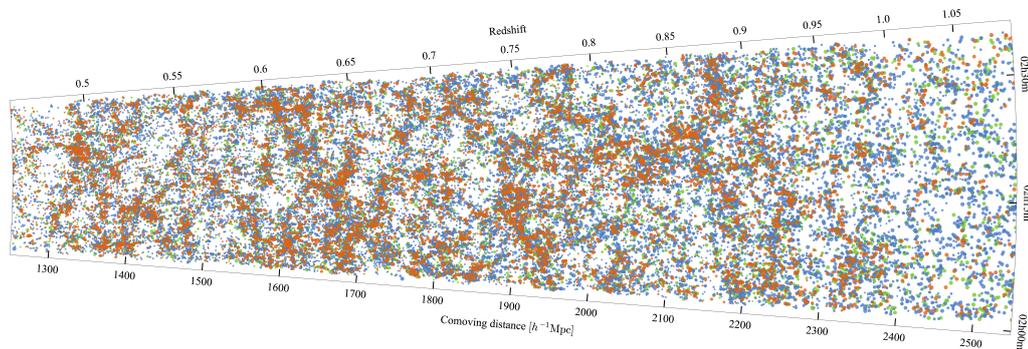
Figure 1.4: Redshift vs RA lightcone for the VIPERS survey in the W1 field http://vipers.inaf.it/images/pdr2/cone_pdr2_W1.png.
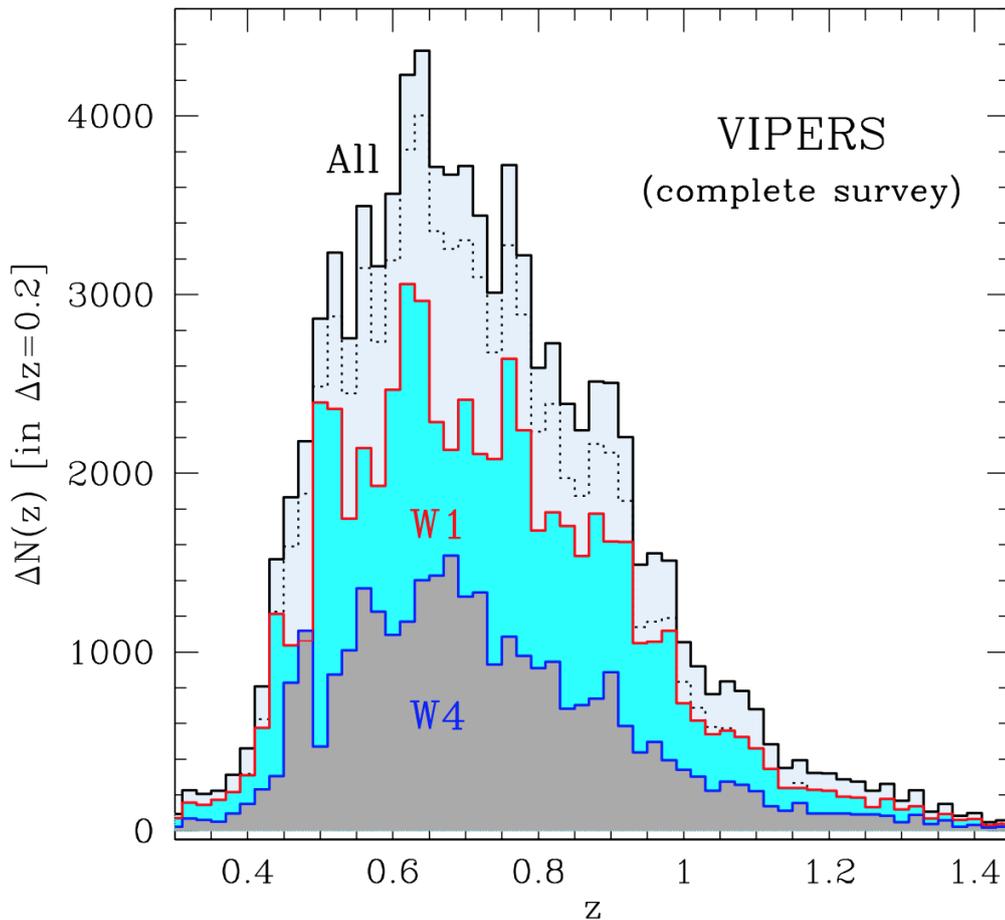
Figure 1.5: The redshift distribution for the two VIPERS fields, after having applied a colour-colour selection to avoid targetting galaxies with redshift below $z \lesssim 0.5$. Taken from Scodeggio et al. (2018).

the pre-selection of targets using galaxy colours, shifts the distribution of redshifts to higher values than found in brighter, local surveys like 2dFGRS, with VIPERS having a median redshift of about $z \sim 0.7$ (see Fig. 1.5).

Since, the data from VIPERS are used extensively in this thesis, a dedicated section (Sect. 2.2) will provide further details. The division between wide and shallow versus deep and narrow is not always well defined. The Physics of the Accelerating Universe Survey (PAUS; Eriksen et al. 2019) for example tries to bridge these two broad classes with the aim of collecting photometric redshifts for about $\sim 10^6$ objects over approximately $100 \, \mathrm{deg}^2$. Fig. 1.6 shows how different surveys compare in terms of the number of galaxy redshifts measured over a given
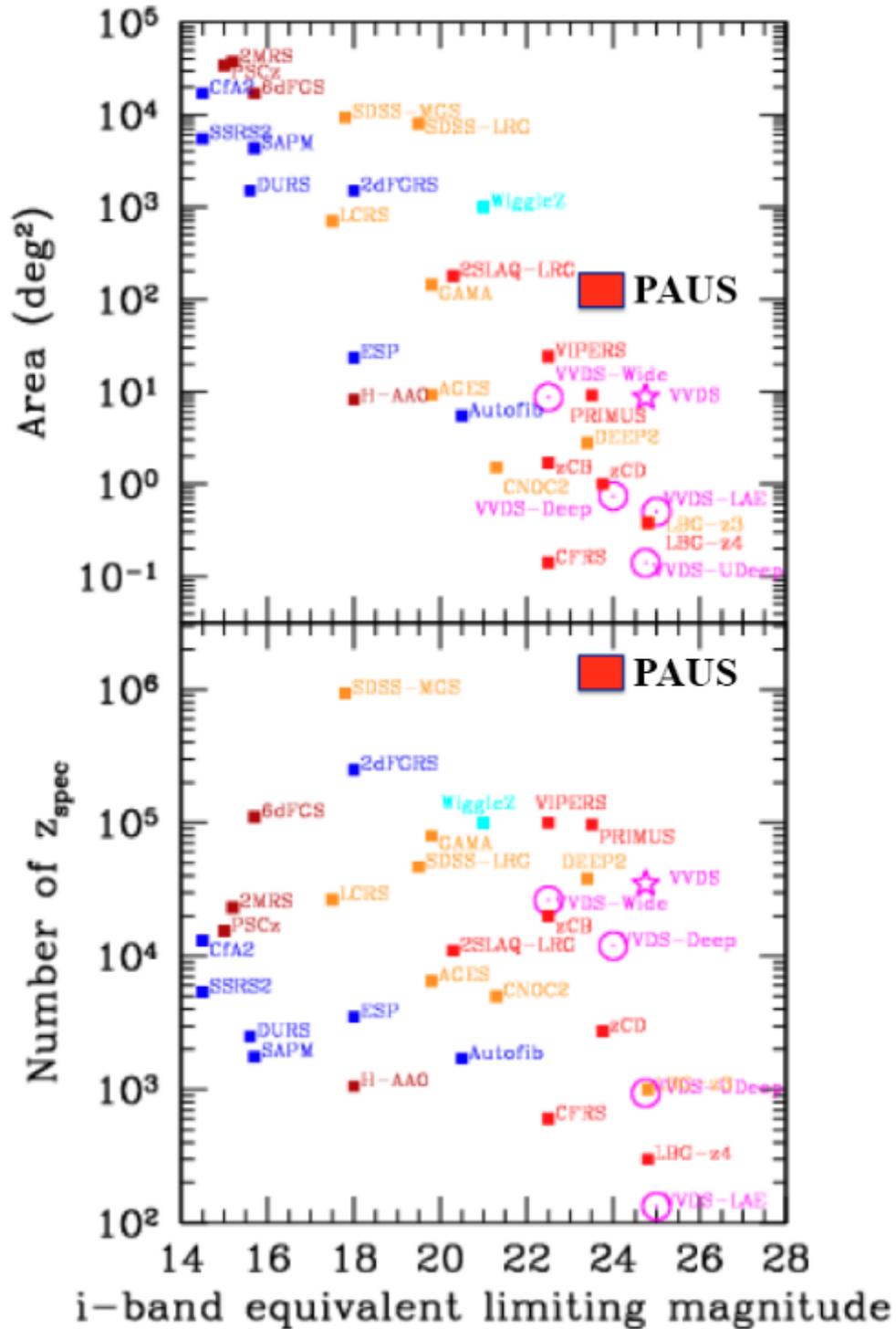
Figure 1.6: A comparison of the performance of galaxy surveys expressed in terms of area and the number of objects observed as a function of the *i*-band limiting magnitude. Taken from https://pausurvey.org/pausurvey/.

solid angle and to a certain limit in brightness. In particular, the brightness limit is plotted on the x-axis for both the upper and lower panels, while the y-axis in the top panel gives the area covered by the survey and in the bottom panel this axis shows the number of unique redshifts measured. Although PAUS has not yet reached its target solid angle, it ranks quite highly in both area, depth and the number of galaxies with a 100% completeness characteristic of a photometric survey as we discuss in the next section. The high completeness of PAUS makes this survey of particular interest for many applications, for example it can be used as a parent survey for another survey without the need for spectroscopic measurements. As well, the narrow bands used in PAUS make this survey unique with the potential of identifying galaxies with strong emission lines that can be seen when the redshifted line falls within a specific filter, while being invisible to the others as too faint to be observed. PAUS is the main survey used in this thesis and because of that Sect. 2.1 will be devoted to a more detailed description of this survey.

1.5   Photometric and spectroscopic surveys

Redshift surveys rely on different redshift measurement or estimation techniques. These might be based on spectroscopic measurement or photometric estimation. Both techniques present advantages and disadvantages that we explore in this section.

On one hand, spectroscopic surveys generally provide more accurate redshift estimates. On the other hand, a photometric approach is less demanding in terms of time at the telescope facilitating the collection of a larger and more homogenous sample of galaxies. To maximise the efficiency of spectroscopic surveys, there are two main techniques that allow for the collection of multiple object during the same pointing. One is the use of fibres located at the exact locations of the objects targeted in a specific pointing. Example of fibre fed surveys are 2dFGRS (Colless et al., 2003), SDSS (York et al., 2000), DESI (DESI Collaboration et al., 2016),
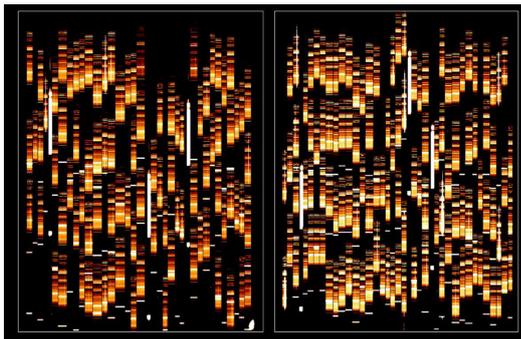
Figure 1.7: Two of the four VIMOS quadrants in a low resolution spectroscopy mode. In this example, 221 galaxies plus 6 reference objects have been observed. Referenced objects are stars placed in square holes to ensure a good alignment. The exposure time is 900 seconds. `http://vipers.inaf.it/`

4MOST (de Jong et al., 2019). The second technique is called multi-object spectroscopy (MOS). The MOS mode consists of a mask with multiple slits located at the positions of the target galaxies, this means one mask for every single pointing. Example of surveys that use MOS are zCOSMSOS (Lilly et al., 2009), DEEP2 (Newman et al., 2013) and VIPERS (Guzzo et al., 2014; Scodeggio et al., 2018). Since VIPERS has been widely used for this study, I will focus on MOS as an example of spectroscopic technique. When observing in MOS mode, each mask must be set directly in the focal plane and the result is the object image dispersed along one axes of the CCD plane (see Figure 1.7). Although this mode optimises the number of objects for a fixed telescope time, it introduces a bias when evaluating clustering statistics or counting galaxies. As can be seen in Figure 1.7, along the dispersion axes we cannot measure galaxies closer than a certain distance defined by the resolution of the spectrum (the higher the resolution the bigger the scale we are unable to probe). This problem can be addressed by multiple pointings at the same area of sky however, this will results in a loss of time efficiency. Fibre-based spectroscopy suffers a similar problem (although to a lesser extent).

Photometric surveys instead are not affected by this problem. Photometric redshifts also have the advantage that they tend to reach fainter galaxies than spectroscopic ones. Although spectroscopic redshifts have higher accuracy ($\sigma_{z_{\mathrm{spec}}} \sim 10^{-4}(1+z)$ versus $\sigma_{z_{\mathrm{photo}}} \sim 10^{-2}(1+z)$), the photometric approach is less de-

manding in terms of time at the telescope and this is crucial when the number of redshifts collected is one of the most important features of a survey.

Here, we are going to use the data from PAUS which is based on forced photometry plus a template based SED fitting to estimate photometric redshifts (Eriksen et al., 2019) and when possible we are going to use spectroscopic redshifts in the overlapping areas with VIPERS or COSMOS. The technique of forced photometry consists of estimating fluxes for galaxies from the imaging knowing *a priori* the exact position of the galaxy from a parent survey. With forced photometry, it is key to select carefully the radius within which the forced photometry flux should be measured. Ideally it should contain the entire galaxy, but that is not always possible. Note also that with forced photometry it is not necessary to resolve the galaxy to estimate its flux, as only the sky coordinates and the radius of the object are required. As mentioned, photometric surveys are not affected by the problem of having galaxies too close to each other to be measured, because they are based on imaging and the space occupied by the slits or the fibres in a spectroscopic survey is not an issue.

The performance advantage of PAUS lies in the number of objects observed in a single pointing, as the completeness is 100%, and the accuracy of the photometric redshift obtained with narrow bands is higher than for normal broad band surveys. Narrow band filters allow the spectral energy distribution of the galaxies to be sampled using more wavelength points, allowing a more accurate fit using a library of galaxy templates. The best fit of the redshifted template determines the photometric redshift. This approach is less accurate than measuring the shift of a feature in a spectrum obtained by a spectroscopic survey. This is because the SED used in the photometric redshift estimation is generally lower resolution and poorer signal-to-noise than spectroscopic measurements.

Another reason why photometric redshift estimates based on template fitting are less accurate than spectroscopic measuremenrs is that a misclassification between galaxies and stars can happen more easily with photometric data. The reason is

that when the spectrum of an object is available, it is easier to distinguish between a galaxy and a star, especially because the shift of the spectrum would yield a redshift close to 0, while when trying to fit a star with a galaxy template, as it could happen in a photometric survey based on template fitting, a random redshift may be assigned.

The conclusion is that photometric and spectroscopic surveys both have advantages and disadvantages, and PAUS with the use of the narrow bands filters inherits the high speed and the completeness typical of a photometric survey with an accuracy on redshifts estimates approaching the one of spectroscopic surveys.

1.6   Outline of the thesis

The focus of this thesis is to connect observations to physically motivated models of galaxy formation. I will describe in Chapter 2 the observational dataset from the Physics of the Accelerating Universe Survey (PAUS), including the observational runs I took part in (Sect. 2.1.2) and the tests I have carried out to improve the quality of the survey (Sect. 2.1.3). One of the important tests is presented in Sect. 2.1.3.4 where I analyse the current way of assessing the quality of photometric redshift estimates. In Chapter 3, I explain the main characteristics of the galaxy formation model used (Sect. 3.1.1) and the construction of a mock catalogue for PAUS (Sect. 3.3). In particular I explain the main features of the new P-Millennium N-body simulation (Sect. 3.2.2) and how the Durham semi-analytical model `GALFORM` takes advantage of this simulation. In Sect. 3.4 I will shortly describe how I improved the performance of `GALFORM` in order to deal with the higher resolution of the P-Millennium N-body simulation and the large number of filters used by the PAUS survey.

Chapter 4 presents some of the main results of the thesis in which I use the PAUS observations to test the `GALFORM` model. In particular, Fig. 4.7 and Fig. 4.9

in Sect. 4.3.2 test the predictions of the `GALFORM` observer frame colours over a wide range of redshifts covered by the PAUS observations.

In Chapter 5 the focus moves to the colour-magnitude relation in the VIMOS Public Extragalactic Redshift Survey (VIPERS). I analyse how the bright end of the colour magnitude relation can help understand the mechanisms that suppress star formation. Different variants of the `GALFORM` model are tested to analyse the effect of the AGN feedback on the bright edge evolution in the colour magnitude relation (see Fig. 5.9).

In a change of topic, Chapter 6 shows how the skills I developed in my astronomy training and research can be applied to industrial applications. I report in Sect. 6.1 on the project I contributed to for Procter&Gamble to help optimise the density of the laundry powder. In Sect. 6.2 I report on the work I have done for the National Health Service (NHS) to predict the normative vital signs in healthy babies to help identifying unhealthy babies earlier, thereby improving patient outcomes. The NHS work has been submitted for publication in a medical journal while the P&G work was showcased in the Science Technology Facilities Council annual Impact Acceleration Award report.

In Chapter 7, I summarise the main achievements of the thesis and discuss possible future directions that the research could follow.

Observational Data

In this chapter I give an overview of the observational data used in this thesis. In Sect. 2.1 I describe the PAUS survey which has been the focus of my PhD, and in Sec. 2.2 the VIPERS survey which I have used to complement the PAUS photometric redshifts with spectroscopic measurements and to carry out a galaxy evolution study.

PAUS is a survey with a novel observing set-up, which started collecting data at the William Herschel Telescope (WHT) in 2015. I have joined the PAUS team in the late 2017 and since then I have performed a variety of tests and investigations that are summarised in Sect. 2.1.3; these were carried out with the aim of familiarising myself with the data and to help the work of the wider collaboration. In this spirit, I also took part in four PAUS observing runs where I learnt the procedures for carrying out observations for a photometric survey; this work is summarised in Sect. 2.1.2. PAUS has stopped collecting new data since about a couple of years now, because of the installation of the new spectrograph WEAVE at the WHT. Because of this, the team is now focusing on obtaining better reductions of the currently available data and to exploit their scientific potential rather than getting new data. With this in mind we can consider the main phase of PAUS data acquisition finished.

The analysis of PAUS data, in conjunction with the interpretation provided

by the use of the galaxy formation model described in Chapter 3 is reported in Chapter 4. The use of the VIPERS spectroscopic data, compared with same physically motivated galaxy formation model, resulted in the publication reported in Chapter 5.

2.1 The PAU Survey

2.1.1 Motivation for the survey

The Physics of the Accelerating Universe Survey (PAUS; Eriksen et al. 2019) is a photometric survey which is unique since it aims to bridge the gap between small solid angle, deep 'pencil-beam' surveys, like zCOSMOS (Lilly et al., 2007) or DEEP2 (Newman et al., 2013), and wide-area, shallow spectroscopic galaxy surveys, like GAMA (Driver et al., 2009) or DESI Bright Galaxy Sample (BGS) (DESI Collaboration et al., 2016; Zarrouk, 2021). PAUS is surveying large contiguous areas, reaching a high density of galaxies with narrow band imaging, achieving sub-percent photometric redshift accuracy for many galaxies (Eriksen et al., 2019). To achieve this precision, the survey has been designed to use 40 narrow band (NB) filters, with an equivalent width of 13 nm and a regular spacing of 10 nm, covering the wavelength range from 450 nm to 850 nm (see Fig. 2.1 for a comparison with standard broad band filters). This use of NB filters makes the photometric redshifts from PAUS up to ten times more precise than those attainable from a standard broad band (BB) survey, reaching an accuracy of at least $0.004\,(1+z)$ for over 50% of the galaxies down to $i_{AB} \approx 22.5$ (Eriksen et al., 2019; Alarcon et al., 2021).

PAUS has collected data in 4 fields: COSMOS, W1, W2, W3, W4 (see Fig. 2.3). Because of the observational strategy and the design of the filter trays, described in Sect. 2.1.2, while the aim is to cover all the area with 40 NB, this is not always true while the survey is progressing. This means that different part of the sky have been

observed with a different number of filters. In Table 2.1, we report the area that has been covered by a specific number of narrow band filters. In addition to the PAUS narrow band filters, there are always 5 broad band optical filters available from the parent catalogue (u, g, r, i and z) in each of the fields (not counted in the table).

	Area photo-z	Area 40 NB	Area 30 NB	Area 20 NB	Area 10 NB
COSMOS	1.5 deg^2 (60×10^3)	1.8 deg^2	2.2 deg^2	3.2 deg^2	3.8 deg^2
W1	9.7 deg^2 (331×10^3)	11.0 deg^2	11.0 deg^2	13.0 deg^2	15.0 deg^2
W2	10.2 deg^2 (545×10^3)	13.0 deg^2	15.0 deg^2	17.5 deg^2	20.0 deg^2
W3	20.4 deg^2 (740×10^3)	21.0 deg^2	21.0 deg^2	22.0 deg^2	26.0 deg^2
W4	0.0 deg^2 (0)	0.2 deg^2	0.4 deg^2	0.8 deg^2	1.0 deg^2
TOTAL	41.8 deg^2 (1.7×10^6)	47.0 deg^2	49.6 deg^2	56.5 deg^2	65.8 deg^2

Table 2.1: Areas covered by PAUS observations with a minimum of NB filters as specified in each column. The first column is the area for which photometric redshift estimates have been obtained. W4 has always been considered low priority and hence no photo-z estimated have been made so far. In the first column I also report the approximate number of galaxy with photometric redshift measurements. PAUS decided to estimate photometric redshifts only for those galaxies with observations for at least 35 NB filters.

Thanks to its depth and galaxy number density (tens of thousands of galaxies per deg^2 with a median redshift of $z \sim 0.5$), PAUS will result in one of the most detailed studies of intermediate-scale cosmic structure ever undertaken. With these features, PAUS has the capability to probe galaxy clustering in the transition from the linear to non-linear regimes (Stothert et al., 2018a). The NB and BB imaging can be modelled to assign intrinsic properties to galaxies, allowing clustering to be measured as a function of these galaxy properties, and hence to constrain models of galaxy formation. Moreover, PAUS can be used to advance the study of galaxy groups since spectroscopic surveys are either too sparse (e.g. BOSS; Dawson et al. 2012), too shallow (e.g. GAMA;Driver et al. 2009), too narrow (e.g. zCOSMOS; Lilly et al. 2007) or a combination of these characteristics (e.g. VIPERS; Guzzo et al. 2014; Scodeggio et al. 2018). The high accuracy photometric redshifts from PAUS will allow galaxy group finding algorithms to be applied (Stothert et al., 2018a,b), though we do not discuss this possibility further here. Other science

goals for PAUS span from the study of the intrinsic alignments in galaxies to the constraining of cosmological parameters through the study of redshift space distortions, baryonic acoustic oscillations and correlation function.

PAUS is using the specially designed PAUCam (Castander et al., 2012), an optical wide field imaging camera (1 deg^2 Field-of-View, FoV) installed at the prime focus of the William Herschel Telescope (WHT) on La Palma, Spain. The camera is installed with 11 filter trays, each tray contains 18 filters meant to cover the 18 CCDs of the camera (an example of a PAUCam filter tray is shown in Fig. 2.2). Of these 11 trays, 6 are used for broadbands. For these broad-band trays all the 18 filters are the same one (u, g, r, i, z, or Y). The other 5 trays are used for the NBs. Specifically each NB tray is designed to cover the 8 central CCDs with 8 different NB, while the 10 filters on the sides are some configurations of broad-bands filters (see an example in Tables 2.2). This choice has been made to ensuring that the NB filters do not suffer from vignetting, which affects the CCDs on the edges of the focal plane. The large number of NB filters, which are a unique feature of PAUS, makes this survey special, as the expected photometric redshift accuracy will be sufficient to be sensitive to redshift space distortions (Eriksen and Gaztañaga, 2015a,b,c). As an imaging survey, PAUS ought to be more homogeneous in its targets with photo-z compared to most spectroscopic surveys. However, the PAUS photo-z accuracy might not necessarily be homogeneous and would need to be accounted for in most science analyses.

2.1.2 Observing runs

PAUS started its observation in 2015 and since then it has successfully applied for time every semester at the William Herschel Telescope (WHT), a 4.2 m diameter telescope based in La Palma (Spain). The instrument mounted on the WHT for PAUS observations is a large field camera (PAUCam) specially designed for this survey (see Castander et al. 2012 for further details). Because of the commissioning

---

*Note that PAUCam has 11 trays, numbered as follows: 0-5 broad-bands, 8-12 narrow-bands.
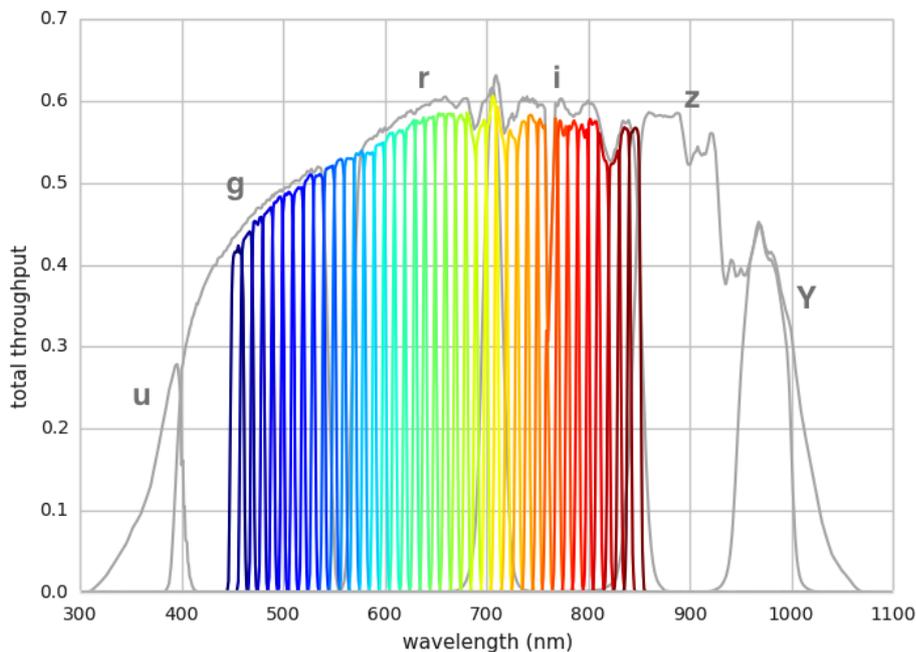
Figure 2.1: Transmission curves for the 40 PAUCam narrow-band filters, together with the u, g, r, i, z and Y PAUCam broad band filters for reference (note that not all of these bands are available in the PAUS photometry). These curves include the effects due to the atmospheric transmission, the telescope optics, the filter and the quantum efficiency of the detector. Image taken from the PAUS website: `https://pausurvey.org/paucam/filters/`.

FT_NB455_NB525 (tray id 12)	
CCD 1	NB455
CCD 2	NB465
CCD 3	NB475
CCD 4	NB485
CCD 5	NB495
CCD 6	NB505
CCD 7	NB515
CCD 8	NB525
CCD 9-18	all broad-band g

Table 2.2: List of filters for an example filter tray (number 12)*. The first 8 filters are the ones that cover the inner CCDS, while from 9 to 18 are the outer ones as described in the text. Tray number 12 is made of the bluest NB filters (those most affected by the presence of the Moon, as the Moon is brighter at bluer wavelengths).

of a new instrument at WHT, the WEAVE spectrograph, combined with the Covid-19 pandemic, December 2019 was the last PAUS observing run, in which I also took
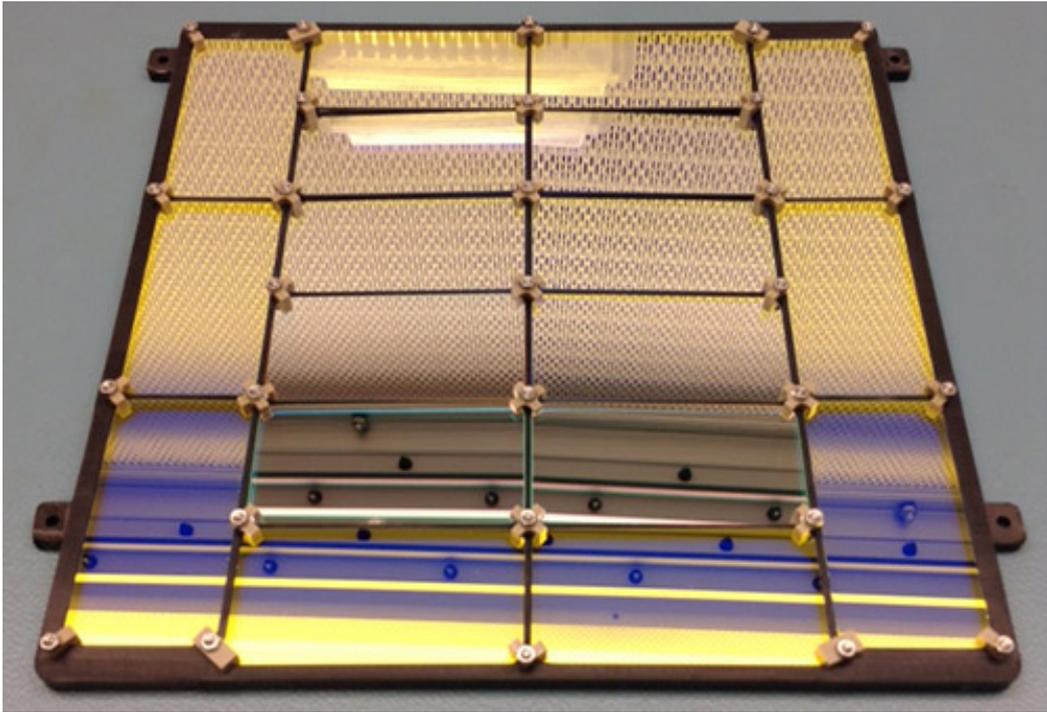
Figure 2.2: Example of a PAUS filter tray, the 8 central filters are narrow-bands while the 10 filters on the sides are broad-bands and are not used by the survey. A broad band PAUS filter tray looks the same but every CCD is covered by the same broad-band filter. Image from the PAUS website: `https://pausurvey.or g/paucam/filters/`.

part[*]. I have taken part in four observing runs (ranging from 4 to 7 days each) at the WHT telescope with the aim of learning the observing strategy of the PAU survey.

The observing shift consists mainly of two parts: the calibration of the telescope in the afternoon and the observing time during the night. Afternoon calibrations include first checking the temperature and pressure of the camera and then acquiring BIAS and FLAT FIELD images. These procedures are aimed to calibrate the CCD. In particular, we are setting the right parameters in order to convert the number of electrons[†] read out from the CCD into an incident number of photons (i.e. the flux). Specifically the BIAS is an image with no light entering the focal

---

[*]There are possibilities for PAUS to observe again in the future, but for this thesis all data are updated to the 2019B observing run.

[†]Photons coming from the source strike the CCD and release electrons that need to be converted into a number of photons in order to obtain the flux.

plane and it is obtained by simply keeping the dome and the petals of the telescope closed. In this way we are setting a certain value of the CCD electric current to be the zero point of our observations. We do this because the CCD works in a linear regime (number of incident photons proportional to the number of electrons released) only for certain values of the electric current. The result of this exercise is that in case of no photons striking the CCD then the electric current released will be the bias current. The BIAS is just the CCD image generated by this bias current. Hence, every scientific image needs to be bias subtracted to obtain the true value of the flux. The reason why the BIAS is an image and not just a number is that every pixel behaves slightly differently. Subtracting the BIAS takes into account all of the imperfections of the CCD pixels. Since the BIAS is a calibration with no light, we also want to calibrate the CCDs when they are actually measuring photons. That is why we measure FLAT FIELD images. These are images of a uniform light source used to calibrate the slope of the proportionality between photons in and electrons released. Some different techniques are used to obtain a uniform source of light. One is to directly observe the light of the sunset. In the case of PAUS, there are specially designed lamps inside the dome which produce uniform light*. It is important at this stage to leave the dome closed, so that no spurious light from other sources can enter, and open the petals of the telescope, so that the light from the lamp can reach the focal plane.

After the BIAS and FLAT FIELDS are taken, everything is set to start observing. Observations take place 20 minutes before the end of twilight. This is because the first thing we want to observe is a calibration star. The calibration star is an SDSS star whose flux is known in order to compare the measured flux and obtain the so-called zero point (that is used to convert the CCD output for the number of photons in units of flux). The observing strategy, i.e. deciding which filter tray, which exposure time and which field to observe, is mainly driven by the Moon's phase and its position on the sky. Basically the aim is to observe at

---

*It has to be uniform spatially, in wavelength and intensity.

any time of the night a field that is furthest from the Moon and to use a redder filter tray for pointings affected by larger fractions of moonlight*. The exposure time depends on the filter tray in use and on the quality of the sky with worse conditions requiring longer exposure times. Specifically, we report in Table 2.3, the time of exposure associated to each filter tray. This values are the standards that we use for values of the seeing lower than $1''$. When the sky conditions are worse, with seeing between $1''$ and $1.6''$, the exposure time is increased as computed by an algorithm written by the PAUS team, with a maximum value of 120 seconds. For the worst sky conditions, i.e. seeing larger than $1.6''$, data are discarded.

Narrow Band Tray ID	12 (bluer)	11	10	9	8 (redder)
Exposure time [sec]	90	90	100	100	120

Table 2.3: Nominal exposure time for each narrow band filter tray in seconds. The numbering of the tray goes from 8 at redder wavelengths to 12 for bluer wavelengths. Since the sky is noisier at redder wavelengths, longer exposure times would be needed to obtain a good signal to noise ratio, hence the strategy is to avoid the redder trays (i.e. tray 8 and 9) unless the Moon is close to the field or it's close to be full Moon.

2.1.3 Characterisation of PAUS data

The PAUS team is constantly working to improve the data reduction and the performance of the photo-z codes. As a member of the PAUS team, I helped with several tests of the PAUS data. In this section I summarise the more relevant ones. In particular the work on the emission lines described in Sect. 2.1.3.2 was useful for the publication of Alarcon et al. (2021) and the work on the k-correction, described in Sect. 2.1.3.3 enabled the clustering measurements in Johnston et al. (2020).

2.1.3.1 Study of force photometry aperture radius

PAUS aims to cover the COSMOS field (COSMOS/D2; Capak et al. 2007) and the four wide fields of the Canada-France Hawaii Telescope Legacy Survey (CFHTLS;

---

*Since the Moon light peaks at blue wavelengths, a filter sensitive to redder wavelengths is less sensitive to the presence of the Moon.
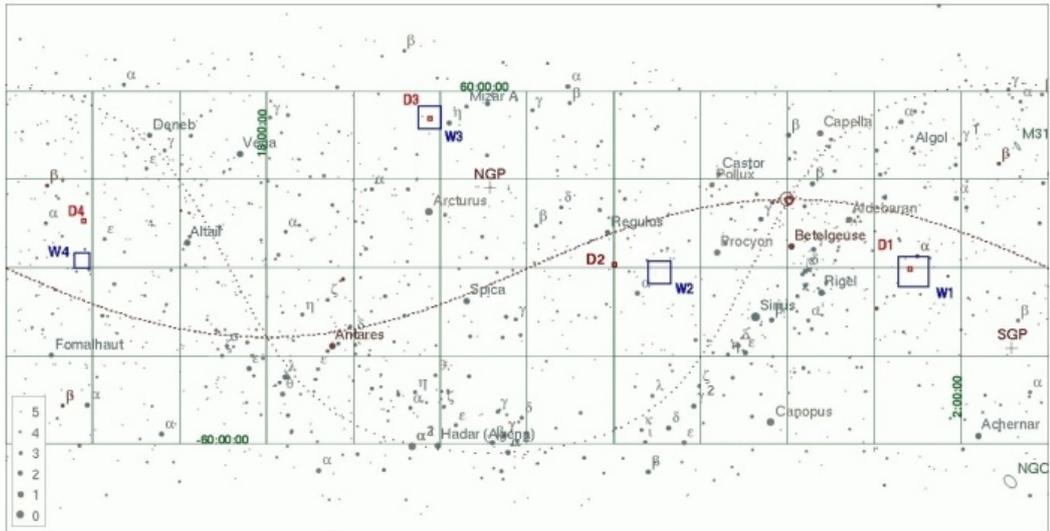
Figure 2.3: The CFHTLS wide (W1, W2, W3, W4) and deep (D1, D2, D3, D4) fields. Out of these fields, PAUS is observing all of the wide fields and D2, which corresponds to the COSMOS field. Image from CFHTLS website: `https://www.cfht.hawaii.edu/Science/CFHLS/cfhtlsdeepwidefields.html`

Erben and CFHTLenS Collaboration 2012; Heymans et al. 2012; see the location of the fields in Fig. 2.3: W1, W2, W3 and W4). For each field, PAUS collects photometric images in all of the NBs, with the aim of performing forced aperture photometry using the broad band photometry. This means that independent of the NB image signal-to-noise ratio, PAUS uses the position of the galaxies from a parent survey with BB images and extracts the NB image flux within a certain radius aperture. Information about the radius to be used also comes from the parent catalogue. For example, one choice is to use the half-light radius of a galaxy, as measured in a particular band. Early photometric results for galaxies in the COSMOS field, which used the COSMOS data as the parent survey (Scarlata et al., 2007), are already available in Eriksen et al. (2019) and Alarcon et al. (2021).

When reducing data from the wide fields, another parent survey needs to be used as there is no longer overlap with COSMOS. The choice of this new parent survey is very important as it may introduce a bias, especially if the definition of the radius is different from that used in the COSMOS field. I contributed to the choice of the parent catalogue for the wide fields by analysing two surveys: the

Canada-France Hawaii Telescope Legacy Survey (CFHTLS; Cuillandre et al. 2012; Coupon et al. 2009; Gwyn 2012; Hoekstra et al. 2006) and the Canada-France Hawaii Telescope Lensing Survey (CFHTLenS; Erben and CFHTLenS Collaboration 2012; Hildebrandt et al. 2012). Even if the two surveys use the same observed data, they have been reduced in different ways and focusing on different areas, according to their science goals. While CFHTLS covers both the wide and deep fields (D1, D2, D3, D4, W1, W2, W3, W4), CFHTLenS covers just the wide ones (W1, W2, W3, W4). Since COSMOS overlaps only with the Deep-2 (D2) field[*], an *object-by-object* comparison between the radius in COSMOS/D2 and the radius in any of the fields of CFHTLenS is not possible. Hence, the first analysis I performed was a statistical comparison between the distribution of radii in COSMOS/D2 and in CFHTLenS/W3 (Fig. 2.5). In fact, as it can be seen from the map in Fig. 2.3, while D1 and D3 overlap with their respective wide fields W1 and W3, this does not happen with D2 and D4 which are outside W2 and W4. In the COSMOS case the radius[†] is estimated by Scarlata et al. (2007) and is defined as the semi-major axis length of the ellipse encompassing 50% of the total light coming from the galaxy in the i-band. In the case of CFHTLenS, the radius[‡] is estimated by the bayesian algorithm *Lensfit*, giving as well an estimate of the size of the galaxy along the semi-major axis (Miller et al., 2007). After that, I used CFHTLS as a "bridge" comparing, *object-by-object* COSMOS/D2 with CFHTLS/D2 and then (assuming that all the CFHTLS Deep fields D1, D2, D3, D4 adopt the same definition of radius) I compared CFHTLS/D3 with CFHTLenS/W3. The top panel of Fig 2.4 shows the squared difference between the COSMOS radius and the CFHTLS radius as a function of the reference magnitude, in the overlapping region D2. The bottom panel of Fig 2.4 instead shows the squared difference between the CFHTLS radius and the CFHTLenS radius in the overlapping region D3/W3. The median squared difference between COSMOS and CFHTLS radius is approx-

---

[*]which is observed in CFHTLS but not in CFHTLenS

[†]r_{50} is the official name in the catalogue.

[‡]*scalelength* is the official name in the catalogue.
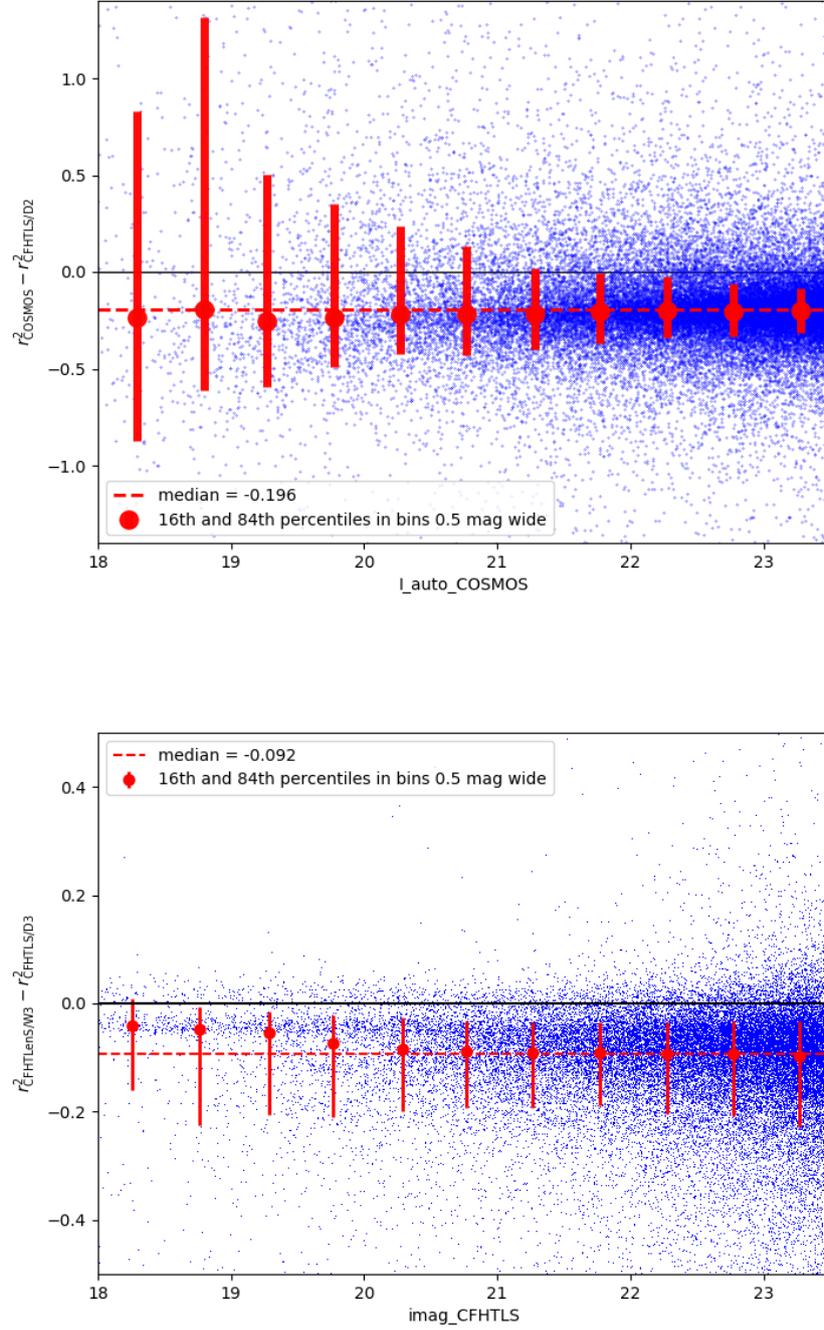
Figure 2.4: **Top**: squared difference (in units of arcsec^2) between the radius in COSMOS/D2 and the radius in CFHTLS/D2 as a function of the reference magnitude in COSMOS up to $i_{AB} = 23.5$. Points represents the median of the squared difference in bins of magnitudes and bars show the 16th and 84th percentile. The red dashed horizontal line shows the median of the squared difference for the entire sample, indicating the square of the offset (in arcsec^2) between the two radii. **Bottom**: same as the top but for the comparison of radii between CFHTLS/D3 and CFHTLenS/W3.

imately ~ 0.2 arcsec^2, while between CFHTLS and CFHTLenS is approximately ~ 0.1 arcsec^2. Analysing the distribution of the radii, we find for COSMOS a standard error of $\sigma_{\text{COSMOS}} \sim 0.002$ arcsec^2 while for CFHTLS and CFHTLenS $\sigma_{\text{CFHTLS}} \sim \sigma_{\text{CFHTLenS}} \sim 0.0002$ arcsec^2. This means that the differences we have found are still too large to consider the radius between COSMOS and CFHTLenS consistent to each other.

We can improve the agreement by applying a linear transformation to the radii. Looking at the statistical distribution of radii of COSMOS and CFHTLenS, we can impose the median and the σ_{68}, defined as the difference between the 16th and 84th percentile, to be the same and derive the linear transformation needed. Calling a and b the coefficients of the linear transformation to be found, we require that:

$$\text{median}(a + b \times r_{\text{CFHTLenS}}) := \text{median}(r_{\text{COSMOS}})$$

$$\sigma_{68}(a + b \times r_{\text{CFHTLenS}}) := \sigma_{68}(r_{\text{COSMOS}}). \tag{2.1}$$

Since σ_{68} is a linear operator, meaning that $\sigma_{68}(a+b\times r) = a+b\times\sigma_{68}(r)$, it follows that:

$$a = \text{median}(r_{\text{COSMOS}}) - \frac{\sigma_{68}(r_{\text{COSMOS}})}{\sigma_{68}(r_{\text{CFHTLenS}})} \times \text{median}(r_{\text{CFHTLenS}}).$$

$$b = \frac{\sigma_{68}(r_{\text{COSMOS}})}{\sigma_{68}(r_{\text{CFHTLenS}})} \tag{2.2}$$

The PAUS collaboration decided to use the CFHTLenS data to define apertures, because this survey has been designed for lensing purposes and this is also one of the goals for PAUS. Using the Equations 2.1 and 2.2 I found the values to transform CFHTLenS radii to COSMOS-like radii:

$$r_{\text{COSMOS-like}} = -0.043 + 1.757 \times r_{\text{CFHTLenS}}. \tag{2.3}$$

We note that taking the squared root from the standard error on the distribution of COSMOS squared radius, we find an error for the radius of $\sigma_{\text{COSMOS}} = 0.045$ arcsecond and doing the same for CFHTLenS we find $\sigma_{\text{CFHTLenS}} = 0.014$ arcsecond,
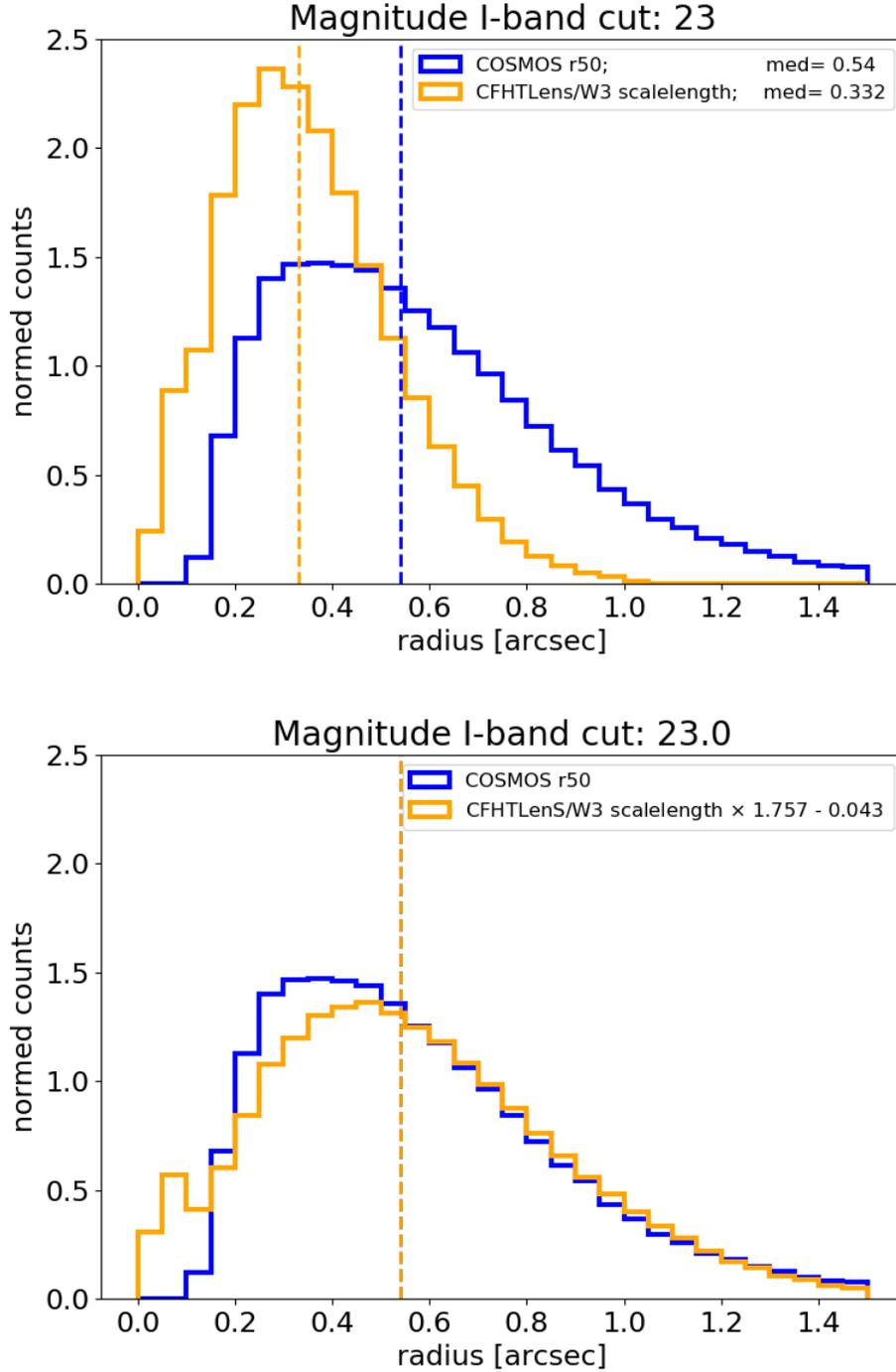
Figure 2.5: **Top**: Distribution of the COSMOS radius (blue histogram) and the CFHTLenS radius in the W3 field (orange histogram). **Bottom**: Same as the top panel but after having applied the linear transformation of Eq. (2.3) to the CFHTLenS radii. Vertical dashed lines show the medians of the respective distributions.

hence we can consider 0.045 arcsecond as an upper limit to the errors on the radius estimates. We can see in the top panel of Fig. 2.5 the original distribution of the COSMOS radius (blue histogram) and of the CFHTLenS radius (orange histogram). The medians of the distribution differ by about $\sim 0.21''$, with the COSMOS radii extending for higher values. Imposing the medians and the σ_{68} of the two distribution to be the same as per Eq. (2.3) we obtain the distribution shown in the bottom panel. The two distributions that now are consistent, with the median and the σ_{68} being the same by construction, ensure us that the forced photometry is not biased *a priori* between the data in the COSMOS field and the data in the CFHTLenS wide fields, as the distribution of radii in which the photons are considered for the photometry is in agreement. For this reason, this is the technique that the PAUS collaboration has adopted to obtain radii for the forced photometry in wide fields.

2.1.3.2   Empirical relations for emission line ratios

Unlike spectroscopic redshifts which come directly from the measurement of the shift of specific features in the spectrum, photometric redshifts are derived from fitting the observed spectral energy distribution (SED) of a galaxy to theoretical stellar population synthesis (SPS) models or empirical templates, derived from high quality observed spectra of galaxies with known redshifts. In the case of theoretical spectra, to improve the quality of the fit, information about emission lines can be taken into account. This is because we are using NB imaging data in PAUS and the narrow width of the filters means that the luminosity of the emission line can have a noticeable impact on the flux measured in a narrow band (Stothert et al., 2018b), and so should be included in the theoretical SED. Eriksen et al. (2019) used a fixed set of emission line ratios in their analysis of PAUS, following the approach and values used by Ilbert et al. (2009). The values of these ratios are shown in Table 2 of Eriksen et al. (2019) and plotted in Fig. 2.6. The emission line ratios vary much more than this and, in principle, better modelling of these ratios can improve the
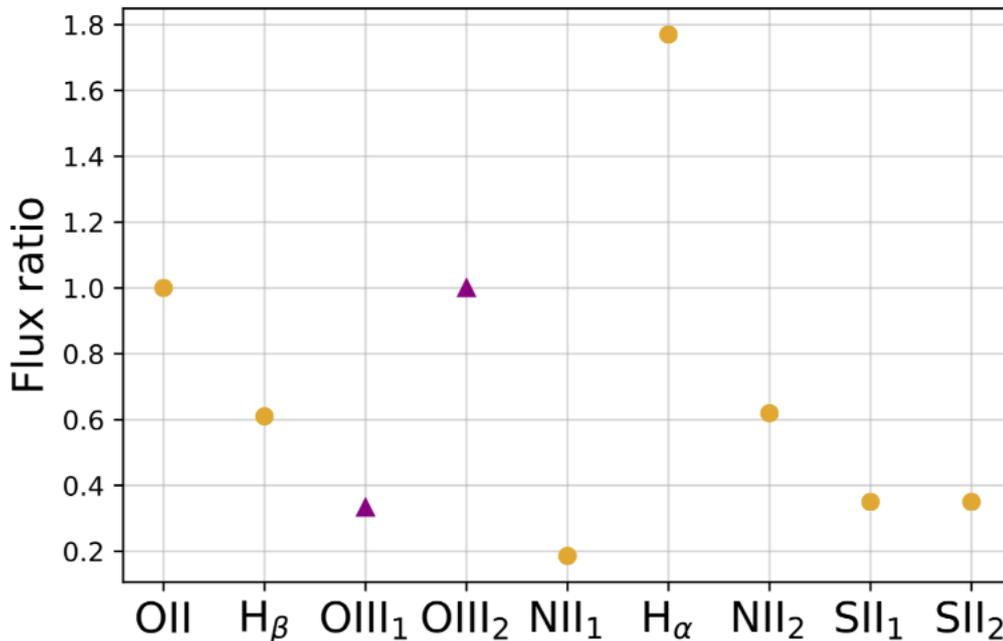
Figure 2.6: The fixed emission line ratios used in the fitting of theoretical SEDs to the PAUS data in the COSMOS field in the photometric redshift estimation by Eriksen et al. (2019). The filled circles are normalised to the OII line luminosity, while the filled triangles are normalised to the OIII$_2$ line

determination of photometric redshifts.

For this reason I considered empirical relations for some specific Baldwin-Philips-Terlevich (BPT) diagrams (Baldwin et al., 1981). These diagram shows the relation between some specific emission line ratios. The more relevant ones, considering the PAUS wavelength range, are:

- $[NII]_{\lambda 6584}$ / H_α versus $[OIII]_{\lambda 5700}$ / H_β

- $[SII]_{\lambda\lambda 6717}$ / H_α versus $[OIII]_{\lambda 5700}$ / H_β

- $[OI]_{\lambda 6300}$ / H_α versus $[OIII]_{\lambda 5700}$ / H_β

We show in Fig. 2.7 an example of the first BPT relation, which has also been used to test the predictions of galaxy formation models in Baugh et al. (2021). The data in Fig. 2.7 (light-blue points) are from the DR2 release of the GAMA survey (Driver et al., 2011). In particular we used the table *EmLinesPhys.fits* available
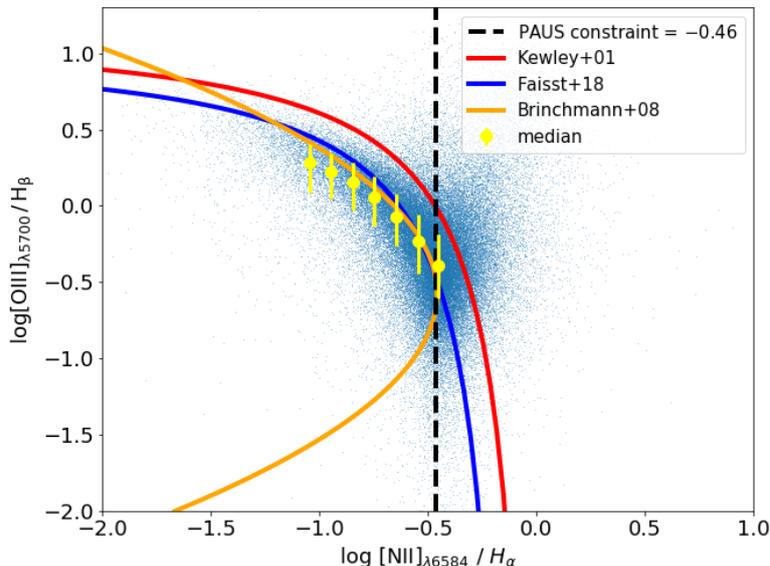
Figure 2.7: Empirical modelling for a particular BPT diagram based on specific emission line ratios, i.e. $[NII]_{\lambda6584}$ / H_α versus $[OIII]_{\lambda5700}$ / H_β. The data (blue points) comes from the GAMA survey (Driver et al., 2011). The vertical dashed black line is the PAUS assumption which brings no information about the $[OIII]/H_\beta$ ratio as they only fix the $[NII]/H_\alpha$ ratio. The yellow filled circles are median values of $[OIII]/H_\beta$ in bins of the $[NII]/H_\alpha$ ratio. The error bars represent the 25th and 75th percentiles. The lines show previous estimates of these emission line ratios derived from other datasets: Brinchmann et al. (2008) and Faisst et al. (2018) (orange and blue line respectively) provide empirical relations for this specific BPT diagram. Kewley et al. (2001) instead (red line) provide an empirical relation to separate star forming galaxies (below the red line) and AGN (above the red line).

on the GAMA website at `http://www.gama-survey.org/dr2/schema/table`
`.php?id=196`. This table select redshifts to be in the range $0.002 < z < 1.35$
(median redshift $z \sim 0.245$) and with a redshift quality selected by NQ > 2 and a
signal to noise ratio $S/N > 4$. This combines with the survey magnitude limit of
$r < 19.8$. The vertical dashed line shows the PAUS assumption, which is a fixed
value for the $[NII]/H_\alpha$ ratio (independent of the value of $[OIII]/H_\beta$). The yellow
filled circles show the median of $[OIII]/H_\beta$ for bins of $[NII]/H_\alpha$, each 0.1 dex wide.
The error bars are obtained from the 25th and 75th percentiles. The other coloured
lines come from the literature as indicated in the legend, and show the line ratios
reported for other observational datasets at a similar redshift to the GAMA sample

plotted. We can see that the PAUS assumption for the [NII]/H_α line ratio, although roughly describing the bulk of the population, may be considered reasonable as a first approximation. Using instead a relation like that reported by Faisst et al. 2018 (dark blue line) can help improve the SED fitting by incorporating a more realistic variation of the emission line ratios, which could possibly lead to better photometric redshift estimation.

2.1.3.3 First order approximation for the K-correction

As explained in Sect. 1.3, when we observe a galaxy, the flux that we receive depends on the distance of the object or equivalently its redshift. This is due to the fact that the number of photons that we receive decreases with increasing distance, following the inverse square law. The number of photons that we receive is not the only thing changing with the distance. The wavelength of the emitted photons is changing as well. This means that when we want to translate the observed properties into intrinsic properties of galaxies, we also need to take into consideration this change in wavelength. Specifically, we observe the galaxy in a set of filters fixed in wavelength at the telescope, the observer frame, as we probe galaxies at increasing redshift, we are actually probing shorter wavelengths in the rest-frame of the galaxy. The k-correction connects these two estimates of the magnitude, the observer frame to the rest frame.

Currently PAUS has not released catalogues with rest-frame magnitudes. Hence to allow some studies of the intrinsic properties of galaxies it is useful to provide first order approximations for the k-correction. In this section I explain an empirical method to transfer information about the k-correction from different surveys. This method allowed Johnston et al. (2020) to make an approximation of rest-frame magnitudes in PAUS and hence perform a study on intrinsic alignments.

Here, k-correction information is taken from the VIPERS survey, a completed spectroscopic survey that has been publicly available since 2016 (see Scodeggio et al.
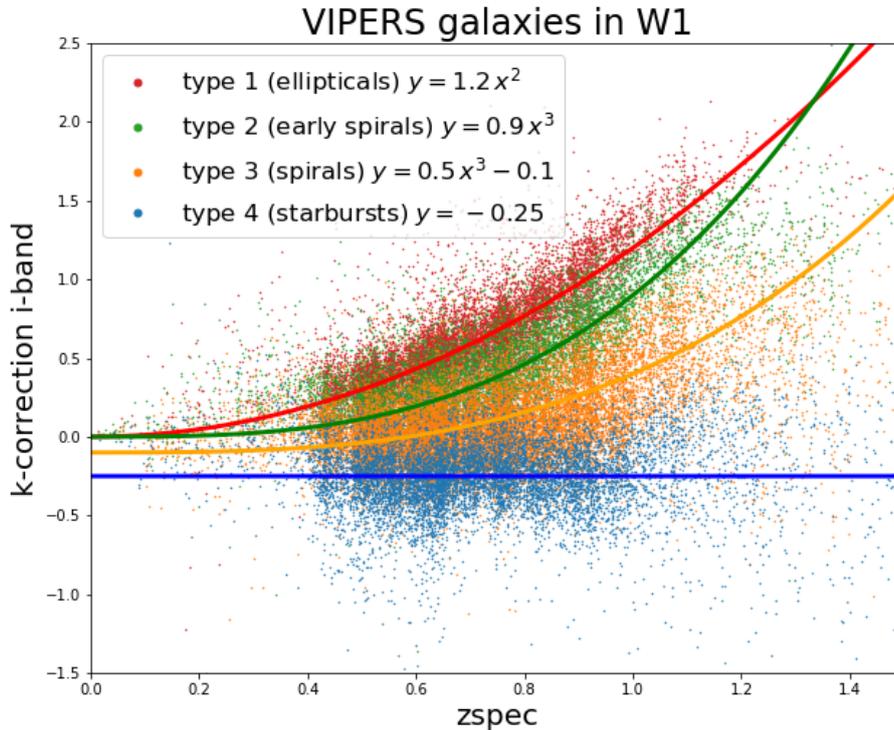
Figure 2.8: *k*-correction as a function of spectroscopic redshift in VIPERS. In this example, we can see that the *k*-correction depends on the morphology of the galaxy. The empirical relations should all converge to zero at $z = 0$, by construction, but in some cases they don't because we have used a simple fit (e.g. the blue horizontal line) that describes the data adequately over the relevant redshift range $(0.4 < z < 1.0)$.

(2018) and Sect. 2.2 for more information about the survey). However, we did not match the VIPERS catalogue in the overlapping areas with PAUS. Instead, we used the trend between *k*-correction and observed properties, to transfer this information in PAUS. One of the advantages of VIPERS is that it includes morphological information about galaxies. From Fig. 2.8, it can be seen that the *k*-correction versus redshift relation can be quite different for different types of galaxies. The first problem we need to solve is that PAUS does not have morphological information, hence we cannot apply directly the empirical relations shown in Fig. 2.8. The first idea I had was to convert this information into rest-frame colours as we know, for example, that redder galaxies are predominantly elliptical while blue galaxies
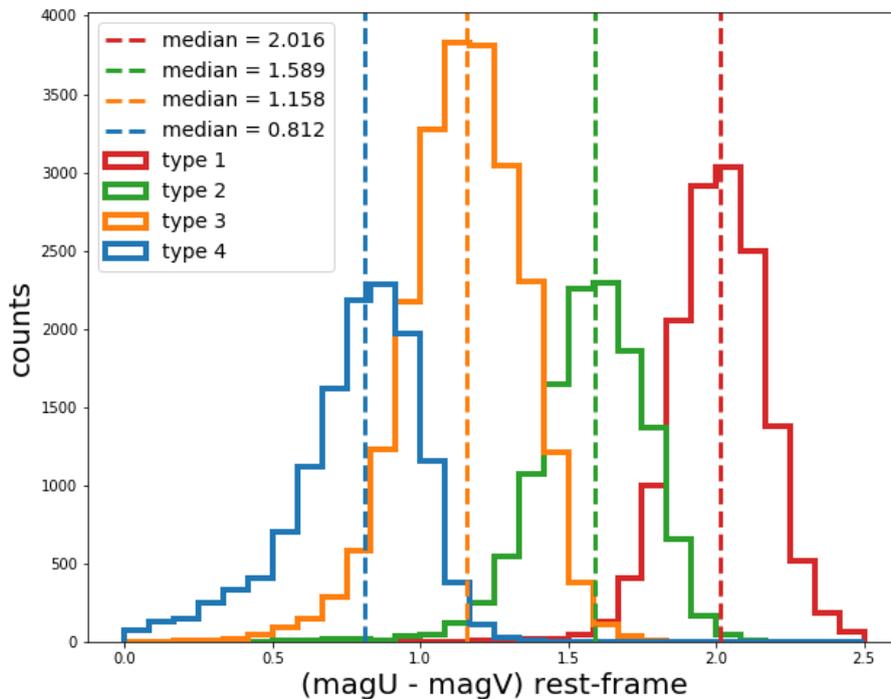
Figure 2.9: Distribution of rest-frame $U - V$ colours for different morphological types of VIPERS galaxies. Type 1 corresponds to ellipticals, Type 2 to early spirals (i.e. those spirals containing older stellar populations hence redder colours), Type 3 to spirals and Type 4 to starbursts.

are mainly star-forming. The rest frame colours are already available for VIPERS galaxies, so we can investigate this hypothesis. In Fig. 2.9, I plotted the distribution of the rest frame $U - V$ colour for the different morphological types showing that there is an association between the two quantities. In fact, for the four types of galaxies we see that the median colour is quite different. This suggests that the rest frame $U - V$ colour is a good proxy for the morphological type of a galaxy.

However, as anticipated earlier in this section, without additional processing, PAUS does not have rest-frame information, and hence no rest-frame colours. What we can use instead is an observer-frame colour as a proxy for the rest-frame colour. The closest choice for PAUS, given its redshift coverage, is to use the apparent colour $u - g$. The complication in using observer-frame colours is that they change

with redshift so instead of a histogram, it is more convenient to plot the $u - g$ observer colour as a function of redshift, as in Fig. 2.10. Summarising the procedure, from Fig. 2.10, given the redshift and the apparent colour $u - g$ of the galaxy, which are observables available in PAUS, we can identify the most likely type of galaxy that we are observing among type 1 (ellipticals), type 2 (early spirals, i.e. spiral with older stellar populations), type 3 (spirals) and type 4 (starbursts). With the apparent $(u - g)$ colour and redshift as a proxy for morphological type, we use the empirical VIPERS relation shown in Fig 2.8 to estimate k-correction of PAUS galaxies. This procedure was used by Johnston et al. (2020) to obtain estimates of the k-correction and perform the clustering and the intrinsic alignment analyses.

2.1.3.4 The photometric redshift quality factor

Some scientific analyses require us to use only 'reliable' redshifts, which can be referred to as 'secure' or 'high-quality' redshifts. Hence, it becomes necessary, especially with photometric redshift surveys, to carefully evaluate the quality of the estimated redshifts from which a sub-set of reliable ones can be identified. In this section I explain how the PAUS team evaluates the quality of their photometric redshifts and how this can affect some statistical analyses.

Eriksen et al. (2019) used the BCNz2 photo-z code to estimate photometric redshifts from the PAUS catalogue, using NB and BB information. The BCNz2 code is a template based photo-z code that has been tailored to work with the PAUS data, adapted from the BPZ code of Benítez (2000). Template based photo-z codes are not the only option to get estimates of redshifts, for example an increasingly larger variety of machine learning techniques are in the market to estimate both fluxes and photometric redshifts (see for example Cabayol et al. 2021 and references therein). As most of the machine learning algorithms in the market, a large training sample with a known solution (in our case the redshift of the galaxies) is needed to train the algorithm to get accurate prediction. On the other hand, a template based photo-z algorithm uses the observed flux in different filters and compares this
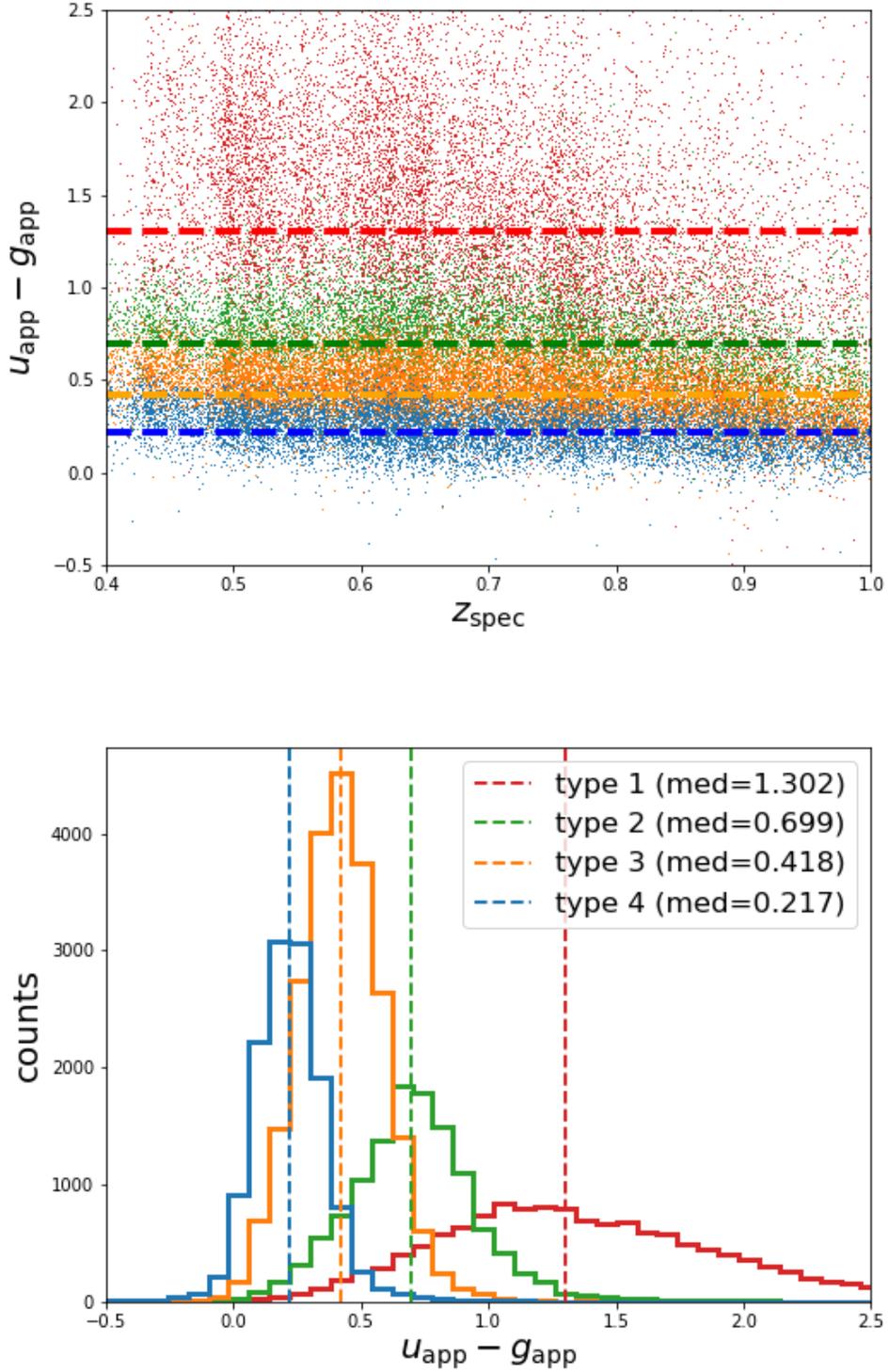
Figure 2.10: **Top**:Observer-frame $u - g$ colours as a function of redshift for the VIPERS galaxies. **Bottom**: Histogram of the observer-frame $u - g$ colours with respective medians as vertical dashed lines (values in the key). In both panels, the colours denote the types of the VIPERS galaxies, as per the legend in Fig. 2.8.

with a theoretical spectral energy distribution (SED). In other words, a theoretical SED is redshifted to different z and the z value that makes the theoretical SED best match the observed fluxes is the one selected to be the estimated photo-z.

There are many galaxy templates available, so the task is not straightforward, especially with low signal-to-noise ratio flux measurements, as is often the case with the PAUS NBs. Moreover when a star is misclassified as a galaxy and is fitted with a galaxy template SED, the resulting redshift could be at any location in the redshift interval accessible or allowed in the fitting. Template based photo-z algorithms can fail in different ways in getting the right galaxy template, for example the treatment of dust extinction can play a crucial role and when failing can produce a large number of outliers.

For these reasons, sometimes it can be convenient to work only with 'secure' or 'high-quality' redshifts, i.e. the ones for which we are confident that the template fitting is 'good' according to some metric. There are many ways to quantify the quality of photometric redshifts. Arguably, the most intuitive and easiest to define is the one introduced by Benítez (2000) for use in the BPZ code, referred to as ODDS:

$$\text{ODDS} \equiv \int_{z_b - \Delta z}^{z_b + \Delta z} \mathrm{d}z\, p(z), \tag{2.4}$$

where $p(z)$ is the distribution of redshifts obtained, related to the probability density function (PDF), z_b is the redshift at which the peak of the distribution occurs (as defined by the mode) and Δz is a fixed value that is chosen to be related to the expected scatter. For the measure of ODDS in the COSMOS field, Eriksen et al. (2019) used $\Delta z = 0.0035$ which is smaller than the values commonly used with broad band photometry as, with narrow bands, we expect better accuracy and hence more peaked $p(z)$. With this definition it is easy to identify and to deal with double-peaked distributions as the $p(z)$ will be spread around two peaks and the integral around the highest peak will result in a lower value. Apart from the extreme case of double-peaked distributions, the ODDS method is very effective in judging the quality of "well-behaved" redshifts as it will get a very low value for

a largely spread PDF, which means a very low quality redshift, because the area of the PDF that falls within the fixed $z_b \pm \Delta z$ would be small. For good quality redshifts instead, since we expect sharper PDF centred around the peak, the value of ODDS would be larger as a larger fraction of the PDF would be included in $z_b \pm \Delta z$.

The ODDS defined in Eq. (2.4) however, do not include direct information about the quality of the fit. One solution would be to include the χ^2 of the fit between the observed and redshifted theoretical SED in the metric. In an attempt to include information about the quality of the template fit in the definition of the redshift quality, Brammer et al. (2008) defined the redshift quality parameter, Q_z, as:

$$Q_z \equiv \frac{\chi^2}{N_f - 3} \left(\frac{z_{\text{quant}}^{99} - z_{\text{quant}}^{1}}{\text{ODDS}(\Delta z = 0.01)} \right), \tag{2.5}$$

where in addition to the χ^2 value, this definition includes information on the number of filters used, N_f, and on the width of the redshift distribution function, as characterized by the 1st and 99th percentiles of the $p(z)$. The numerical coefficient $\chi^2/(N_f - 3)$ is the reduced χ^2, which is the χ^2 divided by the degree of freedom, i.e. the number of observables (in our case the number of filters N_f) minus the number of fixed parameters (in our case the 3 fixed parameters are the redshift of the template, the amplitude of the template SED and the choice of the template used). Note that in the definition reported in Eq. (2.5), which is the one used by the PAUS team, the ODDS are defined with $\Delta z = 0.01$ which is a smaller value than in the original definition in Eq. 8 in Brammer et al. (2008), who set the value to $\Delta z = 0.2$; again this is due to the higher precision achieved by the narrow bands.

The trend of Q_z with the quality of the photometric redshift is opposite to the ODDS. There are many factor that contribute to this trend. First is the ODDS itself that appear in the formula at the denominator. We said that good quality redshifts means a sharp PDF around the peak z_b, hence high values of ODDS that drive the Q_z to smaller values. A sharp PDF also means a tighter $1 - 99$ percentile range $(z_{\text{quant}}^{99} - z_{\text{quant}}^{1})$ that also contribute to smaller values of Q_z. Finally, a better

fit also brings to small values for the reduced χ^2 hence making the Q_z even smaller. On the other hand, for the same reasons just explained, a bad quality redshift will results in higher values of Q_z.

The common choice in all of the PAUS studies to date has been to use Q_z as the indicator of the quality of the estimated photometric redshifts. One way to test if Q_z is a good choice to measure the quality of redshifts is to compare the photometric redshifts (z_p) with spectroscopic redshifts (z_s), assuming that the error on z_s is negligible compared to the error on z_p. In this way we have a direct measure of the *absolute error* $\delta_z \equiv |z_p - z_s|$ and since this scales with redshift, we can define a *relative error*:

$$\sigma_z \equiv \frac{|z_p - z_s|}{1 + z_s}. \tag{2.6}$$

We define *outliers* as galaxies with a relative error greater than a certain threshold, for example $\sigma_z > 0.02$ (as in Eriksen et al. 2019) or $\sigma_z > 0.1$ (as in Alarcon et al. 2021).

To get z_s for PAUS galaxies, we need to match the PAUS catalogue with spectroscopic surveys. Following Eriksen et al. (2019), we match the ~ 1.5 deg^2 of PAUS data in the COSMOS field with the zCOSMOS spectroscopic DR3 catalogue (Lilly et al., 2007), which covers ~ 1.6 deg^2 (see Fig. 2.11 for the sky distribution of PAUS and zCOSMOS data). PAUS has photometric redshifts over an area of ~ 9.7 deg^2 of W1, and for this field we can get spectroscopic measurements from VIPERS (Scodeggio et al., 2018), which covers about ~ 9.5 deg^2 (see Fig. 2.12 for the sky distribution of PAUS and VIPERS data in W1).

In Fig. 2.11 and Fig. 2.12, we show, before any matching, the position of galaxies (right ascension, RA, and declination, DEC) for PAUS (blue points) and the relevant spectroscopic survey (orange points). For the COSMOS field (Fig. 2.11), as expected the distribution of galaxies of the spectroscopic sample is similar to that

---

[*]PAUS photo-z as per production 961 (`http://paudm.pau.pic.es/#/production`)
[†]PAUS photo-z as per production 979 (`http://paudm.pau.pic.es/#/production`)
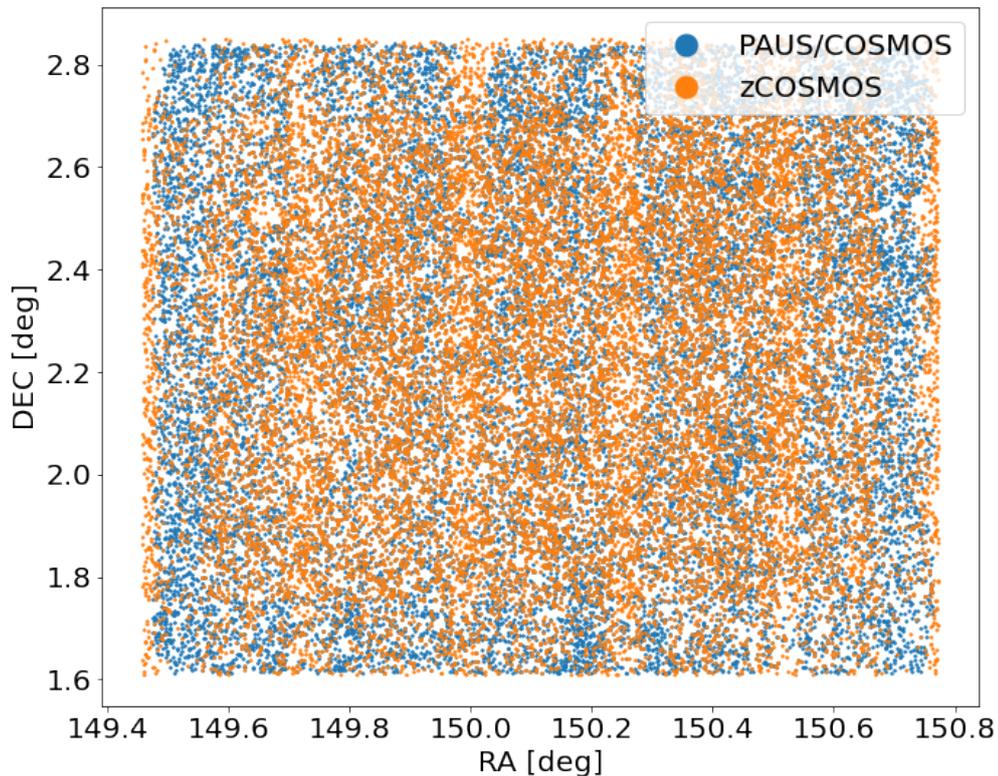
Figure 2.11: Location in degrees expressed as right ascension and declination for the PAUS/COSMOS photometric redshift catalogue* (blue points) and for the zCOSMOS/COSMOS spectroscopic catalogue (orange points). The area covered is approximately the same for both the catalogues.

of the PAUS galaxies resulting in a more homogeneous matched sample, hereafter named as PAUS/zCOSMOS. The resulting area is also very similar (~ 1.4 deg^2).

For W1 (Fig. 2.12), matching the PAUS galaxies with VIPERS can change the characteristic of the resulting sample, hereafter named PAUS/VIPERS. First we note a key difference in the observing strategy of VIPERS, which introduces gaps between different pointings. The main reason for this is the design of the VIMOS spectrograph used in VIPERS with 4 quadrants $7.0' \times 8.0'$ each, separated horizontally by $2.0'$ and vertically by $2.4'$ (see Fig. 6 of Guzzo et al. 2014 for an example of a VIMOS pointing and the upper panel of Fig. 2 of Scodeggio et al. 2018 for the complete layout of pointings of W1). Hence, even if the effective area of the two samples is rather similar (~ 9.7 deg^2 for PAUS and ~ 9.5 deg^2 for VIPERS),
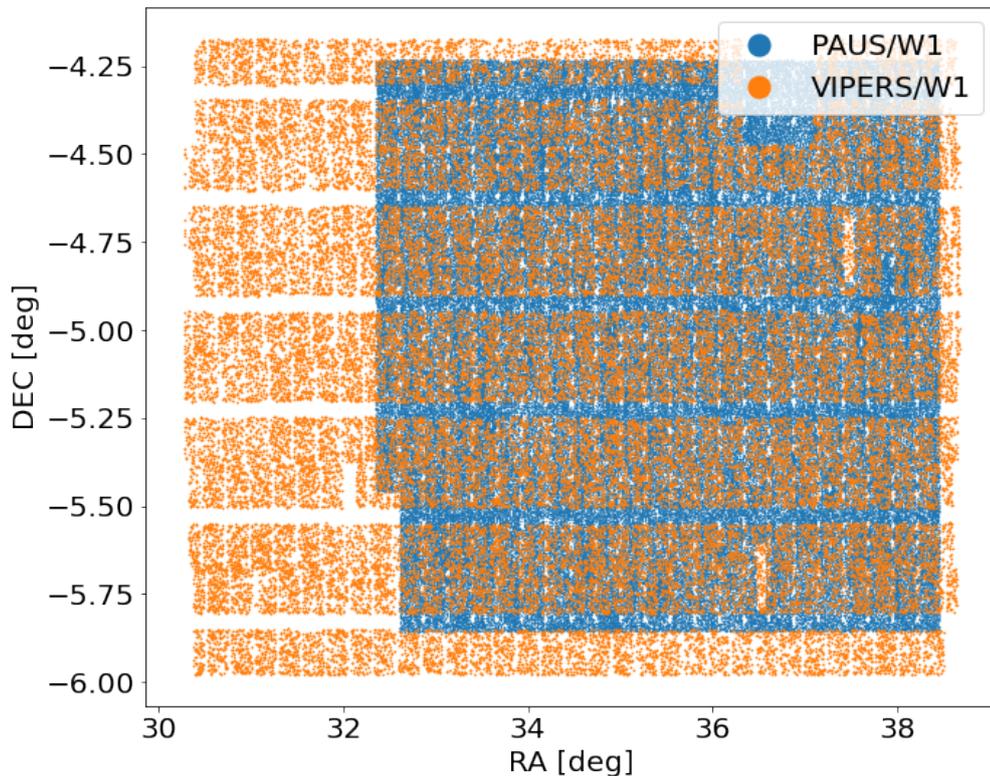
Figure 2.12: Location in degrees expressed as right ascension and declination for the current[†] PAUS/W1 photometric redshift catalogue and the full VIPERS/W1 spectroscopic catalogue.

when the two samples are matched, the common area is reduced to ~ 3.5 deg^2, resulting in a slightly smaller common sample of galaxies. The other effect that comes into play when matching PAUS with VIPERS in W1, is that the two surveys have different target selections. While PAUS and VIPERS share the same depth of $i_{AB} = 22.5$, VIPERS has an additional colour-colour pre-selection (see more details on Sect. 2.2.1) which excludes from the sample galaxies with redshift $z \lesssim 0.5$. This results in the median redshift of VIPERS being $z \sim 0.7$ while in PAUS is at $z \sim 0.5$. This also makes the number counts for bright objects in VIPERS incomplete, resulting in PAUS being ~ 0.2 magnitudes brighter than VIPERS. These differences in the VIPERS sample in W1, have an effect on the resulting matched sample PAUS/VIPERS which will have intrinsically different properties from the matched sample PAUS/zCOSMOS in the COSMOS field. However, with

the aim of studying the effectiveness of Q_z in selecting good quality redshifts, our main interest is to have spectroscopic redshifts to be used in the definition of relative error σ_z in Eq. (2.6). Nevertheless, when interpreting the results, it is important to note that statistical differences for the values of Q_z between PAUS/zCOSMOS in COSMOS and PAUS/VIPERS in W1 might be mainly driven by the different nature of the spectroscopic sample.

In Fig. 2.13 we can see the relation between the photometric and spectroscopic redshifts after matching the surveys as described above. There are two features that can be noticed. In the top panel which shows the COSMOS data, some preferred spectroscopic redshifts are apparent as vertical bands or clumps along the spectroscopic redshift axis. These bands are due to the clustering of galaxies. This is a consequence that COSMOS covers a small area of the sky (~ 1.5 deg^2). This means that the number of clusters observed is small and easy to distinguish one another but note that these features would be washed out in a much larger field, with more structures occurring at a range of redshifts. Galaxies that fall in the same galaxy cluster show the same spectroscopic redshift but the photometric redshifts, which are less accurate, are spread out over a wider range of redshifts. In the bottom panel, for the VIPERS data, we need to keep in mind that we are only looking at redshifts greater than $z \gtrsim 0.4^*$ because of the survey strategy described in Sect. 2.2. Because of this, the bottom panel is more zoomed in than the top one and we can see some horizontal lines instead. These lines are still under investigation by the PAUS team, and by now there is no clear explanation. Vertical lines instead are less evident because of the wider area from which the W1 galaxies are sampled (~ 9.7 deg^2 for W1 versus ~ 1.5 deg^2 for COSMOS)†. Another way to study the accuracy of the photometric redshifts is to plot their relative error as defined in Eq. 2.6. In Fig. 2.14, we plot $(z_p - z_s)/(1 + z_s)$ as a function of the spectroscopic redshift. We can see again some vertical striping due

---

*Although the colour-colour pre-selection is aimed at targeting galaxies at redshifts $z \gtrsim 0.5$, an incomplete sample extends up to $z \sim 0.4$ as it can be seen from the x-axis of Fig. 2.13.

†Note that although the effective area of the PAUS/VIPERS sample in W1 is ~ 3.5 deg^2, the sampling is sparse over the full ~ 9.7 deg^2 making the clustering less apparent
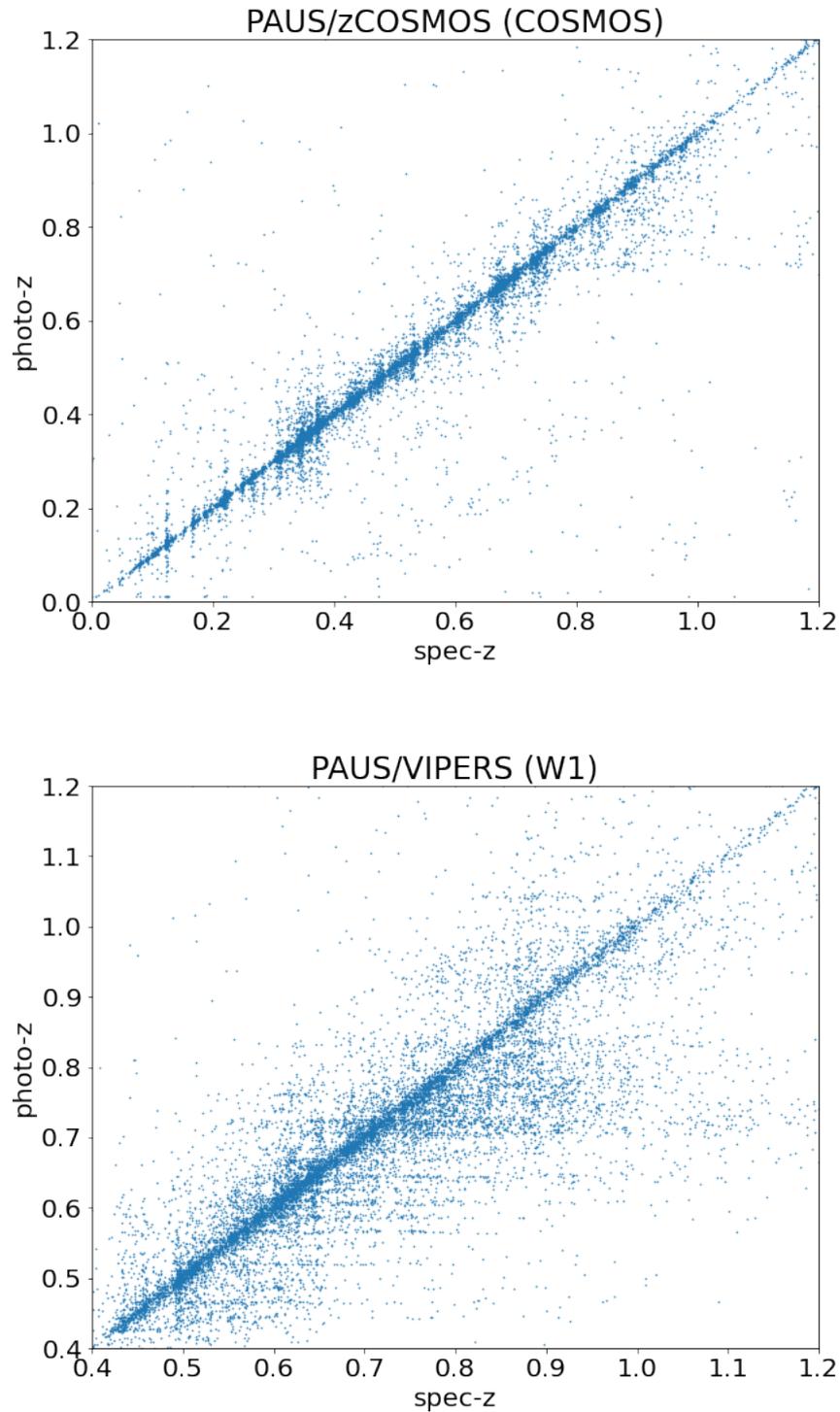
Figure 2.13: Relation between the estimated photometric redshift (photo-z) and the spectroscopic redshift (spec-z) from matched spectroscopic surveys, i.e. using zCOSMOS in the top panel and VIPERS in the bottom panel. Note the change in the axis range in the bottom panel, due to the colour selection applied in the VIPERS data.
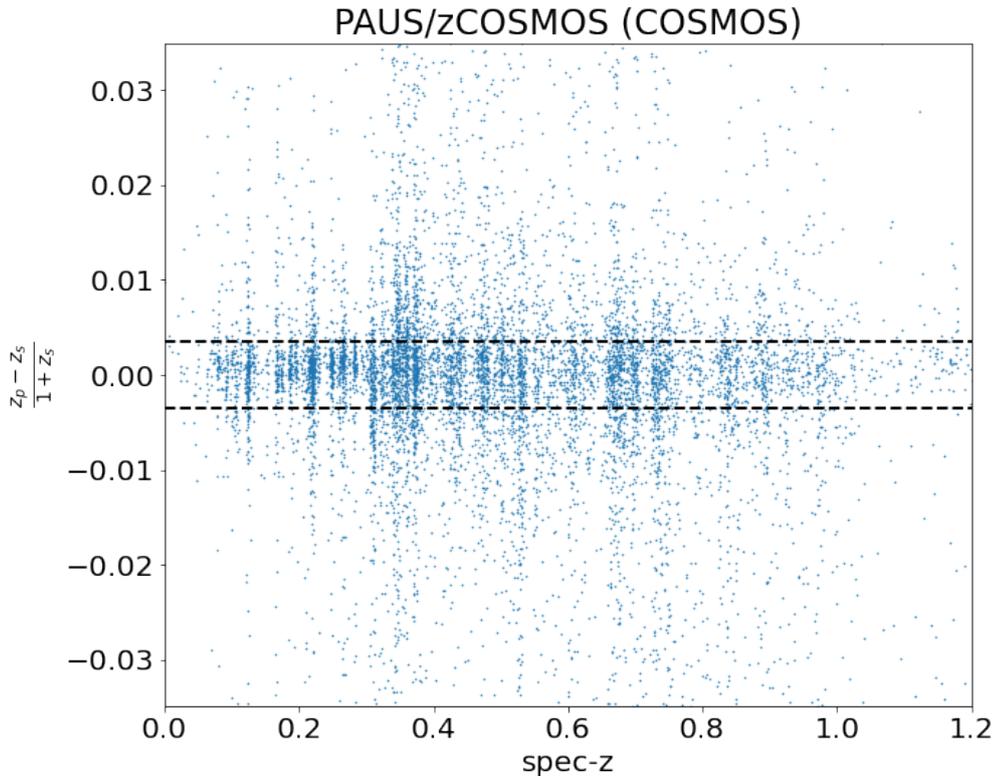
Figure 2.14: Estimate of the photometric redshift error as in Eq. (2.6) (but without taking the absolute value of the numerator) as a function of the spectroscopic redshift for the matched PAUS/zCOSMOS data. Horizontal dashed lines indicate the PAUS requirement to have the best 50% of the sample with a relative error smaller than $\sigma_z < 0.0035$.

to the underlying galaxy clustering. We also highlighted with horizontal lines the accuracy that PAUS is aiming for the best 50% of the sample.

In the context of the quality factor Q_z, we can now study how the error $\sigma_z{}^*$ correlates with the associated quality of the redshift. If we find a relation between Q_z and σ_z, then we do not need anymore spectrocopic redshift to estimate the accuracy of the measurements but we can directly use Q_z as a proxy for σ_z. One common choice for some PAUS studies is to select the best 50% of the sample, by computing the median Q_z of the sample and considering only galaxies with a value of Q_z below the median. In Fig. 2.15 we can see the relation between

---

*Even if the definition of σ_z include the absolute value, it is convenient to study simply $(z_p - z_s)/(1 + z_s)$ as it carries more information.
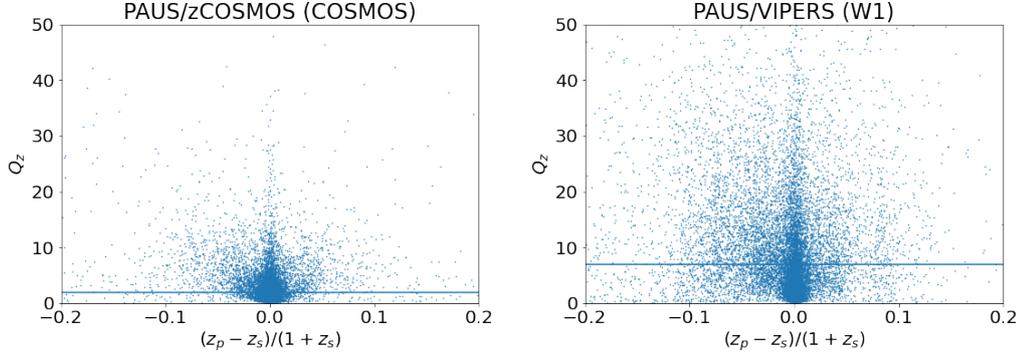
Figure 2.15: Q_z as a function of the relative error for PAUS/zCOSMOS galaxies (left panel) and for PAUS/VIPERS (W1) galaxies (right panel). The horizontal line represents the median value of Q_z, which is 1.87 for the COSMOS data and 6.89 for the W1 data. Quantitative differences between the two samples is mostly driven by different sample selections (with PAUS/VIPERS typically fainter and higher-z than PAUS/zCOSMOS). Additional differences in the PAUS depths would contribute as well, with PAUS data in the COSMOS field being somewhat deeper than PAUS data in the W1 field.
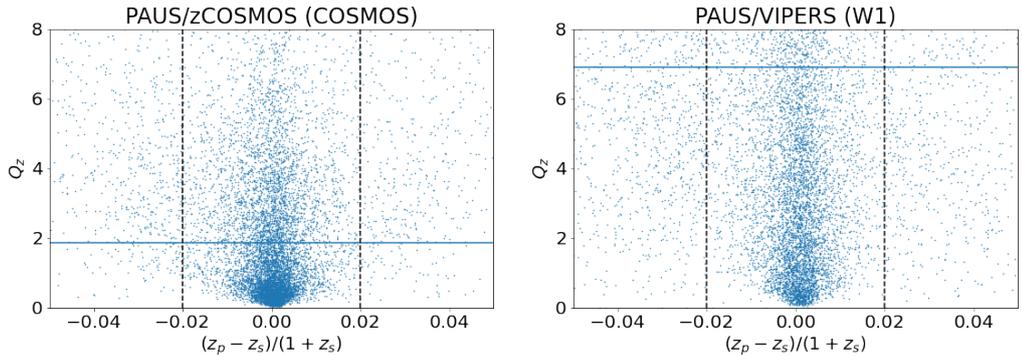
Figure 2.16: Zoomed-in version of Fig. 2.15. The vertical dashed lines denote the threshold for outliers following Eriksen et al. (2019). Points outside the vertical lines are outliers. The horizontal line shows the median of the Q_z, hence the best 50% of the sample according to Q_z is below this line. We stress that we are not looking at the full PAUS sample in COSMOS and W1, but only galaxies with a match in the associated spectroscopic survey.

σ_z and Q_z for the PAUS data, both in the COSMOS (left panel) and in the W1 field (right panel), after being matched with their respective spectroscopic surveys. The median Q_z of the sample is given by the horizontal line, highlighting below it the best 50% of the sample according to Q_z. The median Q_z for COSMOS is lower (better quality redshifts) than in W1 as expected by the selection in VIPERS, targeting galaxies at $z \gtrsim 0.5$ while COSMOS extends at lower redshifts and brighter objects. What we expect to see in an ideal scenario is that below the median Q_z galaxies have low σ_z but as Q_z increases over the median, galaxies with low σ_z should disappear and being replaced by galaxies with high values of σ_z. Instead, what we actually see in Fig. 2.15 is that galaxies with low σ_z are always present independently from the value of Q_z. However if we define for example galaxies with low σ_z as those with $\sigma_z < 0.01$, we can see that that the percentage of this galaxies decrease from 88% below the median to 50% per cent above the median in the COSMOS sample. For W1 the low σ_z galaxies drop from 62% for Q_z lower than the median Q_z to 30% above the median. This means that selecting good quality redshift by requiring Q_z to be lower than its median value has a positive impact as the number of galaxy with low σ_z is higher than in the sample with Q_z higher than its median. However, with this technique we are also cutting on some low σ_z redshifts which instead should be considered as good quality. If we zoom in to this distribution as in Fig. 2.16, we can see that the 'desired' relationship between σ_z and Q_z arguably only holds for very low values of Q_z (i.e. $Q_z \lesssim 1$ for both COSMOS and W1) as the distribution of points spreads out to cover a wider range of σ_z with increasing Q_z (again we do not see galaxies with low σ_z disappearing as Q_z increases but their percentage drops as expected). Note that on the x-axis we are not considering the absolute value as specified in Eq. (2.6). Thanks to this, we can check if redshifts are biased with photometric redshifts being consistently higher or lower than the spectroscopic ones. Although visually for very little value of the Q_z, the distribution of σ_z can appear slightly offset towards positive value, we computed the medians of σ_z for both the entire sample and the one for Q_z lower

than its median, finding for both COSMOS and W1 a symmetry with respect to the axis $\sigma_z = 0$, so that we can exclude the hypothesis of a systematic bias. The results showed in Fig. 2.15 and Fig. 2.16 suggest that applying a cut based on Q_z can select galaxies with low σ_z but it also removes some other galaxies that could be classified as accurate redshifts. In other words, the Q_z is able to select good photometric measurements, but it also reduce the sample dramatically leaving out some redshifts with low σ_z.

Finally, we look into the effect of using Q_z to identify the best photometric redshifts on the number of outliers as defined in Eriksen et al. (2019), i.e. those galaxies with a photometric redshift that satisfies the following relation (we define as "non-outliers" those galaxies that do not satisfy the following):

$$\text{Outliers:} \qquad \frac{|z_p - z_s|}{1 + z_s} > 0.02. \qquad (2.7)$$

Although the choice to set the threshold at $\sigma_z = 0.02$ is somewhat arbitrary, the motivation comes from the accuracy that PAUS aim at achieving. Since it aims of having $\sigma_z \lesssim 0.0035$ for the best 50% of the sample, galaxies with $\sigma_z > 0.02$ are approximately 4 sigma away, which is reasonable to be considered outliers.

In Fig.2.17, we plot the cumulative fraction of outliers up to a given magnitude in the *i*-band, both for the COSMOS and the W1 data. We compare the outliers in the overall sample (solid lines) with the outliers in the best 50% of the sample according to the Q_z criterion (dashed lines). As the plot is cumulative, the point at the faintest magnitude represents the full fraction of outliers. The fraction of outliers is defined as the number of outliers (galaxies with $\sigma_z > 0.02$) normalised to the total number of objects in the subsample brighter than the magnitude on the *x*-axis. Hence the fraction of outliers for the best 50% of the sample is normalised to the number of objects selected to be the best 50% and not the entire sample of objects. To help visualise how the fraction of outliers is computed, we can keep as a reference Fig. 2.16. Best 50% means below the horizontal line, outliers means outside the vertical dashed lines, hence the normalisation for the best 50% consists in all the
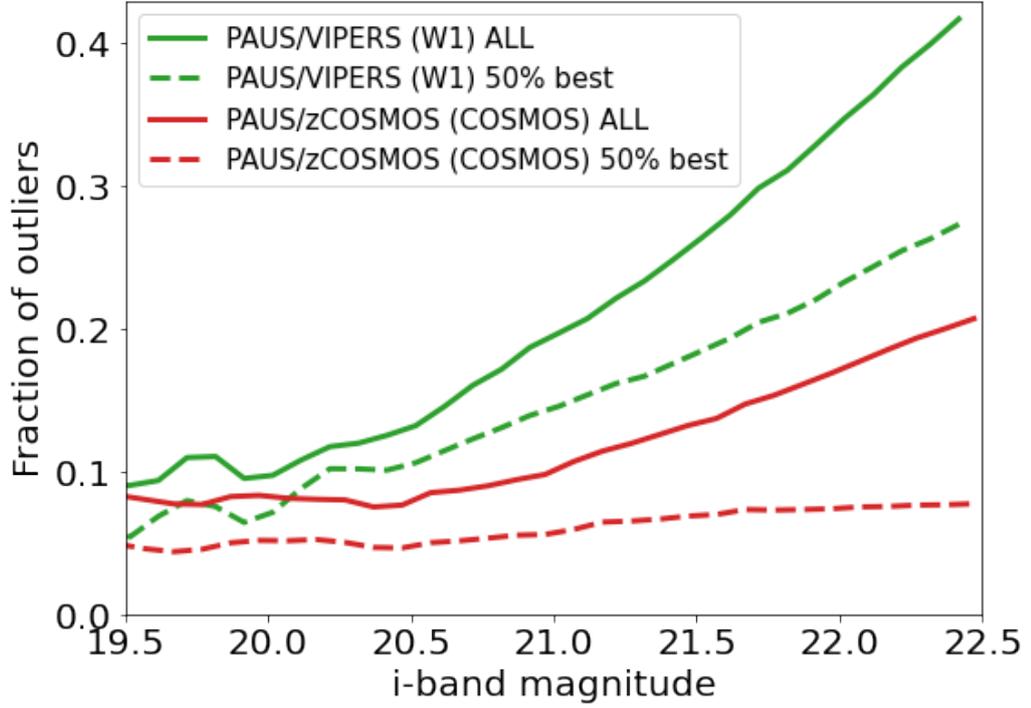
Figure 2.17: Cumulative fraction of outliers, as defined by Eq. 2.7, as a function of the apparent I-band magnitude. PAUS data are shown in red (green) when matched with the spectroscopic survey zCOSMOS (VIPERS). Solid lines are for the entire sample while dashed lines are for the best 50% according to Q_z. The total fraction of outliers are 21% for the entire COSMOS sample and 8% for the 50% best of the COSMOS sample. For W1 they are respectively 42% for the entire sample and 27% for the best 50%.

points below the line (selecting only objects up to the magnitude considered). The first thing to note in Fig. 2.17 is the higher total fraction of outliers in the W1 field (42%) compared to the COSMOS field (21%). This holds true also when we select the best 50% data according to the Q_z method. In fact, the total number of outliers for the best 50% within W1 is 27% and within COSMOS 8%. One potential reason to explain the higher fraction of outliers in PAUS/VIPERS with respect to PAUS/zCOSMOS is its selection. We already discussed that VIPERS has a pre-selection of targets favouring galaxies with redshifts greater than $z = 0.5$. This makes the PAUS/VIPERS sample intrinsically fainter than PAUS/COSMOS which instead extends to bright objects up to $z \sim 0$. A second reason is that

COSMOS has been used by PAUS as a reference field for calibrations and for this reason the exposure times in the narrow band images are longer than in the other PAUS fields. This can results in a higher signal to noise ratio and a consequent lower fraction of outliers. Note that although the zCOSMOS catalogue offers a large number of broad band filters, only 5 have been used from PAUS in addition to the narrow bands to estimate redshifts, and this is true for all the PAUS field. Because the number of broad band filters used in PAUS/zCOSMOS is the same as in PAUS/VIPERS, this does not contribute to a difference in outliers number. The other important fact to note in Fig. 2.17 is that in both COSMOS and W1 fields, the fraction of outliers for the best 50% of the sample (dashed lines) selected on Q_z is always lower than the fraction of outliers for the full sample (solid lines). This means that selecting Q_z lower than its median value is successfully removing redshift outliers from the sample. Even if we know from Fig. 2.15 and Fig. 2.16 that the Q_z cut excludes some good quality redshifts, the important thing that Fig. 2.17 shows is that the Q_z method is improving on the removal of outliers, as the fraction of outliers has been reduced.

To further test the validity of using Q_z as a metric to select reliable redshifts, I analysed the distribution of Q_z for the galaxies classified as outliers (those that satisfy Eq. 2.7) and the galaxies classified as "non-outliers" (those that do not satisfy Eq. 2.7). If the Q_z method is effective in identifying the quality of redshifts, then we expect to find the distribution of non-outliers more peaked at lower values and the distribution of outliers spread at higher values and less peaked. Fig. 2.18, shows the distribution of Q_z for outliers in blue and for non-outliers in orange for both the COSMOS and the W1 fields. We note that both histograms have a low counts tail that extends to much higher values of Q_z, which explains why the y-axes ranges are different, as the Q_z distributions in the two fields are quite different. The medians of the distributions are shown using vertical dashed lines of the same colour. The vertical black dashed line is the median of the overall population, which is the one used to separate the best 50% of the sample from the
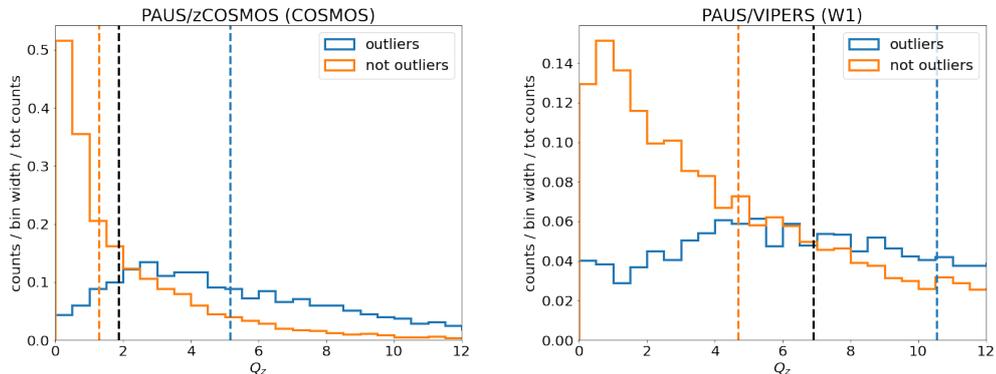
Figure 2.18: Histogram of Q_z for outliers (blue) and non-outliers (orange) as per Eq. 2.7. The left panel is for the PAUS/zCOSMOS sample in the COSMOS field and the right panel is for the PAUS/VIPERS sample in the W1 field. Blue and orange vertical dashed lines indicate the medians of each distribution, with the black dashed line showing the median of the combined sample. All the histograms are normalised to unity. We note that all samples have tails with low counts up to higher Q_z values, which explains why the y-axes ranges are different. In both cases, we notice that the "non-outlier" distribution peaks at lower Q_z values in both fields, and is more compact in COSMOS field than the "outlier" distribution. More details in the main text.

worst 50% of the sample. We normalised the distributions to unity to facilitate the comparison between the distributions of outliers and non-outliers even when the numbers of objects for the two samples are very different. We can see that the median Q_z of outliers is consistently larger than for non-outliers, as expected if Q_z can be used reliably to discern bad from good quality redshifts. For COSMOS we have 1.87 as an overall median for the Q_z, 5.17 for the outliers and 1.29 for the non-outliers. For W1, we have 6.89 as an overall median, 10.54 for the outliers and 4.69 for the non-outliers. Not only the medians are in agreement with what expected from the Q_z method but also the shape of the distributions between outliers and non-outliers are very different with the non-outliers more peaked at low values and a more shallow distribution for the outliers with higher counts at larger values of Q_z.

We conclude that, although the Q_z method can dramatically reduce the number of objects in the sample excluding sometimes even objects with good photometric

redshifts, it is quite effective in removing the outliers from the sample and can be used as a first approximation to identify the best quality redshift in the sample. Because of the loss of some good quality redshift in this method, we argue that what is usually referred to as "the best 50% of the sample" is not exactly so but, thanks to this analysis, we can state that such sample has a lower fraction of outliers.

2.2 VIPERS

The VIMOS Public Extragactic Redshift Survey (VIPERS) has been crucial in my studies as it offers another source of spectroscopic redshifts as already discussed in Sect. 2.1.3.4, but also because it has been the focus of a galaxy evolution study which led to the publication reported in Chapter 5. In this section I will give a brief introduction to VIPERS highlighting the main features of the survey.

2.2.1 Motivation for the survey

The VIPERS survey has the objective of probing the Universe at intermediate redshifts ($0.5 < z < 1.2$) at wavelengths between $5500 - 9500$Å. Scientific goals span from the investigation of large scale structure and estimation of cosmological parameters (e.g. Rota et al. 2017; Marulli et al. 2017; Pezzotta et al. 2017), to the study of galaxy properties and their evolution at a time when the Universe was half of its current age (e.g. Gargiulo et al. 2017; Cucciati et al. 2017; Manzoni et al. 2021). VIPERS has a depth in the i-band magnitude of $i_{\mathrm{AB}} < 22.5$ and a spectroscopic completeness that averages 40% of the targeted galaxies (Guzzo et al., 2014). To maximise the observations of galaxies in the redshift range of interest, target galaxies were selected using an empirical method based on the data from the VIMOS deep surveys, like VVDS and zCOSMOS. In particular the $(r-i)$ vs $(u-g)$ colour plane is used to reject galaxies with redshifts $z \sim 0.5$ (see Figure 2.19). The selection criterion is described by the following set of inequalities:

$$(r-i) > 0.5(u-g) \quad \text{OR} \quad (r-i) > 0.7 \quad \Rightarrow \quad z \gtrsim 0.5. \tag{2.8}$$

This colour-colour selection is one of the main feature of VIPERS and guarantees
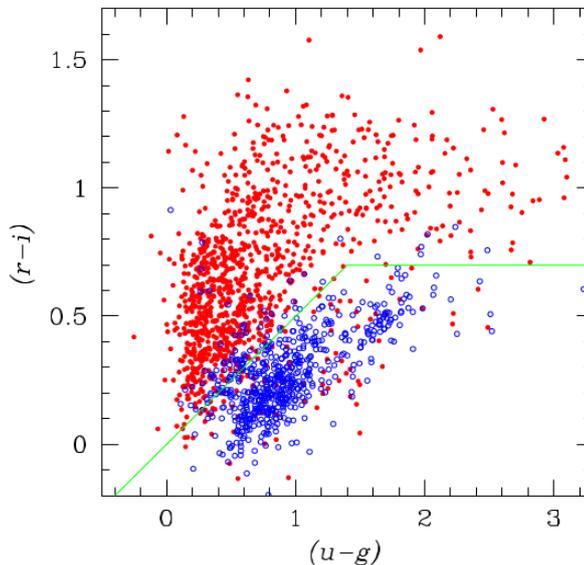
Figure 2.19: Colour-colour diagram showing galaxies in the VVDS-Deep survey. With *a priori* knowledge of the redshifts, we note that galaxies with $z > 0.5$ (red points) lay above the green line and galaxies with $z < 0.5$ (blue points) lay below the green line. The observing strategy of VIPERS targets only galaxies that lay above the green line. Figure from Guzzo et al. (2014).

that VIPERS is only observing galaxies in the redshift range of interest ($z \gtrsim 0.5$). VIPERS obtained spectra using multi-slit spectroscopy at the Very Large Telescope (VLT). This means that the focal plane is covered by masks with multiple slits that lay exactly at the position of the galaxy. Hence the dispersion of the spectrum happens directly in the focal plane. As a consequence VIPERS cannot observe every galaxy as the slits need to be separated by a certain amount and the dispersion also occupies a region in the focal plane where other galaxies cannot be observed. The reduction in the surface density of target galaxies to the depth of the survey after applying the colour selection makes it feasible to measure spectra for galaxies with $z > 0.5$ with a completeness of 40% which is the best achievable given the spectroscope set-up. VIPERS decided to use the lowest resolution available ($R = 220$) in order to have a shorter dispersion axis, thereby minimising the number of galaxies that cannot have spectra measured as they are too close to other targets.
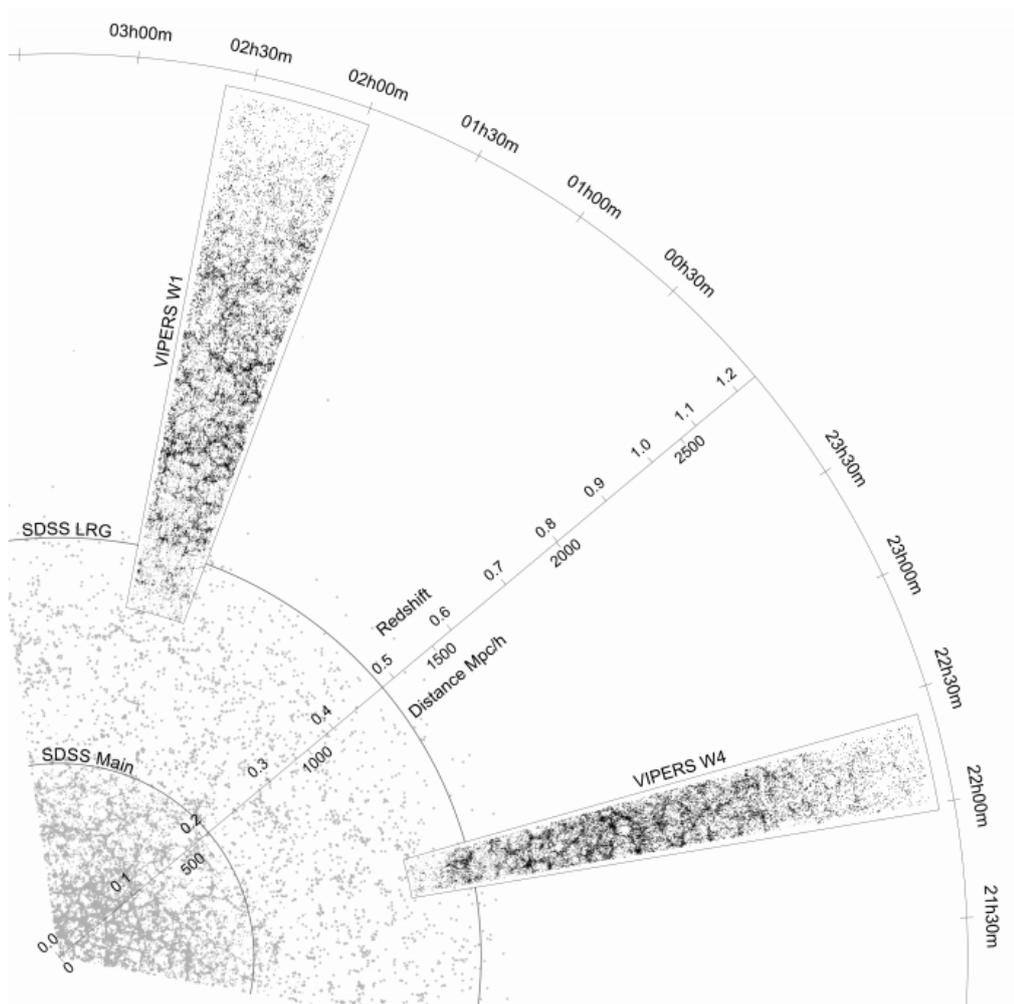
Figure 2.20: Vipers W1 and W4 fields compared to other redshift surveys. (Taken from Guzzo et al. 2014).

VIPERS covers about 23.5 deg^2 of sky, split over the two wide CFHTLS fields W1 and W4 (see Fig. 2.20). We already exploited in Sect. 2.1.3.4 the fact that W1 overlaps with PAUS, offering the possibility to compare the accuracy of photometric redshifts with spectroscopic redshifts. In particular, the VIPERS team has estimated the quality of their redshifts using 3000 multiple observations of the same objects. They determined an accuracy of $\delta_z \sim 0.00054\,(1+z)$ (Scodeggio et al., 2018).

2.2.2 Quality of the spectroscopic redshifts

We have seen in Sect. 2.1.3.4 how it is essential in photometric redshift surveys to estimate the quality of the redshift obtained. In spectroscopic surveys we have the same interest in quantifying the reliability of the redshifts measured. However, the technique to assign a quality factor or quality flag can be completely different. As explained in Scodeggio et al. (2018), for the VIPERS spectroscopic sample, which is made up of 86,775 objects, the reliability of the redshift measurements has been encoded with a flag made of a decimal number whose units have the following meaning (see Fig. 2.21).

- Flags 4 and 3: highly secure redshift, with confidence $> 99\%$

- Flag 2: still fairly secure, $> 95\%$ confidence level

- Flag 1: tentative redshift measurement, with $\sim 50\%$ probability to be wrong

- Flag 9: redshift based on a single emission feature, usually $[OII]\lambda 3727\text{Å}$

This method is very similar to that of other precursor surveys (Le Fèvre et al., 2005; Lilly et al., 2009) and has been described in detail in Garilli et al. (2010, 2012, 2014) and Guzzo et al. (2014).

To avoid including uncertain redshift measurements all analyses of the VIPERS data to date have considered only galaxies with a quality flag greater or equal to 2 ($z_{\text{flag}} \geq 2$). Using this selection reduces the galaxy sample to $76\,552$ objects.

For all of VIPERS objects a visual validation of the reliability of the redshifts has been carried out by the team. The visual validation add information to the quality flag in form of a decimal figure. To validate the redshift, a comparison has been made with the photometric redshift estimated from the CFHTLS photometry (Erben and CFHTLenS Collaboration, 2012; Heymans et al., 2012). The "full agreement" is defined when the spectroscopic redshift falls within the 68% confidence level of the photo-z pdf, and is encoded by adding 0.5 to the quality
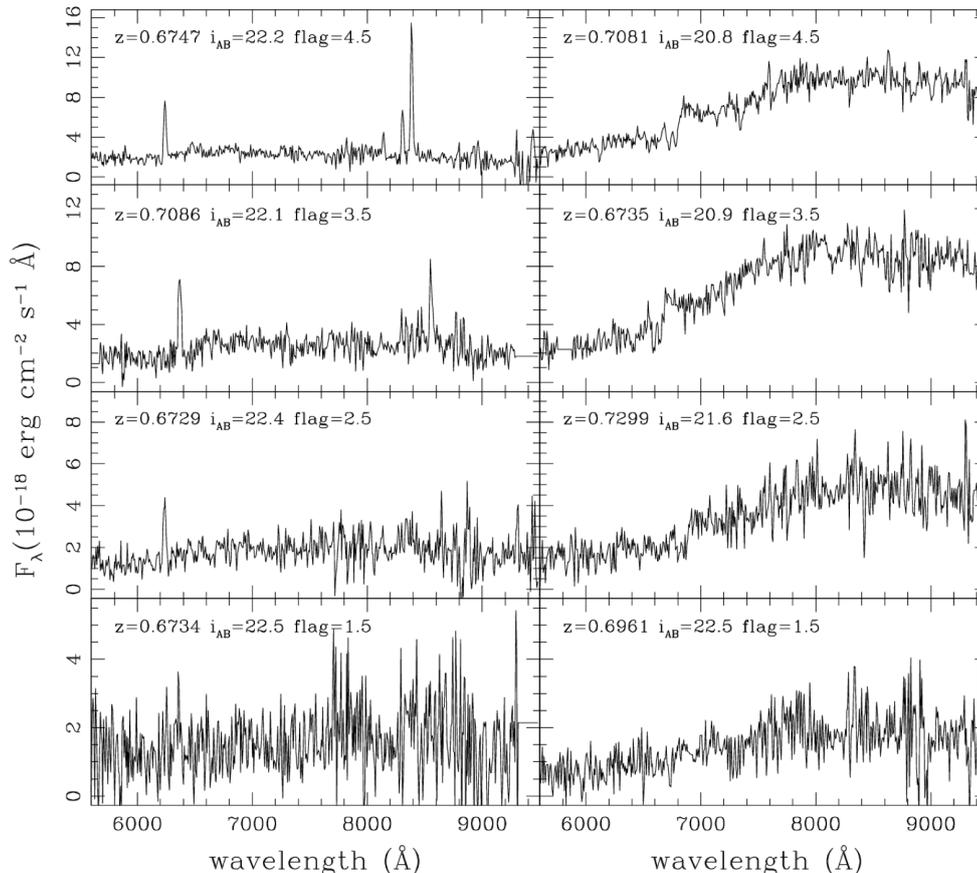
Figure 2.21: Examples of VIPERS spectra with different quality flags as described in the text and labelled in the legend. The quality of the spectra decrease moving from top to bottom. The left column shows samples of late-type galaxies while the right column shows a sample of early-type galaxies. (Taken from Guzzo et al. 2014).

flag. If the spectroscopic redshift is not in the 68% range but is within the 95.4%, then 0.4 is added to the quality flag. In all the other cases 0.2 is added to the quality flag. In the case that the photometric redshift is not available, a value of 0.1 is added to the quality flag. In Fig. 2.21, some examples of spectra with different redshift quality flags are shown. Moving from top to bottom we can see how the signal-to-noise of the spectra decreases, with spectral features and emission lines becoming less defined.

In conclusion, we have compared two different ways in which the quality of the redshifts measurements can be estimated: the Q_z for PAUS and the z_{flag} for

VIPERS. The two approached are intrinsically different because of the different nature of photometric and spectroscopic redshifts. For PAUS, to estimate redshifts, the SED resulting from the narrowband and broadband measurements is fitted to galaxies templates created with stellar population synthesis models. The result is a probability density function of redshifts whose mode is taken to be the photometric redshift estimate. The width of the pdf and information about the quality of the fit are included in the Q_z to estimate the quality of the photometric redshifts. For VIPERS, redshifts are directly measured from the shift of features in the spectra. Repeated observations for the redshift of the same object are compared to see how similar they are, and assess the quality of the measurement through the z_{flag}. Of course for VIPERS, and in general for spectroscopic surveys, the quality of the redshifts is strictly related to the quality of their spectra, as this define how well we can distinguish spectroscopic features (i.e. emission or absorption lines). We have explored this in Fig. 2.21 looking at spectra with different signal to noise ratios. We have discussed that spectroscopic surveys are able to achieve higher accuracies in redshift and how much PAUS obtains better redshift than standard broad band photometric surveys. Nevertheless, VIPERS obtains accuracies which are approximately an order of magnitude better than PAUS ($\sigma_{z,\text{VIPERS}} \sim 0.00054$ compared to $\sigma_{z,\text{PAUS}} \sim 0.0037$ for the best 50% of the sample up to the same magnitude limit of $i < 22.5$). Given the higher accuracy of VIPERS, it is necessary to discuss what PAUS can give us more. A key improvement of PAUS is the completeness, i.e. the number of object for which we obtain redshift over the total number of object observable. With VIPERS the completeness is approximately 40% of the objects. For PAUS, the imaging can cover all the objects observable, and even if for some of that the photo-z code might fail in getting redshift estimates, the completeness can score much higher values than VIPERS. Other key reasons include the possibility to obtain redshifts for a wider area of the sky given the speed and efficiency of photometric measurements compared to spectroscopic ones. Moreover, PAUS can probe all the galaxies at low redshift that are missing in VIPERS due

to the colour-colour pre-selection, that allows only objects with $z \gtrsim 0.5$. This way PAUS can use VIPERS to validate redshifts and extend the measurements both in area and gaining a wider redshift range. In the remaining chapters, spectroscopic measurements from VIPERS will be always considered as "true redshifts" given the higher accuracy. The photometric redshifts from PAUS instead will be usually selected accordingly to the Q_z. In particular, following the approach of previous PAUS studies (e.g. Eriksen et al. 2019; Alarcon et al. 2021 and Johnston et al. 2020) the best 50% of the sample will be selected as those galaxies with Q_z lower than its median. In particular, in Chapter 4, we will discuss how this quality cut can affect some studies like the number counts of galaxies and how this effect can be taken into account.

Semi-analytical models of galaxy formation

In this chapter I describe GALFORM (Cole et al., 2000), the semi-analytical model of galaxy formation that I have used to create a PAUS mock catalogue (Chapter 4) and to study the physics behind the evolution of the colour-magnitude relation in VIPERS (Chapter 5). Adapting GALFORM to build lightcone mock catalogues using the new P-Millennium N-body simulation (Baugh et al., 2019) is one of the main achievements of my PhD. This work will be described in this chapter. To keep Chapters 4 and 5 self-contained, some of the information reported in this chapter will be reprised in a less detailed way in those chapters. The reader who is already familiar with galaxy formation models can skip this chapter without missing any key information needed to understand the following chapters.

3.1 The motivation behind semi-analytical models of galaxy formation

In order to interpret observations we need to compare them with simulations that follow the evolution of the baryonic component of the Universe using a physically motivated theoretical model. The cold dark matter (CDM) model in its simplest

form does not make predictions for the formation and evolution of galaxies. It merely predicts the growth of structure in the dark matter. This is why we need to couple the CDM model with a model of galaxy formation. Today, galaxy formation models are built upon an N-body simulation that follows the evolution and the assembly of dark matter halos, producing a collection of halo merger trees in which galaxies will form and evolve. To populate dark matter halos with galaxies, different approaches have been followed. One of these is semi-analytical modelling. Semi-analytical models and hydrodynamical simulations share many similarities. Both approaches involve modelling processes that are not fully resolved and for which the physics are poorly understood. Examples of such processes include the formation of stars from cold gas or the impact of heating of the interstellar medium by supernovae. Semi-analytical models tend to make more approximations in their implementation of the physics than hydrodynamical simulations. Nevertheless, both approaches have equations describing sub-grid physics which contain parameters that have to be set to specify a model. The parameters are set by comparing the model to a range of observations, and choosing the parameters so that the model gives its best reproduction of these data. Other model outputs are then considered as predictions (see e.g. the discussion in Schaye et al. 2015).

Semi-analytical models tend to be faster than hydrodynamical simulations because, due to the simplifying assumptions used (such as the assumption of spherical symmetry in gas cooling), they consider fewer resolution elements within a galaxy, and compute the hydrodynamical properties of the gas more quickly. As an example, when modelling the process of supernova feedback, hydrodynamical simulations do not model the suppression of star formation directly. Instead, they model the input of thermal or kinetic energy into the ISM; a suppression of the star formation rate may then result from this action. On the other hand, semi-analytical models model supernova feedback by directly ejecting material, typically in proportion to the star formation rate, which by construction produces the desired feedback on star formation.

The computational speed of semi-analytical models allows the rapid exploration of the model parameter space (e.g. Elliott et al. 2021). Also, different physical processes can be readily switched on and off to develop physical intuition. The models predict the star formation and merger histories of the galaxy population in a cosmological volume, including the chemical evolution of the gas and stars. `GALFORM` follows the disk and bulge components of galaxies separately. Using a stellar population synthesis model (SPS), the code can predict the luminosity of the galaxy in a given passband or filter. The models are generally calibrated using local data, since historically, this is the epoch with the best measurements. High redshift observations can then be used to test the predictions of the semi-analytical model. An example of how we can use a galaxy survey to test the predictions of the galaxy formation model is reported in Chapter 4, where we test the redshift evolution of observer frame colours predicted by `GALFORM` against observations from the PAU survey. Another test is reported in Chapter 5 in which we compare the evolution of the colour-magnitude relation predicted by `GALFORM` to observations from the VIPERS survey.

3.1.1 The Durham semi-analytical galaxy formation model, GALFORM

I now describe how the semi-analytical model of galaxy formation, `GALFORM` is constructed. A full description of the model can be found in Cole et al. (2000); Lacey et al. (2016). The starting point is an N-body simulation which models the growth of structure in the dark matter due to gravitational instability. N-body simulations aim at reproducing the distribution of dark matter structures throughout the cosmic history. The small fluctuations in temperature observed in the Cosmic Microwave Background (CMB; see for exmaple Planck Collaboration et al. 2014) bring information about the density field that is regulating the distribution of dark matter. Since the epoch of decoupling between matter and radiation, when the CMB was released ($z \sim 1100$ which is approximately $400\,000$ years after the Big Bang),

up to the starting redshift of the N-body simulation (which can be typically some-what around $z \sim 100$) the perturbations to the density field are evolved following the linear perturbation theory. The N-body simulation is made of computational particles whose mass depends on their number and the volume of the simulation box. The mass of the computational particle is not meant to match the mass of the real dark matter particles but is order of magnitudes bigger, and related to the required resolution of the simulation. The resolution is determined by the problem being studied, for example if we are probing a large cosmological volume or we are interested in the detailed physics zoomed in in a small volume. Given the size of the particles, the N-body simulation model the gravitational interaction between them creating a distribution of dark matter at different time-steps (general reviews on how N-body simulations work can be found in Springel et al. 2006; Kuhlen et al. 2012; Angulo and Hahn 2021). Dark matter halos are virialised structures within the dark matter distribution. Halo finders algorithm aim at finding these structures. A way to identify them is to use percolation techniques that associate particles that are closer together than a specific fraction of the mean separation. Fine tuning the right distance to consider particle bounded, which is usually called linking length, results in groups of dark matter particles that have the same density of the virialised structures (i.e. the dark matter halos). Modern halo finder algorithms, also check that this particles are actually part of a structure and not just close together. Within halos, it is also possible to find subhalos, using similar algorithms but only within particles in a halo. In other words, subhalo finders look for local maxima of the denisty field within the halo. Halos and subhalos can be matched between the simulation snapshots in order to build halo merger trees (Jiang et al., 2014).

The novelty of this work is that the input N-body simulation used is the latest in the Millennium series, with a superior resolution in time and mass than the original simulation of Springel et al. (2005). In particular I have used the Planck Millennium N-body simulation (hereafter PMILL), which uses the updated cosmology from the

first year Planck cosmic microwave background data (Planck Collaboration et al. 2014; see Baugh et al. 2019). In particular, in the context of a flat universe, the matter density at the current epoch (including cold dark matter and baryonic matter) is set to $\Omega_M = \Omega_{\mathrm{CDM}} + \Omega_b = 0.307$ where the density of baryons is $\Omega_b = 0.04825$. The reduced Hubble parameter is set to $h = 0.6777$, the normalisation of the density fluctuations at the current epoch is $\sigma_8 = 0.8288$ and the spectral index of primordial density fluctuations is $n_{\mathrm{spec}} = 0.9611$. To compare these cosmological parameters to previous N-body simulations used in earlier versions of `GALFORM` see Table 1 of Baugh et al. (2019). The box of the simulation is about 27% bigger than the previous Millennium simulation based on the Wilkinson Microwave Anisotripy Probe 7 (WMAP7), Guo et al. (2013), with PMILL having a box side of $L_{\mathrm{box}} = 542.16\,h^{-1}$Mpc versus the WMAP7 run which has a box side of $L_{\mathrm{box}} = 500\,h^{-1}$Mpc. The number of particles in PMILL is more than an order of magnitude larger than in earlier runs with PMILL having 5040^3 particles versus the WMAP7 run which used 2160^3 particles. This leads to the PMILL simulation being able to track dark matter halos down to masses of $2.12 \times 10^9\,h^{-1}$Mpc; again this is almost an order of magnitude better than the WMAP7 run which was limited to halos bigger than $1.87 \times 10^{10}\,h^{-1}$Mpc (Guo et al., 2011). To construct a merger tree from a dark matter N-body simulation, three are the fundamental steps:

1. First a halo finder needs to be run on it to identify gravitationally bound groups of dark matter particles in each of the simulation redshift outputs. In the PMILL there are 271 output redshift snapshots at fixed epochs compared to the 64 available in the WMAP7 run. The most common algorithm is the Friend of Friend (FoF), however Stothert et al. (2018a) argue that more accurate techniques exist and they suggest a new implementation of the Markov clustering (MCL) technique for which the FoF is a subset.

2. Once identified the dark matter halos, we can identify subhalos within the halos running a subhalo finder, in our case we used `SUBFIND` Springel et al.

(2001). A common outcome of running `SUBFIND` is to find a big sub-halo that accounts for the bulk of the mass in the halo and some other smaller satellite sub-halos. A minimum of 20 dark matter particles is set for a sub-halo to be considered (for a discussion of the number of particles required to resolve a halo, see Armijo et al. 2021).

3. After having identified halos and subhalos in all of the 271 snapshots, the next step is to connect the halos in a merger tree structure where every halos is connected through the previous snapshot with a progenitor and to the following snapshot with a descendant. For `GALFORM` we used `DHALOS` (Jiang et al., 2014). For `GALFORM` the requirement is for this structure to be purely hierarchical, which means that after two halos have merged they have no possibility to split again. `DHALOS` uses criteria such as subhalo mass loss to decide if a subhalo has merged into a more massive structure.

The `GALFORM` calculation starts with the dark matter halos organised into a merger tree. `GALFORM` attempts to model a wide range of galaxy properties, including luminosities, based on the predicted star formation, merger and chemical evolution histories. To simulate the different baryonic components in a galaxy, `GALFORM` models the main physical processes that are believed to happen inside a galaxy. These processes are listed in Merson et al. (2013), and we restate them here for completeness:

- merging of dark matter halos,

- shock-heating and radiative cooling of the gas (this process regulates the formation of disks),

- star formation in disks (referred to a 'quiescent' star formation to distinguish it from star formation in bursts),

- feedback processes including feedback from active galactic nuclei, supernovae and the photo-ionisation of the intergalactic medium,

- chemical enrichment of gas and different generations of stars,

- dynamical friction of galaxies leading to mergers.

See Lacey et al. (2016) for a full description of the physical processes involved in the latest version of the `GALFORM` model.

The predicted SFH of a galaxy, when combined with a stellar population synthesis (SPS) model, results in the composite stellar population of the simulated galaxy. For historical reasons, `GALFORM` does not explicitly store the full SED of the model galaxies at high resolution, but instead tracks the mass-to-light ratios in a series of filters that are specified prior to runtime*. These filters can be in the rest frame or observer frame of the galaxy at the snapshot redshifts. In estimating luminosities, a treatment of dust extinction is included so that the light at different wavelengths can be attenuated by different amounts. The dust is assumed to be mixed together with the stars, rather than being in the form of a foreground screen. The dust attenuation depends on the dust content of the model galaxies and their optical depth, which in turn depends on the metallicity of the cold gas, and the size of the disk and bulge components (see Lacey et al. 2016 for a description of the calculation of galaxy sizes). In the `GALFORM` model described in this thesis, the SPS model used is from Bruzual and Charlot (2003) and the stellar initial mass function (IMF) has a Kennicutt form (Kennicutt, 1983).

As with all semi analytic models, `GALFORM` needs to be calibrated using observational data. Traditionally `GALFORM` has been calibrated using the luminosity function of local galaxies. In particular, optical and near-infrared luminosity functions have been the common choice (Bower et al., 2010). Including the luminosity function in the calibration of `GALFORM` means that the model needs to reproduce the exponential break in the slope of the luminosity function at bright magnitudes. This phenomenom is named the over-cooling problem and has been addressed using feedback mechanisms that quench the cooling of gas in massive central galaxies

---

*This way, the amount of memory needed is drastically lower, but it also means that for every different set of filters, a new run is needed.

(see Benson et al. 2000). With the introduction of the AGN feedback in `GALFORM` by Bower et al. (2006), the model is able to predict the evolution of the luminosity function, especially at the bright end, up to $z \sim 2$.

The properties of `GALFORM` galaxies also depend on their location within the dark matter halo, in terms of whether they are considered to be the central galaxy or a satellite. Central galaxies are located at the centre of mass of the most massive sub-halo within the host dark matter halo. The central galaxy accretes gas that cools from the hot halo, which can potentially be used to create new stars. Satellite galaxies instead are usually affected by ram-pressure stripping of their hot gas while travelling in the dense environment of the host halo, hence quenching any star-formation activity in the long term. In the standard treatment, this stripping is assumed to be instantaneous as soon as the galaxy becomes a satellite; in more detailed calculations, the stripping is assumed to be more gradual and depends upon the orbit of the satellite (Font et al., 2008). When two halos merge, then the central galaxy of the most massive progenitor halo will become the central of the merged descendant, with all the other galaxies becoming satellites. The time of the merger between a central and a satellite galaxy is estimated using the kinetic energy and angular momentum of the satellite galaxy, its mass and the mass of the host halo, and its orbit, using dynamical friction arguments.

3.2 Current model variants

3.2.1 Gonzalez-Perez et al. (2014) versus Lacey et al. (2016)

The most recent models under consideration before the availability of PMILL were the Gonzalez-Perez et al. (2014)* (hereafter GP14) and the Lacey et al. (2016) (hereafter LC16) models. These models are based on the WMAP7 N-body simulation, and were recalibrated for PMILL in Baugh et al. (2019). One thing that these

---

*This is the model used for the analysis of the colour-magnitude relation in Chapter 5.

models have in common is that they have been calibrated using the observations of the luminosity functions in the b_J and K-bands at redshift $z \sim 0$. Both models are able to reproduce the evolution of the luminosity function to high redshift. One difference between GP14 and LC16 is the choice of the IMF for the stars that form in bursts. These bursts are generated by instabilities in disks or the compression of gas caused by merger events. The choice of a mildly top-heavy IMF made it possible for the LC16 model to reproduce the number counts and redshift distribution of galaxies at wavelengths between 250 and 850μm, whilst still producing the observed number of galaxies today (see also Baugh et al. 2005). The choice of the IMF for stars created in quiescent star formation in disks is the same in both the variants of the model. In this case, both GP14 and LC16 use a solar neighbourhood IMF.

3.2.2 Recalibration of the model for PMILL

When recalibrating a `GALFORM` model, the first thing to do is to adapt the model to the different cosmology used. For the PMILL simulation the cosmology is that from Planck Collaboration et al. (2014), which is somewhat different from the best fitting WMAP7 model (see for example Guo et al. 2011). To see how the change in cosmology from WMAP7 to Planck affects the `GALFORM` predictions, we need to leave all the other parameters unaltered. Since the PMILL run has a better mass resolution than the WMAP7 simulation, we first need to degrade the resolution of PMILL to that in WMAP7. This means that, for this exercise, we consider only halo masses above $1.87 \times 10^{10} \, h^{-1} M_\odot$. In Fig. 3.1, we can see the predictions of `GALFORM` for both the LC16 (top panel) and GP14 (bottom panel) models for the optical b_J-band luminosity function. The blue dashed lines show the respective model predictions for the WMAP7 N-body simulation. The black dotted lines show the predictions using merger trees from the PMILL simulation degraded to the resolution of WMAP7. As expected the difference is tiny, at least for the galaxies brighter than the turnover at the faint end which is determined by the simulation
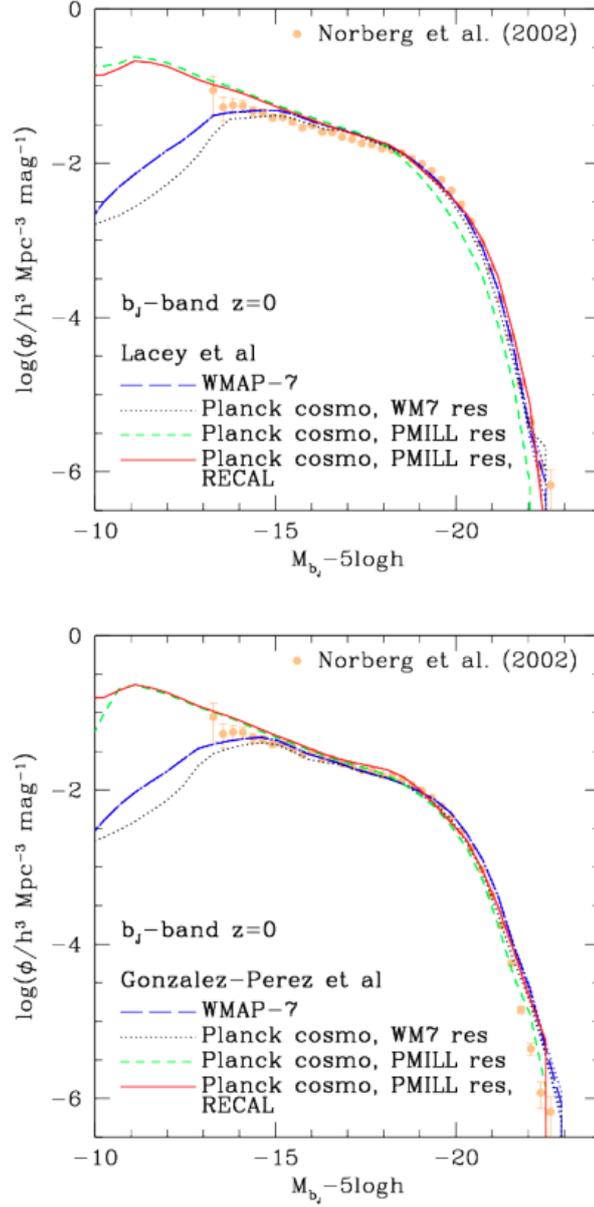
Figure 3.1: Luminosity function in the b_J band at $z = 0$. Symbols show observational data. The top panel shows the `GALFORM` prediction for LC16 and the bottom panel for GP14. Different lines represents different recalibration stages of the model as described in the legend and explained in the text.

resolution. This reflects the small changes in the cosmological parameters between the two simulations as listed in Table 1 of Baugh et al. (2019). Next we can see how the `GALFORM` predictions for the luminosity function change when using the full resolution of the PMILL halo merger trees. This is shown by the green dashed lines in Fig. 3.1. For both the GP14 and LC16 models, the important change is at the faint end with the simulation now predicting far more faint galaxies, reaching up to 4 magnitudes fainter than with the WMAP7 resolution trees. There is also a small difference at the bright end which is slightly more visible in LC16, predicting fewer bright galaxies than WMAP7 and the degraded PMILL. Only two parameters need to be finely retuned, and those two parameters are different in LC16 and GP14. In particular, for LC16 we need to change γ_{SN} into $\gamma_{\mathrm{SN}} = 3.4$ (instead of 3.2) and $\alpha_{\mathrm{ret}} = 1.0$ (instead of 0.64). These are two parameters that control the supernova feedback. The supernovae transmit energy to the intergalactic medium which in turns ejects gas from the galaxy. The rate of depletion of gas mass from the galaxy is proportional to the instantaneous star formation rate ψ and a mass loading factor β which scales with the depth of the gravitational potential well of the galaxy which in turn scales with the circular velocity of the galaxy V_C. In other words, we are computing how many times the mass that has been turned into stars, through star formation, is ejected in the wind (e.g. a mass loading factor of $\beta = 2$ means that the mass that the gas mass that has been converted into stars has been ejected twice in the time step). The equation regulating this process is:

$$\dot{M}_{\mathrm{eject}} = \beta(V_C)\,\psi = \left(\frac{V_C}{V_{\mathrm{SN}}}\right)^{-\gamma_{\mathrm{SN}}} \psi, \qquad (3.1)$$

where γ_{SN} define the dependence of the mass loading factor β from the circular velocity of the galaxy V_C and V_{SN} set the normalisation. Assuming $V_C < V_{\mathrm{SN}}$, increasing γ_{SN}, keeping all the other parameters fix, results in a bigger rate of mass ejection $\dot{M}_{\mathrm{eject}}$.

α_{ret} instead is a parameter that controls the rate at which the gas ejected outside the viral radius of the galaxy (and accumulated in a form of reservoir mass M_{res}) is "returning" inside the galaxy in form of hot gas. The equation regulating this

process is:

$$\dot{M}_{\mathrm{return}} = \alpha_{\mathrm{ret}} \frac{M_{\mathrm{res}}}{\tau_{\mathrm{dyn,halo}}}, \tag{3.2}$$

where $\tau_{\mathrm{dyn,halo}}$ is the halo dynamical time defined as $\tau_{\mathrm{dyn,halo}} = r_{\mathrm{vir}}/V_{\mathrm{vir}}$ with r_{vir} and V_{vir} being the virial radius and velocity respectively.

For the GP14 model the retuned parameters are V_{SN} (the normalisation to the circular velocity as already explained in Eq. 3.1) and α_{cool}, with $V_{\mathrm{SN}} = 380\,\mathrm{km/s}$ (instead of 425 km/s) and $\alpha_{\mathrm{cool}} = 0.72$ (instead of 0.60). Regarding V_{SN}, increasing its value would result in a bigger rate of mass ejected $\dot{M}_{\mathrm{eject}}$. α_{cool}, instead, is a parameter that regulates AGN feedback. In particular a higher value for α_{cool} implies that more galaxies are affected by the AGN feedback, with this heating mechanism operating in lower mass halos. For more details about the equations governing `GALFORM` and the different parameters involved see Lacey et al. (2016) or for a faster summary see Baugh et al. (2019). The b_{J} luminosity function for the recalibrated PMILL `GALFORM` model is shown by the red lines in Fig. 3.1. As can be seen from the figure, the agreement with the observations is better than the green line representing the non-recalibrated PMILL model.

3.3   Creation of a mock for PAUS

3.3.1   Construction of a lightcone mock

As we will describe in more detail in Sect. 4.2.3 (the reader interested in the details of the lightcone construction can read that section as an alternative to this or for an even deeper discussion read Merson et al. 2013), there is not a unique way to construct a mock catalogue of galaxies. However, the aim of a mock catalogue is always the same, namely to create a sample of galaxies as similar as possible to what can be observed in a real survey. What can change is the complexity of this catalogue. For example in a simple case, in which we might be interested only in a property like the luminosity in a certain band, we could simply sample the luminosity func-

tion for that band and obtain a mock catalogue of galaxy luminosities. However to build a more detailed mock that can track the main processes of galaxy formation and relate different galaxy properties together, the semi-analytical galaxy formation approach is one of the most promising possibilities. A semi-analytical model like `GALFORM` is based on an N-body simulation that describes the evolution of the distribution of gravitationally interacting dark matter halos at a set of discrete redshifts. Provided with hierarchical merger trees for the dark matter halos in the N-body simulation, the role of a semi-analytical model is to model the evolution of the baryonic component of the universe and, as a result, populate the halos with galaxies. We note that, semi-analytical models deal with baryons differently from simple halo occupation distribution (HOD) models. HOD are used to empirically model the relation between dark matter and baryons within a specific halo of a certain mass. The main predictions of HOD are the number of galaxies that usually live in a DM halo of a specific mass, the spacial distribution of galaxies and the distribution of velocities. The approach used by semi-analytical model is different. These quantities are not just related to the mass of the dark matter halo, but instead they are derived from the entire merger tree history of the simulation. The combination of an N-body simulation like PMILL (described in Sect. 3.2.2) and a semi-analytical model such as `GALFORM` has the potential to create a physically motivated model universe that predicts the evolution of different properties, both environmental and intrinsic to galaxies and their position in the sky. The last step in the creation of a mock is to generate a smooth distribution of galaxy redshifts interpolating between the discrete redshifts output by `GALFORM`. To do this, after choosing an observer within the simulation box, the redshift relative to that observer can be calculated for every galaxy. This redshift will not precisely match one of the discrete redshift outputs of `GALFORM` hence the properties and positions need to be derived from the closest `GALFORM` outputs. This is the role of the lightcone and it is crucial for making a realistic mock.

Interpolation of the galaxy position is treated in a different way from the inter-

polation of galaxy properties. First of all, a single simulation box can only cover a limited redshift range which is usually smaller than the redshift interval covered by a galaxy survey. For this reason the simulation box needs to be replicated with some boundary conditions to fill the survey volume. Then, the position of galaxies relative to the observer needs to be derived from the position of the galaxies in the snapshots adjacent to the redshift of lightcone crossing. This procedure is different for central galaxies (the one at the central of the dark matter halo) and satellite galaxies (the ones that orbit around the central). In particular for centrals, a simple linear interpolation between the two outputs including the observer's redshift is sufficiently accurate. For the satellites it is necessary to consider their orbit around the central and different approaches are available and discussed in Merson et al. (2013). Properties of galaxies are instead more complicated and a simple interpolation would be inadequate. For example, unpredictable events like bursts of star formation or unstable disks, can lead to very different properties from those that would result from a simple interpolation. For this reason it is more accurate to use the galaxy property from the redshift just above the lightcone crossing redshift. A different argument applies to observer frame magnitudes as they are redshift dependent and this means that the correction for the band-shifting of the set of filters used is predictable and a correction can be applied for the difference between the output redshift and the observer's redshift.

3.3.2 The PAUS mock

Using the techniques described in Sect. 4.2.3, I used `GALFORM` to create a mock for the PAU survey. One of the benefits of having a PAUS mock is, for example, to evaluate the performance of the photo-z codes developed by the PAUS team. The reason why we need a mock to evaluate the performance of the photo-z code is that we can compare the estimated redshift with the real value, hence estimating the error. This is not possible with real data as we only have the estimated value*. The

---

*However, as we have done in Sect. 2.1.3.4, instead of a true value, spectroscopic measurements can also be used when available as they usually have lower errors than photometric redshifts.

reason why we need a new mock based on a new N-body simulation like PMILL (described in Sect. 3.2.2), is that when running the photo-z code on the old PAUS mock based on the WMAP7 N-body simulation (Stothert et al., 2018b), the redshifts returned by the photo-z code were quantised along the exact values of the `GALFORM` outputs indicating that the redshift outputs were too far apart for the interpolation to work properly (see Fig. 3.2). With PMILL we have 271 snapshots instead of the 64 in the old WMAP7 simulation. This means that between every snapshot in the old simulation we now have three additional ones in the new simulation. This means that any errors introduced by the interpolation scheme applied to compute the observer frame magnitudes are smaller than before. In Fig. 4.5 we show the results of running the BCNz2 photo-z code (Eriksen et al., 2019) on a subsumple of 6 random subvolumes of our mock after adding to the flux a gaussian error with a variance of 10%. We can see that the focusing at the `GALFORM` outputs is not present in the new mock.

The photo-z application is only one of the many applications for which my PAUS mock can be used. For example, the output of the lightcone, or even a small subsample of it (in this exercise I have used 1 subvolume out of the available 1024), can be used as input to an imaging simulation like UFig (`https://people.phys.ethz.ch/~ipa/cosmo/pau/`). The distribution of the galaxy positions in the lightcone that I have used for this exercise is shown in Fig. 3.3. The output of the Ufig simulation using the little `GALFORM` run as input, is shown in Fig. 3.4. In particular this imaging simulation uses the `GALFORM` predictions for the scale lengths of the bulge and the disk components of the model galaxies. The use of my PAUS mock for galaxy imaging simulation will be part of a project described in Tortorelli et al. (in prep).

However, biases may be present in the spectroscopic galaxy sample, for example with a over-representation of blue, star forming galaxies with stronger emission lines.
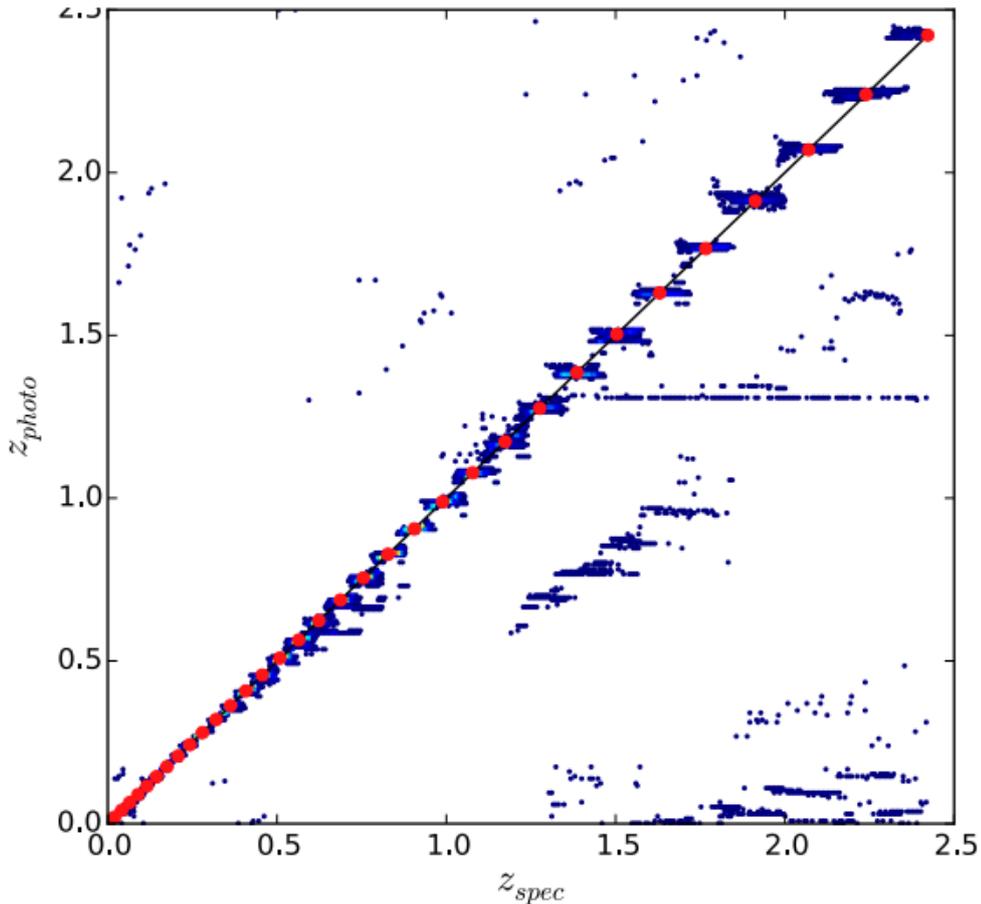
Figure 3.2: Relation between the lightcone redshifts, z_{spec}, and the photometric redshift, z_{photo}, estimated by the BCNz2 code (Eriksen et al., 2019) after running on the 40 narrow-bands of the old lightcone (Stothert et al., 2018b), which is based on the WMAP7 Millennium N-body simulation (Guo et al., 2013). The blue points show the galaxy redshifts while the red ones are the location of the GALFORM outputs in the WMAP7 simulation. Taken from Stothert et al. (2018a).

3.4 Optimisation

The higher time and mass resolution that the PMILL N-body simulation provides, combined with the large set of filters (40 narrow-bands plus 6 broad-bands) needed to reproduce the PAUS settings makes the creation of a PAUS mock a particularly demanding task in terms of computing power. The PMILL simulation also has a large number of subvolumes to process (each subvolume is a random sampling of all the merger trees in the simulation, rather than an actual spatial subvolume).
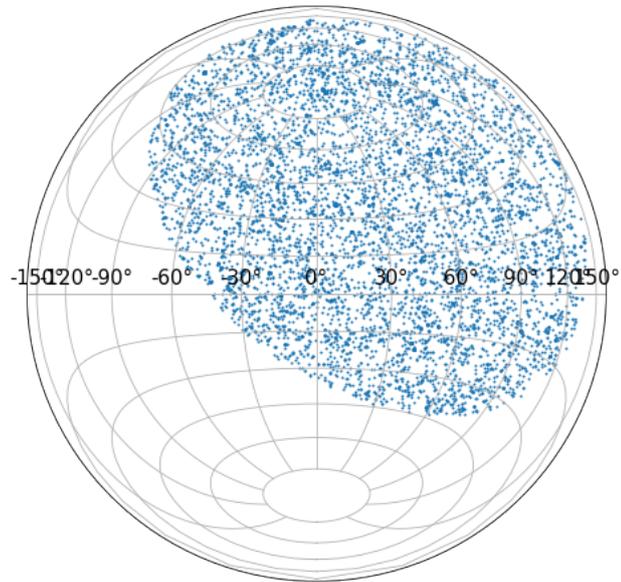
Figure 3.3: Distribution of galaxies on the sky for a `GALFORM` run on a single subvolume (the complete `GALFORM` run would use all 1024 subvolumes, resulting in a more crowded distribution of galaxies).
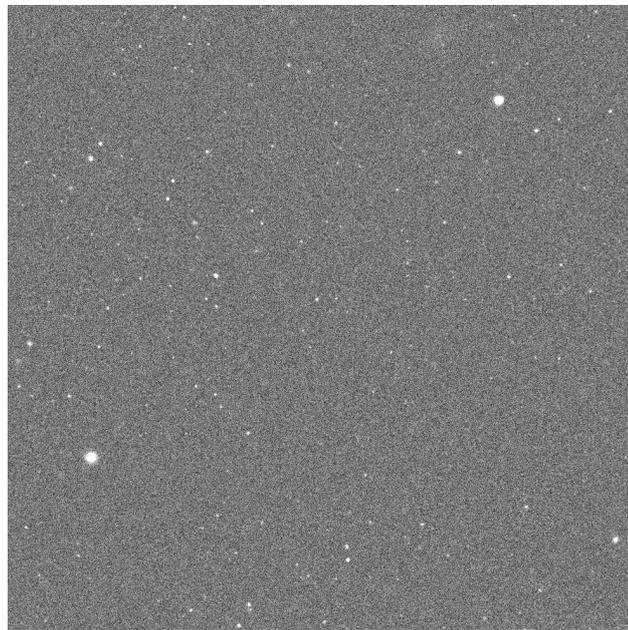
Figure 3.4: Output of the Ufig imaging simulation when run using `GALFORM` as an input. Simulated galaxies in this patch of the sky are very sparse as the `GALFORM` run is limited to 1 out of 1024 subvolumes. Credit Luca Tortorelli from Ufig team at ETH.
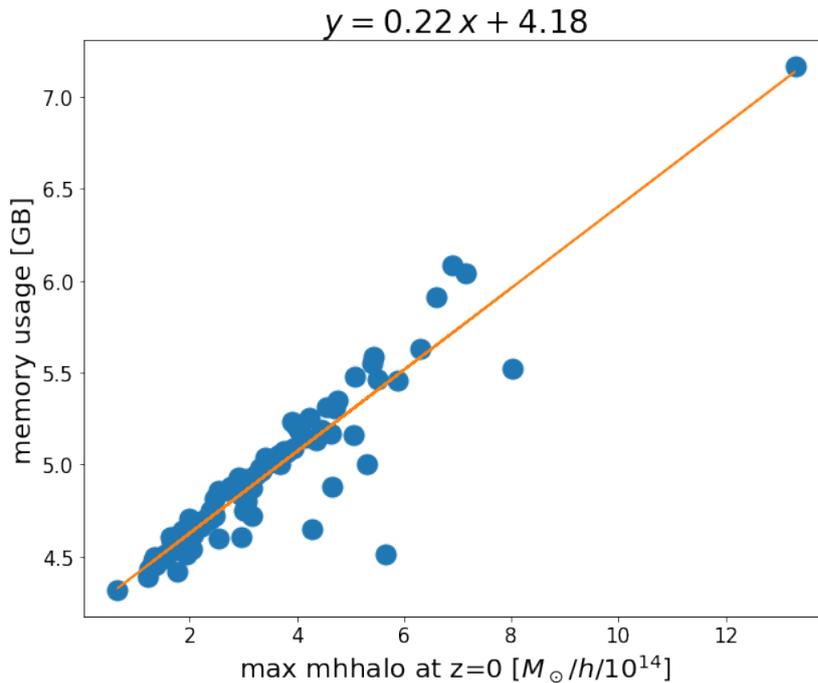
Figure 3.5: Relation between the biggest dark matter halo at redshift zero and the amount of memory required to process the subvolume in which the DM halo lives in.

This required me to carefully consider the scheduling of the `GALFORM` jobs. Running the 1024 subvolumes in the queues using the previous methodology, without any consideration about the memory requirements, led to jobs crashing or taking up large wall clock times to complete.

The first improvement was to predict the amount of system memory needed to process each subvolume of the simulation. I found a relation between the amount of system memory needed and the size of the biggest dark matter halo in each subvolume. This allowed me to reserve in every COSMA node just the right amount of memory for every subvolume, allowing the maximum number of tasks to run simultaneously, hence speeding up the overall wallclock time needed to complete the processing of the subvolumes. Fig. 3.5 shows this linear relation.

A second improvement made to the processing of the subvolumes is related to the way `GALFORM` is designed to run. Traditionally `GALFORM` has been always used on a single-core. This does not mean that every subvolume needs to wait for the

previous one to be completed before starting but it means that I need to submit an array of tasks, with each task executing a subvolume independently on a different core or node rather then submitting a single task for a range of subvolumes that progress in parallel at the same time. I adapted the code for the submission of `GALFORM` to run in parallel using Message Passing Interface (MPI) to test if this new mode is more efficient. The efficiency of running `GALFORM` sequentially or in parallel is not dramatically different (especially when reserving the right amount of memory as just described), what makes a big difference is the number of machines (or nodes) that are available for parallel computing and the amount available to only run sequentially. The supercomputer set-up in Durham is limited to 8 nodes in the sequential queue (each node has 8 CPUs) while the nodes for parallel queue has 302 nodes.

With the new PMILL N-body simulation a complete PAUS mock occupies about 30 TB of disk space instead of about 1 TB that was needed for the old WMAP7. This results in a longer run time. With the sequential approach and only 8 nodes available, a single lightcone run of the full PMILL simulation can take up to several months, depending on the redshift range required. For example setting the redshift range between $0 < z < 1$ (even though our final mock is designed for $0 < z < 2$), a rough estimate for the sequential approach to end is of about 372 days which is approximately 12 months. This would make it almost impossible to run `GALFORM` multiple times with the aim of comparing different parameters. With the new parallel setting for `GALFORM` the time of each run is reduced to about 15 days. This new way of running `GALFORM` has never been implemented before and it will become the new standard for `GALFORM` lightcone runs.

In conclusion, with this new implementation of `GALFORM` I have created a PAUS mock based on the PMILL N-body simulation and following the parametrisation of Gonzalez-Perez et al. (2014) adapted to the new cosmology and resolution of PMILL according to Baugh et al. (2019) and explained in Sect. 3.2.2. This new mock improves the interpolation between snapshots creating a smooth distribution

of redshifts up to $z \sim 2$, solving the discretisation problem discussed in Fig. 3.2, typical of N-body simulations with less timesteps resolution as in Stothert et al. (2018b). In the next chapter we are going to fully exploit this new mock, testing its prediction in the galaxy observer frame colours. Along with galaxy colours, we will test standard diagnostics like galaxy redshift distribution and number counts. The promising results discussed in the next chapter prove that the physics behind this new PAUS mock is consistent with the PAUS observations.

The PAU survey: a new constraint on galaxy formation models using the colour redshift relation.

In this Chapter we use the GALFORM semi-analytical galaxy formation model implemented in the Planck Millennium N-body simulation to build a mock galaxy catalogues on an observer's past lightcone. The mass resolution of this N-body simulation is almost an order of magnitude better than previous ones used for this purpose, allowing us to probe fainter galaxies and hence build more complete mock catalogues at low redshifts. The higher frequency of simulation outputs allows us to make improved calculations of galaxy properties and positions in the mock. We test the predictions of the mock against the Physics of the Accelerating Universe Survey, a narrow band imaging survey with high accuracy photometric redshifts, which probes the galaxy population over a lookback time of 8 billion years. We compare the model against the observed number counts, redshift distribution and evolution of the observer frame colours with redshift; these statistics avoid the need for model-dependent processing of the observations. The model produces red and blue populations that have similar median colours to the observations. However, the bimodality of model colours is stronger than in the data, with different relative

numbers of red and blue galaxies at higher redshifts.

4.1 Introduction

In the effort to understand how the Universe evolves and to probe the physics that governs the formation and evolution of galaxies, mock galaxy catalogues have become an important tool for comparing theoretical models to observations. Wide-field galaxy redshift surveys are covering larger areas of sky with increasing depths in redshift. A mock catalogue models the selection effects that dominate every galaxy survey, and hence allow us to understand how these observational effects shape any measurements made from the survey, and thus in turn to disentangle physical results from observational effects. For example, some observations, like the evolution of observer frame galaxy colours with redshift, that can be modelled in an accurate mock built with a galaxy formation model, might appear to be different when errors due to observational effects are realistically modelled.

Here we build a replica of an ongoing survey, the Physics of the Accelerating Universe Survey (PAUS; Eriksen et al. 2019; Padilla et al. 2019). PAUS is a novel narrow-band imaging survey that aims to eventually cover around 100 deg^2 to an initial depth of $i_{AB} = 22.5$, with some observations reaching $i_{AB} = 23$. The PAU Survey is being carried out using a new camera, PAUCam (Padilla et al., 2019), which is mounted on the William Hershel telescope (WHT) in La Palma (Spain). PAUS has observed the COSMOS field and the Canada-France-Hawaii-Telescope Lensing Survey (CFHTLS) W1, W2, W3 and W4 fields in 40 narrow bands filters. The narrow band filters have a width of 130Å with their central wavelengths separated by 100Å and cover the wavelength range from 4500Å to 8500Å. Eriksen et al. (2019) measured photometric redshifts for PAUS galaxies in the COSMOS field, estimating a scatter that is around an order of magnitude below the few percent level that is typically obtained when using a handful of broad band filters (see also Alarcon et al. 2021; Cabayol et al. 2021). Here we focus instead on two of

the largest fields in PAUS, the CFHTLS W1 and W3 fields, which at present cover about 38 deg². These fields inherit the properties of the parent catalogue, the CF-HTLenS (Erben and CFHTLenS Collaboration, 2012), in particular photometry in the standard u,g,r,i,z broad band filters. Despite the much improved precision in the photometric redshifts produced from PAUS photometry, the associated positional errors remain an observational effect of concern. These errors could alter the perceived evolution of a statistic by mixing galaxies with different properties between redshift bins. If the property evolves with redshift over a redshift range comparable to the errors in the photometric redshift, or if there are significant numbers of redshift outliers, i.e. galaxies with catastrophic redshift errors, this will alter the evolution of the statistic. A mock catalogue with realistic photometric redshift errors provides a way to address the impact of such errors and selection effects on measured statistics.

The PAU Survey complements and extends spectroscopic studies of galaxy evolution. PAUS is deeper than the Galaxy and Mass Assembly (GAMA) Survey (Driver et al., 2009). The deepest GAMA fields are limited to $r = 19.8$. For the typical galaxy colour of $r-i \sim 0.4$ (González et al., 2009), this corresponds roughly to $i_{AB} = 20.2$, which is over a magnitude shallower than the fiducial PAUS limit of $i_{AB} = 22.5$. The GAMA redshift distribution peaks at $z \sim 0.2$ and extends to $z \sim 0.5$. PAUS has the same depth as the VIMOS Public Extragalactic Redshift Survey (VIPERS; Guzzo et al. 2014; Scodeggio et al. 2018), which measured 100 000 galaxy redshifts in the interval $0.5 < z < 1.2$, over 24 deg², around 2/3rds of the combined solid angle of the W1 and W3 fields considered here. VIPERS used a colour preselection to target galaxies with $z \gtrsim 0.5$. As we will see, this is the peak in the redshift distribution for galaxies brighter than $i_{AB} = 22.5$. Hence PAUS samples the full range of galaxy redshifts to this magnitude limit, covering $0 < z < 1.2$. Moreover, the galaxy selection in PAUS is simply magnitude limited. There is no requirement on finding spectral features to measure a redshift with a high degree of certainty, so there is no bias against objects with weak spectral

breaks or emission/absorption lines.

The redshift range covered by PAUS galaxies corresponds to a look back time of around 8 billion years or about two thirds of cosmic history. Within this period a dramatic change took place in the global star formation rate (SFR) density (Madau and Dickinson, 2014). The present day star formation rate density is around one tenth of the value at the peak, which occurred just above $z \approx 1$. Hierarchical models of galaxy formation have traditionally struggled to reproduce this drop in star formation activity (e.g. Baugh et al. 2005). The inference of the global star formation rate from observations is fraught with difficulties, such as accounting for the attenuation of starlight by dust, which is important at the short wavelengths that are most sensitive to recent star formation, and the 'correction' for galaxies that are too faint to be observed. Instead, we take the more direct approach of considering observer frame galaxy colours. The $g - r$ colour is less affected by dust attenuation than the UV fluxes used to deduce star formation rates.

Optical galaxy colours are sensitive to the star formation activity in galaxies and other intrinsic properties such as the metallicity and overall age of the composite stellar population and the galaxy stellar mass (e.g. Daddi et al. 2007; Taylor et al. 2011; Robotham et al. 2020). Galaxy colours are also correlated with morphology (Strateva et al., 2001b). Hence by measuring galaxy colour we can in principle constrain some of the physical process that change the star formation history of a galaxy and the chemical evolution of its stars. The relative importance of gas cooling, and heating by supernovae and AGN is expected to change over the time interval accessible in the PAUS data.

The traditional way to analyse galaxy surveys, particularly ones that cover a substantial baseline in redshift, is to estimate rest-frame luminosities. This involves correcting for band-shifting effects, which lead to filters in the observer frame sampling progressively shorter wavelengths in the galaxy's rest frame with increasing redshift (Hogg et al., 2002; Kasparova et al., 2021). This correction depends on the shape of the galaxy's spectral energy distribution which depends on its star

formation history, chemical evolution, stellar mass and dust content. Corrections may also be required for changes in the stellar populations over time, called evolutionary corrections, in luminosity function studies (Loveday et al., 2015). Here we take a simpler approach and try to avoid any model dependent processing of the observations. We aim instead to compare the model predictions with raw, unprocessed observational quantities based on apparent magnitudes and redshift. In addition to basic statistics like the number counts and redshift distribution of galaxies, we also consider the evolution of the observer frame galaxy colours with redshift, exploiting the wide redshift baseline and homogeneous selection of PAUS.

To compare the evolution of observer frame colours with theoretical models it is necessary to include the band shifting effects in the model predictions. We do this by building a mock catalogue on an observer's past lightcone by implementing a semi-analytical model of galaxy formation into an N-body simulation (Kitzbichler and White, 2007; Merson et al., 2013). This opens up a new set of tests of galaxy formation models: the overall galaxy number counts, the redshift distribution and the evolution of the observer frame colours; in the latter two cases the statistics are measured for a specified magnitude limit. Hence, we extend the datasets typically used to calibrate galaxy formation models, such as the local luminosity function or stellar mass function, to include statistics that cover a range of redshifts and are relevant to ongoing and upcoming surveys such as DESI (DESI Collaboration et al., 2016) and Euclid (Laureijs et al., 2011). We use the `GALFORM`(Cole et al., 2000; Lacey et al., 2016) implemented in the Planck Millennium N-body simulation Baugh et al. (2019). This extends the work of Stothert et al. (2018b) as the simulation used here has superior resolution in mass and time. This allows us to include fainter galaxies in the mock catalogue and to make more accurate predictions for galaxy positions and luminosities. Also, since Stothert et al. (2018b), sufficient PAUS data has been collected to allow accurate measurements of the basic galaxy statistics to be made.

The remainder of the paper is laid out as follows: we first describe the theoretical

framework used to build our PAUS mock on (Sect. 4.2), then we will present our main analysis and results (Sect. 5.5) and finally discuss the implication of our findings in the current understanding of our universe (Sect. 4.4).

4.2   Theoretical model and observational dataset

Here we describe the theoretical model, covering the galaxy formation model (§ 2.1), the N-body simulation in which it is implemented (§ 2.2), the construction of the lightcone mock catalogue (§ 2.3), before introducing the PAUS dataset in § 2.4.

4.2.1   Galaxy formation model

We use the `GALFORM`-analytical model of galaxy formation (Cole et al., 2000; Bower et al., 2006; Lacey et al., 2016). The model follows the key physical process that shape the formation and evolution of galaxies in the cold dark matter cosmology (for reviews of these processes and semi-analytical models see Baugh 2006 and Benson 2010). The model tracks the transfer of mass and metals between different reservoirs of baryons, predicting the chemical evolution of the gas that is available to form stars and the full star formation history of galaxies. When implemented in an N-body simulation, the semi-analytical model also provides predictions for the spatial distribution of galaxies (Kauffman, 1999; Benson et al., 2000).

Here we use the version of the model introduced by Gonzalez-Perez et al. (2014) (hereafter GP14), as recalibrated by Baugh et al. (2019) following its implementation in the P-Millennium N-body simulation, as described in Sect. 4.2.2. The model parameters are calibrated mostly using local observations of the galaxy population.

4.2.2   The P-Millennium N-body simulation

The Planck Millennium N-body simulation is the latest in the 'Millennium' series of simulations of structure formation (Springel et al. 2005; Guo et al. 2013, see

Table 1 in Baugh et al. 2019 for a summary of the specifications of these runs and the cosmological parameters used). The Planck Millennium follows the evolution of the matter distribution in a slightly larger volume (by a factor of $\times 1.43$, after taking into account the differences in the Hubble parameters assumed) than the simulation described by Guo et al. (2013), which was used by Stothert et al. (2018b) to build an earlier mock catalogue for PAUS.

The Planck Millennium uses over 128 billion particles (5040^3) to represent the matter distribution, which is more than an order of magnitude more than was used in the earlier Millennium runs. This, along with the simulation volume used, places the Planck Millennium at a resolution intermediate to that of the Millennium-I simulation of Springel et al. (2005) (hereafter MSI) and the Millennium-II run described in Boylan-Kolchin et al. (2009). The Planck Millennium has many more outputs than the MSI, with the halos and subhalos stored at 271 redshifts compared with the ~ 60 outputs used in the MSI. Dark matter halo merger trees were constructed from the SUBFIND subhalos using the DHALOS algorithm described in Jiang et al. (2014) (see also Merson et al. 2013). Halos are retained that contain at least 20 particles, corresponding to a halo mass resolution limit of $2.12 \times 10^9 \, h^{-1} \mathrm{M}_\odot$.

4.2.3 Building a lightcone mock catalogue

The construction of a mock catalogue for a cosmological redshift survey can be accomplished in different ways resulting in predictions with different accuracies and which inform us to different extents about the physics behind galaxy formation. In principle, a simple approach would be to sample a population of galaxies randomly from an observed statistical distribution such as the luminosity function. However, this would lead to a catalogue with information limited to the property studied in the statistical distribution, ignoring any other properties and their relation with other observables. Moreover the biggest limitation is that such a simplistic catalogue would not even be able to track the evolution of the galaxy population with

redshift. To build a more realistic catalogue we need to track the evolution of the dark matter structures and populate the dark matter halos with galaxies at different epochs. Here, we make use of the Planck Millennium N-body simulation described in the previous section. To populate dark matter halos in the simulation with galaxies, we implement the `GALFORM`-analytic model of galaxy formation on the merger histories of the dark matter halos extracted from the simulation. The combination of the Planck Millennium and `GALFORM` results in a physically motivated model which includes environmental effects related to the merger histories of halos, and gives predictions for the spatial distribution of galaxies. `GALFORM` predicts the chemical evolution of the gas and stars in each galaxy, along with the size of the disk and bulge components and their star formation histories. The model outputs the mass-to-light ratios in a list of filters that are specified at run time. Along with the model for attenuation of stellar emission by dust described in Cole et al. (2000), this allows the model to predict the brightness or magnitude of the model galaxies in these bands.

The output of `GALFORM` is the properties and positions of the galaxy population in the simulation box at a discrete set of redshift outputs. The *lightcone* is built by interpolating galaxy magnitudes and positions between the values at these discrete redshifts, using the redshift at which the galaxy crosses the observer's lightcone. Thanks to the high time resolution of the Planck Millennium, the reliability of the interpolation process described below is increased compared to that in earlier Millennium simulations.

To build the PAUS mock we follow the procedure described in Merson et al. (2013). We first place an observer at some position inside the simulation box, and chose a line of sight direction* for the mid-point of the survey, and a solid angle. Given the size of the simulation box, using this volume on its own we would only be able to probe redshifts out to $z \approx 0.19$. Hence, to cover the volume sampled by

---

*It is good practice to choose a line of sight that does not coincide with one of the axes of the box to maximise the distance (and hence time) between repetitions of the same structure.

PAUS we need to replicate the simulation box in space using the periodic boundary conditions. A galaxy crosses the past lightcone of the observer in between two of the simulation output redshifts or snapshots. The positions of the galaxy in the two snapshots are used to estimate its position at lightcone crossing. Merson et al. (2013) apply different interpolation procedures for central and satellite galaxies. Central galaxies are assumed to be at the centre of mass of the host dark matter halo and hence track its motion between the snapshots. In this case, a simple linear interpolation is sufficient. Satellite galaxies, on the other hand, follow more complicated paths and can enter the observer's past lightcone either before or after their associated central. For this reason, a more sophisticated treatment is needed to compute the position of a satellite galaxy, taking into account its orbit around the central (see Fig. 2 of Merson et al. 2013). Interpolating the galaxy positions in this way minimises artificial jumps in the correlation function measured from the lightcone.

Assigning properties to galaxies as they cross the observer's past lightcone using a simple interpolation between snapshot could lead to inaccuracies. The evolution of some properties, such as the SFR, is too complicated to be modelled by simple linear interpolation. Star formation can result from stochastic events, such as galaxy mergers and mass flows triggered by dynamically unstable disks, as well as smoother quiescent star formation in the galactic disk. For this reason, we follow Merson et al. 2013 and simply retain the galaxy properties from the higher redshift snapshot just above the redshift of lightcone crossing (as suggested by Kitzbichler and White 2007). Given the higher frequency of simulation outputs in the Planck Millennium run, the errors associated with this treatment are smaller than in previous Millennium simulations.

The one exception to this is the magnitude of the galaxy in the pre-specified filters in the observer frame. The definition of the observer frame depends on redshift and so is slightly different at the two redshifts that straddle the lightcone crossing redshift. We perform a linear interpolation between these two versions of

the observer frame magnitudes to compute magnitude at the redshift of lightcone crossing. In addition to the bandshifting of the observer frame, we need to use the luminosity distance that corresponds to the lightcone crossing redshift to compute the apparent magnitude of the galaxy in the mock. This approach does not take into account any change in the spectral energy distribution of the galaxy between the higher redshift snapshot and the lightcone crossing redshift. However, the resulting colour-redshift relation is smooth and contains no trace of the locations of the simulations snapshots, as shown in Fig. 4 of Merson et al. (2013).

4.2.4 The PAUS Survey

We test the `GALFORM` lightcone against the Physics of the Accelerating Universe Survey (PAUS) and have designed our lightcone to match the specifications of the survey. As briefly described in the introduction, PAUS is a novel imaging survey, with the key feature being the 40 narrow-band filters of width 130Å, covering the wavelength range from 4500Å to 8500Å, spaced by 100Å. In the W1 and W3 PAUS fields the narrow-bands are complemented with the standard u,g,r,i,z broad-band filters from the CFHTLenS catalogue (Erben and CFHTLenS Collaboration, 2012). The 40 PAUS narrow bands overlap the wavelength range covered by the CFHTLenS u,g and r broad band filters, as shown in Fig. 1 of Stothert et al. (2018b). Fluxes are estimated in the narrow band images using forced photometry apertures from the broad band imaging. The narrow bands are particularly important when estimating photometric redshifts. The precision that PAUS can achieve is intermediate between that which can typically be achieved with a handful of broad band filters and that obtained with spectroscopy in a large-scale structure survey, in which case the spectral resolution and exposure time are chosen to maximise the number of redshifts that can be measured; Eriksen et al. (2019) report an error of $\sigma_z = (z_{\text{photo}} - z_{\text{true}})/(1 + z_{\text{true}}) \sim 0.0037$ when selecting the 'best' 50 per cent of the PAUS photometric redshifts in the COSMOS field limited at $i_{\text{A}B} < 22.5$. Since this first estimation of photometric redshifts by Eriksen et al., PAUS has covered

more fields besides COSMOS, with observations available for the CFHTLS wide fields: W1, W2, W3 and W4. For this study we have decided to use the larger fields in PAUS which are currently W1, covering 13.71 deg^2 and W3 covering 24.27 deg^2 (giving a total of 37.98 deg^2). This choice ensures a uniform set of broad band filters is available, as W1 and W3 are both covered by CFHTLenS.

Our PAUS mock provides 'true' values for fluxes and redshifts without measurement errors. We therefore decided to estimate a photometric redshift for each model galaxy using the BCNz2 code, as in Eriksen et al. (2019), after introducing some 'artificial' gaussian errors to the fluxes, with variance fixed to a given percentage of the flux. This means that in addition to the mock catalogue we can provide a photo-z catalogue that can be used to test PAUS selection effects, such as the impact on galaxy properties when selecting galaxies according to the redshift quality flag, Q_z, (see Eriksen et al. 2019 for the definition of this property and its usage).

4.3 Results

4.3.1 Basic results

We have built a mock catalogue for the PAU survey which covers approximately $100 \, \mathrm{deg}^2$, is magnitude limited at $i_{AB} < 22.5$ and potentially spans the redshift range $0 < z < 2$. The narrow band photometry has been computed using the transmission curves estimated by Casas et al. (2016) and Padilla et al. (2019) for the PAUCam optical system and the broad band photometry has been computed from the transmission curves used in the CFHTLenS (Erben and CFHTLenS Collaboration, 2012).

The distribution of the mock galaxies on the sky for three representative redshift bins is shown in Fig. 4.1, where we have split the galaxy population according to their observer frame $g-r$ colour (see later for a discussion of this split; we split the
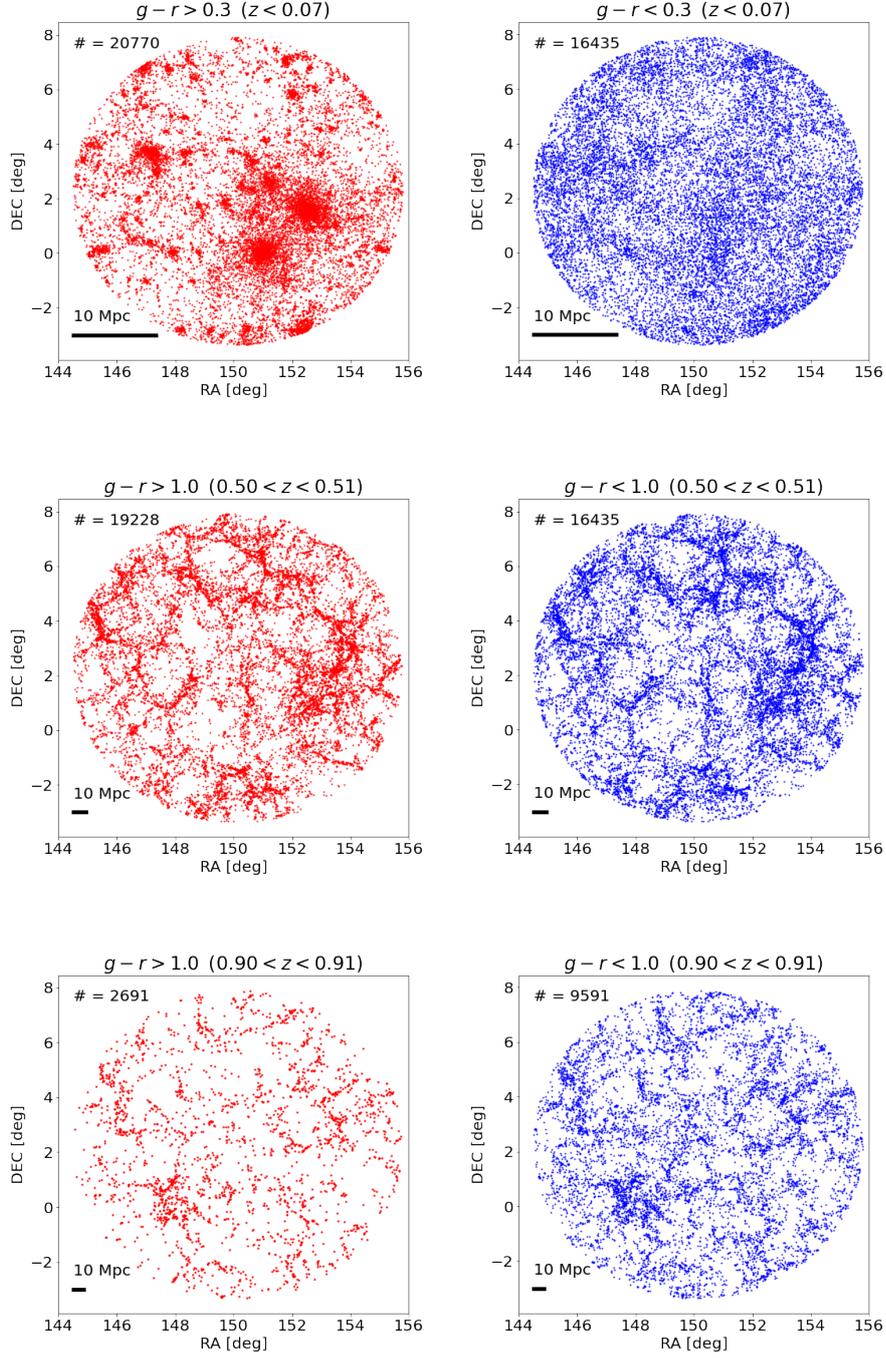
Figure 4.1: The projected angular positions of lightcone galaxies (right ascension and declination in degrees) in three different redshift intervals (**top**: $z < 0.07$, **middle**: $0.50 < z < 0.51$ and **bottom**: $0.90 < z < 0.91$), separated into red from blue galaxies according to their observer frame $g - r$ colour (see Fig. 5). The lightcone covers approximately 100 deg^2 and is magnitude limited in $i_{AB} \lesssim 22.5$. The presence of two big cluster at low redshift (top panels) can have an effect on the number counts. For reference, the thick black bar in each panel indicates a scale of 10 Mpc. The number of galaxies is reported in the top left of each panel.

population in red and blue galaxies using the boundary shown in Fig. 4.7 by the white line, i.e. red galaxies are those which satisfy $g-r > 1.7\,z + 0.35$ or $g-r > 1.1$). The spatial scale in these images is indicated by the bar which shows a scale of 10 Mpc, and allows us to compare the size of the structures at different redshifts. As shown in previous studies (e.g Zehavi et al. 2011), red galaxies tend to cluster more strongly than blue galaxies. This is driven by environmental effects, such as the quenching of gas cooling and star formation when galaxies fall in the potential well of a more massive host dark matter halo (for example due to ram pressure stripping or other similar phenomena related to the removal of gas from galaxies due to gravity or tidal interactions). In the first row of Fig. 4.1 ($0 < z < 0.07$), this effect is clearly visible with structures traced out by red galaxies being sharply defined compared to the more 'diffuse' distribution of blue galaxies seen in the right panel. In the middle row of Fig. 4.1 ($0.50 < z < 0.51$) as we zoom out, a larger region of the cosmic web is visible. The difference in the contrast of the structures seen with red or blue galaxies is now less pronounced, but still present, with the structures traced by blue galaxies appearing somewhat less sharp than those mapped by the red galaxies. In the bottom row of Fig. 4.1, which shows the redshift slice $0.90 < z < 0.91$, we can see that although the total number of galaxy is lower than it is in the other lower redshift bins, the relative number of red and blue galaxies is reversed (i.e. we now have more blue galaxies than red), in agreement with the general uplift in star formation activity with increasing redshift.

Now that we have gained a visual impression of the galaxies in the lightcone, and have seen how different colour populations trace out structures, we are ready to perform more quantitative analyses. The first simple characteristic measure of an optically selected galaxy sample is the number counts as a function of magnitude. We plot the i-band number counts in Fig. 4.2. The blue line represents an estimate of the observed galaxy number counts for PAUS in the W1 and W3 fields (which cover, respectively, areas of 13.71 deg^2 and 24.27 deg^2, giving a total of 37.98 deg^2). This is the area covered by the PAUS galaxies with at least one measurement in
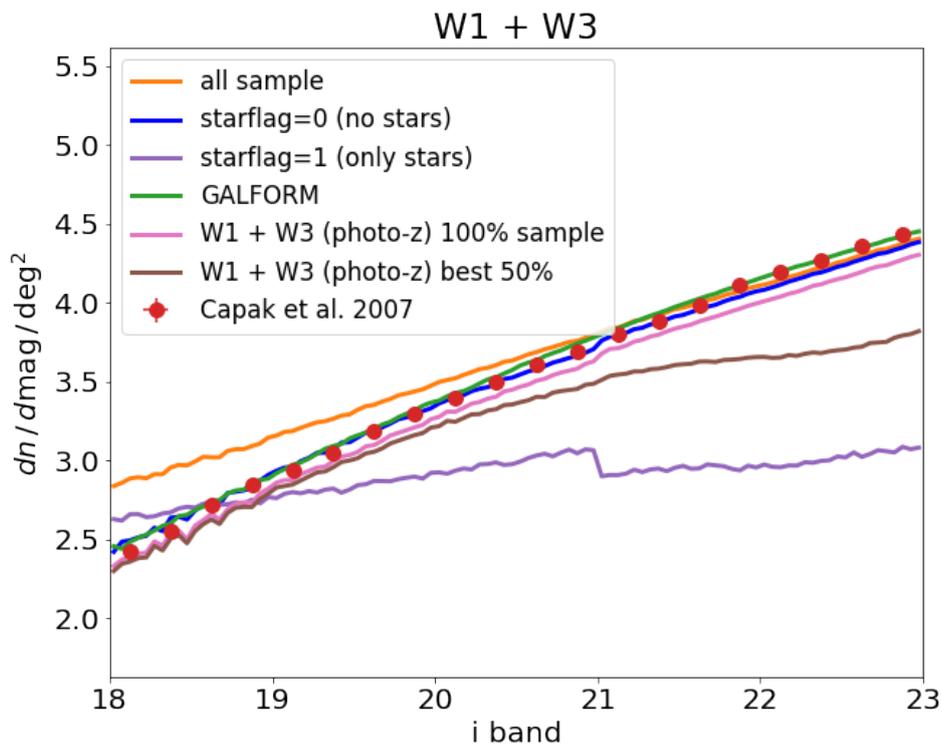
Figure 4.2: i-band number counts for the GALFORM mock (green line) compared with the number counts from Capak et al. (2007) (red points) and the PAUS data in the W1 and W3 for different selections: all photometric sample (orange line), this includes all the galaxies that have been observed in the NB filter NB455 (this means that they might not have a redshift estimate), galaxies with star_flag$= 0$ (blue line) which are those that has been classified as galaxies from a CFHTLenS star-galaxy separation algorithm, galaxies with star_flag$= 1$ (violet line) which are those that has been classified as stars, total photo-z sample (pink line), which are the galaxies that have a PAUS redshift estimates (they need to be observed in all NB filters) and 50% of the best quality redshift sample (brown line) according to the quality flag Q_z as described in Eriksen et al. (2019).

the narrow band filter at 455 nm. This results in a more complete sample than the PAUS photo-z catalogue, because in order to measure a photometric redshifts, there is a requirement for the galaxy to be imaged in all the 40 narrow band filters (as well as the 5 CFHTLenS broadbands from the parent catalogue). This target is not always met for the PAUCam imaging (Padilla et al., 2019). We also include the number counts of galaxies with photometric redshifts (pink line). The photo-z catalogue covers an area of 9.73 deg^2 and 20.37 deg^2 for W1 and W3 respectively, for a total of 30.10 deg^2 which is 79% of the photometric sample area. The important thing to notice here is that the shape of the number counts is the same for the photometric and the photo-z catalogue ensuring that the statistical tests we perform are correct modulo a *sampling factor* (median ratio between the photo-z and photometric sample number counts, the pink and blue lines respectively in Fig. 4.2) that we estimate to be about `sampling factor = 0.897`. As it is common practice in photometric redshift studies to apply cuts on the quality of the redshift estimates, the number counts for the best 50% of the photo-z sample are shown by the brown line. In this case, the shape of the number counts starts to deviate from that of the photometric sample for magnitudes fainter than $i_{AB} \sim 20$. This is an important factor to consider when performing statistical tests and the impact of this cut on galaxy colours will be considered later on.

The blue curve is our best estimate of the galaxy number counts, after attempting a simple cut to remove stars from the photometric catalogue. The raw uncorrected counts of all objects in the PAUS photometric catalogue is shown by the orange curve. The property `star_flag`, defined in the CFHTLenS catalogue, is used to remove stars. Objects with `star_flag = 1`, which are deemed to be stars, are shown by the purple curve. Note that there is a change in the methodology used to assign `star_flag` close to $i_{AB} = 21$. After removing stars in this way, the galaxy counts (blue curve), agree reasonably well with a previous estimate from the COSMOS field Capak et al. (2007) (red points). The number counts predicted by GALFORM, measured from the lightcone, are shown by the green line. This agrees
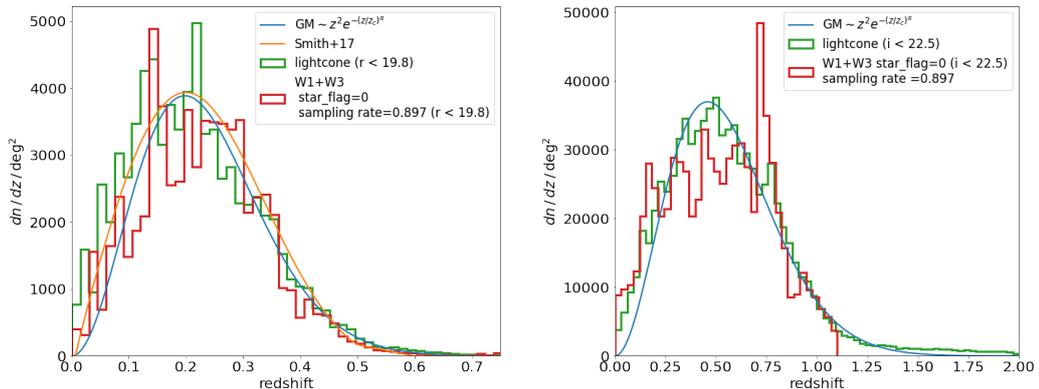
Figure 4.3: The redshift distribution of galaxies brighter than $r = 19.8$ (left) and $i_{AB} = 22.5$ (right). In both cases the red histograms show the measurements from the PAUS W1 and W3 fields combined, after imposing the starflag=0 cut to reject stars. The green histograms show the lightcone redshift distributions. The blue curves show a simple parametric fit to the green histograms (see text). The orange curve in the left panel shows a fit to the redshift distribution measured from the GAMA survey from Smith et al. (2017).

remarkably well both with the COSMOS and PAUS measurements, particularly in view of the fact that mainly local observations were used to calibrate the model.

As a further test of the GALFORM predictions for galaxy number counts, we compare with the target density of galactic sources in the Dark Energy Spectroscopic Instrument Bright Galaxy Survey (BGS) input catalogue estimated by Ruiz-Macias et al. (2020, 2021). These authors find an integrated surface density of sources to $r < 19.5$ of $808 \, \mathrm{deg}^{-2}$. In the GALFORM mock we find $837 \, \mathrm{deg}^{-2}$ to the same depth, which is within 5 per cent of the DESI BGS value. The surface density of sources measured from PAUS is within 10 per cent of the DESI value. Combining the W1 and W3 fields we estimate a surface density of $719 \, \mathrm{deg}^{-2}$, about 10 per cent lower than the DESI BGS value. However, we note that the combined area of the W1 and W3 fields (for the photometric sample) is $37.98 \, \mathrm{deg}$, which is about 400 times smaller than the imaging data used to obtain the DESI BGS estimate, and so the counts from the PAUS fields could be subject to sample variance.

After the number counts, the next statistic to consider, that characterises the galaxy population, is the redshift distribution, the number of galaxies per square

degree as a function of redshift. We show the redshift distribution of galaxies to two flux limits in Fig. 4.3, $r < 19.8$ in the left panel, the depth of the deepest fields in the GAMA survey (Driver et al., 2011) and the PAUS limit of $i_{AB} < 22.5$ in the right panel, which is substantially deeper.

The distribution of photometric redshifts in the combined W1 and W3 PAUS fields is shown by the red histograms in the panels of Fig. 4.3. These distributions are obtained by imposing the respective flux limits used in each panel, along with a selection on a star-galaxy separation parameter to reduce the contamination by stars (i.e. only retaining objects with `star_flag = 0`). The normalisation of the redshift distribution has been corrected for the offset between the number counts of objects in the photometric sample and the photo-z sample (this is the sampling factor described above). The left panel of Fig. 4.3 also shows a fit to the observed redshift distribution from the GAMA survey, made by Smith et al. (2017).[*] This agrees well with the distribution of photometric redshifts from the W1 and W3 PAUS fields, which correspond to about one fifth of the total solid angle probed by GAMA. Note that in the right panel of Fig. 4.3, by construction the photometric redshift code does not return redshifts above $z = 1.1$. It is also clear from this panel that there is a preference for photometric redshifts around $z \sim 0.75$, which is a systematic in the estimation that is being investigated by the PAUS team, rather than due to large-scale structure.

The green histograms in Fig. 4.3 shows the corresponding redshift distributions predicted using the `GALFORM` lightcone. A simple fit to the lightcone redshift distribution is given by $n(z) = A z^2 \exp\left[-(z/z_c)^\alpha\right]$. We find the best parameters to be $A = 321\,428$, $z_c = 0.18$, and $\alpha = 1.7$ for the $r < 19.8$ magnitude limited $n(z)$ (left panel). While for the $i_{AB} < 22.5$ magnitude limited $n(z)$, the best fit is given by $A = 610\,000$, $z_c = 0.4$ and $\alpha = 1.6$. The predicted redshift distributions agree well

---

[*]The equation for the fit is:

$$n_{\mathrm{GAMA}}(z) = N_1 \, z^a \cdot \exp\left[-b\, z^c\right] + (0.5\, N_2 (\mathrm{sign}[z - 0.35] + 1) \cdot \exp\left[-d\, z^e\right]) + f$$

with parameters values: $N_1 = 2.71 \times 10^4$, $N_2 = 1.96 \times 10^2$, $a = 9.22 \times 10^{-1}$, $b = 1.92 \times 10^1$, $c = 2.44$, $d = 1.08 \times 10^{-8}$, $e = -2.77 \times 10^1$, $f = -2.60 \times 10^2$.
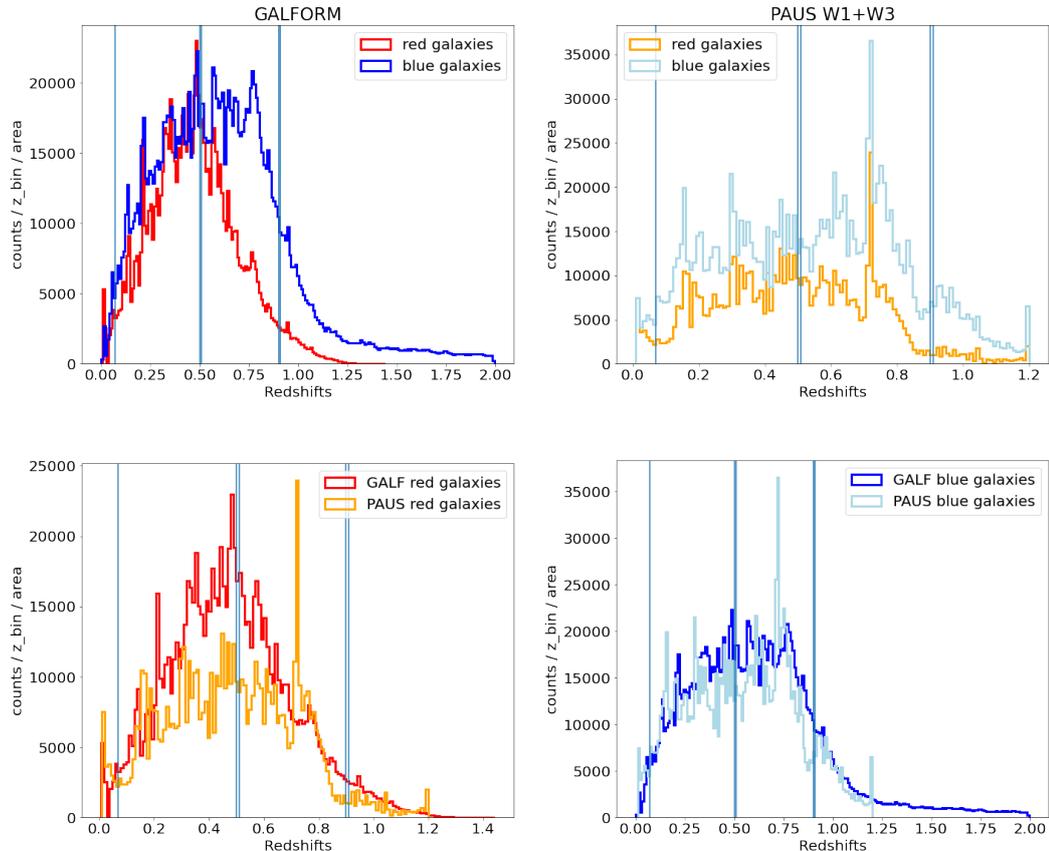
Figure 4.4: $n(z)$ distribution for red and blue galaxies. **Top left:** lightcone model. **Top right:** PAUS observed data in the W1 and W3 fields. **Bottom left:** comparison between $n(z)$ of red galaxies for the lightcone model and the PAUS data (same colour code of top row). **Bottom right:** comparison between $n(z)$ of blue galaxies for the lightcone model and the PAUS data (same colour code of top row). The vertical cyan lines indicate the three redshift bins that have been sampled in the three rows of Fig. 4.1.

with the observed ones for both magnitude limits shown in Fig. 4.3. To further analyse the predictions of the $n(z)$, we can split it for red and blue galaxies as we have done for Fig. 4.1. This is what is shown in Fig. 4.4 both for the model and the PAUS galaxies. In Fig. 4.1 we have already noticed that the number of blue galaxies is higher in the higher redshift bin ($0.90 < z < 0.91$) as expected by the overall decrease in star formation rate density observed by Madau and Dickinson (2014). We reported in Fig. 4.4 with vertical lines, the redshift bins that have been used in Fig. 4.1. In the top row of Fig. 4.4, we see that both for the model and the

PAUS galaxies in the highest redshift bin, the number of blue galaxies is higher than the red ones. For the low redshift bin, it's harder to see that we have more red galaxies, but we need to consider that the vertical line just define the redshift upper limit ($z < 0.07$), hence to have the real number of red galaxies in the lower redshift bin, we need to add up all the bins of the histogram below that line. For the PAUS data however this is not that obvious as it seems to have an excess of blue galaxies also in the lowest redshift bin, although not as pronounced as in the highest redshift bin. This can be potentially interpreted as an observational bias of PAUS in observing preferentially blue galaxies. The bottom row of Fig. 4.4 instead show that the shape of the $n(z)$ for red and blue galaxies roughly agree between model and observations.

Later we aim to quantify how the colour distribution of galaxies evolves with redshift. To minimise the processing of the observations, we use observer frame colours, which naturally change with redshift. This is mostly due to the band shifting of the filters in the galaxy's rest-frame, which dominates over any intrinsic changes in the colours (see for example the top two panels of Fig 2 from Cole et al. 2005). We need to assess how any trends we predict in the colour evolution are affected by photometric redshift errors. If these errors lead to the mixing of galaxies with very different observer frame colours, this could substantially alter any colour evolution we infer from the observations. Note that with this simplistic error model, the signal-to-noise of the measurements does not depend on flux, so we pay most attention to the scatter and outlier fraction at the flux limit of the sample, rather than try to reproduce the results in Eriksen et al. (2019) as a function of magnitude.

A factor in determining the performance of a photometric redshift estimator is the error on the measured fluxes. We perturb the narrow band fluxes of the model galaxies by adding an error with a Gaussian distribution with variance equal to some fixed percentage of the predicted flux. The BCNz2 algorithm (Eriksen et al., 2019) is then run on the perturbed model fluxes to estimate photometric redshifts
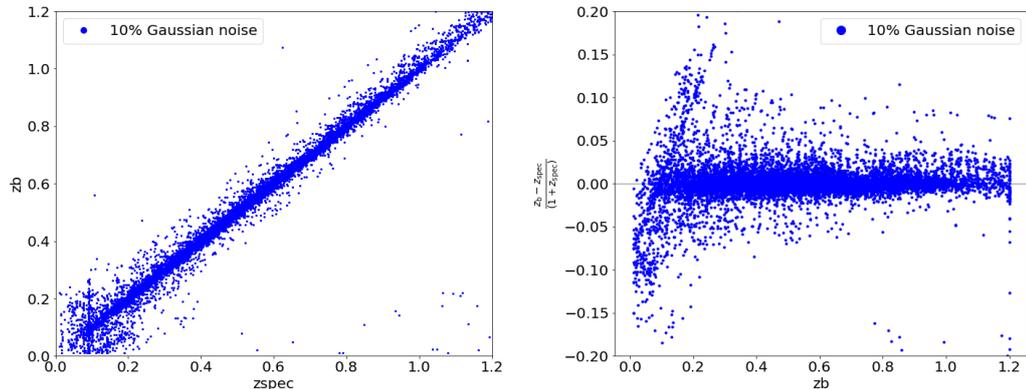
Figure 4.5: **Left panel**: relation between the lightcone redshifts (z_{spec}) and the photometric redshifts (z_b) estimated by the BCNz2 photo-z pipeline used to estimate redshifts for PAUS (Eriksen et al. (2019)). The photo-z's are the results of running BCNz2 on the broad-band and the narrow-band filters when errors has been added as 10 per cent of the `GALFORM` flux. **Right panel**: relative error on the redshift estimated as difference between photometric redshift and spectroscopic (`GALFORM`) redshifts.

for a subsample of over 14 000 galaxies from the lightcone. We then compare the scatter and fraction of outliers in the resulting photometric redshifts with those found for the observed galaxies, and adjust the errors introduced into the model fluxes to match the photometric redshift metrics inferred for the observations.

Fig. 4.5 shows the results of this exercise for errors with a variance equal to 10 per cent of the flux. The left panel shows the estimated photometric redshift, z_{b}, as a function of the true value, z_{spec}, which is the redshift including the effects of peculiar motions taken from the lightcone. This is the equivalent of a spectroscopic redshift with no error. We quantify the scatter in the photometric redshifts in a similar way to Eriksen et al. (2019) using a centralised estimate, σ_{68}, defined as:

$$\sigma_{68} = \frac{1}{2}\left(Q_{84} - Q_{16},\right) \tag{4.1}$$

where Q_{84} and Q_{16} are the 84th and the 16th percentiles, respectively, of the distribution of the photometric redshift relative errors: $|z_p - z_s|/(1 + z_s)$. This quantity is plotted as a function of the estimated photo-z in the right panel of Fig. 4.5. As well as the scatter, the performance of the photometric redshift estimation can be

quantified using the fraction of outliers produced. Following Eriksen et al. (2019), we define the fraction of outliers as the number of galaxies, normalised by the total number of galaxies in the sample, that satisfy:

$$\frac{|z_p - z_s|}{(1 + z_s)} > 0.02. \tag{4.2}$$

We have tested two examples for the flux errors, perturbing the narrow and broad band fluxes in the model by errors drawn from Gaussians of widths of either 5 per cent or 10 per cent of the predicted narrow band flux. Using the metrics defined by Eqns. (4.1) and (4.2), we compared the results of carrying out this exercise on the model lightcone to the PAUS observations in the COSMOS field, as presented in Fig. 3 of Eriksen et al. (2019). In the case of the 5 per cent flux error, we find $\sigma_{68} = 0.0037$ for the full sample and 0.0029 for the 50 per cent of the sample with the 'best' photometric redshifts (according to the Q_z photometric redshift quality indicator used by Eriksen et al. 2019), while with 10 per cent flux errors we get $\sigma_{68} = 0.0088$ for the entire sample and 0.0074 for the best 50 per cent. For the observations, the scatter is 0.0081 for the full magnitude limited sample and 0.0037 for the 50 per cent of galaxies with the 'best' photometric redshifts. Hence, the scatter obtained in this way for the model photometric redshifts is similar to that inferred for the observed galaxies for the full magnitude limited sample. However, when we restrict our attention to the 'best' 50 per cent of photometric redshifts in the model, we find little improvement in σ_{68}, in contrast to what happens for the observations.

The reason for this behaviour of the photometric redshift scatter in the model when selecting subsamples of galaxies using Q_z can be traced to the distribution of the Q_z values produced by this simple model for the flux errors. Recall that the Q_z property depends on the goodness of fit of the templates used to estimate photometric redshifts and the width of the peak in the resulting probability distribution function. Hence, the absolute values of Q_z matter. We draw the histogram of the Q_z in Fig. 4.6. We notice how the width of the distribution of Q_z in the model (blue and orange histograms) is much narrower than it is for the data (green histo-
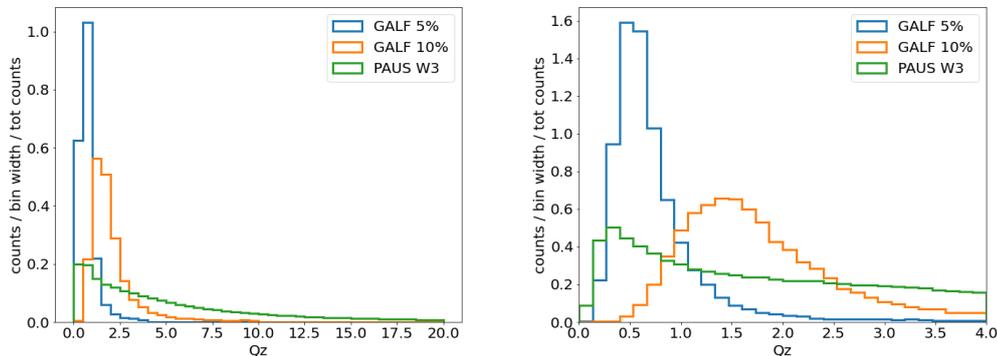
Figure 4.6: Normalised distribution of the redshift quality factor Q_z for three different samples: lightcone model with 5% variance in the flux error (blue line), lightcone model with 10% variance in the flux error (orange line) and observed PAUS data in W3 (green line). The right panel is the zoom in version of the left panel.

gram). For `GALFORM` $\sigma_{68}(Q_z) \sim 0.36$ for 5 per cent flux errors and $\sigma_{68}(Q_z) \sim 1.13$ for the 10 per cent flux error case. For the PAUS W3 field, the distribution is much broader with $\sigma_{68}(Q_z) \sim 6.35$. This partly reflects the fact that catastrophic errors or outliers are often due to unpredictable events such as poor weather conditions that are very difficult to reproduce with a simple model for the flux errors. To investigate this further we looked at the outlier fractions in the two error cases. Using the definition in Eq. (4.2), for 5 per cent flux errors, we find that 5 per cent of `GALFORM` galaxies to $i_{AB} < 22.5$ are outliers. This reduces to about 1 per cent when considering only the best 50 per cent of photometric redshifts. For the 10 per cent flux error scenario, we find an outlier fraction of 16 per cent for the entire sample and 13 per cent for the half of the sample with the best quality photometric redshifts. We can compare these numbers to the lower panel of fig. 3 of Eriksen et al. (2019) which shows that the outlier fraction for the PAUS COSMOS field limited to $i_{AB} = 22.5$ reaches approximately 17 per cent, falling to about 5 per cent when considering the 50 per cent best photometric redshifts. Again, the change in number of outliers from considering the full sample and the best 50 per cent of redshifts is more pronounced in the observations than in the simulated lightcone,

reflecting the broader spread in spread in Q_z for the observed data.

If we look deeper into the Q_z distribution for the model and observations, the centralised scatter is not the only difference. The shape of the Q_z distribution is quite different with a rise and decline for our simplified Gaussian error model and a $Q_z \sim 0$ peak with a decline for the PAUS data (see Fig. 4.6 in the Appendix). This is a limitation in our flux error modelling which however has no consequences in our work as we are not using photo-z's in the testing of galaxy colours. However, to get the most realistic flux errors that our simple model can provide, it is more important to reproduce the fraction of photometric redshift outliers, which can have a larger impact on the form of the colour redshift relation, than the centralised error, which typically scatters galaxies between adjacent redshift bins. For this reason we chose the larger error as this gives a closer match to the observed outlier fraction, even though it gives a somewhat larger centralised scatter.

Finally, it is reassuring that in Fig. 4.5 we can see no trace of any preferred values for the photometric redshifts recovered for the model galaxies. In particular, the redshifts of the original output snapshots in the N-body simulation are not apparent. This provides a validation of the treatment of the observer frame magnitudes in the model lightcone. Recall that the observer frame is defined at the simulation output redshifts on either side of the redshift at which the galaxy crosses the observer's past lightcone, and a linear interpolation is used to estimate the magnitude at the lightcone crossing reshift (Merson et al., 2013).

4.3.2 Evolution of galaxy colours

Here, we study the evolution of the observer frame $g - r$ colour with redshift. In an effort to keep the results from the observational data as model independent as possible, we use observer frame quantities to simplify the analysis, thereby avoiding the need to devise k-corrections to transform colours to the rest-frame. Fig. 4.7 shows the number counts of galaxies with photometric redshifts in the $g-r$ observer
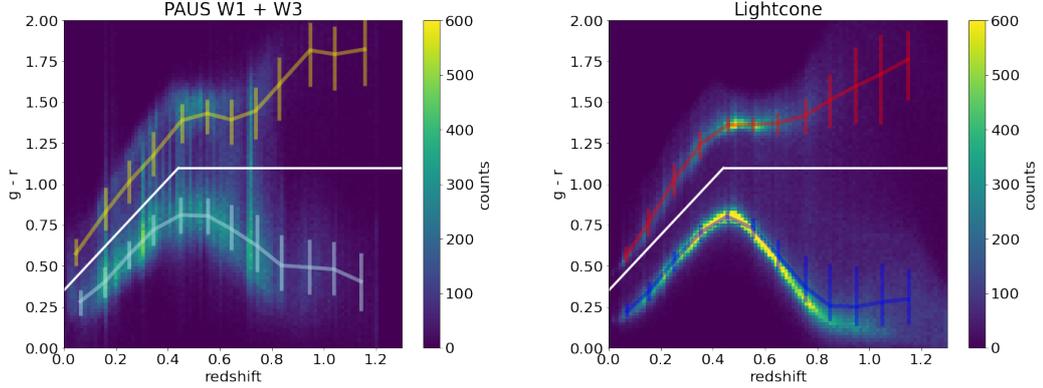
Figure 4.7: 2D histogram of galaxy counts in the $g - r$ colour vs redshift plane, for galaxies brighter than $i_{AB} = 22.5$. The $g - r$ colour is in the observer frame. The width of the bins arw 0.13 in redshifts and 0.20 in $g - r$ colour. The left panel shows the galaxy counts from the combined W1 and W3 fields from PAUS. The white line is used to separate red and blue galaxies (see text for equation). This is the same criteria used to separate red and blue galaxies in Fig. 4.1. Stars have been removed using the CFHTLenS property `star_flag = 0`. The lines with bars show the median colour and 25-to-75 percentile range for the red and blue populations. The right panel shows the same plane for the model lightcone. As the model lightcone covers a roughly three times larger area than the observations, we have randomly samples the model galaxies to match the total number of observed galaxies. To compare the two panels, we set the same colour bar knowing that the most populated bins of the model lightcone are saturated with counts above the limit of 600 galaxies per bin.

frame colour $-$ redshift plane (in bins of 0.13 in redshift and 0.20 in $g - r$ colour) for the combined PAUS W1 and W3 fields (left) and the model lightcone (right), in both cases to a magnitude limit of $i_{AB} = 22.5$. Focusing on the left panel first, the shading shows that there are two distinct populations of galaxies, the well known red sequence and blue cloud. Motivated by this, we place a dividing line to set the boundary between these populations:

$$g - r \;=\; 1.7\,z + 0.35 \qquad z < 0.44 \;, \tag{4.3}$$

$$g - r \;=\; 1.1 \qquad\qquad z > 0.44.$$

Blue galaxies are those below this line and red galaxies are above it. Whilst there is a clear peak in the counts of galaxies in the red and blue clouds, there is a low count bridge with intermediate colours connecting these two clouds. Having split

the population into two using this line, we can compute the median colours of the sub-populations on either side of the dividing line, along with the respective interquartile ranges (shown by the coloured lines and bars). The striping along the redshift axis is due to large-scale structure in the W1 and W3 fields.

The observer frame $g - r$ colour evolves with redshift. There are two main physical contributions to the shape of the galaxy spectral energy distribution which affect this evolution: the shape of the stellar continuum, which depends on the amount of ongoing star formation and the age of the composite stellar population, and the attenuation of the starlight by dust. In the rest frame, the effective wavelength of the g-band is 4792.9Å and for r it is 6212.1Å. The main spectral feature at these wavelengths is the 4000Å break, a combination of various metal absorption lines over a range of several hundred angstroms which are stronger in older stellar populations. PAUS images galaxies using narrow band filters that span the wavelength range from 4500Å to 8500Å. A wavelength of 4000Å in the rest-frame is sampled by the PAUS filterset for redshifts between $0.125 < z < 1.125$, and by the g and the r bands in particular for redshifts in the range $0.16 < z < 0.36$. The decline in the spectrum associated with the 4000 Å break actually starts around 4500 Å, close to the effective wavelength of the g-band. As redshift increases, the $g-$band in the observer frame samples progressively shorter wavelengths in the rest-frame, moving down the 4000Å break. The observed $g - r$ colour gets redder with increasing redshift, with the gradient being somewhat steeper for red galaxies (with deeper 4000Å breaks). Note that star-forming galaxies display a modest reddening of the stellar continuum around 4000 Å, albeit not as pronounced as in galaxies with older composite stellar populations. Hence the observer frame $g - r$ colour for star-forming galaxies in the blue cloud also gets redder with increasing redshift. At $z = 0.4$, the observer frame r-band samples the rest-frame effective wavelength sampled by the g-band at $z = 0$, and the g filter starts to move down to redder wavelengths than the break. At higher redshifts than this, there is a divergence in the observer frame $g - r$ colours found for the red and blue clouds,
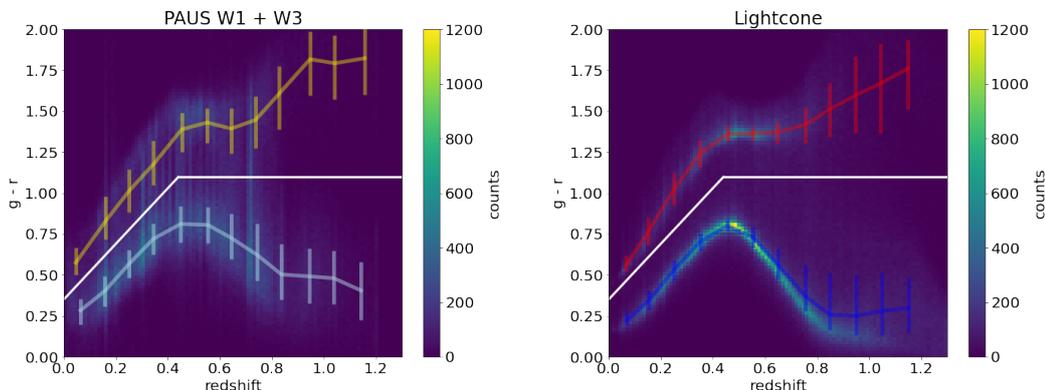
Figure 4.8: Same as Fig. 4.7 but with the colour bar limit set to 1200 counts instead of 600. To compare the two panels, we set the same colour bar to the limit of the most populated bin. Since the bimodality is stronger in the lightcone (i.e. more galaxies laying in fewer bins), the PAUS histogram looks shallower in colours.

with both filters now sampling rest-frame wavelengths that are shortwards of the 4000Å break.

The right panel of Fig. 4.7 shows the equivalent information for the model lightcone. As the lightcone covers a larger solid angle than the combined W1 and W3 fields, we have randomly sampled the model galaxies to match the total number of galaxies in the observed sample (583 992 galaxies). In principle this allows us to use the same colour scale for the density shading for the observations and the model. However, as the colour bimodality is noticeably tighter in the model, the yellow bins in the right panel are all saturated as the counts are around a thousand per pixel. For a fair comparison we also reproduced the same plot in Fig. 4.7 but for a higher limit in the colour bar set to the most populated bin. In Fact, in Fig. 4.8 we see how the bimodality in galform looks less pronounced (as there are not saturated bins anymore) but the PAUS bimodality looks less defined. The larger solid angle of the model lightcone also means that large-scale structure has a smaller impact on the number of galaxies, so we see little evidence of any striping in redshift. The overall locus of galaxies in the red and blue clouds in the model is similar to that seen in the observations, so we are able to use the same line to
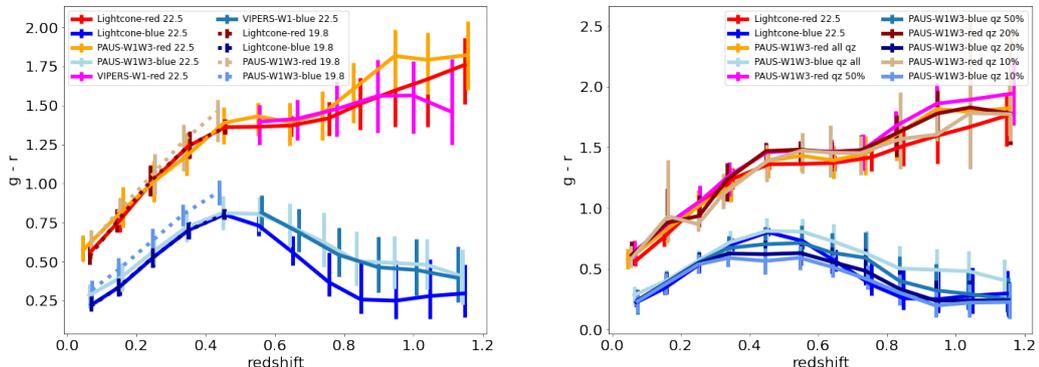
Figure 4.9: Running medians for the observer frame $g - r$ colour vs redshift. In each case (lightcone, PAUS and VIPERS) red and blue galaxies have been split according to the white line in Fig. 4.7 and the median has been computed in the two populations of galaxies separately. **Left panel**: The running median computed for different apparent magnitude limits. **Right panel**: the running median has been computed for different quality cuts, using the property Q_z (see Eriksen et al. 2019) to identify the 50, 20 and 10 per cent best quality redshifts of the sample.

divide the model galaxies into red and blue subsamples.

To make a more quantitative comparison of the colour evolution between the observations and the model, we compute the median and interquartile range of the distribution of $g - r$ colour in narrow redshift bins, considering the blue and red populations separately. One thing that is readily apparent is the stronger bimodality in the model colours compared with the observed ones. This was already visible in the relative tightness of the shaded regions in the colour- redshift plane in Fig. 4.7, and is backed up by the narrower interquartile range of colours in the model compared with the observations. This behaviour of the model had already been noticed in previous comparisons (González et al., 2009; Manzoni et al., 2021).

We make further comparisons between the evolution of the observer frame colour distributions in the model lightcone and observations in Fig. 4.9. For clarity we drop the density shading in this plot and show only the median colour and interquartile range for different selections. The left panel of Fig. 4.9 extends the standard colour - redshift comparison made at the PAUS depth of $i_{\mathrm{AB}} = 22.5$ in two directions. First

we consider a brighter magnitude cut, $r_{AB} = 19.8$, which corresponds to the depth of the faintest fields in the GAMA survey. As expected, median colours can only now be plotted out to a lower redshift of $z = 0.45$, as there are very few galaxies at higher redshifts. The median colours in the model are insensitive to this change in magnitude limit, though the observations suggest that both red and blue galaxies get redder with the brighter apparent magnitude cut. In the left panel of Fig. 4.9 we also compare the model with an alternative sample of higher redshift galaxies, using the VIPERS spectroscopic sample (Scodeggio et al., 2018), which is limited to the same depth as PAUS ($i_{AB} = 22.5$). Colour pre-selection is used to identify VIPERS targets, which limits this survey to redshifts $z \gtrsim 0.5$ (see Fig. 3 of Guzzo et al. 2014 for the colour-colour selection used to select high redshift target galaxies). The high redshift tail of the colour - redshift relation agrees remarkably well between VIPERS and PAUS, suggesting that this result is not sensitive to errors in the estimated photometric redshifts. The red galaxies in the model lightcone are in somewhat better agreement with those measured from VIPERS, whereas the blue model galaxies are bluer than the results from both observational datasets. This comparison shows the usefulness of the PAUS measurements which span a much wider redshift baseline than comparable spectroscopic surveys, which are either shallower and hence only cover the lower redshift half of the PAUS redshift range, as is the case with the GAMA survey, or which do not measure low redshift galaxies, as in the case of VIPERS.

The right panel of Fig. 4.9 investigates if the selection of higher quality photometric redshifts changes the appearance of the colour-redshift relation. Eriksen et al. (2019) and Alarcon et al. (2021) show that the quality factor property can be used to define a subset of galaxies with fewer redshift mismatches or outliers and a smaller scatter in the estimated redshift than would be found in the full apparent magnitude limited sample. We want to rule out two effects: firstly that the distribution of quality factors might be different for red and blue galaxies due to a dependence of photometric redshift accuracy on galaxy colour, and secondly,

that changing the fraction of outlier redshifts could alter the appearance of the colour - redshift relation. In the right panel of Fig. 4.9, we plot the median colour for the entire sample, and for subsamples comprising the best 50, 20 and 10 per cent of redshifts. Although the median colours agree within the 25th - 75th interquartile range, we note a slight shift in the blue cloud medians to bluer colours when restricting the sample to better quality redshifts. The colours measured for better quality photometric redshift samples seem to agree better with the lightcone predictions.

Finally we dig deeper into the evolution of galaxy colours by considering galaxies selected to be in narrow ranges of apparent magnitude and redshift. In Fig. 4.10, we plot the distribution of the $g-r$ observer frame colours for both the GALFORM and the PAUS samples. We consider three representative magnitude bins: $18.5 < i < 18.9$, $19.7 < i < 20.0$ and $21.7 < i < 22.0$, which for convenience we call bright, medium and faint respectively. We split each apparent magnitude sample into two redshift bins: a 'low redshift' one spanning $0.1 < z < 0.3$ and a 'high redshift' one covering $0.4 < z < 0.7$. As noted when commenting on Fig. 4.7, the bimodality of the colour distribution predicted in the model is more pronounced than that recovered in the observations. This can be seen quite clearly in the high redshift bins of the medium and faint samples. However, the predicted $g - r$ colour covers the same range as the data in every panel of Fig. 4.10. Reassuringly, the shape of the PAUS distribution does not change when selecting the best 50 per cent of photometric redshifts using a cut on the quality parameter. We note as well that in the high redshift bin of the faint sample, the model predicts an excess of red galaxies, although the position of the peak of the red sequence is in agreement with that seen in the data. In the high redshift bin for the bright sample the model instead seems to underpredict the number of blue cloud galaxies, showing less bimodality than the data, in contrast to the other magnitude/redshift bins. Although the high redshift bin shows some anomalies in the location and height of the blue cloud and red sequence peaks, the low redshift bins seems to agree almost
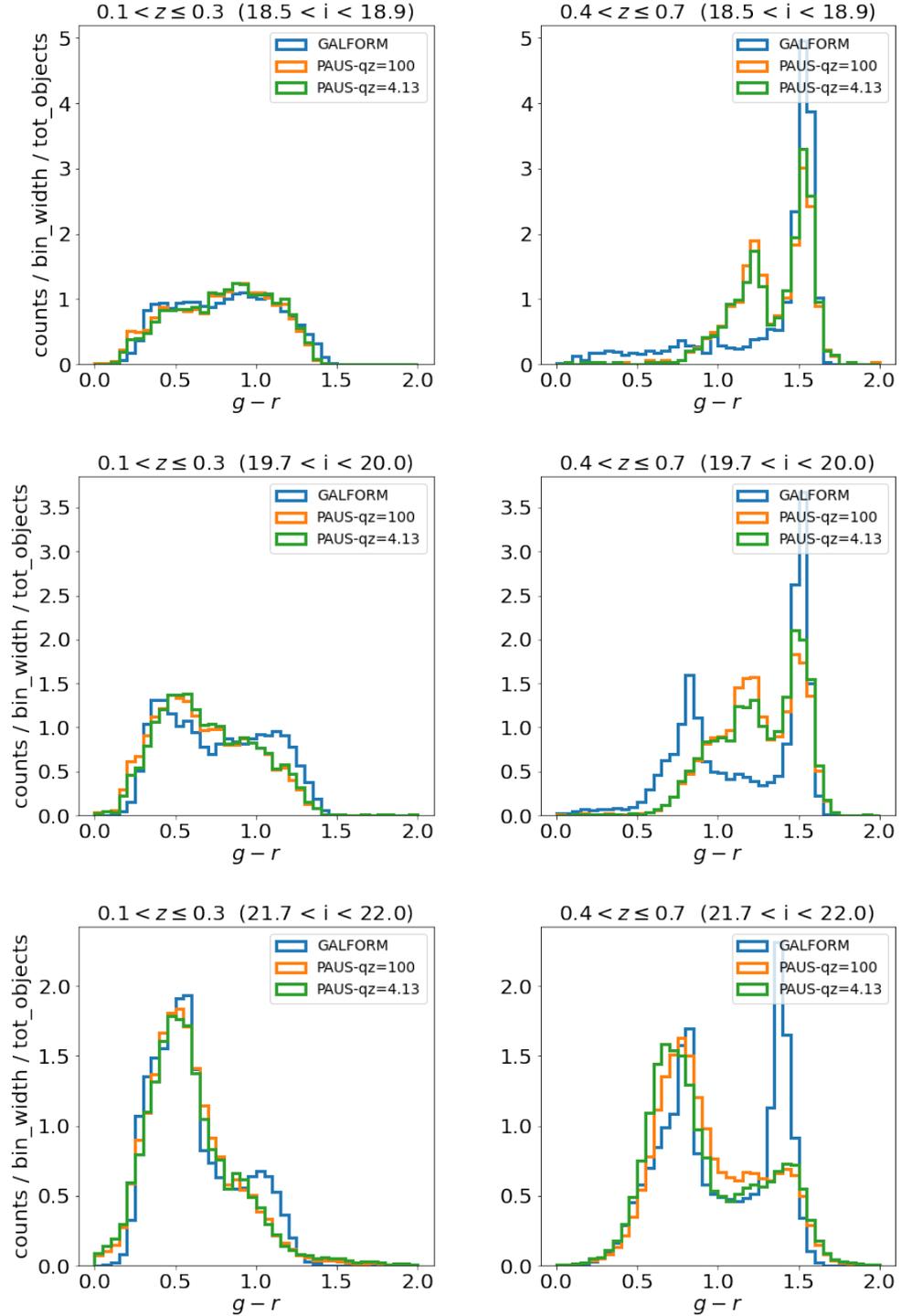
Figure 4.10: Histogram of the $g - r$ colour, for the lightcone and PAUS W1 + W3 fields, split in different bins of apparent magnitude and redshift, as labelled. The PAUS histograms are plotted for different cuts of the quality of the photometric redshifts. $Q_z < 100$ includes more than 99 per cent of the sample while applying $Q_z < 4.13$ retains the best 50 per cent of the sample.

perfectly between the model and the PAUS observations.

4.4 Conclusions and discussion

We have presented a new observational test of galaxy formation models using a novel narrow band imaging survey, the PAU Survey. The narrow band imaging provides accurate photometric redshifts, which allow us to measure how galaxy properties evolve with redshift. The use of photometric redshifts removes any potential biases associated with the successful measurement of spectroscopic redshifts, and allows us to quantify the evolution of galaxy colours over an unprecedented baseline in redshift for a single survey with a homogeneous selection. We focus on observer frame galaxy colours to minimize the processing applied to the data. Hence, we do not need to model the *k*-correction needed to estimate a rest-frame magnitude from the observed photometry. To connect the observations to a theoretical model of galaxy formation, we build a mock PAUS survey by implementing the `GALFORM` model into the P-Millennium N-body simulation Baugh et al. (2019).

The PAUS survey is magnitude limited to $i_{AB} \lesssim 22.5$, with redshifts that are mainly distributed between $0 < z < 1.5$ with a peak occuring at about $z \sim 0.5$ (see Fig. 4.3). Over this redshift range a significant change in the global star formation rate per unit volume is observed (Madau and Dickinson, 2014).

We focus on the observer frame $g - r$ colour and its evolution with redshift. The observed colour distribution shows a clear division into red and blue populations (as shown in Fig. 4.7). The observer frame colours evolve strongly with redshift. This is driven mostly by the redshifting of the filters, which sample different features in the spectral energy distribution of galaxies with increasing redshift. A secondary driver of the colour evolution is the change in the intrinsic galaxy properties with redshift, such as the typical star formation rate.

Hence to compare theoretical predictions to the observations, it is necessary to model the bandshifting effects on the filters and to build a mock catalogue on an

observer's past lightcone, rather than focusing on fixed redshift outputs (Baugh, 2008). We do this by implementing the `GALFORM` semi-analytical model of galaxy formation into the P-Millennium N-body simulation, using one of the recalibrated models presented in Baugh et al. (2019). The construction of a lightcone mock catalogue is described in Merson et al. (2013). An earlier PAUS mock was made using this approach, but with a different N-body simulation by Stothert et al. (2018b). The mass resolution in the P-Millennium N-body simulation is almost an order of magnitude better than that in the simulation available to Stothert et al. (2018b), allowing intrinsically fainter galaxies to be included in the mock. Also, the P-Millennium has four times as many snapshots as the previous simulation, which means that the calculation of galaxy positions and magnitudes is more accurate than before.

The galaxy formation model used to build the mock is calibrated against mostly local observations. In particular, Baugh et al. (2019) focused on the reproduction of the optical b_J-band luminosity function and the HI mass function in the recalibration of the model parameters (the recalibration was necessary because of the change of cosmology in the Planck Millennium, compared with earlier runs, and the improvement in the mass resolution). Hence, a useful entry level test of the model is that it reproduces the number counts in the PAUS survey as a function of apparent magnitude and redshift.

The observed number counts are reproduced closely by the mock catalogue (Fig. 4.2). This exercise also showed the importance of a robust and accurate algorithm for star-galaxy separation, in order to make a reliable comparison of galaxy counts with the model. This is particularly relevant at bright apparent magnitudes where stars make up a larger fraction of the total counts of objects. We also investigated if the number counts of galaxies change when we restrict our attention to galaxies with an estimated photometric redshift. In the first instance, when a galaxy has a photometric redshift estimated, the shape of the number counts is unchanged. There is a small reduction in amplitude because photometric

redshifts are only estimated for galaxies that have been observed in all of the 40 narrow band filters, and not all galaxies in the PAUS W1 and W3 fields meet this criteria. If we restrict attention to galaxies which, on the basis of the quality parameter (see Eriksen et al. 2019), are inferred to have good photometric redshifts, the shape of the number counts is changed, with the fraction of galaxies with high quality photometric redshifts varying strongly with apparent magnitude. The model gives a good match to the overall galaxy redshift distribution, limited to the GAMA or PAUS survey apparent magnitude cuts.

We use the clear separation between galaxies in the colour - redshift plane (Fig. 4.7) to divide galaxies into red and blue populations. This definition works well both for the PAUS observations and the `GALFORM` mock catalogue. Reassuringly, when we limit our attention to those galaxies with high quality photometric redshifts in the observations, the colour distribtuion does not change, unlike the overall galaxy counts. The observer frame colour redshift relation from a photometric redshift survey like PAUS is therefore robust statistic to compare with galaxy formation models. Qualitatively, the colour-redshift plane looks similar in the model and observations. The red and blue sequences are more sharply defined in the model than in the observations. However, there is good agreement between the median colours (and interquartile range) of the red and blue galaxies as a function of redshift. PAUS is able to probe the colour - redshift relation over a wide baseline in redshift (from $z = 0$ to $z = 1.2$) with a homogeneous selection.

We conclude our study by looking at the distribution of the observer-frame colour $g-r$ in bins of apparent magnitude i_{AB} and redshift. Again, this test seems to be unaffected when only considering the 50 per cent of galaxies with the best quality redshifts. The comparison between the model of the data is good at low reshifts. However, at high redshift, there are some discrepancies in the position of the peak of blue galaxies, especially for bright objects. The red peak appears at the same position as in the observations in each of the apparent magnitude samples. One possibilities is that we need to improve the treatment of dust extinction in

GALFORM (see Lacey et al. 2016 for a description). The relative number of red and blue galaxies in the model is also something that can be improved. Although, there is still room for improvements in the accuracy of GALFORM prediction, the tests developed in this study are well fulfilled by GALFORM and they seem to be a good indicator of the accuracy of the model predictions for future galaxy surveys.

Modelling the quenching of star formation activity from the evolution of the colour-magnitude relation in VIPERS

We study the evolution of the colour-magnitude relation for galaxies in the VIMOS Public Extragalactic Redshift Survey (VIPERS) by introducing the concept of the bright edge, and use this to derive constraints on the quenching of star formation activity in galaxies over the redshift range $0.5 < z < 1.1$. The bright-edge of the colour-magnitude diagram evolves with little dependence on galaxy colour, and therefore on the amount of star formation taking place in bright galaxies. We modelled this evolution with delayed exponential star formation histories (SFHs), to better understand the average time-scale of the turn-off in star formation activity. We show that using SFHs without quenching, the transition from the blue cloud to the red sequence is too slow. This indicates that a scenario purely driven by the consumption of the gas inside each galaxy does not reproduce the observed evolution of the colour-magnitude bright edge. For instantaneous quenching, the best match to the observations assumes that galaxies stop their star formation at

a randomly distributed time up to $\sim 2 - 2.5$ Gyr after observation. We argue that quenching is required over a wide range of stellar masses. Qualitatively similar evolution of the bright edge is found in the predictions of a semi-analytical galaxy formation model, but quantitatively there are marked differences with the observations. This illustrates the utility of the bright edge as a test of galaxy formation models. The evolution changes and no longer matches the observed trend if feedback from heating by active galactic nuclei is turned off.

5.1 Introduction

Over the past two decades galaxy evolution studies have provided us with fundamental insights into galaxy formation. The global star formation rate density in the Universe peaked at a redshift of $z \sim 2$, and has then steadily declined, by an order of magnitude, to the present day (Madau et al. (1996); Lilly et al. (1996); see Madau and Dickinson (2014) for a comprehensive review). This decline is associated with the gradual transfer of star formation activity from more massive galaxies at high redshift to progressively less massive ones over cosmic time, an effect referred to as downsizing Cowie et al. (1996); Gavazzi and Scodeggio (1996); Thomas et al. (2005); Treu et al. (2005); Juneau et al. (2005); Siudek et al. (2017). This means that by today, smaller and smaller galaxies have experienced a star-forming phase and then moved into a passive stage. This results in a progressive extension of the passive galaxy population towards lower stellar masses (see for example De Lucia et al., 2007; Kodama et al., 2007; Rudnick et al., 2009), as star-forming "blue cloud" galaxies migrate to the quiescent, passively evolving "red sequence". The observed bimodality in many photometric, spectroscopic, and morphological galaxy properties (see, for example, Strateva et al., 2001a; Baldry et al., 2004; Balogh et al., 2004; Kauffmann et al., 2003; Krywult et al., 2017) has been put forwards as an indication that the transition between the red and blue populations might take place quite rapidly (see for example Faber et al., 2007). This would

imply the existence of a physical process capable of suppressing the star formation activity that operates on a much shorter time-scale than that on which the gas is consumed inside a galaxy. We refer to this physical process as quenching.

The origin of the star formation quenching remains controversial and may not be due to one process. One of the first mechanisms proposed to quench star formation in galaxies was ram pressure stripping Gunn and Gott (1972), but its effectiveness appears to be limited to clusters of galaxies, based on where we have been able to identify galaxies suffering ram pressure stripping (see for example Giovanelli and Haynes, 1985). This "galaxy strangulation" quenching mechanism has received renewed attention as the possible primary driver for star formation quenching Peng et al. (2015). With the advent of galaxy formation simulations, a simple AGN feedback model was introduced to shut down gas cooling in massive halos, in order to match the bright end of the observed galaxy luminosity function Benson et al. (2003); Croton et al. (2006); **?**); De Lucia et al. (2007). Observationally the effectiveness of AGN feedback in shutting off star-formation has been studied in Vergani et al. (2018) using the NUVrK diagram for VIPERS galaxies with stellar masses greater than $5 \times 10^{10} M_\odot$. However, the observational evidence for such feedback, in particular for the range of halo masses over which it is required to be effective is still unclear Bongiorno et al. (2016); Taylor and Kobayashi (2016). Henriques et al. (2017) argued that the star formation quenching in their semi-analytical model produces predictions that agree qualitatively with observations, but is too effective in dense regions and predicts too much recent star formation in massive galaxies. A similar conclusion was reached by Bluck et al. (2016) on comparing galaxy formation models with Sloan survey observations.

From the observational point of view, even establishing that quenching is taking place inside previously star-forming galaxies is not trivial.

E+A galaxies * experienced quenching in their recent past, but their rarity,

---

*The spectra of E+A galaxies have strong Balmer absoprtion features but do not show evidence of ongoing star formation, such as [OII] or Hα emission lines. This suggests that they experienced

while lending support to the hypothesis of a short time-scale transition from the blue cloud to the red sequence, makes the understanding of both their connection with the wider galaxy population, and of the details of the quenching process, complicated (see for example Kaviraj et al., 2007; Yesuf et al., 2014; Wild et al., 2016). Similar uncertainties affect the study of the "green-valley" galaxies Wyder et al. (2007); Martin et al. (2007), which have been considered either as a "normal" evolutionary stage common to all galaxies Martin et al. (2007); Salim (2014), or as "peculiar" objects representative of the evolution of a small fraction of the overall galaxy population Smethurst et al. (2015). Schawinski et al. (2014) claim instead that the green valley is just populated by normal star-forming galaxies at very high masses. A number of studies have attempted to model the properties of the overall galaxy population to derive constraints on the quenching of star formation (see for example Ciesla et al., 2016; Abramson et al., 2016; Lian et al., 2016; Bluck et al., 2016; Davies et al., 2019). The main results are a confirmation of a short time-scale for the quenching (on the order of 200 to 500 Myr, Ciesla et al. (2016)), and an estimate that quenching affects a relatively large fraction of galaxies, around 30 to 45% of the overall population Lian et al. (2016). However, Abramson et al. (2016) argue that the very idea of quenching comes from the use of over-simplified canonical parametrizations of the star formation history (SFH) which in general are not able to reproduce both the tail of high star formation rate (SFR) at $z \sim 1$ and the low SFRs seen today.

Here, we take $65\,000$ galaxies from the VIPERS galaxy redshift survey Guzzo et al. (2014) to study the evolution of the colour-magnitude relation for the overall galaxy population. In particular, we use the evolution of the "bright edge" of the galaxy distribution in the rest-frame $U - V$ colour vs. absolute V-band magnitude plane to derive illustrative constraints on the SFH quenching time-scale, and on the ability of this process to affect galaxies over a large range of stellar masses. The

a starburst about 1Gyr prior to observation, and so do not have the canonical spectrum of an elliptical galaxy, which are typically assumed to have had no star formation over a much longer period, but rather that of an elliptical combined with an A-star. They are also referred to as post-starburst galaxies; see Dressler and Gunn (1983); Wild et al. (2009).

large number of galaxies in VIPERS allows us to develop a statistical understanding of quenching time-scales. In terms of a single galaxy, the quenching is implemented as the instantaneous truncation of star formation activity. Given the depth of VIPERS our study primarily focuses on bright galaxies, so we are unable to draw conclusions about quenching in faint galaxies (see e.g. Davies et al. (2019) for constraints on quenching in faint galaxies at somewhat lower redshifts than those considered here).

This chapter is set out as follows: in Section 5.2 we describe the modelling and assumptions made to obtain galaxy properties from the VIPERS data; in Section 5.3 we explain how we model different SFH scenarios; in Section 5.4 we present the observed colour-magnitude relation and its evolution tracked using the bright edge concept; in Section 5.5 we show the results of our synthetic evolution compared to the observed sample to constrain quenching; in Section 5.6 we compare our findings with the evolution of the colour-magnitude relation predicted by the GALFORM semi-analytic models and, finally, in Section 5.7 we discuss our main results.

We use a flat Λ CDM cosmology with $\Omega_{\mathrm{m}} = 0.3$, $\Omega_{\Lambda} = 0.7$ and $H_0 = 70$ km/s/Mpc, unless stated otherwise.

5.2 Modelling of galaxy properties from the data

5.2.1 The VIPERS data

The galaxy sample used here is based on the full data release of the VIPERS spectroscopic survey. VIPERS is a galaxy redshift survey carried out with the VIMOS spectrograph at the ESO Very Large Telescope (see Guzzo et al. (2014) for a full description of the survey), covering approximately 23.5 deg^2 of sky, and targeting a sample of galaxies brighter than $i_{\mathrm{AB}} = 22.5$, selected to be at redshift $z > 0.5$ on the basis of a simple, but rather effective, colour-colour selection criterion.
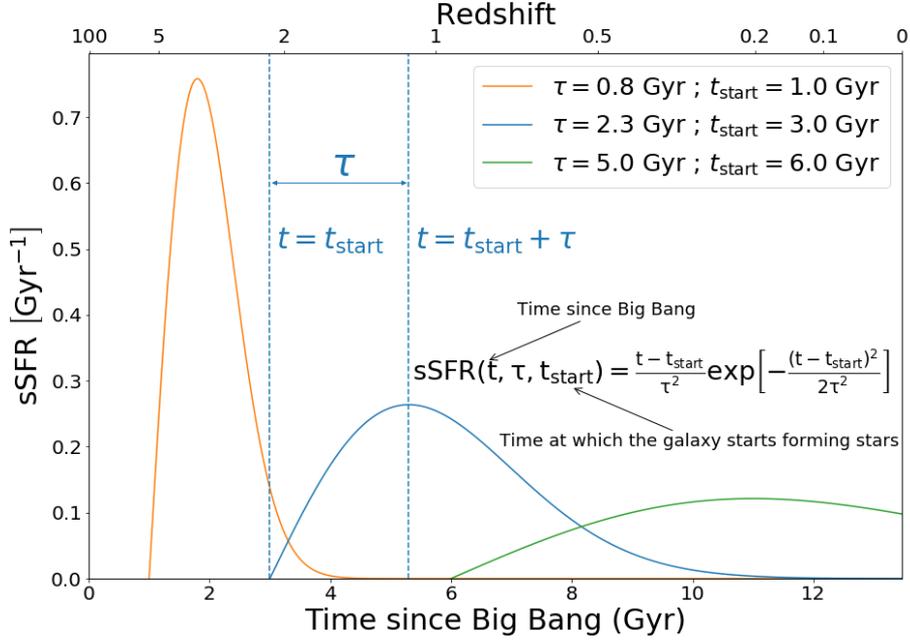
Figure 5.1: Examples of delayed exponential SFHs for different τ, offset by t_{start} from the Big Bang, which corresponds to $t = 0$. Through SED fitting, which is based on photometric and spectroscopic data (see Franzetti et al. (2007)), every galaxy is assigned an age, $t - t_{\text{start}}$, and a characteristic time-scale of star-formation, τ, which determine the form of the SFH. We stress that each SFH plotted has a different t_{start}, equivalent to the redshift at which the galaxy starts to form stars.

The full VIPERS data release Scodeggio et al. (2018) provides a spectroscopic catalogue with redshift measurements for $86,775$ galaxies, coupled with a parent photometric catalogue largely based on the VIPERS Multi-Lambda survey Moutard et al. (2016b), providing photometric data that include the GALEX FUV and NUV bands, the CFHTLS data release T0007 u, g, r, i and z bands, and the WIRCAM or VIDEO infrared K_{s} band (see Scodeggio et al. (2018) and Moutard et al. (2016b) for details).

Here we use the subset of galaxies with a reliable redshift measurement (i.e. a measurement with a probability larger than 95% of being correct, corresponding to a reliability flag ≥ 2 in the VIPERS catalogue, see Scodeggio et al. (2018) for details), limited to the redshift range $0.5 < z < 1.1$, giving a total of $64,889$ objects. This subset is fully representative of the galaxy population over this redshift range,

thanks to two important properties of the VIPERS survey: the high sampling rate achieved by VIPERS, whereby on average 47% of the complete parent photometric sample has been observed, and the very high success rate for the redshift measurements, with on average 90% of the targeted objects having a redshift measurement (note that the spectroscopic success rate is only weakly dependent on galaxy properties, as shown by Fig. 7 of Scodeggio et al. (2018)).

5.2.2   Galaxy properties and SED fitting

Here, we are interested in studying the observed evolution of the bright edge of the V-band rest frame absolute magnitude vs $U - V$ rest frame colour. These quantities come from the Public Data Release 2 (PDR-2) which is available at `http://vipers.inaf.it/rel-pdr2.html` and presented in Scodeggio et al. (2018). To analyse the redshift evolution of the colour-magnitude relation, we divide the sample into six redshift bins, with a width of 0.1, from $z = 0.5$ to $z = 1.1$ (which corresponds to a look-back time which ranges between approximately 5 and 8 Gyr).

We reconstruct the SFH of individual galaxies using SED fitting carried out with the GOSSIP software Franzetti et al. (2008). We start from the $ugrizKs$ photometry, supplemented with the spectroscopic data, in order to reduce the well known degeneracies between age, star formation timescale and dust extinction that afflict SED fitting results derived purely from photometric data (see the discussion in Thomas et al., 2017). We use a template library based on the PEGASE 2 model Fioc and Rocca-Volmerange (1997), assuming a delayed exponential SFH according to the prescription from Gavazzi et al. (2002)[*]:

$$\text{sSFR}(t, \tau, t_{\text{start}}) = \frac{t - t_{\text{start}}}{\tau^2} \exp\left[-\frac{(t - t_{\text{start}})^2}{2\tau^2} \right], \qquad (5.1)$$

where t is the cosmic time (with $t = 0$ corresponding to the Big Bang), t_{start} is the moment at which the galaxy starts to form stars and τ is the characteristic timescale

---

[*]We write the SFH in terms of the specific SFR (sSFR = SFR/M) as in our model the SFH is normalised to produce $1 M_\odot$ of stars.

of star formation which identifies the maximum of the sSFR. This form is often referred to as a SFH *"a la Sandage"* as Sandage (1986) was the first to discuss such a SFH. Fig. 5.1 shows some example SFHs generated using this parametrization to illustrate the influence of the parameters on the SFH.

The SFH parameters that we constrain in our SED fitting are the characteristic time-scale, τ, and the age of the galaxy, $t - t_{\text{start}}$ (since t is related to redshift, t_{start} can also be deduced). The benefit of using a delayed exponential SFH, as in Eq. 5.1, is that such a SFH displays an initial increase of the SFR that peaks at $t - t_{\text{start}} = \tau$ (see Fig. 5.1), so that late-type galaxies which are still actively forming stars can be described as well as passive early-type galaxies: late-type galaxies will tend to be fitted with larger values of τ than early-types. Recall that a small value of τ means that the majority of stars are formed in the early stages of the life of the galaxy, which is usually the case for early-types.

We have chosen to use the PEGASE model because it can compute galaxy SEDs with self-consistent evolution of the metallicity and the internal extinction, driven by the input SFH. The template library used here covers a grid of galaxy ages, $t - t_{\text{start}}$, from 0.1 to 15 Gyr with a step of 0.1 Gyr, and a grid of star formation time-scales, τ, ranging from 0.1 to 25 Gyr, again with a step of 0.1 Gyr. For each galaxy in our sample we estimate an age, $t - t_{\text{start}}$, and a star formation time-scale, τ, based on the value of these two quantities for the best-fitting template, with the constraint that the galaxy age is less than the age of the Universe at the redshift of the galaxy. We have checked the SFRs inferred from our best-fitting SFHs are in general agreement with observationally inferred SFRs (A.1).

The delayed exponential SFH model is undoubtedly an over simplification of the actual SFH history in galaxies. Several studies have compared simple empirical SFH models with the output of physical models of galaxy formation Pforr et al. (2012); Gladders et al. (2013); Mitchell et al. (2013); Simha et al. (2014); Diemer et al. (2017). Mitchell et al. (2013) showed that simple, declining exponential SFHs, when used to fit the photometry of GALFORM galaxies, could nevertheless

give a reasonable estimate of properties such as stellar mass. Simha et al. (2014) compared a wider range of parametric SFHs to those predicted in a hydrodynamic simulation of galaxy formation. They found that a simple exponential SFH gave systematic errors in galaxy colours. Their "lin-exp" model, which is equivalent to the delayed-exponential used here, performed much better overall, experiencing problems mainly for the very bluest and reddest galaxies.

5.3 Modelling the evolution of the colour-magnitude relation

The modelling of SFHs discussed in Section 5.2 provides us with a tool to predict quantitatively the evolution of the colour-magnitude relation as a function of redshift for the galaxies in our sample. The quality of this modelling is tested in A.1, in which we compare the SFR predicted by our model with that inferred from the luminosity of the [OII]λ3727 emission line. We follow the recipe of Moustakas et al. (2006) to estimate the SFR from the luminosity of the [OII]λ3727 emission line, using the luminosity of the line and the rest-frame B-band absolute magnitude, as given in Eq. A.1. This estimate is completely independent from our SED fitting modelling. In A.1 we show that the SFR vs $U - V$ colour and the SFR vs redshift relations, whilst yielding different absolute values, follow the same trend for the two estimates. This gives us some confidence that the SED modelling is giving a reliable prediction of the SFR at the epoch of the observation.

In this section we describe the different scenarios (Fig. 5.2) that we test to predict the photometric evolution of galaxies found in a given redshift bin. We then compare this predicted evolution with the observed distribution within different redshift bins, to select which of our SFH scenarios best describes the observed galaxies, and thereby derive constraints on the quenching of star formation activity.

5.3.1 Model description

We use a combination of observations and predictions based on our SED fitting results to estimate the amount of photometric evolution the galaxies in our sample are most likely to undergo. The starting point is the set of observed properties for galaxies in a given redshift bin (which we call the start-redshift bin), while the end point is the predicted properties for these objects at some later time (the end-redshift epoch). First, we associate with each galaxy in the start-redshift sample an evolutionary model expressed in terms of a SFH, by selecting the model which provides the best-fitting SED template to the galaxy's observed broad band magnitudes and spectrum. In doing so we assume that the evolutionary model provides a good description of the galaxy properties for an extended time around the cosmological epoch when the galaxy was observed. Since this model provides us with a synthetic SED at all possible times (from the start of star formation activity, assumed to take place at z=4, to the present epoch), we can use it to predict how much the galaxy luminosity changes with time in the various photometric bands. In particular, we compute the change in luminosity (for each band) after a time interval corresponding to the difference in look-back time between end and start-redshifts ($\Delta L_{\mathrm{m}odel}$), and we use these predictions to compute the expected absolute magnitudes and rest-frame colour of the galaxy at the end-redshift epoch ($L_{zend} = L_{obs} + \Delta L_{\mathrm{m}odel}$, with L_{obs} being the luminosity at the epoch of the observation, and L_{zend} the predicted luminosity at the end-redshift epoch).[*]

To test other SFH scenarios we add the possibility that the SFH is truncated or quenched. The quenching is always assumed to be both complete (i.e. the SFR is set equal to zero after the quenching), and instantaneous (limited to the time-resolution of the models). These two assumptions are extreme but allow us

---

[*]We caution the reader that we have used different SED templates from those used to derive properties in the VIPERS database, and so the absolute values of properties that we obtain should not be compared to those in the database. However, since we are primarily interested in the variation of fitted model parameters with redshift rather than their absolute values, this is not an issue for our analysis.
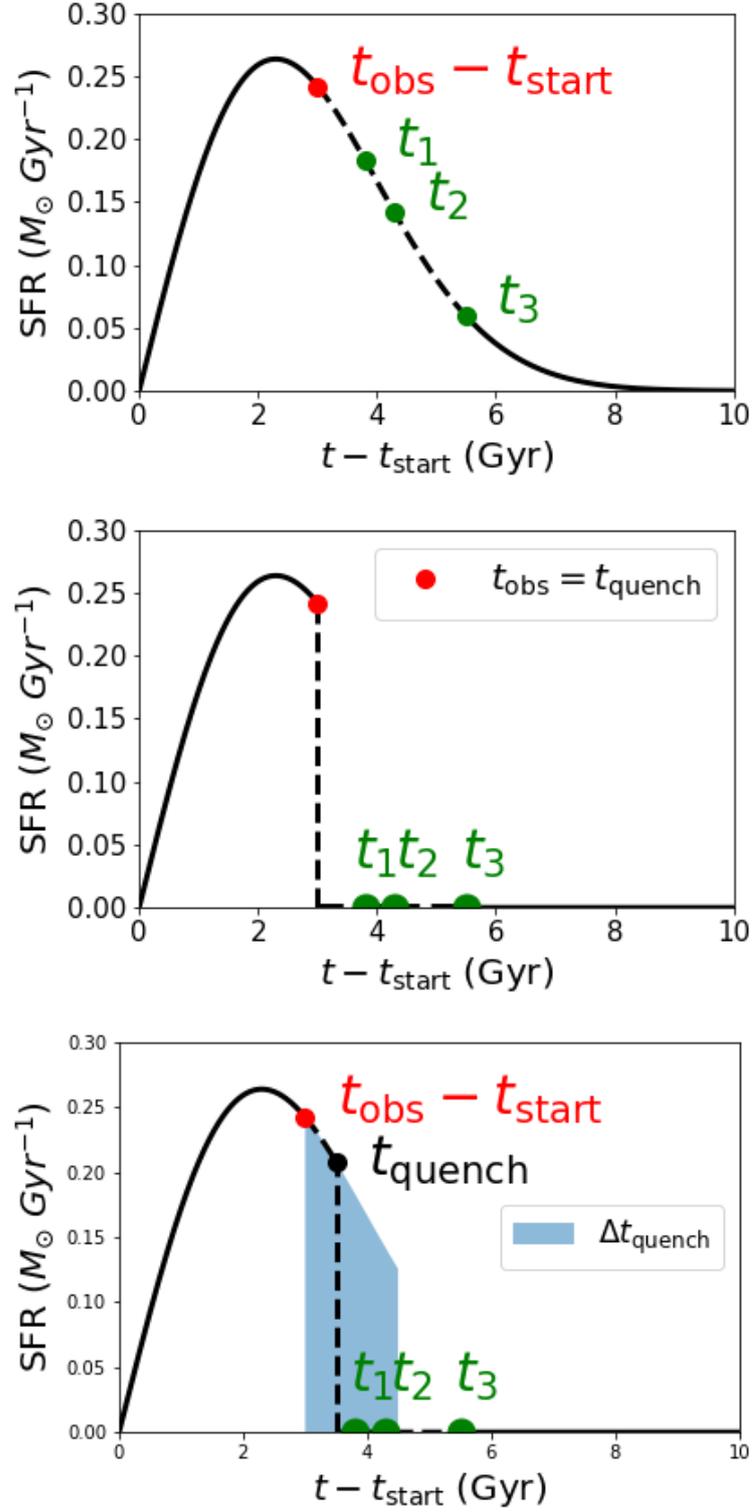
Figure 5.2: Schematic representation of the three SFH scenarios considered. *Top panel*: smooth delayed exponential SFH (as in Eq. 5.1), without any truncation or quenching. *Middle panel*: SFH that is quenched at the redshift at which the galaxy is observed i.e. the subsequent SFR is set to zero. *Bottom panel*: SFH that is quenched at a randomly selected time within a time interval (shown by the shaded area) after the epoch of observation. The x-axis indicates the age of the galaxy. t_1, t_2 and t_3 represent the time at which we test the synthetic evolution of the colour magnitude relation (see Section 5.5). We consider different values for the time interval, Δt_{quench} over which quenching can take place.

to treat the problem in a simple way and to retrieve general trends rather than detailed conclusions. We have experimented with two possible quenching scenarios: the first in which all galaxies are quenched at the same time, immediately after the start-redshift epoch (see the middle panel of Fig. 5.2 for an example of such a SFH), and the second where the quenching time is drawn uniformly from a limited time interval (bottom panel of Fig. 5.2). We have explored three possibilities, specified by the length of the time interval from which the quenching time is selected: 1, 1.5, and 2.5 Gyr. In all cases, the start of the period over which quenching could occur starts immediately after the start-redshift epoch. The reason for the choice of these three interval times is that they are representative of the range of lookback times of the VIPERS survey redshift bins. By varying the time range over which quenching can take place, we vary the fraction of galaxies that are quenched at a given redshift. Of course, for end-redshifts corresponding to a change in time interval that is greater than the time interval from which the quenching epoch is selected, all galaxies will be quenched.

5.3.2 Example tracks for the no-quenching case

Fig. 5.3 shows an example of the evolution expected in the colour-magnitude plane when galaxies follow the basic "no-quenching SFH" illustrated in the top panel of Fig. 5.2. In Fig. 5.3 we highlight, using thick solid lines, the evolution of SFH tracks in the colour-magnitude plane for a few example galaxies over the whole time interval of 2.5 Gyr (corresponding to the evolution from the median redshift in the $1.0 < z < 1.1$ start-redshift bin to the median redshift in the $0.5 < z < 0.6$ end-redshift bin). The points in the background of Fig. 5.3 are the observed galaxies in the start-redshift bin (red circles) and their evolved counterparts in the end-redshift bin (green stars).

The reddest of the example galaxies ($U - V \sim 1.5$, $V \sim -22.6$) has already completed its star formation life cycle, and undergoes purely passive evolution, fading in V magnitude and becoming redder still in $U - V$. The progressively
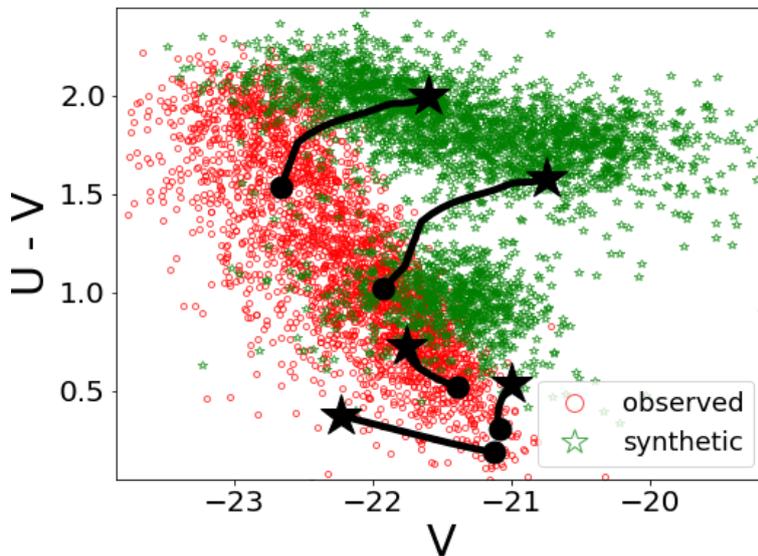
Figure 5.3: Evolution of the colour-magnitude relation starting from the (observed) start-redshift bin $1.0 < z < 1.1$ (red empty circles) over a period of 2.5 Gyr, terminating in the end-redshift bin $0.5 < z < 0.6$ (green empty stars). The evolution is based on the best-fitting PEGASE models built with a delayed exponential SFH (see the schematic representation in the top panel of Fig. 5.2, with the green points being plotted at t_3, which corresponds to the end-redshift). Thick black lines show the evolutionary tracks of a few "example galaxies" which start at the filled circle and end at the filled star.

bluer galaxies can be characterised by increasingly more important star formation activity, with the three bluest objects ($U - V < 0.6$) showing how a combination of different ages and star formation time-scales can result in significantly different evolutionary tracks for galaxies starting with similar properties at the epoch of their observation. If we now consider the population of galaxies instead of individual objects, the overall evolution that we see is that of a global move towards redder colours and fainter magnitudes, creating a more defined bimodality between the blue cloud and the red sequence (see the deficit of green stars around $U - V \sim 1.5$): galaxies in the redder half of the rest-frame colour distribution at the start-redshift epoch evolve to reach the red sequence at the end-redshift epoch, while galaxies that start in the bluest part of the distribution can remain in part of the blue cloud, albeit with significantly redder colours. We stress that this behaviour is not obvious

when examining only a few example tracks but is something that becomes apparent when considering the population of galaxies. For example, the bluest object in the example tracks becomes brighter as it is evolved from its observed colour and magnitude. Other galaxies near the bright edge, however, are predicted to evolve such that they become fainter and redder. These objects drive the bimodalilty in the evolved colour - magnitude relation. Note that we do not require that the evolved population meets the VIPERS selection, so some evolved galaxies would not be observed in VIPERS.

5.4 The evolution of the colour-magnitude relation in VIPERS

To test our modelling of galaxy SFHs using the colour – magnitude relation, we need to choose a robust feature we can use to quantitatively track and describe the evolution of the VIPERS galaxies. We decide to define a bright edge in the colour magnitude distribution. Due to the declining cosmic star formation rate density with increasing cosmic time, we expect a general reduction in the luminosity of the brightest galaxies which can be tracked by the bright edge. Of course, both luminosity and colour can change in response to different SFHs, as shown in Fig. 5.3. However, since studies like Davidzon et al. (2013) have already focused on galaxy colours, we have decided instead to devote our attention to studying the evolution in galaxy magnitudes within the colour-magnitude plane.

5.4.1 Defining the bright edge of the colour – magnitude relation

To define the bright edge of the colour – magnitude relation in an objective and quantitative way, we partition the plane into a grid of cells 0.10 mag wide along both axes. For a fixed colour bin we count the number of galaxies in each absolute magnitude bin and find the most populated bin. Moving from this bin in the
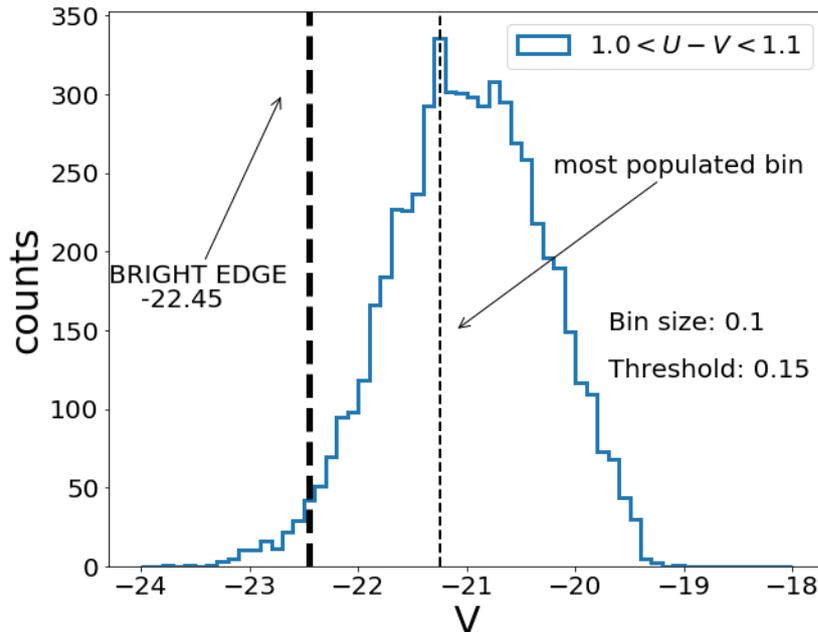
Figure 5.4: Histogram of *V*-band absolute magnitudes in the colour bin $1.0 < U - V < 1.1$ for the VIPERS sample, along with the details of the operational definition of the bright edge. The thin dashed vertical line indicates the most populated magnitude bin and the thick dashed vertical line identifies the location of the bright edge in that colour bin, where the differential galaxy counts drop below 15% of that in the most populated bin.

direction of brighter magnitudes, we define the edge location as the first bin for which the occupancy falls below 15% of that in the most populated bin (see Fig. 5.4 for an illustration of this process for one colour bin). This process is repeated for each colour bin.

Since the values of the bin size and occupancy threshold are arbitrary, we have checked that our results are not significantly affected by these choices. Specifically, we have tested the robustness of the edge definition against the size of the bins in both the rest-frame colour and absolute magnitude, and against the occupancy threshold with respect to the most populated bin. The typical variation of the bright edge location is approximately 0.15 mag. This value receives contributions from two sources: 1) the statistical uncertainty arising from the number of galaxies in the bins used in the colour magnitude plane (we varied the rest-frame colour bin size between 0.06 and 0.22 mag, and the absolute magnitude bin between

0.04 and 0.20 mag) and 2) a systematic error due to the choice of occupancy threshold (which we varied between 1% and 50%). We therefore consider 0.15 mag as the uncertainty in the location of the bright edge, to be compared with the observed evolution of approximately 1.0 mag (for a U-V colour of 1.25, at the centre of the colour distribution) across the redshift range covered by our data. The relative insensitivity to the choice of the occupancy threshold also ensures that the edge definition is insensitive to the details of the luminosity distribution within the different colour bins (like, for example, the faint-end slope of the luminosity function, which, in turn, depends on galaxy colour).

In A.2 we carry out a test to check if the number density of galaxies has any effect on the definition of the edge. Specifically, in Fig. A.3 we draw the bright edge in the colour-magnitude which comes from the Gonzalez-Perez et al. (2014) model which makes use of the GALFORM semi-analytic code. Sub-sampling the data to the number of VIPERS galaxies in every analogue redshift bin (top panel of Fig. A.3) does not affect the location of the bright edge in a systematic way.

5.4.2 The evolution of the edge of the colour – magnitude relation

In Fig. 5.5 the thick solid lines mark the bright edge of the galaxy colour – magnitude relation, calculated as defined in Sect. 5.4.1. We can see that the bright edge evolves significantly with redshift. Galaxies in the blue cloud (i.e. those with $U - V \lesssim 1.6$), display a shift of the bright edge that is only weakly dependent on galaxy rest-frame colour, with a reduction in brightness of 1.4 to 1.7 mag in the V band. The edge evolves less for the red sequence, shifting faintwards by 0.7 mag over the redshift range shown.

The rest-frame $U - V$ colour correlates strongly with the SFR of a galaxy. However, the bright edge for blue galaxies appears to evolve as a coherent block. Hence, this seems to indicate that the shift of the bright edge of the colour –
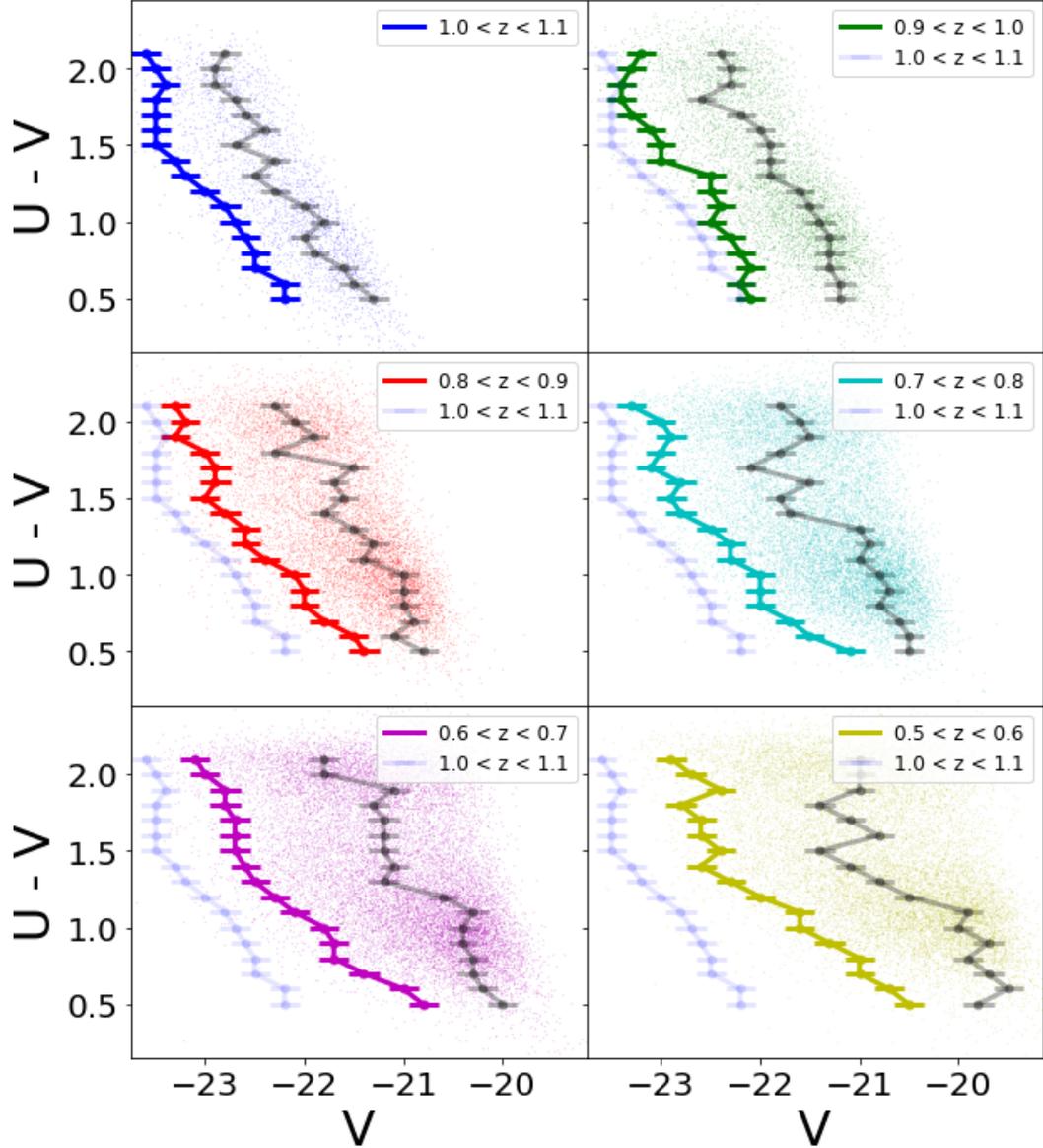
Figure 5.5: The colour-magnitude relation for the VIPERS sample, split into six redshift bins as labelled on each panel. The thick solid lines mark the bright edge of the distribution in the various bins, with an indicative uncertainty of 0.15 mags shown by the horizontal error bars
(see Section 5.4.1 for the operational definition of the location of the bright edge).
The grey thick lines mark the most populated magnitude bin for each colour bin.
The faint blue line is the bright-edge from the highest redshift bin that is
reproduced in every panel for comparison.
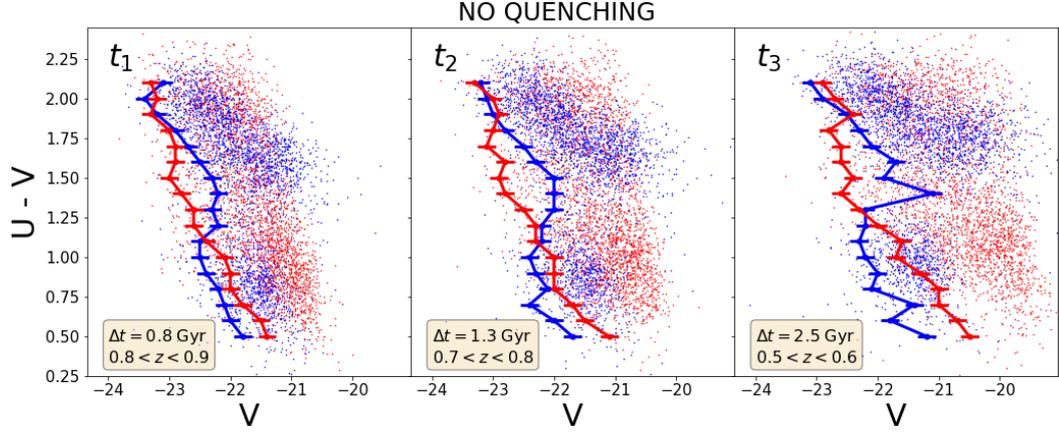
Figure 5.6: Colour – magnitude relations for the synthetically evolved population (blue points) in three arrival or end redshifts (corresponding to t_1, t_2 and t_3 in Fig. 5.2) and of the observed VIPERS data in each end redshift bin (red points). The bright edge location of each sample is drawn using the same bins in colour. The evolution is based on the smooth delayed exponential SFH which characterises the no-quenching scenario illustrated in the top panel of Fig. 5.2. The horizontal error bars show an indicative average error of 0.15 mag

.
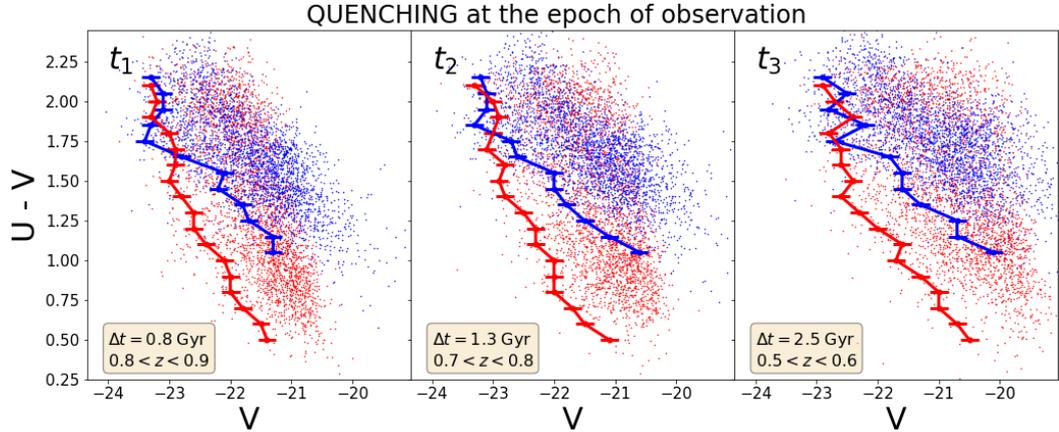
Figure 5.7: Same as Fig. 5.6 but with evolution computed using an instantaneously quenched delayed exponential SFH (i.e. SFR set to zero at the redshift at which the galaxy is observed). This SFH scenario corresponds to the schematic representation in the middle panel of Fig. 5.2. The horizontal error bars show an indicative error of 0.15 mag

.
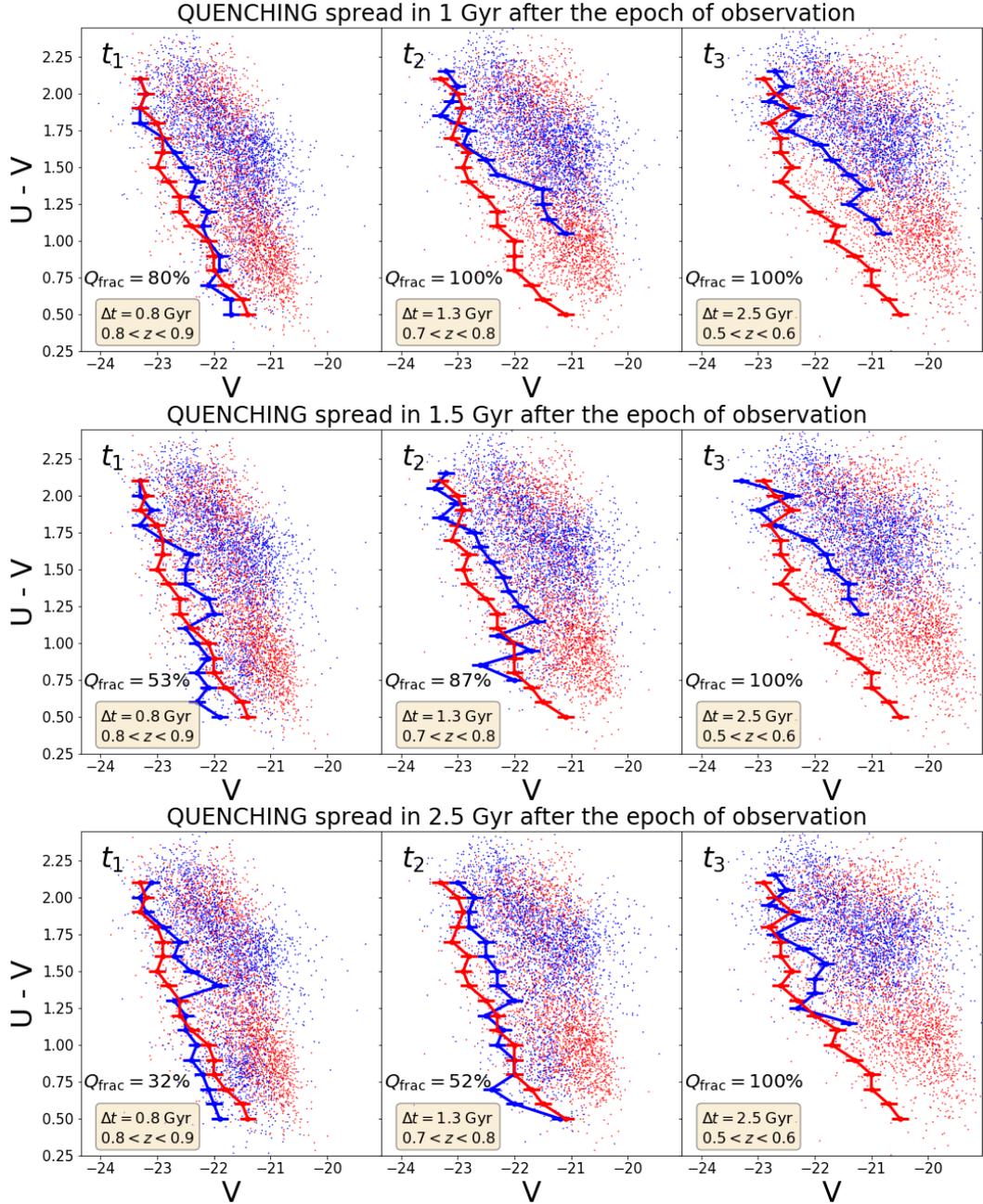
Figure 5.8: Same as Fig. 5.6 but considering different quenching scenarios for the SFH. This time the evolution is based on the "delayed-quenching" scenario which means that for each galaxy the SFR is set to zero at a random time within a time interval after the epoch of observation of duration Δt_{quench}. Three different Δt_{quench} values are explored: 1 Gyr (top panel), 1.5 Gyr (middle panel) and 2.5 Gyr (bottom panel). A schematic representation of the delayed-quenched SFH is shown in the bottom panel of Fig. 5.2, with the shaded area representing Δt_{quench} of 1.5 Gyr. The fraction of galaxies that is quenched, Q_{frac}, at each end-redshift is written in each panel (see Section 5.5.2 for a discussion of how Q_{frac} is calculated and interpreted). The horizontal error bars show an indicative error of 0.15 mag .

magnitude relation is less sensitive to the instantaneous star formation rate. Of course galaxies with $U - V \gtrsim 1.6$ are already in a quiescent phase and hence display less of a change in colour than star-forming galaxies that are making the transition to the red sequence.

In measuring the bright edge location we are dealing with the bright part of the galaxy luminosity function, so we do not have to worry about completeness effects in the VIPERS sample, for any redshift bin we consider. To show that this is indeed the case, i.e. that the bright edge is not driven by the luminosity cut at faint magnitudes, in Fig. 5.5 we show, using thick grey lines, the location of the most populated bin in the magnitude distribution and we notice that it does not coincide with the faintest bin, ensuring that the depth of the survey has no effect on the definition of the bright-edge in the different redshift bins.

A concern could arise due to the limited volume that is sampled by VIPERS. Since bright objects are intrinsically rare, one might worry they could be missed at low redshifts, due to the lower volume sampled, compared with that probed at higher redshifts, for a fixed solid angle. In Section A.2 we assess the impact the volume probed has on the number of bright galaxies by subsampling the GAL-FORM output to contain the same number of objects as VIPERS. We find that the bright edge is still in the same position, within the errors (Fig. A.3).

5.5 Evolution of synthetic SFH compared to observations

Making use of the modelling developed in Section 5.3, we can synthetically evolve the observed VIPERS galaxies to different cosmic times, and hence see where they would appear in the colour – magnitude plane in different redshift bins. We can then compare this synthetically evolved population with the observed population at the same redshift and repeat this process for different redshift bins. Comparing the level of agreement between the bright edges of the colour – magnitude relations

for the synthetic and observed galaxies gives us some insight into simple SFH quenching scenarios. In the next sections, we explore the different SFHs in order from top to bottom from Fig. 5.2. We consider first a scenario that does not involve any quenching (Section 5.5.1) and then two scenarios which impose quenching differently (Section 5.5.2): in the first the quenching event occurs at the epoch of observation (Section 5.5.2.1) while in the second the quenching takes place at a time that is randomly selected from selected time intervals after observation (Section 5.5.2.2).

Note that our approach does not attempt to model the whole of the observed population at each end-redshift. We are simply tracking the forward evolution of the VIPERS galaxies observed at $1.0 < z < 1.1$, assuming that the evolution is described by the best-fitting SFH to the observed photometry, with various quenching scenarios applied that truncate the star formation (see next sections). We assume that these galaxies preserve their identity from the observation redshift to the end redshift i.e. they do not merge with another galaxy. Also, we consider all of the evolved population of galaxies without requiring that the galaxies meet the VIPERS selection at the end-redshift. We remind the reader that our aim is not to reproduce the whole of the observed VIPERS colour-magnitude relation at redshifts below $z \sim 1$, but rather to focus on the evolution of the bright edge and how it compares to the observed one. Comparing the evolved and observed galaxy populations in the colour-magnitude plane is an interesting test which requires more sophisticated modeling. Moreover, such a test would be model-dependent and we feel that this goes beyond the scope of this chapter.

When comparing the synthetic and observed bright edges in the colour-magnitude plane, we need to bear in mind the following subtle point. The sample we are evolving using the best-fitting SFH, is defined at high redshift. VIPERS is a magnitude limited survey ($i_{\mathrm{AB}} < 22.5$). Hence, galaxies fainter than this limit in the high redshift bin are not considered from the outset in the analysis described in this section. This means that for substantial evolution times after the epoch cor-

responding to the high-redshift bin, the blue cloud will inevitably become depleted as star-forming galaxies that would naturally enter the observed sample at lower redshifts are not considered in the modelling. This is because their progenitors in the high redshift bin were too faint to be included in VIPERS. For this reason, if we had found an excess of blue star-forming galaxies in the lower redshift bins this would indicate the need for a faster and more efficient mechanism to suppress star-formation. However, the absence of blue galaxies when evolving a high-redshift sample, is expected and does not provide any new information about the nature of the quenching nor should it be interpreted as a mismatch between the observations and the modelling.

5.5.1 The no-quenching scenario

The synthetic evolution of VIPERS galaxies observed at $1.0 < z < 1.1$ to lower redshifts is shown without any quenching in Fig. 5.6. The evolution is modelled using the best-fitting SFH to the observed photometry (corresponding to the schematic SFH in the top panel of Fig. 5.2). The colour – magnitude relation for this evolved set of galaxies is shown by the blue points in each panel of Fig. 5.6, along with the associated bright edge (solid blue line). Each panel in Fig. 5.6 shows the evolved colour – magnitude relation at a different time interval after the observation redshift (left: $t_1 - t_{\mathrm{obs}} = 0.8$ Gyr, middle: $t_2 - t_{\mathrm{obs}} = 1.3$ Gyr, and right: $t_3 - t_{\mathrm{obs}} = 2.5$ Gyr). The observed VIPERS galaxies at each redshift plotted in Fig. 5.6 are shown by the red points and their associated bright edge by the solid red line. Except for the reddest colour bins, there is a mismatch in the observed and synthetically-evolved bright edges, with the sense of the discrepancy depending on the colour. In the "green valley" ($1.2 < U - V < 1.5$), the synthetic bright edge is fainter in the V-band than the observed one (by $\approx 0.5 - 0.75$ mag). This situation is reversed for blue galaxies ($U - V < 1.2$) for which the synthetic bright edge is ≈ 0.5 mag brighter than the observed one.

The excess of bright galaxies predicted with the no-quenching SFHs seems to

point towards the need for a scenario with widespread quenching of star formation activity for bright galaxies. However, no conclusion can be reached about the SFH of fainter galaxies, i.e. those galaxies fainter than the peak of the distribution of luminosities (see Fig. 5.4), as they do not feature in defining the location of the bright edge.

Another important property of the quenching suggested by Fig. 5.6 is that it must take place over a wide range of colours, and hence affect observed galaxies with very different levels of star formation activity. Our stellar population modelling suggests that these galaxies also have a range of stellar masses, implying that stellar mass is not the only factor that governs the SFH of galaxies (see A.4).

5.5.2 Exploration of quenching scenarios

Our aim is not to build a complete and physically motivated star formation quenching model, but rather to provide some indicative constraints on the quenching, as derived from the observed evolution of the galaxy properties in our sample. We therefore explore only a small number of simplistic quenching models (corresponding to the SFHs sketched in the lower two panels of Fig. 5.2), to help us gain some insight into the quenching time-scales. We stress that the modified SFHs we have built to include quenching all assume that the quenching is complete, i.e. that no residual SFR remains after the quenching, and that the transition takes place almost instantaneously (effectively over a period of less than 100 Myr).

5.5.2.1 Quenching the SFH at the epoch of observation

The first and simplest quenching model we consider is one in which the best-fitting SFH to each galaxy is quenched immediately after the epoch of observation (i.e. corresponding to the schematic in the middle panel of Fig. 5.2), thereby truncating the SFH and setting the subsequent SFR to zero. As we are using the high-redshift bin $1.0 < z < 1.1$ as our starting point, the quenching takes place at the redshift

of observation for each galaxy. Even if the quenching redshift is very similar over the sample, this does not mean that the galaxies are at the same stage in their evolution, because their SFHs are described by different parameters. This can be easily seen from Fig. 5.1. In fact, if we draw a vertical line at the same redshift, this will intersect every SFH at different stages in the evolution for different galaxies (i.e. t will be similar for every galaxy but $t - t_{\mathrm{start}}$ will be different and for different SFH (different τ) the evolutionary stage can be very different: the galaxy can be still star-forming or already in its passive phase).

Fig. 5.7 shows, using the same format as Fig. 5.6, the evolution of the synthetic colour-magnitude relation for this SFH-quenching scenario. We can see clearly from Fig. 5.7 that instantaneous quenching is too extreme, resulting in the bright edge for synthetic galaxies being fainter than the observed one. This is particularly noticeable for bluer galaxies. Again, as with the no quenching case, the exception is the reddest galaxies, for which the synthetic and observed bright edges coincide. These objects already have a SFR that is almost zero at the epoch of observation, and therefore their SFH, and consequently their photometric properties, are not significantly affected by any quenching we might introduce.

5.5.2.2   Delayed quenching

To mitigate the excessive evolution of the bright edge found on quenching the SFH of all galaxies at the epoch of observation, we have explored delayed quenching scenarios, in which the quenching takes place at a time that is drawn uniformly between t_{obs} and $t_{\mathrm{obs}} + \Delta t_{\mathrm{quench}}$ (a schematic representation of this scenario is shown in the bottom panel of Fig. 5.2). Another possibility would be to associate a quenching time delay with a specific galaxy property, but that would require us to know which property might regulate the quenching.

Given that the redshift interval covered by our sample corresponds to a cosmic time interval of 2.5 Gyr, we have explored three values for the maximum delay

time: 1, 1.5, and 2.5 Gyr, as shown in the top, middle and bottom rows of Fig. 5.8. While the scenario with a maximum delay time of 1 Gyr produces a bright edge evolution which is quite similar to that found with instantaneous quenching, the two scenarios with maximum delay times of 1.5 or 2.5 Gyr produce a bright edge which is in better agreement with the observed one.

In each delayed quenching scenario explored we are testing the evolution at three end-redshifts which correspond to the cosmic times t_1, t_2 and t_3 in the bottom panel of Fig. 5.2. For each of these times the fraction of quenched galaxies (Q_{frac} in Fig. 5.8) changes according to the scenario explored, with the exception of t_3 where we always have 100% of the galaxy population quenched. We stress that Q_{frac} is an indirect consequence of the simple empirical quenching model that is useful to quote as it demonstrates one of the limitations of the model. As galaxies quench following a uniform distribution of times limited by Δt_{quench}, Q_{frac} is simply defined by $Q_{\text{frac}} = \Delta t / \Delta t_{\text{quench}}$ which gives the probability that a galaxy has already experienced the quenching. We note that a Q_{frac} value of 100% at a given redshift implies that there are no star-forming galaxies at lower redshifts, which disagrees with observations. For the quenching event spread over $\Delta t_{\text{quench}} = 1$ Gyr (top panel) we have 80% of galaxies quenched at t_1 and 100% at the other times. For $\Delta t_{\text{quench}} = 1.5$ Gyr, instead, we have 53% of quenched galaxies at t_1 and 87% at t_2. Finally, for $\Delta t_{\text{quench}} = 2.5$ Gyr, we have 32% quenched at t_1 and 52% at t_2. If we focus exclusively on the bright edge location, and we define a good model as one that gives a good match between the observed and synthetic bright edges, then a scenario with $t_{\text{quench}} = 2.5$ Gyr is the best among the three explored. This is particularly true if we focus our analysis only on t_3 (the right panels in Fig. 5.8), so that for each scenario (each row in Fig. 5.8) we are comparing a 100% quenched sample. This suggests $2.5/2 = 1.25$ Gyr as an estimate of the average quenching time-scale for our sample of galaxies.

5.6 Contrasting the colour-magnitude evolution with galaxy formation models

The stellar population synthesis models and simple delayed exponential SFH – quenching scenarios discussed in the preceding sections serve the purpose of developing some insight into galaxy evolution from the behaviour of the bright edge in the colour – magnitude relation. Several studies of quenching have been performed using both semi-analytical (e.g. Hirschmann et al. (2014); Henriques et al. (2017)) and hydrodynamical (e.g. Bluck et al. (2016); Wright et al. (2019)) models of galaxy formation. In this section we compare the VIPERS observations against the predictions of the semi-analytical galaxy formation model GALFORM Cole et al. (2000); Lacey et al. (2016).

GALFORM models a wide range of physical processes that govern the fate of the baryonic component in the universe, in the context of the hierarchical growth of the dark matter (for reviews see Baugh (2006) and Benson (2010)). Of particular relevance to the quenching of star formation in galaxies is the radiative cooling of gas from hot halos. The cooling flow can be staunched by the luminosity of an active galactic nucleus Bower et al. (2006). In simple terms this occurs when the cooling time of the hot halo gas exceeds the free-fall time and the cooling luminosity is balanced by the energy released by material falling onto the supermassive black hole at the centre of the galaxy. Star formation in a galaxy for which there is no cooling flow would be truncated once the existing cold star-forming gas is consumed and if it is not replenish by cold gas brought in by a merger. The aim here is to compare the colour – magnitude relation predicted by a standard version of GALFORM with the VIPERS observations. Exploiting the speed and modularity of semi-analytical models, we also examine a variant of the fiducial model in which we turn off AGN feedback to see the impact on the model predictions.

The GALFORM model that we consider here is the version introduced by
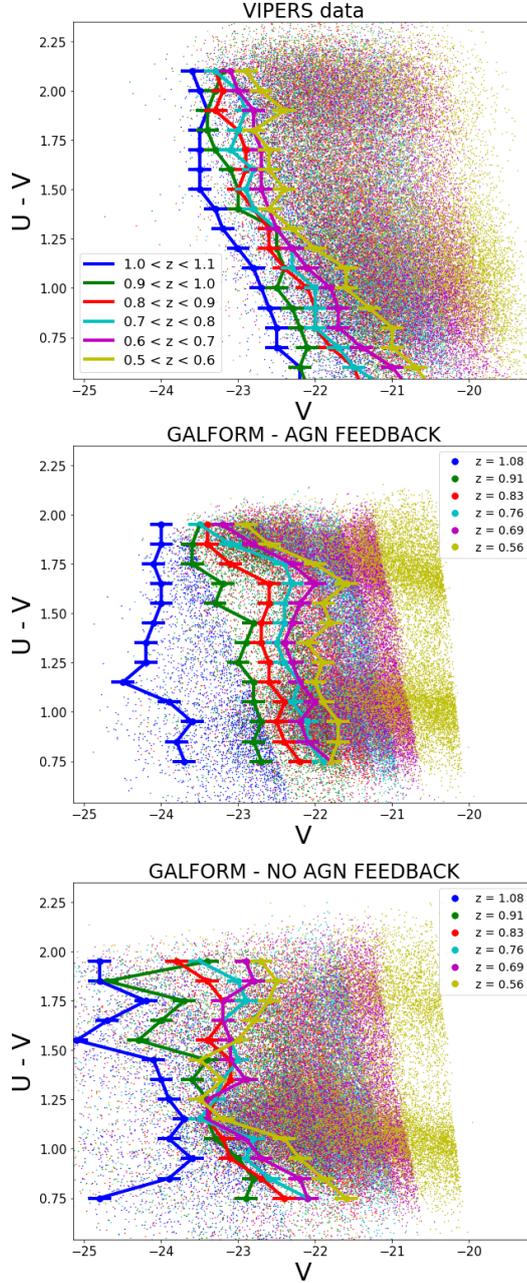
Figure 5.9: *Top panel:* VIPERS colour-magnitude diagram as in Fig. 5.5 to be compared with the GALFORM snapshots in lower panels. *Middle panel:* GP14 GALFORM colour-magnitude diagram (the default includes AGN feedback). A cut mimicking a $i_{\text{AB}} \leq 22.5$ cut (like VIPERS) has been applied to the model galaxies. *Bottom panel:* same as middle panel except that AGN feedback has been turned off. The horizontal error bars show an indicative error of 0.15 mag.

Gonzalez-Perez et al. (2014), hereafter GP14. This model is implemented in a version of the Millennium N-body simulation that adopts a cosmology consistent with the 7 year WMAP results Guo et al. (2011). The GP14 model assumes a standard solar neighbourhood stellar initial mass function (IMF) Kroupa (1998) for quiescent and burst star formation, which is the main feature which distinguishes it from the dual IMF models of Lacey et al. (2016) and Baugh et al. (2019). The parameters of the GP14 model have been calibrated to reproduce a range of observations, including the $z = 0$ galaxy luminosity function in the b_{J} and K bands. The luminosity function predicted by GALFORM has been compared with observations in the optical to $z \sim 0.3$ by McNaught-Roberts et al. (2014) for red and blue galaxies and for different environments, using the Galaxy And Mass Assembly (GAMA) survey. These authors found that the model predictions agreed reasonably well with the observations for bright galaxies, with the biggest discrepancy being the over prediction of faint-red galaxies, which can be traced to the treatment of gas cooling in satellite galaxies (see the discussion in Font et al. (2008)) *. The N-body simulation is a cube of volume $(500 \, \mathrm{M}pc/h)^3$ which we note in passing is substantially bigger than the effective volume of VIPERS, which is equivalent to a box of volume $(368 \, \mathrm{M}pc/h)^3$.

We consider the GP14 model at simulation outputs that are close to the centres of the VIPERS redshift bins. We apply the VIPERS apparent magnitude cut of $i_{\mathrm{AB}} \lesssim 22.5$. Using GALFORM snapshots at precise redshifts rather than VIPERS redshift ranges results in a sharp well-located cut in the GALFORM colour-magnitude plane at faint magnitudes. However, since the focus of the test is on the bright-edge, this does not introduce additional uncertainties. The majority of the model galaxies selected in this way are central galaxies in intermediate to massive halos, accounting for at least 75% of the total at all redshifts. Satellites galaxies without an identifiable dark matter subhalo represent a small fraction of the sample, reaching a peak of 8% at redshift 0.56 for colours redder than $U - V > 1.5$,

---

*Similar agreement with observed luminosity functions is found in other semi-analytical models (e.g. Hirschmann et al. (2016); Henriques et al. (2017); Lagos et al. (2019))

leaving the evolution of the blue cloud unaltered.

The primary quenching mechanism for central galaxies is AGN feedback (in particular the hot halo – radio mode AGN feedback), which shuts down gas cooling in halos above a mass that is determined by the parameters describing the AGN feedback (see Lacey et al. (2016)). This motivates our choice to explore a variant model in which this quenching is turned off, by switching off AGN feedback (by setting $\epsilon_{\text{heat}} = 0$ and leaving the other parameters unchanged; see section 3.5.3 in Lacey et al. (2016)). Note that this is not a viable model as it produces too many bright galaxies. Nevertheless it is illustrative to see the impact on the colour – magnitude relation of turning off this quenching mechanism.

Note that AGN feedback is not the only star formation quenching mechanism in GALFORM. Satellite galaxies have their star formation quenched by stripping of their hot gas halo after they are accreted into a more massive dark matter halo. This stops any further gas cooling onto the satellite, which leads to less star formation than may have been the case if the galaxy had remained a central galaxy. However, the effect of this process on the colour – magnitude diagram is negligible as central galaxies dominate the GALFORM sample for the VIPERS selection. Also, the quenching due to AGN feedback in GALFORM is not as dramatic as that in the simple model considered in earlier sections of this chapter as GALFORM galaxies do not stop their star formation instantaneously but in a gradual way as the molecular gas reservoir is exhausted. Bright galaxies in the GALFORM model, which have had their quiescent star formation quenched by the suppression of gas cooling by AGN feedback, can still display episodes of star formation activity through bursts involving the cold gas brought in by merging galaxies.

The evolution of the colour – magnitude relation in the observations and models is compared in Fig. 5.9. The VIPERS observations in different redshift bins are collected in the upper panel to give a different view of the evolution of the bright edge from that shown in Fig. 5.5. The middle panel shows the predictions of the

GP14 model and the lower panel the variant of GP14 with no AGN feedback. The rest frame magnitudes and colours used in the GALFORM predictions have been chosen to match the transmission curves of the filters used in VIPERS and include attenuation by dust (see Gonzalez-Perez et al. (2013) and Lacey et al. (2016) for a description of the implementation of attenuation by dust in GALFORM). To make the GALFORM colour-magnitude plot more visually comparable to those from VIPERS we randomly subsample the model galaxies to account for the difference in volume between the GALFORM simulation and VIPERS.

The top panel of Fig. 5.9 shows the steady evolution of the bright edge to fainter luminosities with increasing redshift in the VIPERS observations. This evolution is strongest in blue $U - V$ colour bins, with the bright edge becoming approximately 1.5 mag fainter from $z \sim 1$ to $z \sim 0.5$, and weakest for red colour bins, with the edge being around 0.75 mag fainter over the same redshift interval.

The middle panel of Fig. 5.9 shows the colour – magnitude relation for the fiducial GP14 GALFORM model. The first thing we notice on comparing with the VIPERS data is the overall shift in the locus of the model points to brighter magnitudes, reflecting the difference between the GALFORM and VIPERS luminosity functions. Fritz et al. (2014) measured the evolution of the luminosity function using VIPERS and find a sharp break at the bright end, across the redshift range considered here. Our comparison of the Fritz et al. (2014), results with the GALFORM predictions shows GALFORM produces a weaker break, and hence more bright galaxies than estimated from VIPERS, with a dip in the model luminosity function relative to that from VIPERS around L_*.

Focusing on the relative change in the bright edge in the GALFORM predictions rather than its absolute position, Fig. 5.9 shows that the model bright edge also moves faintwards with decreasing redshift, preserving the ordering of the bright edge with redshift more clearly than the data. The shift in the position of the bright edge for the bluest colour bins is about 0.5 mag larger than for VIPERS. The shift of the edge for the reddest bin is just over 1 mag, approaching twice the

shift for VIPERS.

The shift of the bright edge towards fainter magnitudes with time is an interesting feature which deserves some discussion here. The key point to bear in mind when interpreting this shift is that the galaxies which define the bright edge are not the same ones at every redshift. The bright edge galaxies have lower stellar masses as we move to lower redshifts. Of course the stellar mass of an individual galaxy increases throughout its lifetime. However, as the star-formation in these galaxies declines, they will become fainter, and will no longer be part of the 15 per cent of objects in a given colour bin which define the location of the bright-edge. Moreover, after sufficient time, they will become fainter than the limiting magnitude of the survey ($i_{AB} < 22.5$) and hence will not appear in the colour - magnitude diagram. The shift of the bright edge to fainter magnitudes with time, observed in both VIPERS and the GALFORM model, reflects the effect of downsizing described in the introduction: lower mass galaxies are the ones most actively forming stars at low redshift, whereas at higher redshift it is the higher mass galaxies.

Finally the lower panel of Fig. 5.9 shows the predictions of the variant of GP14 with AGN feedback switched off. The locus of model galaxies is shifted to brighter magnitudes, even compared to the fiducial GP14 model shown in the middle panel. This reflects the additional gas cooling in intermediate and massive halos compared to the fiducial model with AGN feedback switched on. This emphasises that this variant is not a viable model as it produces too many bright galaxies. The ordering of the bright edges with redshift is also lost, with the bright edges for several redshifts overlapping for the blue cloud.

Another notable feature of the GALFORM predictions in Fig. 5.9 is the strong bimodality in colour, as pointed out by Bower et al. (2006) and González et al. (2009). This is also apparent in Fig. 5.6, when we use smooth delayed exponential SFHs without quenching.

In addition, we note that in the VIPERS data the bright edge is vertical for red

colours, and becomes increasingly diagonal moving to bluer colours. The edge shifts as a coherent block back to lower luminosities with time. The fiducial GALFORM model does not reproduce this behaviour. The bright edge is vertical for the blue sequence, and diagonal for the red sequence. In the VIPERS data, the bright edge traces the blue edge of a diagonal blue sequence, while in the GALFORM output, it traces the bright-edge of a horizontal blue sequence.

Whilst there are qualitative differences between the colour-magnitude relations of VIPERS and the GALFORM model (e.g. shift to brighter magnitudes, the shape of the bright edge and stronger colour bimodality in GALFORM than in VIPERS, at approximately $U - V \sim 1$ and $U - V \sim 1.75$), the ordering of the bright edges with redshift and the breaking of this ordering in the variant model without AGN feedback indicate that AGN feedback plays an important role in quenching star formation activity in the models.

5.7   Discussion

The very notion of quenching star formation in galaxies is somewhat dependent on the galaxy evolution paradigm adopted to interpret observations or build models, as discussed extensively by Abramson et al. (2016). It is possible that the need for quenching is merely the result of incorrectly assuming that star formation is a simple process. However, as this simplifying assumption is often the first step in any attempt to model galaxy evolution, it is worthwhile to try and characterise any quenching that may take place.

The need for quenching remains controversial. Ciesla et al. (2016) advocated for the quenching of star formation on the basis of SED analysis of the Herschel Reference Survey galaxy sample Boselli et al. (2010), applying delayed exponential SFHs, similar to those used here, and adding a sharp quenching to the SFR*. On the

---

*The only difference with our model is that the quenching invoked by Ciesla et al. (2016) is not complete, but reduces the SFR to 35% of its prior value.

other hand Pozzetti et al. (2010) claimed that the colour evolution in the zCOSMOS sample could only be reproduced by including extended SFHs or secondary bursts of star formation in the SED modeling, rather than by a reduction or suppression in the level of star formation activity. One reason for this disagreement might be the SFH modelling adopted by Pozzetti et al. (2010), which differs in two key ways from that adopted here, namely that all galaxies follow exponentially declining SFHs*, and that no evolution of the dust content takes place inside galaxies as their star formation evolves. Some studies (see for example the discussions in Citro et al., 2016; Tomczak et al., 2016; Abramson et al., 2016) claim that the use of purely exponentially decreasing SFHs is not ideal for studying the evolution of galaxy properties as this does not allow for an initial increase of the SFR. The exponentially declining SFH results in reddening of galaxy colours by construction, without the flexibility to describe the population of star-forming galaxies which are still moving towards bluer colours and brighter magnitudes.

Much recent work on quenching has focused on a global description of the galaxy population, often using the stellar mass function, as in Bundy et al. (2006) and Peng et al. (2010), or measuring the transition of galaxies across the green valley, as in Schawinski et al. (2014) and Lian et al. (2016) (see also Wright et al. (2019) for a measurement of a quenching time based on the green valley and other techniques relying on the time at which galaxies leave the main sequence of star formation, for a hydrodynamical simulation of galaxy formation). Here instead we study how different SFHs both with and without a truncation of the star-formation activity can affect the bright edge of the colour-magnitude plane, over a substantial lookback time, corresponding to the redshift range $0.5 \lesssim z \lesssim 1.1$.

We use two approaches to interpret the evolution of the bright edge in the VIPERS colour – magnitude relation. The first is a simple empirical model in which the evolution of VIPERS galaxies is predicted using a smooth SFH that is quenched at or after the epoch of observation. The SFH is a delayed exponential

---

*$SFR\left(t, \tau, t_{\text{start}}\right) = (1/\tau) \exp\left[-\left(t - t_{\text{start}}\right)/\tau\right]$.

that is the best-fitting description of the galaxy's photometric properties (rest frame $U - V$ colour and rest frame V-band absolute magnitude). The second approach is a physically motivated semi-analytical model of galaxy formation, which predicts the evolution of the colour – magnitude relation directly.

The SFHs predicted by physical galaxy formation model appear to be much more complicated than the smooth delayed exponentials adopted in the empirical model (see the examples from GALFORM plotted in Baugh (2006)). Simha et al. (2014) compared a range of parametric SFHs to those predicted in a hydrodynamic simulation of galaxy formation. Their "lin-exp" model, which is equivalent to the delayed-exponential used here, performed much better overall, experiencing problems mainly for the very bluest and reddest galaxies. Without a truncation of the SFH, lin-exp models result in higher values of SFR at early times and lower values of SFR at late times (as any truncated SFH would be interpreted as a smooth SFH with a very small τ^*). The use of contrasting approaches to model the evolution of the colour – magnitude relation lends robustness to any consistent conclusions reached about the importance and nature of quenching.

Our simple empirical analysis of the evolution of the bright edge of the colour – magnitude relation suggests that quenching must be a widespread phenomenon, taking place over the full range of redshift ($0.5 < z < 1.1$) and stellar mass (approximately $9.0 \lesssim \log(\mathcal{M}/M_\odot) \lesssim 11.0$) probed by VIPERS. The range of stellar masses that is quenched is an interesting result. Following the identification by Kauffmann et al. (2003) of a threshold stellar mass ($\sim 3 \times 10^{10} M_\odot$) above which local galaxies are dominated by passive early-types, the concept of a transition mass above which galaxies are quenched has become popular (see for example Bundy et al., 2006; Davidzon et al., 2013). However, our results imply instead that quenching takes place over a wider range of stellar masses than what proposed by Kauffmann et al. (2003). (See A.4 for the justification of the range of stellar masses

---

*The limitation of having SFHs defined by only one parameter, τ, is that early and late times in the life of a galaxy are related. Introducing a quenching event overcomes this limitation.

involved.) Other studies such as Schreiber et al. (2015) study the evolution of the main sequence of star formation with redshift, and their results are consistent with quenching over a wide range of stellar masses.

The detection of the widespread quenching presented in Section 5.5.1 is a robust result of this work, since the SFH modelling it is based upon reproduces quite well the main characteristics of star formation activity in the VIPERS galaxy sample, including the instantaneous measurement of SFRs at all redshifts and colours (see A.1). The characterisation of the quenching time-scale that we discuss in Section 5.5.2 is instead based on a simple toy model, with the main purpose of demonstrating that a viable quenching history capable of describing the observations does indeed exist.

Finally, as a consequence of using a simplified SFH model, we do not attempt to identify a single galaxy property to replace stellar mass as the clearest driver of quenching and overall galaxy evolution. We note, however, that Haines et al. (2017) discuss at length the possibility that this property could be the mean stellar mass density, i.e. the amount of galaxy stellar mass located within the galaxy central kiloparsec. Of course our reliance on the evolution of the bright edge of the colour-magnitude relation to characterize quenching prevents us from drawing reliable conclusions about the possible quenching of galaxies that, at any epoch, are significantly fainter than the bright edge (i.e. fainter than the magnitude at which the number of galaxies in a given colour bin peaks). Still, the very simplistic assumption we make that only the galaxies whose evolution we are able to constrain (i.e. those that are close to the bright edge in terms of magnitudes) are actually undergoing quenching over a limited time-span after observation matches the results of Lian et al. (2016), who estimate that only approximately one quarter of the galaxies in their sample start the quenching transition every gigayear. Lian et al. (2016) quench their SFHs in a somewhat less dramatic way than we do. These authors use what they call a "two-phase exponentially declining SFH", with one exponential describing the secular star-forming stage and the other describing a

rapid quenching stage (see Fig. 1 in Lian et al. (2016)). Although the quenching is introduced as an exponential decline, their approach is not very different from ours as they estimate a quenching e-folding time of 500 Myr while our truncation is limited in time by the resolution of our models which is 100 Myr. With these assumptions, Lian et al. (2016) study the drop in the number density of the NUV$-u$ vs $u-i$ colour-colour diagram, finding a time to migrate from the star-forming to the passive population of 1.5 Gyr (Fig. 2 of Lian et al. (2016) shows how these two populations are defined in the NUV$-u$ vs $u-i$ colour-colour diagram).

An indication of a physical processes that could explain the quenching of galaxy star formation rates since the peak epoch of global star formation was offered by the comparison of the predictions of the GALFORM semi-analytical model of galaxy formation with the VIPERS colour – magnitude relation. The qualitatively similar evolution of the bright edges in GALFORM and the observations, and the break down of this evolution when AGN heating of cooling gas is turned-off by hand, reveals that AGN feedback heating is quenching the SFR by turning off the fuel supply for star formation. The bright edge evolves too much in GALFORM, which might point to the need to revise the treatment of the reincorporation of gas heated by supernovae, as argued by Mitchell et al. (2016) in their study of the evolution of the stellar mass – halo mass relation.

In conclusion, our work points towards a SFH scenario in which quenching of star formation gives a better match to the evolution of bright galaxies in the colour – magnitude plan that is not reproduced in models in which star formation is able to proceed unfettered.

CHAPTER **6**

Dealing with big data and large data-sets

Astronomical studies often involve the systematic study and processing of large data-sets. Especially when dealing with galaxy redshift surveys, as in the analysis carried out in preceding chapters of this thesis, large amounts of information is collected for every galaxy, and the aim is to have increasingly large samples. Astronomy, though, is not the only field that requires us to deal with large amounts of information, and the skills developed in astronomy research are often transferable to other fields. With this aim, the Centre for Doctoral Training (CDT) at Durham, provided me with additional training and the possibility to apply my skills in industry. The first project I undertook is described in Sect. 6.1. This was part of an internship at Procter & Gamble (P&G), with the aim of trying to model the contribution of the different chemical ingredients on the appearance of laundry powder, focusing on the density of the granules. The second project, described in Sect. 6.2, was a collaboration with the National Health Service (NHS). In this case the aim was to establish the expected values for the vital signs for a sample of healthy babies to help doctors make decisions about the treatment to provide allowing an early diagnosis of unhealthy babies, thereby increasing their chance of survival.

6.1 Optimisation of laundry powder production at Procter & Gamble (P&G)

The aim of the project was to help the P&G team to find a more reliable analytic form of the function which describes the density of the laundry powder. Experiments were performed by P&G at their powder spray drying test facility near Newcastle. This mixing tower is a scaled down version of the towers used at their production plants. Experiments can be carried out in which the physical conditions and the chemical ingredients are varied and the impact on the resulting density of the particles of washing powder measured. P&G measures the density of the laundry powder by pouring it into a cup of known volume and calculating the mass of the 'bulk powder' captured in that volume. For this reason they call it 'repour cup density'. The density of the individual grains of the powder is also important but not the focus of this work. The density of the laundry powder in general is important as it is related to how well the powder functions in the washing machine. The P&G team has previously identified a library of *basis functions* suggested by the chemistry processes behind the mixing and drying of the laundry powder ingredients. Each basis function might depend on up to 13 of the available chemical ingredients:

$$f_i = f_i(x_1, \cdots, x_{13}), \tag{6.1}$$

where f_i are the basis functions ($i = 1, \cdots, N$) and x_j are the ingredients ($j = 1, \cdots, 13$). Each basis function is meant to describe a single physical process that affects the density of the powder and the linear combination of them aim at describing the density as a function of the chemical ingredients. Empirically P&G have chosen the combination that works the best, setting the coefficient of their basis functions f_i to their empirically determined values $\hat{a}_i$:

$$\text{density} = \sum_{i=1}^{N} \hat{a}_i f_i(x_1, \cdots, x_{13}) \tag{6.2}$$

where N is the number of basis functions used. The way P&G currently set their coefficients is based on a trial and error approach, testing different sets of coefficient and choosing the one that better reproduce the observed density.

The first step to make this process more quantitative and reproducible is to use Eq. 6.3 as a fitting function leaving the a_i as free parameters to be found through the minimisation of the χ^2:

$$f_{\text{fit}} = \sum_{i=1}^{N} a_i f_i(x_1, \cdots, x_{13}), \tag{6.3}$$

$$\chi^2 = \sum_{k=1}^{M} \frac{(y_k - f_{\text{fit}}(x_{k_1}, \cdots, x_{k_{13}}))^2}{M}, \tag{6.4}$$

where N is the number of basis functions and M is the number of data-points that comes from a set of measurements from the different runs on the test spray drying tower.

The minimisation of χ^2, although computationally expensive because of the high number of basis functions (hence the high number of parameters a_i), will result in the best fit, i.e. the one which minimises the square of the distance of the model to the data points. The best fit is not necessarily what we want as it might rely on our choice of basis functions f_i and the specific data-set that we are using (x_k, y_k). For example if we add a further basis function to the current set of basis functions, the χ^2 minimisation will also make use of this further basis function to obtain a better fit. This makes the resulting fit dependent on our arbitrary choice to add a basis function. At the same time, if we change data-set (x_k, y_k), the fit obtained with the old data-set will not minimise the χ^2 any longer (as the best fit is the best for a specific data-set). This makes our results data dependent, and hence not robust. This is why it is better to find a more general fit that may be slightly worse in terms of χ^2, but which is still a adequate fit for different data-sets.

The two problems (arbitrary choice of basis functions and having a data-dependent fit) are related. In particular, the more basis functions we use, the more the χ^2 fit

will be data-dependent (the so-called *overfitting problem*). Therefore, it seems that minimising the number of basis functions can help to provide a more robust fit.

If we succeed in reducing the number of basis functions, f_i, (or equivalently having more of the coefficients set to zero, $a_i = 0$, for many i) then we might obtain a further advantage from the fact that not all of the f_i depend on all 13 ingredients x_j. In other words, in practical terms, most of the basis functions in this case would be a function of a single ingredient. (i.e. we would have for example the case $f_{i_0} = f_{i_0}(x_7)$, instead of $f_{i_0} = f_{i_0}(x_1, \cdots, x_{13})$). Following this example, it is also possible that the dependence on the ingredient x_7 only happens in the case of the function f_{i_0}, with all the other basis functions, f_i, not depending on x_7. On the other hand, if we manage to remove the function f_{i_0} setting its parameter $a_{i_0} = 0$, then this means that the ingredient x_7 is not important anymore for changing the density of the laundry powder, hence saving money by not buying that ingredient.

A possible way to address (at least partially) this problem is to use the Least Absolute Shrinkage and Selection Operator (LASSO, Tibshirani 1996) which adds a *penalty term* to the usual χ^2 to penalise the use of a larger number of parameters, i.e. favouring a fit with a small value of $\sum_{i=1}^{N} |a_i|$. The classic analytic form of LASSO is the following:

$$\text{LASSO} = \boxed{\sum_{k=1}^{M} \frac{(y_k - f_{\text{fit}}(x_{k_1}, \cdots, x_{k_{13}}))^2}{M} + \lambda \sum_{i=1}^{N} |a_i|} \equiv \chi^2 + \text{Penalty}, \qquad (6.5)$$

where, as always, M is the number of data points, N is the number of basis functions and λ is a free parameter that we can tune case by case (the choice of the ideal value of λ is still an open debate; one possible solution is to use a machine learning approach to train the algorithm on cases with a known solution). This approach helps to discard the basis functions that are not particularly relevant as, when minimising Eq. 6.5, a fit with a lot of basis functions will result in a bigger penalty term than a fit with fewer basis functions.

However, we note that the traditional LASSO method, as set out in Eq. 6.5 may be improved to work in a P&G-like case, where we want to minimise only the num-
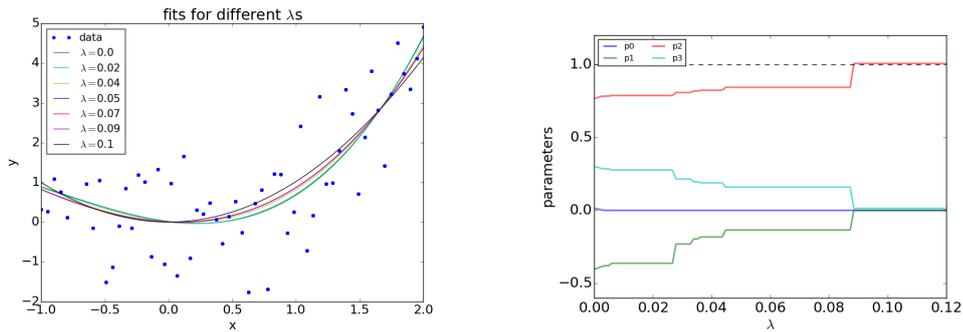
Figure 6.1: Example of the performance of the modified LASSO in recovering a known function when gaussian noise is added. **Left**: examples of modified LASSO fits for different λs to 60 data points generated from an x^2 function ($f_{\text{true}}(x) = x^2$), with the addition of gaussian noise with a standard deviation of 0.9. The fitting function is a third order polynomial. **Right**: the values of the parameters of the fitting function ($f_{\text{fit}} = p_0 + p_1 x + p_2 x^2 + p_3 x^3$) as a function of the λ parameter. Since we know f_{true}, we know that the right answer is $p_2 = 1$ (red line) and $p_0 = p_1 = p_3 = 0$. This solution is achieved only for $\lambda \gtrsim 0.09$.

ber of functions and not the actual values of the function coefficients $|a_i|$ (whereas in the traditional LASSO approach, both are minimised). In fact, minimising the current penalty will result in favouring solutions with small values of $|a_i|$, which is different from favouring a solution where some coefficients are exactly $a_i = 0$ (and having some $a_i = 0$ means using fewer basis functions). We developed a new, *modified LASSO* to deal with this problem. In particular we changed the penalty function slightly in the following way:

$$\text{New Penalty} = \lambda \left[\left(\sum_{i=1}^{N} |a_i| \right)^2 - \left(\sum_{i=1}^{N} a_i^2 \right) \right]. \tag{6.6}$$

With this new penalty function, parameters that are zero are favoured as they appear only in cross terms. For example, let us assume we have just 3 parameters. The new penalty function will be: $(|a_1| + |a_2| + |a_3|)^2 - a_1^2 - a_2^2 - a_3^2 = |2a_1a_2| + |2a_1a_3| + |2a_2a_3|$. If one of the parameters is null, it will null the product with another parameter and this will make the penalty smaller than if we had small, non-zero parameters. Another improvement that can make the LASSO technique more effective is the normalisation of the basis functions. Although logically normalisation would be the first thing to do, we introduce it now because this is part

of our improvement to LASSO, which, until now, has always been used in the literature without normalisation. Specifically, the problem that we want to address is that as long as we do not normalise the basis functions, different parameter values could affect in very different ways the LASSO functions, and hence the result of the fit. For example, if a basis function is $f_{i_0} = x$ or $f_{i_1} = 5x$, the parameter a_{i_0} and a_{i_1} will have the same weight in the penalty function ignoring the fact that they convey different information. This is why we decided to normalise the data and the basis function image in the following way:

$$\hat{x} = \frac{x - x_{\min}}{x_{\max} - x_{\min}} \quad \hat{y} = \frac{y - y_{\min}}{y_{\max} - y_{\min}} \quad \hat{f}(\hat{x}) = \frac{f(x(\hat{x})) - f_{\min}(x(\hat{x}))}{f_{\max}(x(\hat{x})) - x_{\min}(x(\hat{x}))}, \quad (6.7)$$

where $x \in [x_{\min}, x_{\max}] \Rightarrow \hat{x} \in [0,1]$, $y \in [y_{\min}, y_{\max}] \Rightarrow \hat{y} \in [0,1]$ and $f(x) \in [f_{\min}(x), f_{\max}(x)] \Rightarrow \hat{f}(\hat{x}) \in [0,1]$. To deal with normalised variables, the χ^2 needs to be normalised in order to have the same order of magnitude as the penalty function. We introduce the ϵ^2 parameter which is the minimum value of the χ^2 (without the penalty) to normalise our modified LASSO to unity when $\lambda = 0$:

$$\epsilon^2 = \min \left\{ \sum_{k=1}^{M} \frac{(y_k - f_{\text{fit}}(x_{k_1}, \cdots, x_{k_{13}}))^2}{M} \cdot \right\} \quad (6.8)$$

With these definitions, our modified LASSO acquires the following form:

$$\text{MODIFIED LASSO} = \boxed{\frac{1}{\epsilon^2} \sum_{k=1}^{M} \frac{(y_k - f_{\text{fit}}(x_{k_1}, \cdots, x_{k_{13}}))^2}{M} + \lambda \left[\left(\sum_{i=1}^{N} |a_i| \right)^2 - \left(\sum_{i=1}^{N} a_i^2 \right) \right]} .$$
$$(6.9)$$

To test our new implementation of LASSO, we created increasingly difficult known functions (increasing the number of variables and combining polynomials with exponential terms). After having added various kinds of noise with different amplitudes, we tried to recover the original functions, fitting with the *modified LASSO* of Eq. 6.9. A simple scenario is shown in Fig. 6.1 where we generated 60 datapoints using the function $f_{\text{true}} = x^2$ adding Gaussian noise with a standard deviation of 0.9. We fitted the data-point using a third order polynomial, $f_{\text{fit}}(x) = a_0 + a_1 x + a_2 x^2 + a_3 x^3$, knowing that the solution is $a_2 = 1$ and $a_0 = a_1 = a_3 = 0$.
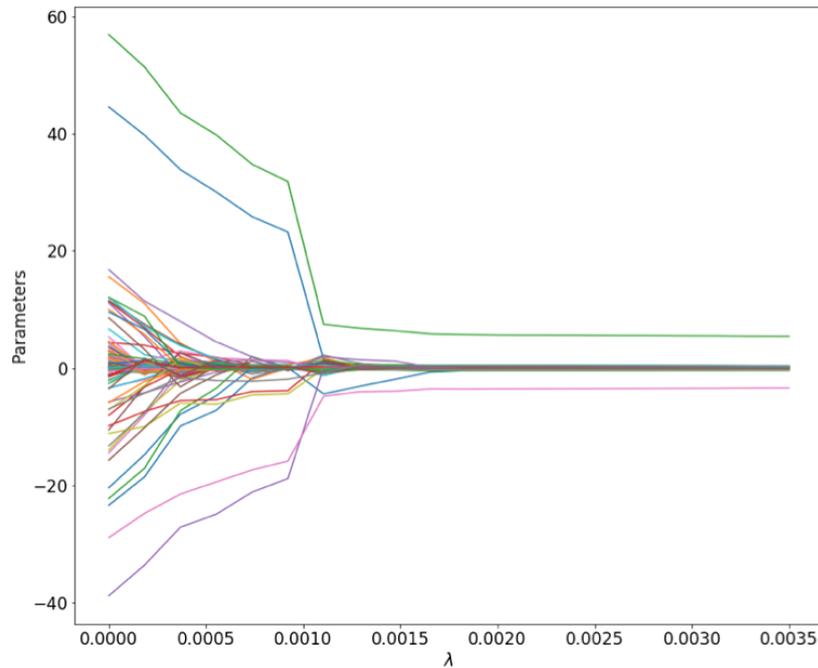
Figure 6.2: Same as the right panel of Fig. 6.1 but instead of finding the coefficient of a known function like x^2, we try to find the coefficients for the density function of the P&G laundry powder (for which we don't know the right answer).

Although, looking at the left panel of Fig. 6.1, the fits for different λ do not look very different, in the right panel we notice that we recover the true solution only for $\lambda \gtrsim 0.09$. Picking the right λ is not trivial, and currently there are no rules in the literature to decide which is the right value. In the future, it might be interesting to train our algorithm to choose the right λ using known case studies like the x^2 one. In Fig. 6.2, instead I report a real example of our technique applied to the P&G case. It can be seen that only few coefficients survive after values of $\lambda \gtrsim 0.0011$. As mentioned above, the choice of the optimal λ is something that is left for future work.

6.2 Trends in heart rate variations in healthy newborns in the first few days of life

This section presents the results of my internship with the National Health Service (NHS) and is presented in the form of a paper submitted to the *Acta Pediatrica*, and so is written in a somewhat different style to the rest of the material in this thesis. To understand this material, some basic medical terms need to be defined. The main observables I needed to consider were the pulse rate (PR, or equivalently heart rate, HR), the oxygen saturation of the blood (SpO2) and the perfusion index (PI). These quantities can be measured for babies using an oximeter like the one shown in Fig. 6.3. The oximeter is attached to babies through a bracelet on the wrist (for so called pre-ductal measurements) or the foot (for post-ductal measurements). The focus of this study is on the heart rate (HR). Following the abstract of the study below, since this material is quite distinct from astronomy, a brief section has been added to the original manuscript to provide further context for readers without a medical background, to explain what is already known in the field and what this study adds.

Abstract

Background: Knowledge of variations in heart rate (HR) is lacking for healthy infants in the first few days of life.

Methods: We conducted a prospective observational study and included all term newborns (≥ 37 weeks) after 6 hours of birth, with normal examination. The consented infants underwent 10 minutes of pre-ductal and post-ductal pulse oximetry recordings under direct supervision. Following that, another 80 minutes of pre-ductal recording were completed at the mother's side. All the recordings were blinded to the study investigators. Oximetry recordings were performed every $12 - 24$ hours prior to discharge. Infants were followed up electronically for a period of 8 weeks to ascertain their health condition. We had pre-set data cleaning rules and the study was approved by our local

research ethics board.

Results: After exclusion we had 268 (91%) babies for the final analysis. Infants with gestational age > 40 weeks, female sex, and age of infants at $24-72$ hours had higher mean HR (~ 4 beats) as compared to the others. Significant bradycardia of HR< 80/min and HR< 2/3rd of baseline were rare, with approximate frequency of 1 episode every 2 hours and lasted for ~ 30 seconds. We plotted all the HR data points against the normative value described ($100-160$/min) and showed $\sim 8\%$ of data points were outside the previously adopted range.

Conclusion: We have provided normative values and variations in HR in healthy infants for the first few days of life. We reported prevalence of bradycardia episodes and significant number of HR data points were outside the normative range.

6.2.1 Context for this study

When babies are born, doctors are trained to quickly recognise whether the baby is healthy or shows any worrying signs that need special treatment. A key factor in preparing the treatment path is the gestation period. If babies are delivered preterm then health issues are more likely. Sometimes, experience is crucial and some signs are simply visual, and so for these instances there is no automated process that can be a substitute for the trained eye of a doctor. However, there are measurements that can help doctors to make decisions regarding treatment, and to improve the timing of these decisions. One such measurement is the heart rate (HR) sometimes referred to as pulse rate (PR). For example, when the heart rate falls below a certain threshold, a phenomenon called bradycardia, doctors consider this as a warning stage and they keep the baby under close observation. This example shows the importance of the value of the threshold for bradycardia and this is part of the investigation reported in this study. Nevetherless despite the importance of the HR threshold, there is limited knowledge of the normative values and variation

in the heart rate of babies in their first few days of life. Given the importance of heart rate in the assessment of newborns and in devising an early warning score, we decide to focus our effort in this direction.

One of our main findings is the identification of classes of babies that have intrinsically higher or lower heart rates. We found that infants with gestational age > 40 weeks as compared to infants with gestational age < 40 weeks, female as compared to male infants, and infants with age of $24 - 72$ hours as compared to infants in the first 24 hours had higher mean heart rates. We also investigated the number and the duration of bradycardia events finding that, in healthy babies, severe bradycardia events (HR< 80/min and HR< 2/3rd Median HR) are rare (1 episode/2 hours) and short lasting ($\leq$ 30 secs). Moreover, compared to the standard in use for healthy babies, which establish a normative range between $100 - 160$/min, we found a higher number of heart rate data points outside this range. We finally analysed pre-ductal (measurements from the wrist) and post-ductal (measurements from the foot) heart rate. We argue that the differences in heart rate we find are not due to actual physiological reasons but instead from the different time of recordings between wrist and foot. In fact, while measurements from the foot are approximately ~ 10 minutes long, measurements from the wrist continue for about ~ 90 minutes. This can introduce a bias that we discuss in Sect. 6.2.4 which can be seen in figures 6.6, 6.7 and 6.8.

6.2.2 Background

Heart rate (HR) forms an important aspect of newborn assessment, intensive care monitoring and early warning scores for babies in the postnatal ward [1]. Healthy term babies do not undergo routine monitoring for HR; hence there is a lack of knowledge regarding the normal values and variations in their heart rate. Previous studies have reported HR immediately after birth [2, 3] and a few other studies have reported HR over a wide age range (0 to 3 months) [1, 4]. The UK National institute for Health and Care excellence reports normal HR as $100 - 160$ beats per

minute (bpm) [5] and the WHO reports HR more than 180 as abnormal [6] and these reported values are not based on strong evidence [7]. Newborn early warning trigger and tracking (NEWTT) is an early warning tool endorsed by the British Association of Perinatal Medicine and is commonly used in the United Kingdom [8] and defines normal HR as $100 - 160$ bpm. Assuming certain values of heart rate as abnormal could potentially introduce a bias and lead to many babies being wrongly classified as "unhealthy". With increasing focus on transitional care where the infants are cared by mother's side and an increase in term infant's admission to neonatal units [9] it is essential to report evidence based normative HR values. Though electrocardiogram (ECG) is the gold standard for accurate estimation of HR, pulse oximeter providing pulse rate is commonly used in clinical practice [4]. In this study we used pulse rate recordings from pulse oximeters to describe the normal reference range for heart rate, HR variations with clinically important variables, and the incidence of bradycardia with varying thresholds for healthy infants ≥ 37 weeks' gestation in the first few days after birth. We also wanted to determine the proportion of babies with HR data from our study cohort which fall outside the normative range as described in the literature.

6.2.3 Methods

Aims and general procedures: This study is part of a prospective, observational study conducted in three separate hospitals in the city of Calgary, Alberta, Canada, from March 2014 to September 2015. The main objective of the primary study was to report longitudinal trends in oxygen saturation which will be reported elsewhere. Here, we analyse, and present only pulse rate measurements reported here as HR measurements. We included all newborns from the postnatal ward with the following characteristics: ≥ 37 weeks' gestation at birth, age between 6 to 24 hours at enrolment, and normal cardio-respiratory examination*. Neonates with

---

*As defined by Acute Care Of At-Risk Newborn – `www.acornprogram.net`)[10].

Figure 6.3: Photo of an oximeter, the machine used to measure heart rate (HR), oxygen saturation (SpO2) and perfusion index (PI) in babies. The machine can be connected to the babies through a strap bracelet that can be applied to the wrist or to the foot. Sometimes wrist and foot can present different measurements because of the physiology of the baby (in particular the wrist is closer to the heart and the foot contains more fat). To leave the main investigator unbiased to this study, some displays have been covered.

an antenatal or postnatal diagnosis of congenital cardio-pulmonary disease, major congenital abnormality, those at risk of neonatal abstinence syndrome, or admission to a neonatal intensive care unit were excluded. We identified potential subjects from hospital electronic health records and enrolled within 24 hours of birth. Parental written informed consent was obtained prior to enrolment. This study was registered with clinicaltrials.gov (NCT 02095041) and local research ethics board approval was obtained. HR of all the enrolled infants were measured using a pulse oximeter (Masimo Radical-7, Irvine California, see Fig. 6.3) chosen because of its resistance to movement artefacts and good performance in states of low perfusion [11, 12]. The pulse oximeter was set to normal sensitivity with 2-second averaging times. HR data were recorded every 2 seconds by the oximeter. We obscured the pulse oximeter readings by fastening a custom-made opaque cover over the oximeter's display (see Fig. 6.3). The perfusion index and wave forms were left visible so the investigator could ensure that a good quality signal was present. The beat-to-beat tone function was turned off and all the alarms were silenced. In this manner, the investigators, staff and families were blinded to the HR readings.

One pulse oximeter probe was placed on the right wrist (pre-ductal) and the

other probe was placed on either foot (post-ductal) to take continuous measurements for ~ 10 minutes, starting from the point of good plethysmographic wave forms. This initial phase of recording occurred under the direct supervision of one of the investigators. Following the 10-minute period, we returned the infant to the mother with one pulse oximeter probe still attached to the right wrist for the completion of the 90-minute recording period. During this 80-minutes period, we recorded only preductal HR, to avoid the inconvenience for the mother of having two probes attached to the infant, and to carry out routine newborn care (e.g. feeding). Oximetry recordings were performed every $12 - 24$ hours prior to discharge during regular working hours, with the first recording occurring between 6 and 24 hours after birth to allow completion of normal transition to the extra-uterine environment [13]. A summary of the study flow is shown in Fig. 6.4. All the recruited infants were followed until 8 weeks of age by reviewing their electronic health record to identify those who died, required readmission to hospital or visited the emergency department. Those infants found to have a diagnosis that could interfere with the creation of healthy HR data were excluded from the primary outcome analysis.

Definitions: In this study one of the critical considerations is what we define as *bradycardia*. In particular we analysed different definitions. The classic definition is one with a fixed threshold, where each episode is defined as a period of ≥ 15 contiguous seconds during which HR values are below a specified threshold (e.g. 120, 100, 80/minute) [14]. We also explore a new definition of bradycardia that takes into account the fact that every baby has a different average HR. Specifically, *dynamic bradycardia* is defined, when the HR falls below $< 2/3$rd of the median HR for the infant [14] (for example, for an infant with a median HR of 120/min, we defined the dynamic bradycardia to be when the HR is < 80/min for 15 contiguous seconds).

Another definition that we will use in this work is the concept of Newborn Early
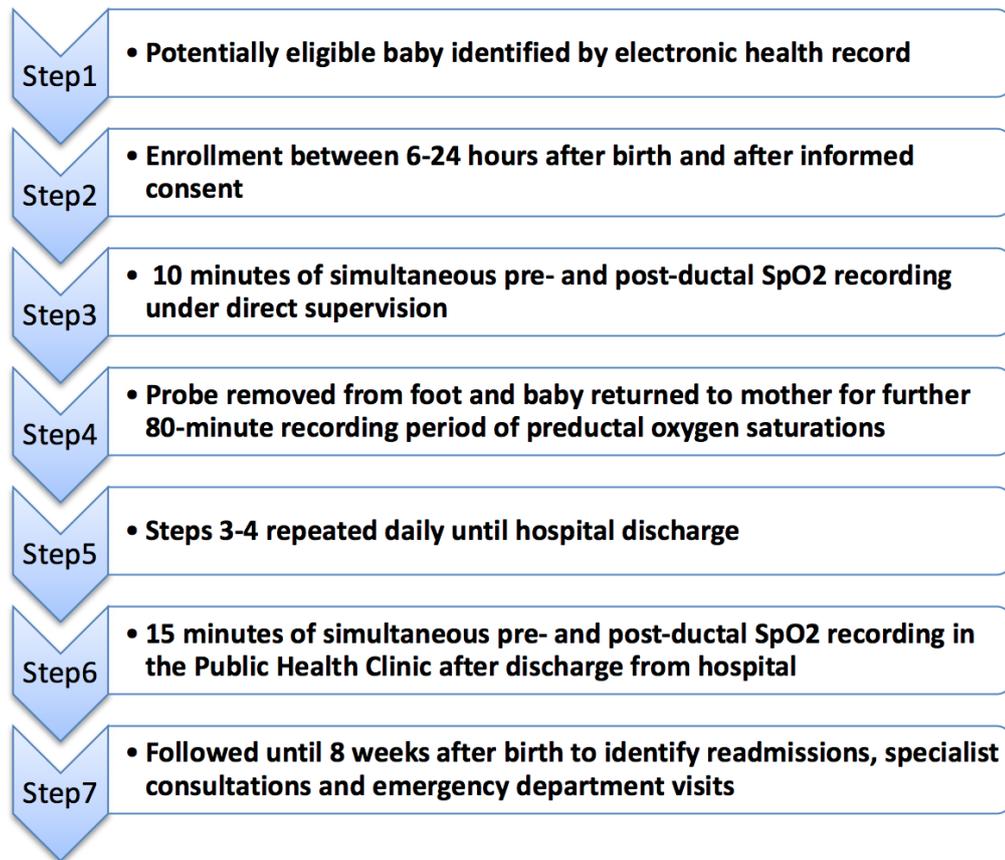
Figure 6.4: Summary of procedures followed in the selection of the babies used for this study. For the purpose of this analysis, the important things to note are that measurements of the babies starts always after at least 6 hours from birth and that in following days measurements are taken at the Public Health Clinic where the machinery used can differ from that in the hospital, with the potential to introduce a bias in the data. It is important to note as well that pre-ductal measurements (wrist) and post-ductal measurements (foot) have different times of recording.

Warning Trigger and Tracking (NEWTT). This is a table that classifies as normal babies those that have HR between 100 and 160 beats per minutes (bpm). HR above 160 or below 100/minute are instead traditionally classified as Amber category which warrants senior review within 30 minutes. In our attempt to redefine new standards for healthy babies, we plotted each HR measurement every 2 seconds and plotted against the NEWTT chart (Fig. 6.5 explained later in Sect. 6.2.4). We plotted median and various centiles for 10 bins between 6 hours and 50 hours of age. We also calculated median and inter-quartile range for the entire population.

Data management: The process of data collection, cleaning and processing is a crucial part of this study. As well as variations in the application of standard data handling procedures, human mistakes and different approaches used by different doctors need to be taken into account to properly interpret the data. Regarding the collection of the data from the hospital, oximeter data is downloaded using "Trendcom" software. Non-identifying study data were collected and managed using Research Electronic Data Capture (REDCap), a secure online research database [15]. Manual and automated SpO2 data cleaning was performed to remove data of questionable validity. Pulse rate < 10/min were removed as well as any data points with 'zero' values.

Regarding the analysis of the data, we aimed at recruiting a convenient sample of ~ 300 infants. We used descriptive statistics for population characteristics. Categorical variables were presented as proportions, while numerical variables were presented as mean with standard deviation (SD) or median with inter-quartile range (IQR) as appropriate. All the analysis was performed using Python 3.6.9. In particular, we choose to exploit the advantage of an Object-Oriented Programming language (OOP) and create the class "baby" in order to collect the properties and the measurements of each baby in a single object. The software created (available on request) was specifically designed for the features of this sample and is able to create simple plots of the heart rate of the baby simply by inputting the anonymised id for each baby. In particular, the software includes an algorithm to identify, count and measure the duration of events of bradycardia (low HR according our definition) and hypoxia (low SpO2 according to a similar definition as used for bradycardia, but not used in this study). We used non-parametric tests and applied a significance level, $\alpha = 0.05$, for all statistical testing.

6.2.4 Results

Demographics: Out of a total of 294 babies recruited, after excluding babies with invalid data, we had 268 (91%) babies in the final analysis. 37 (14%) infants had a second recording and 3 (1.1%) had a third recording before hospital discharge. Due to the hospital's early discharge policy, we had a smaller number of newborns on days 2 and 3. Demographic data are provided in Table 6.1. Most babies received routine care and 3% received some form of minor resuscitation at the time of birth. There are a total of $1,016,801$ data points (equivalent to 564.89 hours $= 23.54$ days) and after cleaning we had $992,678$ (97.62%) valid data points. For the wrist recordings, the number of infants with 1, 2 or 3 recordings were 151, 105 and 5 respectively. For the foot recordings, the number of infants with 1, 2 or 3 recordings were 152, 109 and 6 respectively. Of the recruited infants, 45 (17%) required acute medical care during the 8-week follow-up period and 11 (4%) infants were subsequently admitted to hospital. Based on the investigator's discretion, we excluded 4 infants' data from the original study.

Heart rate percentiles (first vs following days): Table 6.2 shows that in the first 24 hours, median wrist HR was 121.9 (IQR 115, 129) which was similar to median foot HR of 121.5 (IQR 114, 130; $p = 0.29$). Similarly, median wrist HR was 124.9 (IQR 117, 136) and median foot HR was 131.4 (IQR 117, 139: $p = 0.17$) for infants age $24 - 72$ hours.

Heart rate variations for different medical variables: HR variations with gestational age, sex, type of delivery and time of life are provided in Table 6.3. Babies with birth gestational age > 40-weeks had significantly lower HR: this trend is seen for both wrist and foot. The HR in females is higher than in male infants, with a mean difference of ~ 4 beats/min. Similarly, HR tends to be higher for babies who are more than 24 hours old, though the sample size is smaller in this

Demographics		
		Full Cohort (n= 268)
Female sex – n (%)		123 (45.9%)
Birth weight – mean (SD*)		3348 (503) grams
Gestational age – mean (SD)		39.55 (1.15) weeks
Ethnicity	Caucasian	161 (60.07 %)
	African American	12 (4.48 %)
	East Indian	31 (11.57 %)
	Asian	27 (10.07 %)
	Hispanic	15 (5.6 %)
	Other	17 (6.34 %)
	Unknown	2 (0.75 %)
	Native	3 (1.12 %)
Maternal age – Mean (SD)		31.87 (4.54)
Caesarean delivery – n (%)		76 (28.4 %)
Maternal pre-eclampsia – n (%)		12 (4.48 %)
Maternal gestational diabetes – n (%)		26 (9.70 %)
Smoking – n (%)		12 (4.48 %)
Meconium-stained liquor – n (%)		36 (13.43 %)
Apgar 5min - mean (SD)		8.96 (0.33)
Age in hours at first recording – median (IQR#)		16.48 (11.3 to 20.6)
*SD: Standard deviation; #IQR: inter-quartile range		

Table 6.1: Demographic data for the sample of 268 babies used in this study. The number of babies and the percentage respective to the full sample are reported for different categories, along with some average values for some medical variables.

cohort. There was no difference in HR for infants born by cesarean and vaginal delivery.

Trends in Bradycardia: In total there were 475 episodes of HR < 120/min bradycardia, 183 episodes of HR< 100/min, 91 episodes of HR< 80/min and 89 episodes with HR< 2/3rd median HR: all of these episodes lasted for at least 15 seconds (Table 6.4). Durations of bradycardia were similar for all the thresholds. Transient bradycardia (< 15 seconds) is more common than bradycardia of at least 15 seconds duration. In general, bradycardia events (lasting for at least 15 seconds) in healthy term infants were rare with a frequency of $\sim$ 1 episode every 2 hours and lasted for approximately 30 seconds.

Percentiles of heart rate (HR)		
	Wrist	Foot
Age<24hrs	**N=233**	**N=245**
5th centile	106.0	104.3
25th centile	115.2	113.7
50th centile	121.9	121.5
75th centile	128.9	129.4
90th centile	135.4	137.1
95th centile	142.2	143.0
Age 24hrs-72hrs	**N=42**	**N=43**
5th centile	111.8	109.7
25th centile	117.3	117.3
50th centile	124.9	131.4
75th centile	135.9	139.0
90th centile	140.0	145.6
95th centile	142.3	152.0

Table 6.2: Percentiles of heart rate for babies in the first 24 hours of life and babies in their $24 - 72$ hours since the birth. In bold face are reported the number of babies in the respective category.

Pulse rate variations with gestational age, Type of delivery, Sex and time						
	Mean	SD*	Mean	SD	Mean diff (95% CI$)	Statistics
Gestation	**<40 weeks**		**>=40 weeks**			p-value
Wrist	124.87 (n=139, 52%)	10.65	120.66 (n=113, 42%)	10.44	4.21 [2.96,5.46]	0.00077
Foot	124.65 (n=146, 54%)	13.02	121.32 (n=117, 44%)	11.95	3.33 [1.89,4.77]	0.0163
Type of delivery	**Vaginal**		**Caesarean**			
Wrist	122.56 (n=179, 67%)	10.73	124.03 (n=73, 27%)	10.78	1.47 [0.15,2.80]	0.2360
Foot	122.25 (n=187, 70%)	12.07	125.10 (n=76, 28%)	13.57	2.86 [1.28,4.43]	0.0622
Sex	**Male**		**Female**			
Wrist	121.05 (n=135, 50%)	9.77	125.43 (n=117, 44%)	11.37	4.38 [3.13,5.64]	0.00218
Foot	121.60 (n=141, 53%)	10.48	125.16 (n=122, 46%)	14.63	3.56 [2.08,5.04]	0.0643
Timing	**<24hrs**		**24-72hrs**			
Wrist	122.38 (n=233, 87%)	10.52	126.58 (n=42, 16%)	11.31	4.20 [2.43, 5.97]	0.01732
Foot	122.06 (n=245, 91%)	11.87	129.45 (n=43, 16%)	14.94	7.39 [5.13,9.65]	0.0004077
*SD: Standard deviation; $CI: Confidence Interval						

Table 6.3: Pulse rate variations with gestational age, type of delivery, sex and time. Measurements are analysed separately for wrist and foot. To check for statistical differences between the two sample in which babies have been split, we perform the student T-test and we consider a difference to be significant when the p-value is below 0.05.

Trends in bradycardia								
	Number of bradycardia episodes per Hour[1] mean (SD*)		Duration of bradycardia episodes[2] median (IQR#)		Percentage of Time with bradycardia[3] mean (SD)		Number Bradycardia per hour any duration[4] mean (SD)	
	Wrist	**Foot**	**Wrist**	**Foot**	**Wrist**	**Foot**	**Wrist**	**Foot**
HR <2/3 of median	0.388 (1.167)	0.389 (1.510)	34 [24,66]	34 [22,57]	0.0089 (0.0322)	0.0072 (0.0324)	0.689 (1.606)	0.977 (3.107)
HR <120	16.025 (10.758)	17.387 (16.129)	36 [27,54]	41 [26,95]	0.421 (0.299)	0.432 (0.357)	35.117 (21.423)	38.022 (31.368)
HR<100	2.238 (5.279)	2.489 (6.874)	27 [20,39]	27 [20,49]	0.0463 (0.108)	0.0466 (0.121)	6.986 (12.594)	8.600 (17.651)
HR <80	0.418 (1.309)	0.436 (1.560)	36 [24,62]	29 [20,59]	0.00943 (0.0341)	0.00756 (0.0338)	0.785 (1.810)	1.0173 (3.173)

1: A bradycardia episode is defined as a period of ≥ 15 contiguous seconds during which heart rate values are below the specified threshold (e.g., 120,100, 80).

2: Duration of bradycardias includes only infants with at least one bradycardia episode lasting ≥ 15 seconds and refers to the median duration of each bradycardia episode.

3: Percentage of time with bradycardias denotes the ratio of total time with bradycardias of any duration (i.e., not just for episodes lasting 15 seconds).

4: Bradycardias per hour refers to the number of bradycardia episodes of any duration per hour.

*SD: Standard deviation; #IQR: Inter-quartile range

Table 6.4: Statistiscs for the bradycardia events measured through different definition. Different definitions involve different thresholds, 120, 100, 80, and a "dynamic" threshold based on the median HR values of the specific baby. Measurements are reported separately for wrist and foot recordings.

Studying heart rates outside normative range: Fig. 6.5 shows heart rate plotted against the age of the infants (in hours). The normative HR range prescribed in the Newborn Early Warning Trigger and Tracking (NEWTT) chart (HR $100 - 160$/min) is also shown. The majority of the data points fall between a HR of 100 and 160/minute with their median (25th-75th centile) HR for the entire population within the normative range. Similar findings were noted when the median along with IQR were plotted for individual bins for infants' age after birth. Creating 1st-99th centiles with data points for the same bins shows multiple HR data points were plotted outside the normative range. We had $43,787$ (6%) HR data points ≤ 100/min and $13,812$ (2%) HR data points ≥ 160/min.

Impact of heart rate measurements with shorter recording time: We identified infants with median HRs of < 100/min and > 160/min. We then examined infants in these groups with a significant difference in the median HR between the wrist and foot measurements. 6 infants with HR < 100/min and 3 infants with HR> 160/min had different median HR between the foot (see an example in Fig. 6.6) and wrist (see an example in Fig. 6.7) measurements. Since we recorded foot measurements only for a short period (~ 10 minutes), we compared the foot measurements with wrist measurements over a similar duration (i.e., the first ~ 10 minutes of wrist measurement). This comparison showed similar median HR between the two measurements indicating the impact of the shorter period of recording and the variations in HR (see Fig. 6.8). Whether this is due to any underlying physiological variations or technical limitations is unknown. However, this results suggests that before inferring differences in the pre-ductal (wrist) and post-ductal (foot) measurements, a fair comparison with similar time of measurements is needed.

6.2.5 Discussion and conclusions

Our study provides a better understanding of normative values of HR and its variability with various factors in the first few days of life. We have shown that
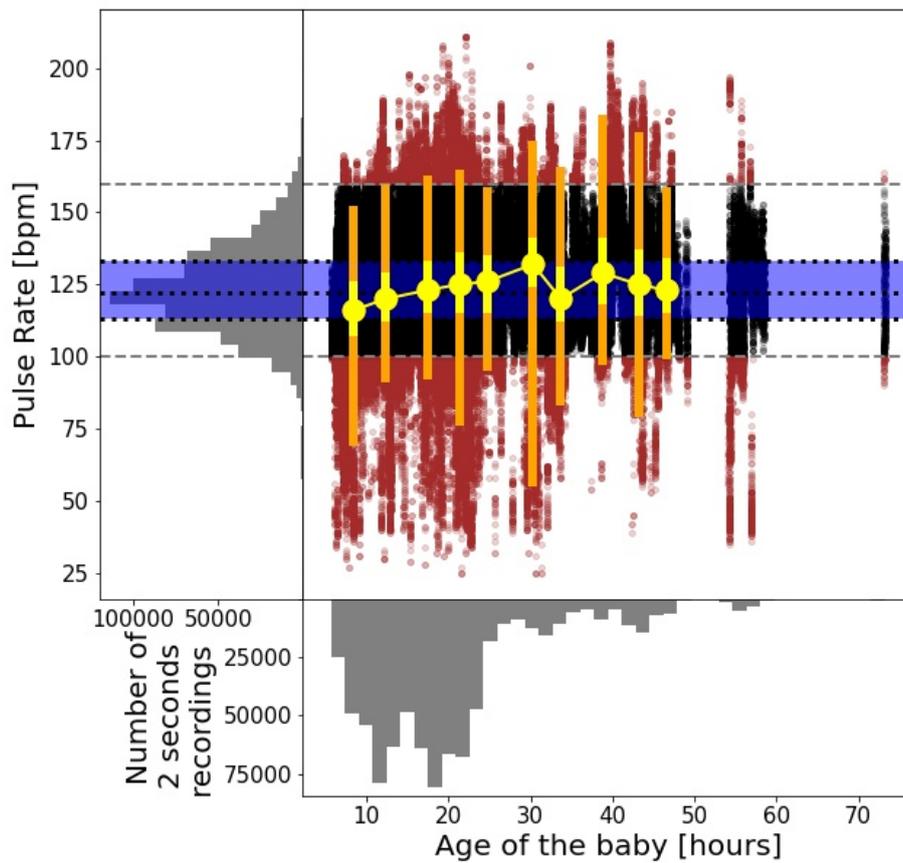
Figure 6.5: Heart rate versus age of the infant in hours plotted against the normal range (HR 100-160/min). The black circles show HR measurements (at 2 second intervals) that fall within the traditional normative range of 100-160 beats per minute; brown circles show HR recordings outside this range. The symbols and bars show the median, 25-75 (yellow) and 1-99 (orange) percentile ranges, for measurements in each bin. Histograms on the side show the distribution of the number of 2-seconds recordings for the baby's age (x-axis) and Pulse rate (y-axis). The horizontal dotted line shows the global median, and the blue shading indicates the global 25-75 percentile range.
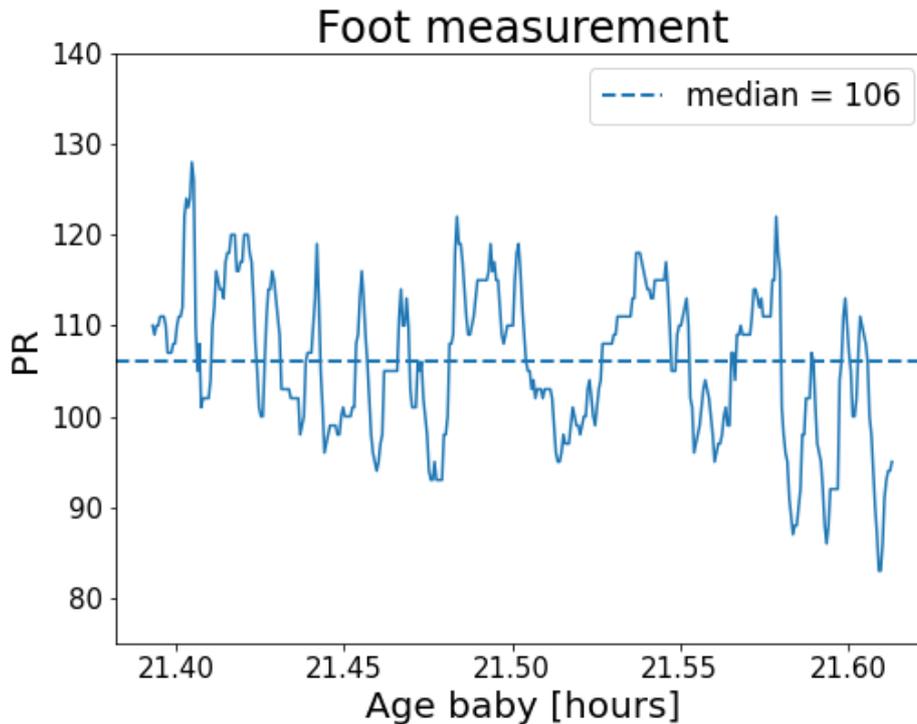
Figure 6.6: Example recording of the pulse rate (PR) from the foot of the baby identified as FMC133. The total time of recording corresponds to 13 minutes. This is typical of any foot recording.

bradycardia events of HR < 80/min or HR< 2/3 of the baseline are rare and short lasting in the first few days of life. Any infant with bradycardia episodes is worth monitoring. We argue that a dynamic definition of the HR threshold for bradycardia, based on the median HR of an individual, is more accurate than the currently used global definition, given the large variation we find in the median HR in healthy infants. We have shown that spot check HR measurements could lead to false labelling as we have shown in Fig. 6.5. Trends in HR over a short period of time would provide the true estimate of HR rather than a spot check. We noted minor variations between foot and wrist measurements which does not reflect actual physiology but instead may result from technical limitations of pulse oximetry related to the quality of the pulse waveform encountered in the upper versus lower limbs.

In a recently published study with a large number of infants, reference ranges
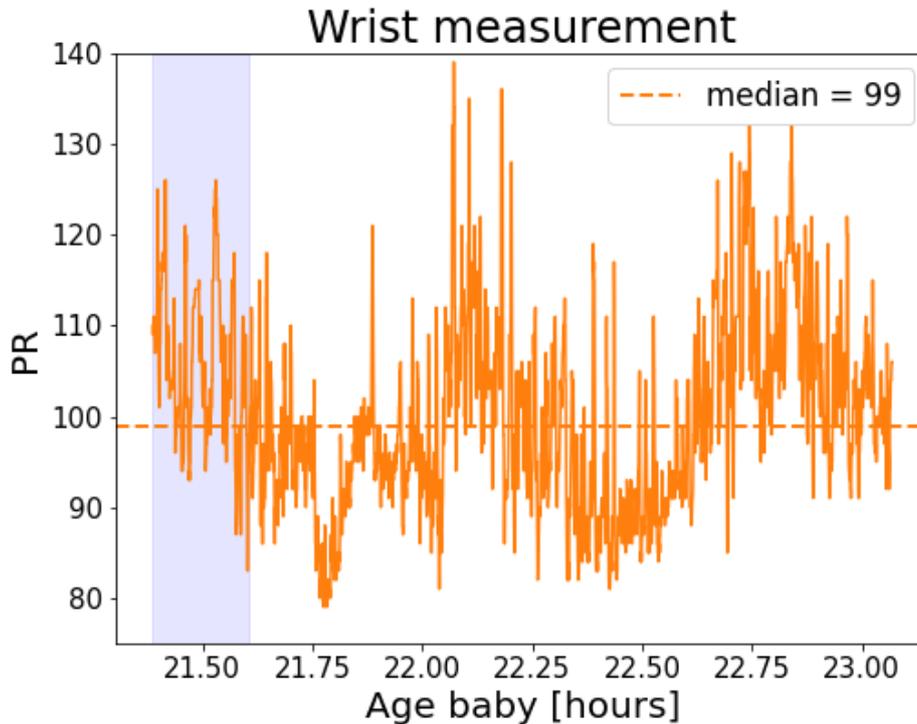
Figure 6.7: Example recording of the pulse rate (PR) from the wrist for the same baby as in Fig. 6.6 (FMC133). The total time of recording corresponds to approximately 100 minutes. Recording from the wrist are typically longer than foot recording. The shaded area covers 13 minutes which is the time typically used for foot recordings.

for HR were obtained by auscultation in the first 24 hours of life [7]. Auscultation findings of HR were validated against ECG recordings. In this study, the median HR reported and the higher values of HR found in girls as compared to boys were similar to our study results. In another large systematic review with 69 studies, reporting normal range of HR from birth until 18 years of age, the median HR at birth was 127/min which is similar to our results [1]. In this review, settings in which measurements were made and methods to collect HR data were variable.

A pulse oximeter can provide reliable results equivalent to ECG when there is a good signal and no rhythm disturbances [3]. A systematic review comparing the performance of ECG and pulse oximeter concluded both devices provided precise results as compared to clinical assessments alone [4]. A pulse oximeter can under-
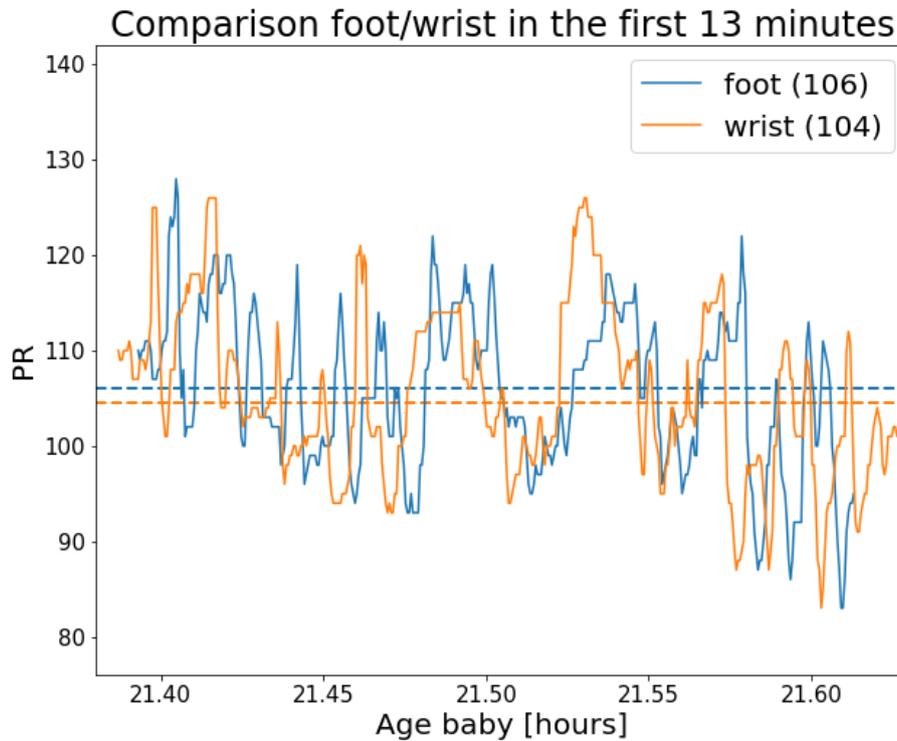
Figure 6.8: Recordings of foot and wrist for the same baby (FMC133) overlapped in time for the first 13 minutes, which is the usual time of recording for foot measurements. As can be seen when limited to the same amount of time the values of the pulse rates are similar. This has to be taken into consideration when comparing wrist and foot results. In fact the median of the entire recording of the wrist (99 bpm) differs from the median of the entire recording of the foot (106 bpm) but when compared in the same simultaneous amount of time, they are similar: 106 and 104 respectively.

estimate the HR compared with an ECG in the first few minutes of life. In this review all the studies included were conducted at the time of birth in resuscitation settings. Though the differences between ECG and pulse oximeter are systematic to the technology which may affect the precise HR values and should not affect our study conclusions.

Our study has a few advantages. We collected all data prospectively with relatively long periods of recording. We collected data both from wrist and foot recordings using similar monitors. We classified infants in our study as "healthy" after a follow up period of 8 weeks of life. We followed a detailed process of data

cleaning. We also defined clinically significant bradycardias as HR< 80/min and HR< 2/3rd median. There are a few limitations we should mention. We did not use ECG monitors, which are the gold standard for HR measurements. Though we collected data on neonatal state, we did not analyse the influence of the neonatal state on HR. In routine clinical practice we don't assess neonatal state, hence our data could be more clinically relevant; this is left to a future study with this dataset.

Though our study was conducted at moderately high altitude ($1,045$ m), variations of HR with altitude have not been previously reported. Hence, we believe this normative HR data and their variations would be applicable to all clinical settings.

To conclude, in this large prospective data from healthy term infants, we have provided normative values of heart rate and its variation with gestational age, sex, mode of delivery and age of life. In this population, bradycardia events were rare with an approximate frequency of 1 episode every 2 hours and are short lasting. Significant HR data points were outside the previously described normative range.

Conclusion and Outlook

7.1 Astronomy

The work presented in this thesis extends the tests of theoretical models of galaxy formation using new observations of galaxy colours. With this aim I made use of different galaxy redshift surveys to devise new tests of the models using colour versus redshift and the colour-magnitude relation at different redshifts. Specifically, the main source of observational data for this work is the Physics of Accelerating Universe Survey (PAUS), a novel photometric galaxy survey using narrow band filters, which spans a wide range of redshifts ($0 \lesssim z \lesssim 1.2$) over a relatively wide solid angle, aiming to reach $\sim 100\,\mathrm{deg}^2$ with redshift uncertainties smaller than $\sigma_z < 0.0035$ for at least 50% of the sample down to a magnitude limit of $i_{\mathrm{AB}} \lesssim 22.5$. To complement observations with a physically motivated model of galaxy formation, I have used `GALFORM` (Cole et al., 2000) implemented in a N-body simulation, the P-Millennium run described in Baugh et al. (2019). Thanks to the improved N-body simulation (Baugh et al., 2019) with an order of magnitude better mass resolution and four times more redshift outputs compared with previous simulations used with `GALFORM` (e.g. Guo et al. 2011), the predictive power of the model now reaches far beyond that of previous simulations. We adapted the `GALFORM` code to create a lightcone mock galaxy catalogue for PAUS. The high number of PAUS narrow-band filters combined with the higher mass resolution of the P-Millennium

N-body simulation made the resulting run computationally expensive. We moved from a regime in which the run outputs where of the order of 1 TB, e.g. for the calculation described by Stothert et al. (2018b), to a regime in which the output takes up approximately 30 TB. We carefully optimised the scheduling of the jobs in order to only use the resources needed, and to avoid jobs from restricting one another's progress. In particular we found a relation between the amount of memory required to process one of the subvolumes the simulation is divided up into and the mass of the biggest dark matter halo at redshift zero in the subvolume. We further optimised the run by using Message Passage Interface (MPI). Thanks to our optimisation exercise, we reduced the time scale of the simulation from several months to less than 20 days.

The creation of a mock lightcone for PAUS has several benefits, compared to using a single redshift output from the simulation. The first is the ability to evaluate the performance of photometric redshift estimators, using a mock with similar numbers of galaxies as a function of redshift to the real observations. This is because we are simulating the 'true' values for the redshifts and narrow-band fluxes which are the inputs to photometric redshift estimation codes. Previous work with this aim was performed by Stothert et al. (2018b). These authors built a mock using the GALFORM semi-analytic model of galaxy formation based on the Millennium N-body simulation Guo et al. (2011). The photometric redshift estimation code was tested on this mock to understand any systematics in the estimation. However, this exercise uncovered a potential systematic in the construction of the mock catalogue, rather than in the photo-z code. This relates to the time spacing between snapshots and the manner in which the photometry is adjusted or interpolated to try to account for the bandshifting with redshift. Using the new p-millenniunm N-body simulation, we tested the presence of the systematic introduced by the interpolation of magnitudes between output times. We observed that this systematic is not visible anymore and this means that if it is still present, at least it is smaller than the statistical error in the photometric redshift, for the redshift range studied. We

proved that up to redshift $z \sim 2$ there is not anymore such effect.

Another advantage of the creation of a lightcone mock for PAUS is to test the predictions of galaxy formation models for model galaxies which meet the observational selection. The lightcone mock produces approximately the same number of galaxies as a function of magnitude and redshift as are measured in the observations. We tested the model predictions for the evolution of observer frame colours over the redshift range probed by PAUS. Galaxy formation models are traditionally calibrated mainly at redshift zero. In the case of `GALFORM` it has been calibrated to match the local observed optical and infrared luminosity functions (see for example Lacey et al. 2016). This means that if the prediction of the colours holds at higher redshifts, the physics that control this evolution is correct. This study on colours is reported in Chapter 4.

The study of colours, magnitudes and the evolution predicted by stellar population synthesis models, along with the predictions provided by the physically motivated `GALFORM` model based, was the focus of the study reported in Chapter 5 (also published as Manzoni et al. 2021). The main focus here was the use of the evolution of the colour magnitude relation to constrain simple parametrisations of the star formation history of galaxies, deriving information about the average quenching time-scale in the $\sim 90,000$ galaxies of the VIMOS Public Extragalactic Redshift Survey (VIPERS). I developed some further analysis, comparing variants of `GALFORM` with different AGN-feedback to study the impact on the colour magnitude relation.

Thanks to the expertise I developed in running the GALFORM semi-analytics model, it is possible to create new mocks with different characteristics in an efficient and relatively fast way. For this reason, one of the future developments of this work is the creation of new mocks for upcoming surveys. The MOONRISE survey (Maiolino et al., 2020) based on the Multi-object Optical and Near-infrared Spectrograph (MOONS) at the Very Large Telescopes (VLT), is a perfect candidate for our study as it offers an unprecedented sampling of high-quality spectra at

intermediate redshifts ($z \sim 1-2.5$). This allows for a robust testing of galaxy formation models and galaxy evolution studies. In particular, having a MOONS mock has the potential of understanding how galaxies move within the BPT diagram and how we can better separate Active Galactic Nuclei (AGN) from star-forming galaxies.

Other future works regard the improvement of the model predictions creating more realistic scenarios for some of the physics involved. For example, the model currently predict a stronger bimodality in galaxy colours than what observed in surveys. A change in the AGN feedback modelling can have an effect on that. The current implementation of AGN feedback has the effect of stopping completely the gas cooling when it is active. A more gradual implementation of gas cooling has the potential of smoothing the dramatic bimodality observed (see Croton et al. 2006 for a gradual implementation of AGN feedback). The current implementation also allow for an AGN to be activated and deactivated multiple times while a scenario in which once the AGN is triggered it will stay permanently active can be explored. Another effect that can be investigated is the compression of gas due to AGN activity. In the current implementation AGN only prevent the gas cooling, however the compression of gas could potentially favour star formation rather then suppressing it. One last improvement that can be considered in `GALFORM` is the treatment of gas cooling in satellite galaxies. Currently, the ram pressure stripping suppress the star formation in a galaxy that becomes satellite instantaneously, removing all of its gas. A more complex modelling can be implemented as a future work where the removal of the gas due to ram pressure stripping can happen gradually as a function of the orbit radius of the satellites with respect to the centre of the dark matter halo.

In conclusion, thanks to the powerful optimisation of `GALFORM` combined with the high resolution of the new p-Millennium N-body simulation, the testing of different physical scenarios for increasingly larger and deeper surveys through the creation of new mocks will allow for a better understanding of the evolution of the

early Universe.

7.2 Centre for Doctoral Training internships

To expand my expertise in analysing large data-sets, as part of my Centre for Doctoral Training (CDT) placements I completed a two month project at Procter & Gamble (P&G) and another eight months internship with the National Health Service (NHS). At P&G, I contributed to building new statistical tools to model the density of laundry powder. In the process of producing laundry powder, lots of ingredients are used to reach the perfect density. However, the way the amount of ingredients are chosen was completely empirical without any mathematical model that supports the choice of the amount of ingredients. To help identifying the ingredients that actually contribute to obtain the optimal density, we developed a modified version of the Least Absolute Shrinkage and Selection Operator (LASSO, Tibshirani 1996) technique. This technique adds a penalty to the χ^2 function used to constrain model parameters, so that complicated functions, prone to overfitting with a lot of terms are disadvantaged with respect to functions with fewer terms. We modify the penalty in order to adapt to the specific problem. This promising technique, has been developed further and used in astronomy as well (Icaza-Lizaola et al., 2021).

In the NHS internship, the focus was on the study of the health rate (HR) variation in a sample of ~ 300 healthy babies. To assess newborns, doctors go through a set of visual checks and vital signs observations in order to ascertain that the baby is safe and healthy. Heart rate is one of the quantities that is always monitored. Too low a HR (bradycardia) is as dangerous, as is too high a HR (tachycardia). Deciding what is too low HR and what is too high is not trivial. In particular, an instant measure of HR does not have the same importance as an average value of HR. If HR goes low for a very short period (less than ~ 15 seconds) is not as dangerous as if it stays low for a more prolonged period. As a consequence,

the time of recording is very important when we are studying variations in HR. We establish new standards for healthy babies heart rates in the first few days of life. We measured episodes of bradycardia, analysing different thresholds, and finding that strong events of bradycardia (those in which the HR goes lower then 80 bpm or lower than 2/3rd of the median HR) are quite rare ($\sim$ 1 every 2 hours) in healthy babies. We also argue that pre-ductal (measurements from the wrist) and post-ductal (measurements from the foot) HR readings do not show any statistical difference as they might be biased by a different time of recording ($\sim$ 10 minutes for the foot versus $\sim$ 90 minutes for the wrist). We find statistical differences in the average HR for different classes of babies: babies with a gestational age greater than 40 weeks (i.e. full term) seem to have lower HR. Boys seems to have lower HR than girls. Babies in their first day of life seem to have lower HR than babies who are more than 24 hours old.

These trends are essential to help doctors to identify unhealthy babies and hence decide when they need a given treatment. This study has already been submitted for publication in a medical journal. A possible development of this study is to apply the same technique to pre-term babies when the decision of the doctor is even more important as the treatments needed might be very invasive and a wrong decision can lead to death.

Appendix to Chapter 5

A.1 SFR from SED and [OII] emission

Here we perform a "sanity check" to test if the SFR deduced from the SED fitting to the $U - V$ colour tracks the SFR inferred independently from an emission line. This test has the limitation of testing the instantaneous SFR and does not probe
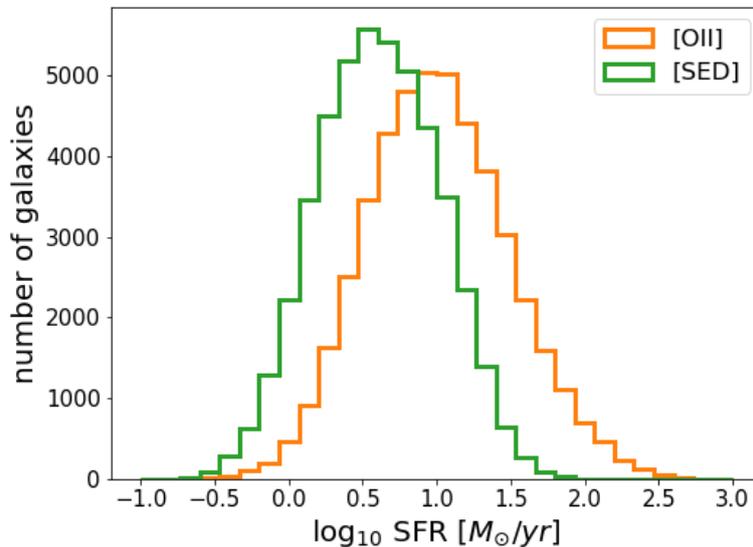
Figure A.1: Distribution of the SFR estimates from the SED fitting (green line) compared to those derived from the [OII]λ3727 line (orange line) according to the Moustakas et al. (2006) prescription, as in Eq. A.1. In this sample we have excluded galaxies with signal-to-noise lower than 1.1.
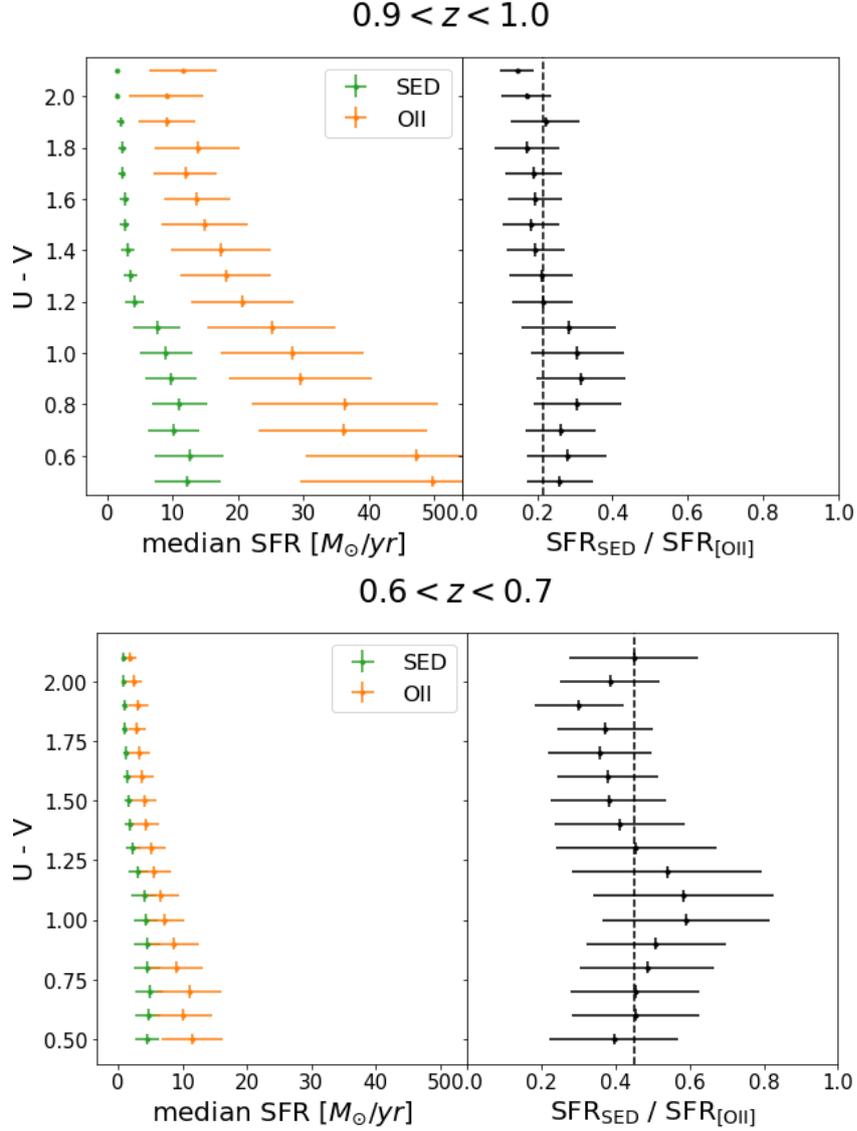
Figure A.2: The distribution of SFR as a function of rest-frame colour for galaxies in the redshift ranges $0.9 < z < 1.0$ (top panels) and $0.6 < z < 0.7$ (bottom panels), as estimated from the OII line luminsity and inferred from SED fitting, as labelled. On the right hand side, the ratio between the two estimates of SFR is plotted on the x-axis for bins of colour plotted on the y-axis. The points show the median values and error-bars are obtained from the median absolute deviation (MAD) of the relative distribution.

the full SFH of galaxies. However, the importance of this test is the fact that we are estimating the same quantity from completely independent properties, i.e. the SED fitting is based on the spectrum sampled using broad filters which is completely independent from the intensity of an emission line.

We first compare the SFR inferred for the star-forming galaxies in the observed sample, estimated using the [OII]$\lambda 3727$ emission line luminosity, with that estimated from the properties of the best-fitting SED template. The prescription to obtain SFR estimates from the [OII] luminosity comes from Moustakas et al. (2006). Specifically, from Table 2 of Moustakas et al. (2006) we made a linear fit to the coefficients M_B and P_{50} (neglecting the two faintest magnitudes which are outliers), resulting in the following relation between [OII] luminosity and SFR:

$$\log_{10}\left(\frac{\text{SFR}}{M_\odot/\text{yr}}\right) = -2.893 - 0.169 \times M_B + \log_{10}\left(\frac{L[OII]}{10^{41}\,\text{erg/s}}\right) \tag{A.1}$$

where M_B is the rest-frame absolute magnitude in the *B*-band and $L[OII]$ is the luminosity of the OII line.

In Fig. A.1, we show the distribution of SFRs derived from the [OII] line luminosity (orange line) compared to the distribution of SFRs derived from the SED fitting (green line). There are several physical reasons why we do not expect these estimates to be exactly the same. One is dust extinction. The [OII] line may suffer from additional dust extinction compared to that experienced by the stellar continuum that is modelled in the SED fitting. Another reason may come from the different star formation time-scales sampled in the two approaches. Kennicutt (1998) suggests that the [OII] emission line samples star formation time-scales $\lesssim 20$ Myr, while in our SED fitting, star formation is sampled for interval times of the order of $100 - 200$ Myr. For this reason, the [OII] line is more likely to sample galaxies which are experiencing a starburst rather than being consistent with a smooth SFH as is the case with the templates used in the SED fitting.

A more accurate test is to check if the SFR inferred from the SED fitting dis-

plays the same qualitative behaviour as the SFR estimated from the [OII] emission line. With this aim, we split the sample by $U - V$ colour and redshift. In Fig. A.2, the median SFR is plotted for the same colour bins used in defining the bright edge of the colour – magnitude relation. The top and bottom panels in the figure show the same analysis in two redshift bins. The right-hand-side panels show the median ratio between the two estimates. The error bars indicate the Median Absolute Deviation (MAD) dispersion around the median values. We use the MAD to estimate the dispersion in the SFR values and ratios distribution because of its robustness against the presence of outliers in the distribution and insensitivity to the particular choice of parameters. What ensures the quality of the SFR estimates from the SED fitting is the fact that, although different from the [OII] SFR estimates, they follow the same trend both in colour (different points of the y-axis) and redshift (top and bottom panels). This can be seen from the fact that the distribution of the ratios is constant within the errors (right-hand-side panels). The value of the mean ratio changes somewhat between the two redshifts considered and this could be due, for example, to an underlying change in metallicity of the gas involved in the star formation. However, this does not affect our results as what is important is that within every redshift bin the distribution of the ratios is constant within the errors as can be seen from the right-hand panels. In particular the relation between redshift and SFR shown in Fig. A.2 assures us that the overall decrease in star formation rate density as a function of cosmic time that took place over the redshift interval $0 < z < 2$ is well reproduced.

Considering that our sample includes galaxies spanning more than two decades in stellar mass and two decades in star formation activity strength (with a strong dependence on redshift), we argue that our stellar population synthesis effort provides consistent estimates of the "visible" SFR within the VIPERS sample (i.e. the star formation measurable using optical emission lines or broadband colours).

Although this test does not provide evidence about the future evolution of the SFR, the consistency in reproducing qualitatively the SFR-colour and SFR-redshift

fundamental relations give us an indication that the SED fitting is based on stellar population synthesis templates which provides a realistic starting point in our evolutionary exercise.

A.2 Robustness of the bright edge to the number of galaxies

One potential worry is that the location of the bright edge as defined in Sect. 5.4.1 is affected by one of the survey properties, such as the number density of galaxies in the colour – magnitude diagram. In Section 5.6 we have used a sub-sampled version of the original GP14 GALFORM output in order to match the number of VIPERS galaxies in every redshift bin. We now want to compare this sub-sampled set of model galaxies to the original sample to see if this affects the location of the bright edge. In Fig. A.3 we plot the colour – magnitude relation and the associated bright-edge for 4 representative snapshots. In the top panel, we show the sub-sampled version, which is the one presented in the middle panel of Fig. 5.9. In the bottom panel instead we use all the data available from the GP14 simulation. Albeit with less scatter, the location of the bright edge is consistent to the one in the top panel within the errors. As in Fig. 5.5 we also draw the location of the most populated magnitude bin, to show that is not coincident with the faint magnitude cut, hence the survey depth does not affect the location of the bright edge.

We have done an additional check to prove that the change in cosmic volume sampled by VIPERS at different redshifts is not the factor responsible for the progressive disappearance of the rare bright galaxies from the sample, and hence to prove that the bright edge evolution is not a volume sampling effect. The volume sampled in the highest redshift bin is in fact approximately ten times bigger than the lowest redshift bin.

To test for this possibility we have focused on the sample in the highest redshift
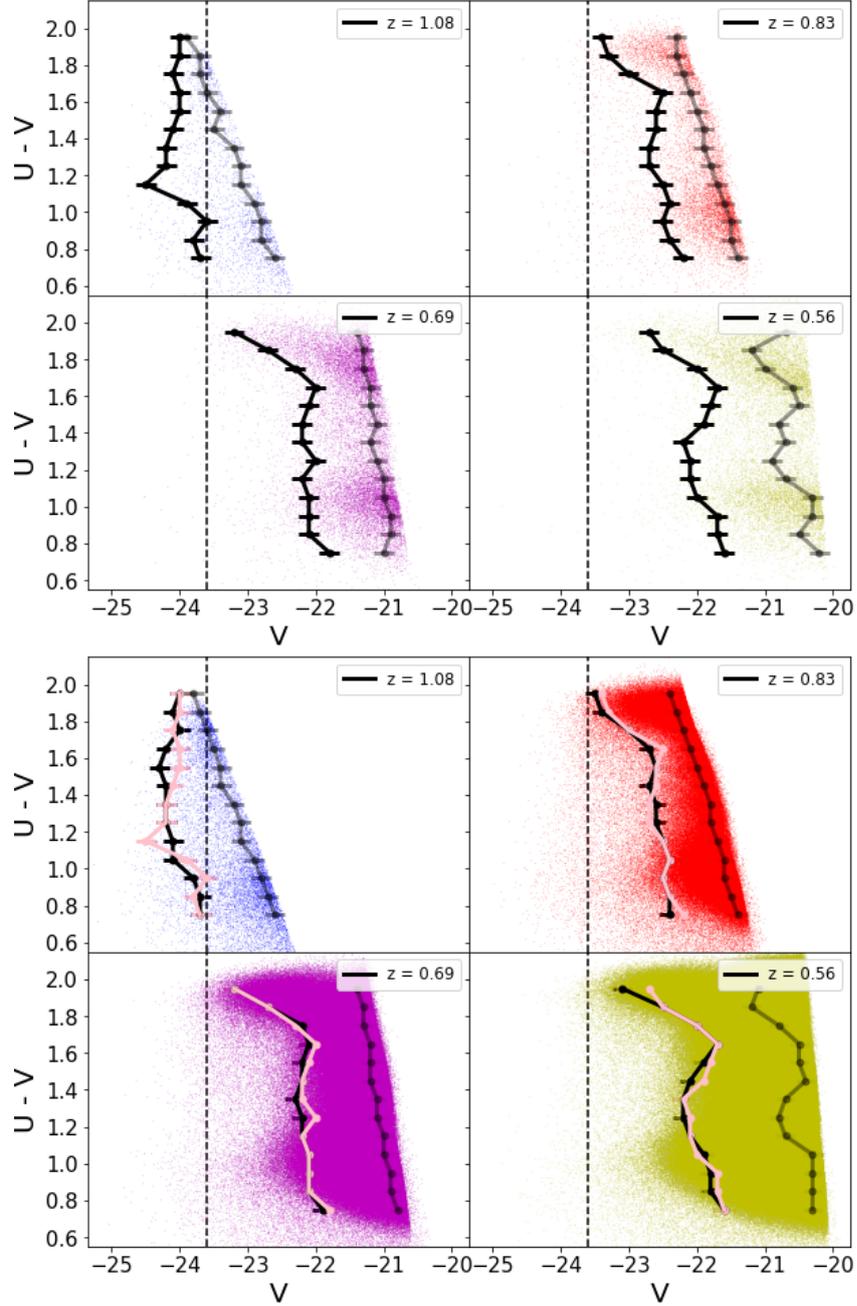
Figure A.3: Colour-magnitude relation for GP14 GALFORM semi-analytic model. The top panel is the randomly sampled version of the bottom panel in order to have the same number of points as in the corresponding VIPERS redshift bins. It can be seen that the definition of the bright edge is consistent in the two cases. For simplicity only four snapshots have been plotted. As in Fig. 5.5, the grey line represents the most magnitude populated bin for every colour bin. In the bottom panel, the edge relative to the sub-sampled sample has been reported for comparison with pink lines.

bin, and computed how many of the galaxies in this sample would still be observed at a lower redshift, under the assumption of no evolution in the galaxy properties but just taking into account the ratio of the volumes sampled in the two different redshift bins. The result of this computation shows that the high redshift edge would still be visible down to $z \simeq 0.5$, if only volume effects were to dominate the VIPERS sample composition. This test therefore demonstrates that the observed bright edge evolution with redshift is real, and must be due to the evolving properties of the galaxies in the sample.

A.3   Comparison with zCOSMOS

One further test of our analysis consists of verifying whether the same evolution of the colour-magnitude bright edge is observed in other redshift surveys. We have taken the available data from the zCOSMOS bright sample Lilly et al. (2009), divided the sample into the same redshift bins used for the VIPERS sample, and computed the zCOSMOS bright edge location using the same procedure described in Sect. 5.4.1. Note that zCOSMOS has the same depth of VIPERS, i.e. it has been cut at magnitude 22.5 in the observed i-band. The difference with VIPERS is that zCOSMOS is a purely magnitude limited sample whereas VIPERS has a colour-colour pre-selection to isolate galaxies with $z \gtrsim 0.5$ (see Fig. 3 of Guzzo et al. (2014) for details). As can be seen in Fig. A.4 (where we plot only two redshift bins for simplicity), the VIPERS and zCOSMOS bright edge locations coincide almost perfectly, albeit the zCOSMOS one is somewhat noisier because of the smaller number of objects in that sample, since the area covered by zCOSMOS is significantly smaller than the one covered by VIPERS. Although only two redshift bins are shown, the agreement is of the same quality for all of the redshift bins used in our VIPERS study.
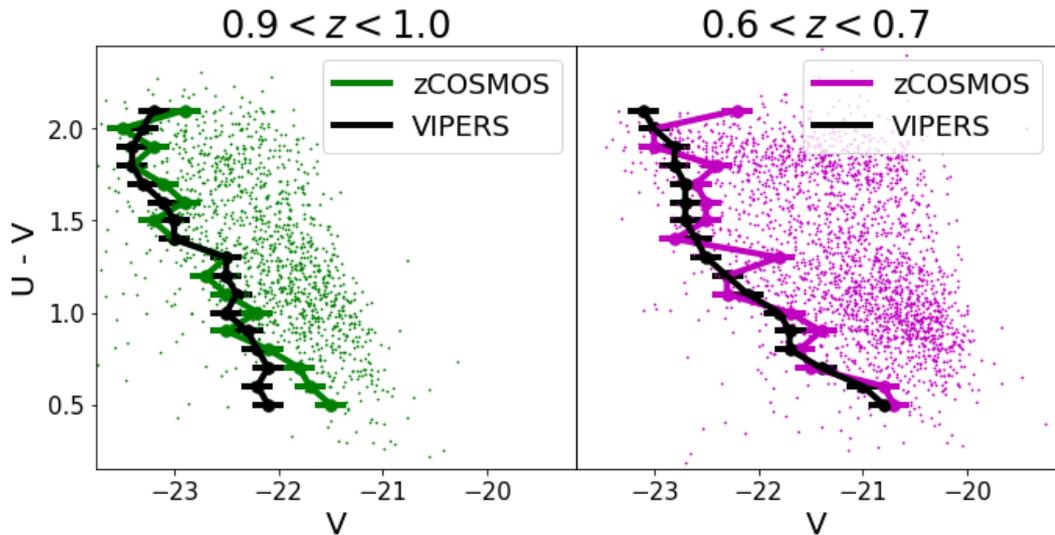
Figure A.4: Comparison of the colour-magnitude bright edges between zCOSMOS and VIPERS data. The coloured points and edges come from the zCOSMOS catalogue while the black edges are relative to the VIPERS data in the same redshift bins (as plotted in Fig. 5.5). Only two redshift bins are shown here, but the matching between the two samples is of similar quality for all bins.

A.4   Stellar masses in VIPERS

The aim of this section is to show how the bright edge of the colour - magnitude relation is made up of galaxies that span a wide range of stellar masses. Here stellar masses are obtained as in Moutard et al. (2016a). The evolution of the bright edge points toward a scenario where quenching is acting on galaxies which are bright in the V-band but which have different stellar masses. To show this, we plot in Fig. A.5 the relation between the rest frame V-band magnitude and stellar mass in the VIPERS sample. We use different coloured symbols in Fig. A.5 to differentiate between galaxies with different $U - V$ optical colours. We observe that the brightest red galaxy (e.g $U - V = 2$) and the brightest blue galaxy (e.g. $U - V = 0.5$) not only have different V-band absolute magnitudes ($V \sim -23$ for the bright red galaxy compared with $V \sim -21.5$ for the bright blue galaxy), but also different stellar masses. We can also look at the distribution of $U - V$ optical colours in Fig. A.6. In this plot we split the analysis into different stellar mass (different line colours) and redshift bins (different line style). We notice that
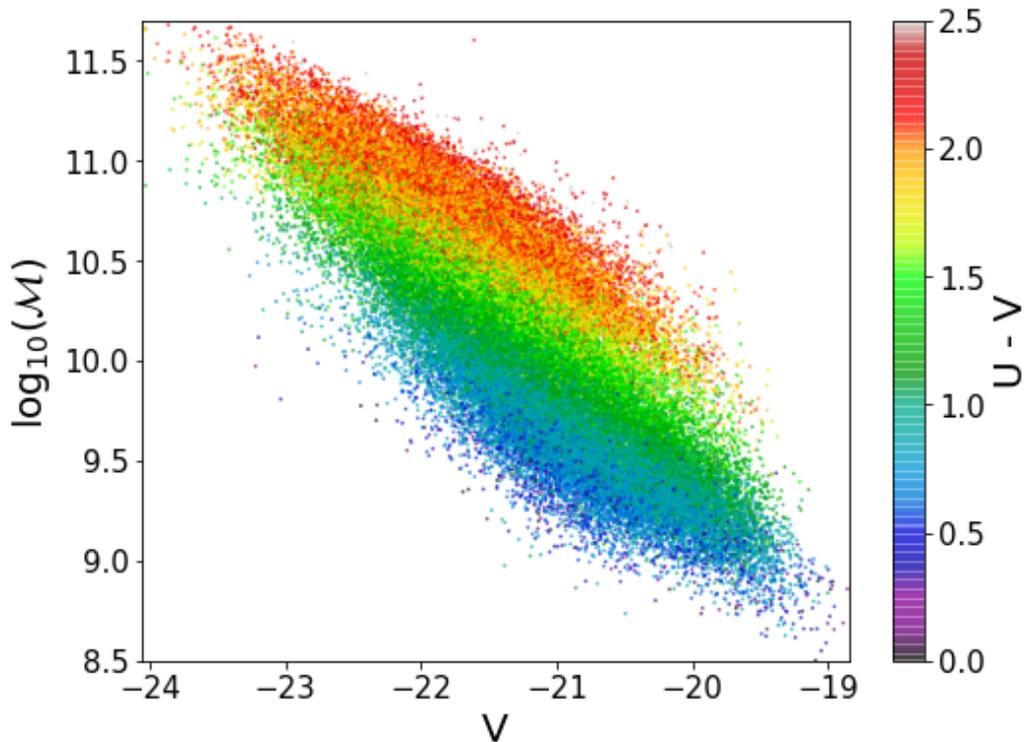
Figure A.5: Relation between the rest frame V magnitude and stellar masses, colour coded by the $U - V$ colour. All stellar masses are in units of $M_\odot$.

higher values of stellar mass dominate at redder $U - V$ colours while lower stellar masses dominate at bluer colours. This holds true both in our low redshift bin ($0.5 < z < 0.6$, solid line histogram) and in our high redshift bin ($0.9 < z < 1.1$, dashed line). Moving from high to low redshift we see an evolution in the $U - V$ colour, with galaxies becoming systematically redder but the order of the stellar mass bins is preserved in colour, with lower stellar masses always being bluer than higher stellar masses. We can state that, in our highest redshift bin, galaxies are more massive and bluer. In fact at $0.9 < z < 1.1$ we do not find any galaxy in our sample with $\log \mathcal{M} < 9.0$. Combining the information from Figs. A.5 and A.6, we can conclude that, over the redshift range ($0.5 < z < 1.1$), galaxies that are bright in the V-band, which are those that define the bright edge, have a wide range of stellar masses (independently of the colour evolution). Since galaxies approaching the bright edge are those which stop becoming bluer and brighter, and start getting fainter and redder, we argue that the turn over is due to quenching and that this
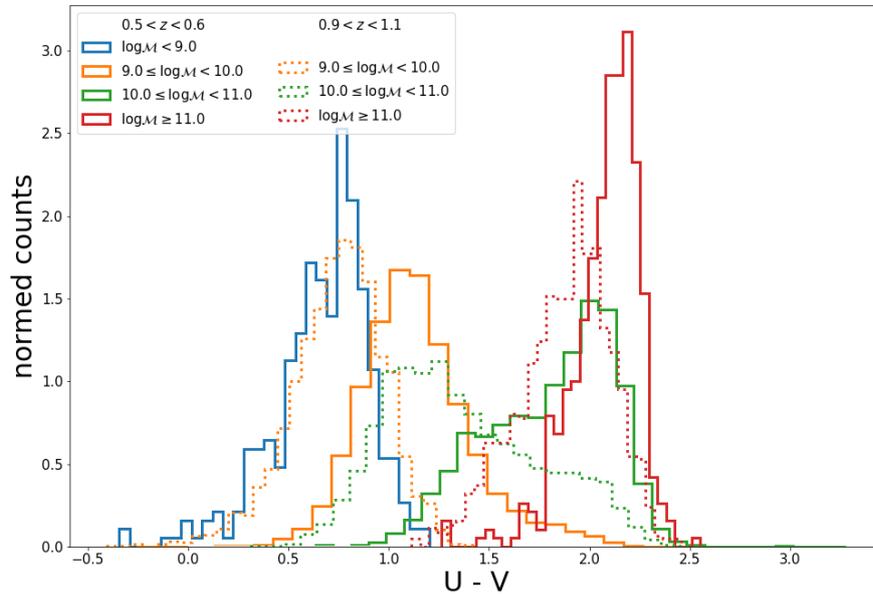
Figure A.6: Histogram of the $U - V$ colour distribution split in 4 mass bins indicated by the colour of the lines, and 2 redshift bin indicated by the shape of the line. All stellar masses are in units of $M_\odot$.

mechanism affects a variety of stellar masses. In Section 5.6, we illustrate the impact of switching off AGN feedback on the colour-magnitude relation. This is a process that mainly affects the cooling onto central galaxies in massive halos, and so without AGN feedback there is an increase in the abundance of bright galaxies. However, we do not expect AGN feedback to have an impact on the galaxies in low mass haloes. Other processes which restrict star formation, such as feedback from SNe and the stripping of hot gas from galaxies that fall into clusters will also act to suppress star formation, particularly at lower masses. A study of how AGN and SNe feedback can change the stellar mass of a galaxy is presented in Mitchell et al. (2016).

Bibliography

L. E. Abramson, M. D. Gladders, A. Dressler, A. Oemler, Jr., B. Poggianti, and B. Vulcani. Return to [Log-]Normalcy: Rethinking Quenching, The Star Formation Main Sequence, and Perhaps Much More. , 832:7, Nov. 2016. doi: 10.3847/0004-637X/832/1/7.

A. Alarcon, E. Gaztanaga, M. Eriksen, C. M. Baugh, L. Cabayol, R. Casas, J. Carretero, F. J. Castander, J. De Vicente, E. Fernandez, J. Garcia-Bellido, H. Hildebrandt, H. Hoekstra, B. Joachimi, G. Manzoni, R. Miquel, P. Norberg, C. Padilla, P. Renard, E. Sanchez, S. Serrano, I. Sevilla-Noarbe, M. Siudek, and P. Tallada-Crespí. The PAU Survey: an improved photo-z sample in the COSMOS field. , 501(4):6103–6122, Mar. 2021. doi: 10.1093/mnras/staa3659.

R. E. Angulo and O. Hahn. Large-scale dark matter simulations. *arXiv e-prints*, art. arXiv:2112.05165, Dec. 2021.

J. Armijo, C. M. Baugh, N. D. Padilla, P. Norberg, and C. Arnold. Making use of sub-resolution haloes in N-body simulations. *Monthly Notices of the Royal Astronomical Society: Letters*, 510(1):29–33, 11 2021. ISSN 1745-3925. doi: 10.1093/mnrasl/slab122. URL https://doi.org/10.1093/mnrasl/slab122.

I. K. Baldry, K. Glazebrook, J. Brinkmann, Ž. Ivezić, R. H. Lupton, R. C. Nichol,

and A. S. Szalay. Quantifying the Bimodal Color-Magnitude Distribution of Galaxies. , 600:681–694, Jan. 2004. doi: 10.1086/380092.

J. A. Baldwin, M. M. Phillips, and R. Terlevich. Classification parameters for the emission-line spectra of extragalactic objects. , 93:5–19, Feb. 1981. doi: 10.1086/130766.

M. L. Balogh, I. K. Baldry, R. Nichol, C. Miller, R. Bower, and K. Glazebrook. The Bimodal Galaxy Color Distribution: Dependence on Luminosity and Environment. , 615:L101–L104, Nov. 2004. doi: 10.1086/426079.

C. M. Baugh. A primer on hierarchical galaxy formation: the semi-analytical approach. *Reports on Progress in Physics*, 69:3101–3156, Dec. 2006. doi: 10.108 8/0034-4885/69/12/R02.

C. M. Baugh. Creating synthetic universes in a computer. *Philosophical Transactions of the Royal Society of London Series A*, 366(1884):4381–4392, Dec. 2008. doi: 10.1098/rsta.2008.0192.

C. M. Baugh, C. G. Lacey, C. S. Frenk, G. L. Granato, L. Silva, A. Bressan, A. J. Benson, and S. Cole. Can the faint submillimetre galaxies be explained in the Λ cold dark matter model? , 356(3):1191–1200, Jan. 2005. doi: 10.1111/j.1365-2 966.2004.08553.x.

C. M. Baugh, V. Gonzalez-Perez, C. d. P. Lagos, C. G. Lacey, J. C. Helly, A. Jenkins, C. S. Frenk, A. J. Benson, R. G. Bower, and S. Cole. Galaxy formation in the Planck Millennium: the atomic hydrogen content of dark matter halos. , 483 (4):4922–4937, Mar 2019. doi: 10.1093/mnras/sty3427.

C. M. Baugh, C. G. Lacey, V. Gonzalez-Perez, and G. Manzoni. Modelling emission lines in star forming galaxies. *arXiv e-prints*, art. arXiv:2112.00129, Nov. 2021.

N. Benítez. Bayesian Photometric Redshift Estimation. , 536:571–583, June 2000. doi: 10.1086/308947.

A. J. Benson. Galaxy formation theory. , 495(2-3):33–86, Oct 2010. doi: 10.1016/ j.physrep.2010.06.001.

A. J. Benson, C. M. Baugh, S. Cole, C. S. Frenk, and C. G. Lacey. The dependence of velocity and clustering statistics on galaxy properties. , 316(1):107–119, July 2000. doi: 10.1046/j.1365-8711.2000.03470.x.

A. J. Benson, R. G. Bower, C. S. Frenk, C. G. Lacey, C. M. Baugh, and S. Cole. What Shapes the Luminosity Function of Galaxies? , 599:38–49, Dec. 2003. doi: 10.1086/379160.

A. F. L. Bluck, J. T. Mendel, S. L. Ellison, D. R. Patton, L. Simard, B. M. B. Henriques, P. Torrey, H. Teimoorinia, J. Moreno, and E. Starkenburg. The impact of galactic properties and environment on the quenching of central and satellite galaxies: a comparison between SDSS, Illustris and L-Galaxies. , 462 (3):2559–2586, Nov 2016. doi: 10.1093/mnras/stw1665.

A. Bongiorno, A. Schulze, A. Merloni, G. Zamorani, O. Ilbert, F. La Franca, Y. Peng, E. Piconcelli, V. Mainieri, J. D. Silverman, M. Brusa, F. Fiore, M. Salvato, and N. Scoville. AGN host galaxy mass function in COSMOS. Is AGN feedback responsible for the mass-quenching of galaxies? , 588:A78, Apr. 2016. doi: 10.1051/0004-6361/201527436.

A. Boselli, S. Eales, L. Cortese, G. Bendo, P. Chanial, V. Buat, J. Davies, R. Auld, E. Rigby, M. Baes, M. Barlow, J. Bock, M. Bradford, N. Castro-Rodriguez, S. Charlot, D. Clements, D. Cormier, E. Dwek, D. Elbaz, M. Galametz, F. Galliano, W. Gear, J. Glenn, H. Gomez, M. Griffin, S. Hony, K. Isaak, L. Levenson, N. Lu, S. Madden, B. O'Halloran, K. Okamura, S. Oliver, M. Page, P. Panuzzo, A. Papageorgiou, T. Parkin, I. Perez-Fournon, M. Pohlen, N. Rangwala, H. Roussel, A. Rykala, N. Sacchi, M. Sauvage, B. Schulz, M. Schirm, M. W. L. Smith, L. Spinoglio, J. Stevens, M. Symeonidis, M. Vaccari, L. Vigroux, C. Wilson, H. Wozniak, G. Wright, and W. Zeilinger. The Herschel Reference Survey. , 122: 261–287, Mar. 2010. doi: 10.1086/651535.

R. G. Bower, A. J. Benson, R. Malbon, J. C. Helly, C. S. Frenk, C. M. Baugh, S. Cole, and C. G. Lacey. Breaking the hierarchy of galaxy formation. , 370: 645–655, Aug. 2006. doi: 10.1111/j.1365-2966.2006.10519.x.

R. G. Bower, I. Vernon, M. Goldstein, A. J. Benson, C. G. Lacey, C. M. Baugh, S. Cole, and C. S. Frenk. The parameter space of galaxy formation. , 407(4): 2017–2045, Oct. 2010. doi: 10.1111/j.1365-2966.2010.16991.x.

M. Boylan-Kolchin, V. Springel, S. D. M. White, A. Jenkins, and G. Lemson. Resolving cosmic structure formation with the Millennium-II Simulation. , 398 (3):1150–1164, Sept. 2009. doi: 10.1111/j.1365-2966.2009.15191.x.

G. B. Brammer, P. G. van Dokkum, and P. Coppi. EAZY: A Fast, Public Photometric Redshift Code. , 686(2):1503–1513, Oct. 2008. doi: 10.1086/591786.

J. Brinchmann, M. Pettini, and S. Charlot. New insights into the stellar content and physical conditions of star-forming galaxies at z = 2-3 from spectral modelling. , 385:769–782, Apr. 2008. doi: 10.1111/j.1365-2966.2008.12914.x.

G. Bruzual and S. Charlot. Stellar population synthesis at the resolution of 2003. , 344:1000–1028, Oct. 2003. doi: 10.1046/j.1365-8711.2003.06897.x.

K. Bundy, R. S. Ellis, C. J. Conselice, J. E. Taylor, M. C. Cooper, C. N. A. Willmer, B. J. Weiner, A. L. Coil, K. G. Noeske, and P. R. M. Eisenhardt. The Mass Assembly History of Field Galaxies: Detection of an Evolving Mass Limit for Star-Forming Galaxies. , 651:120–141, Nov. 2006. doi: 10.1086/507456.

L. Cabayol, M. Eriksen, A. Amara, J. Carretero, R. Casas, F. J. Castander, J. De Vicente, E. Fernández, J. García-Bellido, E. Gaztanaga, H. Hildebrandt, R. Miquel, C. Padilla, E. Sánchez, S. Serrano, I. Sevilla-Noarbe, and P. Tallada-Crespí. The PAU survey: estimating galaxy photometry with deep learning. , 506(3):4048–4069, Sept. 2021. doi: 10.1093/mnras/stab1909.

P. Capak, H. Aussel, M. Ajiki, H. J. McCracken, B. Mobasher, N. Scoville, P. Shopbell, Y. Taniguchi, D. Thompson, S. Tribiano, S. Sasaki, A. W. Blain, M. Brusa,

C. Carilli, A. Comastri, C. M. Carollo, P. Cassata, J. Colbert, R. S. Ellis, M. Elvis, M. Giavalisco, W. Green, L. Guzzo, G. Hasinger, O. Ilbert, C. Impey, K. Jahnke, J. Kartaltepe, J. P. Kneib, J. Koda, A. Koekemoer, Y. Komiyama, A. Leauthaud, O. Le Fevre, S. Lilly, C. Liu, R. Massey, S. Miyazaki, T. Murayama, T. Nagao, J. A. Peacock, A. Pickles, C. Porciani, A. Renzini, J. Rhodes, M. Rich, M. Salvato, D. B. Sanders, C. Scarlata, D. Schiminovich, E. Schinnerer, M. Scodeggio, K. Sheth, Y. Shioya, L. A. M. Tasca, J. E. Taylor, L. Yan, and G. Zamorani. The First Release COSMOS Optical and Near-IR Data and Catalog. , 172(1):99–116, Sept. 2007. doi: 10.1086/519081.

R. Casas, L. Cardiel-Sas, F. J. Castander, C. Díaz, J. Gaweda, J. Jiménez Rojas, S. Jiménez, M. Lamensans, C. Padilla, F. J. Rodriguez, E. Sanchez, and I. Sevilla Noarbe. Characterization and performance of PAUCam filters. In C. J. Evans, L. Simard, and H. Takami, editors, *Ground-based and Airborne Instrumentation for Astronomy VI*, volume 9908 of *Society of Photo-Optical Instrumentation Engineers (SPIE) Conference Series*, page 99084K, Aug. 2016. doi: 10.1117/12.2232422.

F. J. Castander, O. Ballester, A. Bauer, L. Cardiel-Sas, J. Carretero, R. Casas, J. Castilla, M. Crocce, M. Delfino, M. Eriksen, E. Fernández, P. Fosalba, J. García-Bellido, E. Gaztañaga, F. Grañena, C. Hernández, J. Jiménez, L. López, P. Martí, R. Miquel, C. Neissner, C. Padilla, C. Pío, R. Ponce, E. Sanchez, S. Serrano, I. Sevilla, N. Tonello, and J. de Vicente. The PAU camera and the PAU survey at the William Herschel Telescope. In *Ground-based and Airborne Instrumentation for Astronomy IV*, volume 8446 of , page 84466D, Sept. 2012. doi: 10.1117/12.926234.

L. Ciesla, A. Boselli, D. Elbaz, S. Boissier, V. Buat, V. Charmandaris, C. Schreiber, M. Béthermin, M. Baes, M. Boquien, I. De Looze, J. A. Fernández-Ontiveros, C. Pappalardo, L. Spinoglio, and S. Viaene. The imprint of rapid star formation

quenching on the spectral energy distributions of galaxies. , 585:A43, Jan. 2016. doi: 10.1051/0004-6361/201527107.

A. Citro, L. Pozzetti, M. Moresco, and A. Cimatti. Inferring the star-formation histories of the most massive and passive early-type galaxies at z < 0.3. , 592: A19, July 2016. doi: 10.1051/0004-6361/201527772.

S. Cole, C. G. Lacey, C. M. Baugh, and C. S. Frenk. Hierarchical galaxy formation. , 319:168–204, Nov. 2000. doi: 10.1046/j.1365-8711.2000.03879.x.

S. Cole, W. J. Percival, J. A. Peacock, P. Norberg, C. M. Baugh, C. S. Frenk, I. Baldry, J. Bland-Hawthorn, T. Bridges, R. Cannon, M. Colless, C. Collins, W. Couch, N. J. G. Cross, G. Dalton, V. R. Eke, R. De Propris, S. P. Driver, G. Efstathiou, R. S. Ellis, K. Glazebrook, C. Jackson, A. Jenkins, O. Lahav, I. Lewis, S. Lumsden, S. Maddox, D. Madgwick, B. A. Peterson, W. Sutherland, and K. Taylor. The 2dF Galaxy Redshift Survey: power-spectrum analysis of the final data set and cosmological implications. , 362(2):505–534, Sept. 2005. doi: 10.1111/j.1365-2966.2005.09318.x.

M. Colless, G. Dalton, S. Maddox, W. Sutherland, P. Norberg, S. Cole, J. Bland-Hawthorn, T. Bridges, R. Cannon, C. Collins, W. Couch, N. Cross, K. Deeley, R. de Propris, S. P. Driver, G. Efstathiou, R. S. Ellis, C. S. Frenk, K. Glazebrook, C. Jackson, O. Lahav, I. Lewis, S. Lumsden, D. Madgwick, J. A. Peacock, B. A. Peterson, I. Price, M. Seaborne, and K. Taylor. VizieR Online Data Catalog: The 2dF Galaxy Redshift Survey 100k Data Release (2dFGRS Team, 2001). *VizieR Online Data Catalog*, 7226, June 2003.

J. Coupon, O. Ilbert, M. Kilbinger, H. J. McCracken, Y. Mellier, S. Arnouts, E. Bertin, P. Hudelot, M. Schultheis, O. Le Fèvre, V. Le Brun, L. Guzzo, S. Bardelli, E. Zucca, M. Bolzonella, B. Garilli, G. Zamorani, A. Zanichelli, L. Tresse, and H. Aussel. Photometric redshifts for the CFHTLS T0004 deep and wide fields. , 500(3):981–998, June 2009. doi: 10.1051/0004-6361/200811413.

L. L. Cowie, A. Songaila, E. M. Hu, and J. G. Cohen. New Insight on Galaxy Formation and Evolution From Keck Spectroscopy of the Hawaii Deep Fields. , 112:839, Sept. 1996. doi: 10.1086/118058.

D. J. Croton, V. Springel, S. D. M. White, G. De Lucia, C. S. Frenk, L. Gao, A. Jenkins, G. Kauffmann, J. F. Navarro, and N. Yoshida. The many lives of active galactic nuclei: cooling flows, black holes and the luminosities and colours of galaxies. , 365:11–28, Jan. 2006. doi: 10.1111/j.1365-2966.2005.09675.x.

O. Cucciati, I. Davidzon, M. Bolzonella, B. R. Granett, G. De Lucia, E. Branchini, G. Zamorani, A. Iovino, B. Garilli, L. Guzzo, M. Scodeggio, S. de la Torre, U. Abbas, C. Adami, S. Arnouts, D. Bottini, A. Cappi, P. Franzetti, A. Fritz, J. Krywult, V. Le Brun, O. Le Fèvre, D. Maccagni, K. Małek, F. Marulli, T. Moutard, M. Polletta, A. Pollo, L. A. M. Tasca, R. Tojeiro, D. Vergani, A. Zanichelli, J. Bel, J. Blaizot, J. Coupon, A. Hawken, O. Ilbert, L. Moscardini, J. A. Peacock, and A. Gargiulo. The VIMOS Public Extragalactic Redshift Survey (VIPERS). The decline of cosmic star formation: quenching, mass, and environment connections. , 602:A15, June 2017. doi: 10.1051/0004-6361/201630113.

J.-C. J. Cuillandre, K. Withington, P. Hudelot, Y. Goranova, H. McCracken, F. Magnard, Y. Mellier, N. Regnault, M. Bétoule, H. Aussel, J. J. Kavelaars, P. Fernique, F. Bonnarel, F. Ochsenbein, and O. Ilbert. Introduction to the CFHT Legacy Survey final release (CFHTLS T0007). In A. B. Peck, R. L. Seaman, and F. Comeron, editors, *Observatory Operations: Strategies, Processes, and Systems IV*, volume 8448 of *Society of Photo-Optical Instrumentation Engineers (SPIE) Conference Series*, page 84480M, Sept. 2012. doi: 10.1117/12.925584.

E. Daddi, M. Dickinson, G. Morrison, R. Chary, A. Cimatti, D. Elbaz, D. Frayer, A. Renzini, A. Pope, D. M. Alexander, F. E. Bauer, M. Giavalisco, M. Huynh, J. Kurk, and M. Mignoli. Multiwavelength Study of Massive Galaxies at z~2. I.

Star Formation and Galaxy Growth. , 670(1):156–172, Nov. 2007. doi: 10.1086/ 521818.

I. Davidzon, M. Bolzonella, J. Coupon, O. Ilbert, S. Arnouts, S. de la Torre, A. Fritz, G. De Lucia, A. Iovino, B. R. Granett, G. Zamorani, L. Guzzo, U. Abbas, C. Adami, J. Bel, D. Bottini, E. Branchini, A. Cappi, O. Cucciati, P. Franzetti, M. Fumana, B. Garilli, J. Krywult, V. Le Brun, O. Le Fèvre, D. Maccagni, K. Małek, F. Marulli, H. J. McCracken, L. Paioro, J. A. Peacock, M. Polletta, A. Pollo, H. Schlagenhaufer, M. Scodeggio, L. A. M. Tasca, R. Tojeiro, D. Vergani, A. Zanichelli, A. Burden, C. Di Porto, A. Marchetti, C. Marinoni, Y. Mellier, L. Moscardini, T. Moutard, R. C. Nichol, W. J. Percival, S. Phleps, and M. Wolk. The VIMOS Public Extragalactic Redshift Survey (VIPERS). A precise measurement of the galaxy stellar mass function and the abundance of massive galaxies at redshifts 0.5 < z < 1.3. , 558:A23, Oct. 2013. doi: 10.1051/0004-6361/201321511.

L. J. M. Davies, A. S. G. Robotham, C. d. P. Lagos, S. P. Driver, A. R. H. Stevens, Y. M. Bahé, M. Alpaslan, M. N. Bremer, M. J. I. Brown, S. Brough, J. Bland-Hawthorn, L. Cortese, P. Elahi, M. W. Grootes, B. W. Holwerda, A. D. Ludlow, S. McGee, M. Owers, and S. Phillipps. Galaxy and Mass Assembly (GAMA): environmental quenching of centrals and satellites in groups. , 483(4):5444–5458, Mar 2019. doi: 10.1093/mnras/sty3393.

K. S. Dawson, D. J. Schlegel, C. P. Ahn, S. F. Anderson, É. Aubourg, S. Bailey, R. H. Barkhouser, J. E. Bautista, A. Beifiori, A. A. Berlind, V. Bhardwaj, D. Bizyaev, C. H. Blake, M. R. Blanton, M. Blomqvist, A. S. Bolton, A. Borde, J. Bovy, W. N. Brandt, H. Brewington, J. Brinkmann, P. J. Brown, J. R. Brownstein, K. Bundy, N. G. Busca, W. Carithers, A. R. Carnero, M. A. Carr, Y. Chen, J. Comparat, N. Connolly, F. Cope, R. A. C. Croft, A. J. Cuesta, L. N. da Costa, J. R. A. Davenport, T. Delubac, R. de Putter, S. Dhital, A. Ealet, G. L. Ebelke, D. J. Eisenstein, S. Escoffier, X. Fan, N. F. Ak, H. Finley, A. Font-

Ribera, R. Génova-Santos, J. E. Gunn, H. Guo, D. Haggard, P. B. Hall, J.-C. Hamilton, B. Harris, D. W. Harris, S. Ho, D. W. Hogg, D. Holder, K. Honscheid, J. Huehnerhoff, B. Jordan, W. P. Jordan, G. Kauffmann, E. A. Kazin, D. Kirkby, M. A. Klaene, J.-P. Kneib, J.-M. L. Goff, K.-G. Lee, D. C. Long, C. P. Loomis, B. Lundgren, R. H. Lupton, M. A. G. Maia, M. Makler, E. Malanushenko, V. Malanushenko, R. Mandelbaum, M. Manera, C. Maraston, D. Margala, K. L. Masters, C. K. McBride, P. McDonald, I. D. McGreer, R. G. McMahon, O. Mena, J. Miralda-Escudé, A. D. Montero-Dorta, F. Montesano, D. Muna, A. D. Myers, T. Naugle, R. C. Nichol, P. Noterdaeme, S. E. Nuza, M. D. Olmstead, A. Oravetz, D. J. Oravetz, R. Owen, N. Padmanabhan, N. Palanque-Delabrouille, K. Pan, J. K. Parejko, I. Pâris, W. J. Percival, I. Pérez-Fournon, I. Pérez-Ràfols, P. Petitjean, R. Pfaffenberger, J. Pforr, M. M. Pieri, F. Prada, A. M. Price-Whelan, M. J. Raddick, R. Rebolo, J. Rich, G. T. Richards, C. M. Rockosi, N. A. Roe, A. J. Ross, N. P. Ross, G. Rossi, J. A. Rubiño-Martin, L. Samushia, A. G. Sánchez, C. Sayres, S. J. Schmidt, D. P. Schneider, C. G. Scóccola, H.-J. Seo, A. Shelden, E. Sheldon, Y. Shen, Y. Shu, A. Slosar, S. A. Smee, S. A. Snedden, F. Stauffer, O. Steele, M. A. Strauss, A. Streblyanska, N. Suzuki, M. E. C. Swanson, T. Tal, M. Tanaka, D. Thomas, J. L. Tinker, R. Tojeiro, C. A. Tremonti, M. V. Magaña, L. Verde, M. Viel, D. A. Wake, M. Watson, B. A. Weaver, D. H. Weinberg, B. J. Weiner, A. A. West, M. White, W. M. Wood-Vasey, C. Yeche, I. Zehavi, G.-B. Zhao, and Z. Zheng. THE BARYON OSCILLATION SPECTROSCOPIC SURVEY OF SDSS-III. *The Astronomical Journal*, 145(1):10, dec 2012. doi: 10.1088/0004-6256/145/1/10. URL https://doi.org/10.1088/0004-6256/145/1/10.

R. S. de Jong, O. Agertz, A. A. Berbel, J. Aird, D. A. Alexander, A. Amarsi, F. Anders, R. Andrae, B. Ansarinejad, W. Ansorge, P. Antilogus, H. Anwand-Heerwart, A. Arentsen, A. Arnadottir, M. Asplund, M. Auger, N. Azais, D. Baade, G. Baker, S. Baker, E. Balbinot, I. K. Baldry, M. Banerji, S. Barden, P. Barklem, E. Barthélémy-Mazot, C. Battistini, S. Bauer, C. P. M. Bell,

O. Bellido-Tirado, S. Bellstedt, V. Belokurov, T. Bensby, M. Bergemann, J. M. Bestenlehner, R. Bielby, M. Bilicki, C. Blake, J. Bland-Hawthorn, C. Boeche, W. Boland, T. Boller, S. Bongard, A. Bongiorno, P. Bonifacio, D. Boudon, D. Brooks, M. J. I. Brown, R. Brown, M. Brüggen, J. Brynnel, J. Brzeski, T. Buchert, P. Buschkamp, E. Caffau, P. Caillier, J. Carrick, L. Casagrande, S. Case, A. Casey, I. Cesarini, G. Cescutti, D. Chapuis, C. Chiappini, M. Childress, N. Christlieb, R. Church, M. R. L. Cioni, M. Cluver, M. Colless, T. Collett, J. Comparat, A. Cooper, W. Couch, F. Courbin, S. Croom, D. Croton, E. Daguisé, G. Dalton, L. J. M. Davies, T. Davis, P. de Laverny, A. Deason, F. Dionies, K. Disseau, P. Doel, D. Döscher, S. P. Driver, T. Dwelly, D. Eckert, A. Edge, B. Edvardsson, D. E. Youssoufi, A. Elhaddad, H. Enke, G. Erfanianfar, T. Farrell, T. Fechner, C. Feiz, S. Feltzing, I. Ferreras, D. Feuerstein, D. Feuillet, A. Finoguenov, D. Ford, S. Fotopoulou, M. Fouesneau, C. Frenk, S. Frey, W. Gaessler, S. Geier, N. Gentile Fusillo, O. Gerhard, T. Giannantonio, D. Giannone, B. Gibson, P. Gillingham, C. González-Fernández, E. Gonzalez-Solares, S. Gottloeber, A. Gould, E. K. Grebel, A. Gueguen, G. Guiglion, M. Haehnelt, T. Hahn, C. J. Hansen, H. Hartman, K. Hauptner, K. Hawkins, D. Haynes, R. Haynes, U. Heiter, A. Helmi, C. H. Aguayo, P. Hewett, S. Hinton, D. Hobbs, S. Hoenig, D. Hofman, I. Hook, J. Hopgood, A. Hopkins, A. Hourihane, L. Howes, C. Howlett, T. Huet, M. Irwin, O. Iwert, P. Jablonka, T. Jahn, K. Jahnke, A. Jarno, S. Jin, P. Jofre, D. Johl, D. Jones, H. Jönsson, C. Jordan, I. Karovicova, A. Khalatyan, A. Kelz, R. Kennicutt, D. King, F. Kitaura, J. Klar, U. Klauser, J. P. Kneib, A. Koch, S. Koposov, G. Kordopatis, A. Korn, J. Kosmalski, R. Kotak, M. Kovalev, K. Kreckel, Y. Kripak, M. Krumpe, K. Kuijken, A. Kunder, I. Kushniruk, M. I. Lam, G. Lamer, F. Laurent, J. Lawrence, M. Lehmitz, B. Lemasle, J. Lewis, B. Li, C. Lidman, K. Lind, J. Liske, J. L. Lizon, J. Loveday, H. G. Ludwig, R. M. McDermid, K. Maguire, V. Mainieri, S. Mali, H. Mandel, K. Mandel, L. Mannering, S. Martell, D. Martinez Delgado, G. Matijevic, H. McGregor, R. McMahon, P. McMillan, O. Mena, A. Merloni,

M. J. Meyer, C. Michel, G. Micheva, J. E. Migniau, I. Minchev, G. Monari, R. Muller, D. Murphy, D. Muthukrishna, K. Nandra, R. Navarro, M. Ness, V. Nichani, R. Nichol, H. Nicklas, F. Niederhofer, P. Norberg, D. Obreschkow, S. Oliver, M. Owers, N. Pai, S. Pankratow, D. Parkinson, J. Paschke, R. Paterson, A. Pecontal, I. Parry, D. Phillips, A. Pillepich, L. Pinard, J. Pirard, N. Piskunov, V. Plank, D. Plüschke, E. Pons, P. Popesso, C. Power, J. Pragt, A. Pramskiy, D. Pryer, M. Quattri, A. B. d. A. Queiroz, A. Quirrenbach, S. Rahurkar, A. Raichoor, S. Ramstedt, A. Rau, A. Recio-Blanco, R. Reiss, F. Renaud, Y. Revaz, P. Rhode, J. Richard, A. D. Richter, H. W. Rix, A. S. G. Robotham, R. Roelfsema, M. Romaniello, D. Rosario, F. Rothmaier, B. Roukema, G. Ruchti, G. Rupprecht, J. Rybizki, N. Ryde, A. Saar, E. Sadler, M. Sahlén, M. Salvato, B. Sassolas, W. Saunders, A. Saviauk, L. Sbordone, T. Schmidt, O. Schnurr, R. D. Scholz, A. Schwope, W. Seifert, T. Shanks, A. Sheinis, T. Sivov, Á. Skúladóttir, S. Smartt, S. Smedley, G. Smith, R. Smith, J. Sorce, L. Spitler, E. Starkenburg, M. Steinmetz, I. Stilz, J. Storm, M. Sullivan, W. Sutherland, E. Swann, A. Tamone, E. N. Taylor, J. Teillon, E. Tempel, R. ter Horst, W. F. Thi, E. Tolstoy, S. Trager, G. Traven, P. E. Tremblay, L. Tresse, M. Valentini, R. van de Weygaert, M. van den Ancker, J. Veljanoski, S. Venkatesan, L. Wagner, K. Wagner, C. J. Walcher, L. Waller, N. Walton, L. Wang, R. Winkler, L. Wisotzki, C. C. Worley, G. Worseck, M. Xiang, W. Xu, D. Yong, C. Zhao, J. Zheng, F. Zscheyge, and D. Zucker. 4MOST: Project overview and information for the First Call for Proposals. *The Messenger*, 175:3–11, Mar. 2019. doi: 10.18727/0722-6691/5117.

G. De Lucia, B. M. Poggianti, A. Aragón-Salamanca, S. D. M. White, D. Zaritsky, D. Clowe, C. Halliday, P. Jablonka, A. von der Linden, B. Milvang-Jensen, R. Pelló, G. Rudnick, R. P. Saglia, and L. Simard. The build-up of the colour-magnitude relation in galaxy clusters since z ˜ 0.8. , 374:809–822, Jan. 2007. doi: 10.1111/j.1365-2966.2006.11199.x.

DESI Collaboration, A. Aghamousa, J. Aguilar, S. Ahlen, S. Alam, L. E. Al-

len, C. Allende Prieto, J. Annis, S. Bailey, C. Balland, O. Ballester, C. Baltay, L. Beaufore, C. Bebek, T. C. Beers, E. F. Bell, J. L. Bernal, R. Besuner, F. Beut- ler, C. Blake, H. Bleuler, M. Blomqvist, R. Blum, A. S. Bolton, C. Briceno, D. Brooks, J. R. Brownstein, E. Buckley-Geer, A. Burden, E. Burtin, N. G. Busca, R. N. Cahn, Y.-C. Cai, L. Cardiel-Sas, R. G. Carlberg, P.-H. Carton, R. Casas, F. J. Castander, J. L. Cervantes-Cota, T. M. Claybaugh, M. Close, C. T. Coker, S. Cole, J. Comparat, A. P. Cooper, M. C. Cousinou, M. Crocce, J.-G. Cuby, D. P. Cunningham, T. M. Davis, K. S. Dawson, A. de la Ma- corra, J. De Vicente, T. Delubac, M. Derwent, A. Dey, G. Dhungana, Z. Ding, P. Doel, Y. T. Duan, A. Ealet, J. Edelstein, S. Eftekharzadeh, D. J. Eisenstein, A. Elliott, S. Escoffier, M. Evatt, P. Fagrelius, X. Fan, K. Fanning, A. Farahi, J. Farihi, G. Favole, Y. Feng, E. Fernandez, J. R. Findlay, D. P. Finkbeiner, M. J. Fitzpatrick, B. Flaugher, S. Flender, A. Font-Ribera, J. E. Forero-Romero, P. Fosalba, C. S. Frenk, M. Fumagalli, B. T. Gaensicke, G. Gallo, J. Garcia- Bellido, E. Gaztanaga, N. Pietro Gentile Fusillo, T. Gerard, I. Gershkovich, T. Giannantonio, D. Gillet, G. Gonzalez-de-Rivera, V. Gonzalez-Perez, S. Gott, O. Graur, G. Gutierrez, J. Guy, S. Habib, H. Heetderks, I. Heetderks, K. Heit- mann, W. A. Hellwing, D. A. Herrera, S. Ho, S. Holland, K. Honscheid, E. Huff, T. A. Hutchinson, D. Huterer, H. S. Hwang, J. M. Illa Laguna, Y. Ishikawa, D. Jacobs, N. Jeffrey, P. Jelinsky, E. Jennings, L. Jiang, J. Jimenez, J. John- son, R. Joyce, E. Jullo, S. Juneau, S. Kama, A. Karcher, S. Karkar, R. Kehoe, N. Kennamer, S. Kent, M. Kilbinger, A. G. Kim, D. Kirkby, T. Kisner, E. Kit- anidis, J.-P. Kneib, S. Koposov, E. Kovacs, K. Koyama, A. Kremin, R. Kron, L. Kronig, A. Kueter-Young, C. G. Lacey, R. Lafever, O. Lahav, A. Lambert, M. Lampton, M. Landriau, D. Lang, T. R. Lauer, J.-M. Le Goff, L. Le Guil- lou, A. Le Van Suu, J. H. Lee, S.-J. Lee, D. Leitner, M. Lesser, M. E. Levi, B. L'Huillier, B. Li, M. Liang, H. Lin, E. Linder, S. R. Loebman, Z. Lukić, J. Ma, N. MacCrann, C. Magneville, L. Makarem, M. Manera, C. J. Manser, R. Marshall, P. Martini, R. Massey, T. Matheson, J. McCauley, P. McDonald,

I. D. McGreer, A. Meisner, N. Metcalfe, T. N. Miller, R. Miquel, J. Moustakas, A. Myers, M. Naik, J. A. Newman, R. C. Nichol, A. Nicola, L. Nicolati da Costa, J. Nie, G. Niz, P. Norberg, B. Nord, D. Norman, P. Nugent, T. O'Brien, M. Oh, K. A. G. Olsen, C. Padilla, H. Padmanabhan, N. Padmanabhan, N. Palanque-Delabrouille, A. Palmese, D. Pappalardo, I. Pâris, C. Park, A. Patej, J. A. Peacock, H. V. Peiris, X. Peng, W. J. Percival, S. Perruchot, M. M. Pieri, R. Pogge, J. E. Pollack, C. Poppett, F. Prada, A. Prakash, R. G. Probst, D. Rabinowitz, A. Raichoor, C. H. Ree, A. Refregier, X. Regal, B. Reid, K. Reil, M. Rezaie, C. M. Rockosi, N. Roe, S. Ronayette, A. Roodman, A. J. Ross, N. P. Ross, G. Rossi, E. Rozo, V. Ruhlmann-Kleider, E. S. Rykoff, C. Sabiu, L. Samushia, E. Sanchez, J. Sanchez, D. J. Schlegel, M. Schneider, M. Schubnell, A. Secroun, U. Seljak, H.-J. Seo, S. Serrano, A. Shafieloo, H. Shan, R. Sharples, M. J. Sholl, W. V. Shourt, J. H. Silber, D. R. Silva, M. M. Sirk, A. Slosar, A. Smith, G. F. Smoot, D. Som, Y.-S. Song, D. Sprayberry, R. Staten, A. Stefanik, G. Tarle, S. Sien Tie, J. L. Tinker, R. Tojeiro, F. Valdes, O. Valenzuela, M. Valluri, M. Vargas-Magana, L. Verde, A. R. Walker, J. Wang, Y. Wang, B. A. Weaver, C. Weaverdyck, R. H. Wechsler, D. H. Weinberg, M. White, Q. Yang, C. Yeche, T. Zhang, G.-B. Zhao, Y. Zheng, X. Zhou, Z. Zhou, Y. Zhu, H. Zou, and Y. Zu. The DESI Experiment Part I: Science,Targeting, and Survey Design. *arXiv e-prints*, art. arXiv:1611.00036, Oct. 2016.

B. Diemer, M. Sparre, L. E. Abramson, and P. Torrey. Log-normal Star Formation Histories in Simulated and Observed Galaxies. , 839(1):26, Apr 2017. doi: 10.3 847/1538-4357/aa68e5.

A. Dressler and J. E. Gunn. Spectroscopy of galaxies in distant clusters. II - The population of the 3C 295 cluster. , 270:7–19, July 1983. doi: 10.1086/161093.

S. P. Driver, P. Norberg, I. K. Baldry, S. P. Bamford, A. M. Hopkins, J. Liske, J. Loveday, J. A. Peacock, D. T. Hill, L. S. Kelvin, A. S. G. Robotham, N. J. G. Cross, H. R. Parkinson, M. Prescott, C. J. Conselice, L. Dunne, S. Brough,

H. Jones, R. G. Sharp, E. van Kampen, S. Oliver, I. G. Roseboom, J. Bland-Hawthorn, S. M. Croom, S. Ellis, E. Cameron, S. Cole, C. S. Frenk, W. J. Couch, A. W. Graham, R. Proctor, R. De Propris, I. F. Doyle, E. M. Edmondson, R. C. Nichol, D. Thomas, S. A. Eales, M. J. Jarvis, K. Kuijken, O. Lahav, B. F. Madore, M. Seibert, M. J. Meyer, L. Staveley-Smith, S. Phillipps, C. C. Popescu, A. E. Sansom, W. J. Sutherland, R. J. Tuffs, and S. J. Warren. GAMA: towards a physical understanding of galaxy formation. *Astronomy and Geophysics*, 50 (5):5.12–5.19, Oct. 2009. doi: 10.1111/j.1468-4004.2009.50512.x.

S. P. Driver, D. T. Hill, L. S. Kelvin, A. S. G. Robotham, J. Liske, P. Norberg, I. K. Baldry, S. P. Bamford, A. M. Hopkins, J. Loveday, J. A. Peacock, E. Andrae, J. Bland-Hawthorn, S. Brough, M. J. I. Brown, E. Cameron, J. H. Y. Ching, M. Colless, C. J. Conselice, S. M. Croom, N. J. G. Cross, R. de Propris, S. Dye, M. J. Drinkwater, S. Ellis, A. W. Graham, M. W. Grootes, M. Gunawardhana, D. H. Jones, E. van Kampen, C. Maraston, R. C. Nichol, H. R. Parkinson, S. Phillipps, K. Pimbblet, C. C. Popescu, M. Prescott, I. G. Roseboom, E. M. Sadler, A. E. Sansom, R. G. Sharp, D. J. B. Smith, E. Taylor, D. Thomas, R. J. Tuffs, D. Wijesinghe, L. Dunne, C. S. Frenk, M. J. Jarvis, B. F. Madore, M. J. Meyer, M. Seibert, L. Staveley-Smith, W. J. Sutherland, and S. J. Warren. Galaxy and Mass Assembly (GAMA): survey diagnostics and core data release. , 413(2):971–995, May 2011. doi: 10.1111/j.1365-2966.2010.18188.x.

E. J. Elliott, C. M. Baugh, and C. G. Lacey. Efficient exploration and calibration of a semi-analytical model of galaxy formation with deep learning. , 506(3): 4011–4030, Sept. 2021. doi: 10.1093/mnras/stab1837.

T. Erben and CFHTLenS Collaboration. CFHTLenS - Data Handling and Public Data Products. In *American Astronomical Society Meeting Abstracts #219*, volume 219 of *American Astronomical Society Meeting Abstracts*, page 130.09, Jan. 2012.

M. Eriksen and E. Gaztañaga. Combining spectroscopic and photometric surveys:

Same or different sky? , 451(2):1553–1560, Aug. 2015a. doi: 10.1093/mnras/st v1093.

M. Eriksen and E. Gaztañaga. Combining spectroscopic and photometric surveys using angular cross-correlations - I. Algorithm and modelling. , 452(2):2149–2167, Sept. 2015b. doi: 10.1093/mnras/stv1288.

M. Eriksen and E. Gaztañaga. Combining spectroscopic and photometric surveys using angular cross-correlations - II. Parameter constraints from different physical effects. , 452(2):2168–2184, Sept. 2015c. doi: 10.1093/mnras/stv1075.

M. Eriksen, A. Alarcon, E. Gaztanaga, A. Amara, L. Cabayol, J. Carretero, F. J. Castander, M. Crocce, M. Delfino, J. De Vicente, E. Fernandez, P. Fosalba, J. Garcia-Bellido, H. Hildebrandt, H. Hoekstra, B. Joachimi, P. Norberg, R. Miquel, C. Padilla, A. Refregier, E. Sanchez, S. Serrano, I. Sevilla-Noarbe, P. Tallada, N. Tonello, and L. Tortorelli. The PAU Survey: early demonstration of photometric redshift performance in the COSMOS field. , 484(3):4200–4215, Apr. 2019. doi: 10.1093/mnras/stz204.

S. M. Faber, C. N. A. Willmer, C. Wolf, D. C. Koo, B. J. Weiner, J. A. Newman, M. Im, A. L. Coil, C. Conroy, M. C. Cooper, M. Davis, D. P. Finkbeiner, B. F. Gerke, K. Gebhardt, E. J. Groth, P. Guhathakurta, J. Harker, N. Kaiser, S. Kassin, M. Kleinheinrich, N. P. Konidaris, R. G. Kron, L. Lin, G. Luppino, D. S. Madgwick, K. Meisenheimer, K. G. Noeske, A. C. Phillips, V. L. Sarajedini, R. P. Schiavon, L. Simard, A. S. Szalay, N. P. Vogt, and R. Yan. Galaxy Luminosity Functions to z~1 from DEEP2 and COMBO-17: Implications for Red Galaxy Formation. , 665:265–294, Aug. 2007. doi: 10.1086/519294.

A. L. Faisst, D. Masters, Y. Wang, A. Merson, P. Capak, S. Malhotra, and J. E. Rhoads. Empirical Modeling of the Redshift Evolution of the [{\rm{N}}\,{\rm{II}}]/Hα Ratio for Galaxy Redshift Surveys. , 855:132, Mar. 2018. doi: 10.3847/1538-4357/aab1fc.

M. Fioc and B. Rocca-Volmerange. PEGASE: a UV to NIR spectral evolution model of galaxies. Application to the calibration of bright galaxy counts. , 326: 950–962, Oct. 1997.

A. S. Font, R. G. Bower, I. G. McCarthy, A. J. Benson, C. S. Frenk, J. C. Helly, C. G. Lacey, C. M. Baugh, and S. Cole. The colours of satellite galaxies in groups and clusters. , 389(4):1619–1629, Oct 2008. doi: 10.1111/j.1365-2966.2008.136 98.x.

P. Franzetti, M. Scodeggio, B. Garilli, D. Vergani, D. Maccagni, L. Guzzo, L. Tresse, O. Ilbert, F. Lamareille, T. Contini, O. Le Fèvre, G. Zamorani, J. Brinchmann, S. Charlot, D. Bottini, V. Le Brun, J. P. Picat, R. Scaramella, G. Vettolani, A. Zanichelli, C. Adami, S. Arnouts, S. Bardelli, M. Bolzonella, A. Cappi, P. Ciliegi, S. Foucaud, I. Gavignaud, A. Iovino, H. J. McCracken, B. Marano, C. Marinoni, A. Mazure, B. Meneux, R. Merighi, S. Paltani, R. Pellò, A. Pollo, L. Pozzetti, M. Radovich, E. Zucca, O. Cucciati, and C. J. Walcher. The VIMOS-VLT deep survey. Color bimodality and the mix of galaxy populations up to z ˜ 2. , 465:711–723, Apr. 2007. doi: 10.1051/0004-6361:20065942.

P. Franzetti, M. Scodeggio, B. Garilli, M. Fumana, and L. Paioro. GOSSIP, a New VO Compliant Tool for SED Fitting. In R. W. Argyle, P. S. Bunclark, and J. R. Lewis, editors, *Astronomical Data Analysis Software and Systems XVII*, volume 394 of *Astronomical Society of the Pacific Conference Series*, page 642, Aug. 2008.

A. Fritz, M. Scodeggio, O. Ilbert, M. Bolzonella, I. Davidzon, J. Coupon, B. Garilli, L. Guzzo, G. Zamorani, U. Abbas, C. Adami, S. Arnouts, J. Bel, D. Bottini, E. Branchini, A. Cappi, O. Cucciati, G. De Lucia, S. de la Torre, P. Franzetti, M. Fumana, B. R. Granett, A. Iovino, J. Krywult, V. Le Brun, O. Le Fèvre, D. Maccagni, K. Małek, F. Marulli, H. J. McCracken, L. Paioro, M. Polletta, A. Pollo, H. Schlagenhaufer, L. A. M. Tasca, R. Tojeiro, D. Vergani, A. Zanichelli, A. Burden, C. Di Porto, A. Marchetti, C. Marinoni, Y. Mellier, L. Moscardini,

R. C. Nichol, J. A. Peacock, W. J. Percival, S. Phleps, and M. Wolk. The VIMOS Public Extragalactic Redshift Survey (VIPERS): A quiescent formation of massive red-sequence galaxies over the past 9 Gyr. , 563:A92, Jan. 2014.

A. Gargiulo, M. Bolzonella, M. Scodeggio, J. Krywult, G. De Lucia, L. Guzzo, B. Garilli, B. R. Granett, S. de la Torre, U. Abbas, C. Adami, S. Arnouts, D. Bottini, A. Cappi, O. Cucciati, I. Davidzon, P. Franzetti, A. Fritz, C. Haines, A. J. Hawken, A. Iovino, V. Le Brun, O. Le Fèvre, D. Maccagni, K. Małek, F. Marulli, T. Moutard, M. Polletta, A. Pollo, L. A. M. Tasca, R. Tojeiro, D. Vergani, A. Zanichelli, G. Zamorani, J. Bel, E. Branchini, J. Coupon, O. Ilbert, L. Moscardini, and J. A. Peacock. The VIMOS Public Extragalactic Redshift Survey (VIPERS). The distinct build-up of dense and normal massive passive galaxies. , 606:A113, Oct. 2017. doi: 10.1051/0004-6361/201630112.

B. Garilli, M. Fumana, P. Franzetti, L. Paioro, M. Scodeggio, O. Le Fèvre, S. Paltani, and R. Scaramella. EZ: A Tool For Automatic Redshift Measurement. , 122(893):827, July 2010. doi: 10.1086/654903.

B. Garilli, L. Paioro, M. Scodeggio, P. Franzetti, M. Fumana, and L. Guzzo. Easylife: The Data Reduction and Survey Handling System for VIPERS. , 124(921):1232, Nov. 2012. doi: 10.1086/668681.

B. Garilli, L. Guzzo, M. Scodeggio, M. Bolzonella, U. Abbas, C. Adami, S. Arnouts, J. Bel, D. Bottini, E. Branchini, A. Cappi, J. Coupon, O. Cucciati, I. Davidzon, G. De Lucia, S. de la Torre, P. Franzetti, A. Fritz, M. Fumana, B. R. Granett, O. Ilbert, A. Iovino, J. Krywult, V. Le Brun, O. Le Fèvre, D. Maccagni, K. Małek, F. Marulli, H. J. McCracken, L. Paioro, M. Polletta, A. Pollo, H. Schlagenhaufer, L. A. M. Tasca, R. Tojeiro, D. Vergani, G. Zamorani, A. Zanichelli, A. Burden, C. Di Porto, A. Marchetti, C. Marinoni, Y. Mellier, L. Moscardini, R. C. Nichol, J. A. Peacock, W. J. Percival, S. Phleps, and M. Wolk. The VIMOS Public Extragalactic Survey (VIPERS). First Data Release of 57 204 spectroscopic measurements. , 562:A23, Feb. 2014. doi: 10.1051/0004-6361/201322790.

G. Gavazzi and M. Scodeggio. The mass dependence of the star formation history of disk galaxies. , 312:L29–L32, Aug. 1996.

G. Gavazzi, C. Bonfanti, G. Sanvito, A. Boselli, and M. Scodeggio. Spectrophotometry of Galaxies in the Virgo Cluster. I. The Star Formation History. , 576: 135–151, Sept. 2002. doi: 10.1086/341730.

R. Giovanelli and M. P. Haynes. Gas deficiency in cluster galaxies - A comparison of nine clusters. , 292:404–425, May 1985. doi: 10.1086/163170.

M. D. Gladders, A. Oemler, A. Dressler, B. Poggianti, B. Vulcani, and L. Abramson. The IMACS Cluster Building Survey. IV. The Log-normal Star Formation History of Galaxies. , 770(1):64, Jun 2013. doi: 10.1088/0004-637X/770/ 1/64.

J. E. González, C. G. Lacey, C. M. Baugh, C. S. Frenk, and A. J. Benson. Testing model predictions of the cold dark matter cosmology for the sizes, colours, morphologies and luminosities of galaxies with the SDSS. , 397:1254–1274, Aug. 2009. doi: 10.1111/j.1365-2966.2009.15057.x.

V. Gonzalez-Perez, C. G. Lacey, C. M. Baugh, C. S. Frenk, and S. M. Wilkins. The ultraviolet colours and dust attenuation of Lyman-break galaxies. , 429(2): 1609–1625, Feb 2013. doi: 10.1093/mnras/sts446.

V. Gonzalez-Perez, C. G. Lacey, C. M. Baugh, C. D. P. Lagos, J. Helly, D. J. R. Campbell, and P. D. Mitchell. How sensitive are predicted galaxy luminosities to the choice of stellar population synthesis model? *Monthly Notices of the Royal Astronomical Society*, 439(1):264–283, 2014. doi: 10.1093/mnras/stt2410. URL `http://dx.doi.org/10.1093/mnras/stt2410`.

J. E. Gunn and J. R. Gott, III. On the Infall of Matter Into Clusters of Galaxies and Some Effects on Their Evolution. , 176:1, Aug. 1972. doi: 10.1086/151605.

Q. Guo, S. White, M. Boylan-Kolchin, G. De Lucia, G. Kauffmann, G. Lemson, C. Li, V. Springel, and S. Weinmann. From dwarf spheroidals to cD galaxies:

simulating the galaxy population in a ΛCDM cosmology. , 413:101–131, May 2011. doi: 10.1111/j.1365-2966.2010.18114.x.

Q. Guo, S. White, R. E. Angulo, B. Henriques, G. Lemson, M. Boylan-Kolchin, P. Thomas, and C. Short. Galaxy formation in WMAP1 and WMAP7 cosmologies. , 428(2):1351–1365, Jan. 2013. doi: 10.1093/mnras/sts115.

L. Guzzo, M. Scodeggio, B. Garilli, B. R. Granett, A. Fritz, U. Abbas, C. Adami, S. Arnouts, J. Bel, M. Bolzonella, D. Bottini, E. Branchini, A. Cappi, J. Coupon, O. Cucciati, I. Davidzon, G. De Lucia, S. de la Torre, P. Franzetti, M. Fumana, P. Hudelot, O. Ilbert, A. Iovino, J. Krywult, V. Le Brun, O. Le Fèvre, D. Maccagni, K. Małek, F. Marulli, H. J. McCracken, L. Paioro, J. A. Peacock, M. Polletta, A. Pollo, H. Schlagenhaufer, L. A. M. Tasca, R. Tojeiro, D. Vergani, G. Zamorani, A. Zanichelli, A. Burden, C. Di Porto, A. Marchetti, C. Marinoni, Y. Mellier, L. Moscardini, R. C. Nichol, W. J. Percival, S. Phleps, and M. Wolk. The VIMOS Public Extragalactic Redshift Survey (VIPERS). An unprecedented view of galaxies and large-scale structure at 0.5 < z < 1.2. , 566: A108, June 2014. doi: 10.1051/0004-6361/201321489.

S. D. J. Gwyn. The Canada-France-Hawaii Telescope Legacy Survey: Stacked Images and Catalogs. , 143(2):38, Feb. 2012. doi: 10.1088/0004-6256/143/2/38.

C. P. Haines, A. Iovino, J. Krywult, L. Guzzo, I. Davidzon, M. Bolzonella, B. Garilli, M. Scodeggio, B. R. Granett, S. de la Torre, G. De Lucia, U. Abbas, C. Adami, S. Arnouts, D. Bottini, A. Cappi, O. Cucciati, P. Franzetti, A. Fritz, A. Gargiulo, V. Le Brun, O. Le Fèvre, D. Maccagni, K. Małek, F. Marulli, T. Moutard, M. Polletta, A. Pollo, L. A. M. Tasca, R. Tojeiro, D. Vergani, A. Zanichelli, G. Zamorani, J. Bel, E. Branchini, J. Coupon, O. Ilbert, L. Moscardini, J. A. Peacock, and M. Siudek. The VIMOS Public Extragalactic Redshift Survey (VIPERS). Downsizing of the blue cloud and the influence of galaxy size on mass quenching over the last eight billion years. , 605:A4, Aug 2017. doi: 10.1051/0004-6361/201630118.

B. M. B. Henriques, S. D. M. White, P. A. Thomas, R. E. Angulo, Q. Guo, G. Lemson, and W. Wang. Galaxy formation in the Planck cosmology - IV. Mass and environmental quenching, conformity and clustering. , 469(3):2626–2645, Aug 2017. doi: 10.1093/mnras/stx1010.

C. Heymans, L. Van Waerbeke, L. Miller, T. Erben, H. Hildebrandt, H. Hoekstra, T. D. Kitching, Y. Mellier, P. Simon, C. Bonnett, J. Coupon, L. Fu, J. Harnois Déraps, M. J. Hudson, M. Kilbinger, K. Kuijken, B. Rowe, T. Schrabback, E. Semboloni, E. van Uitert, S. Vafaei, and M. Velander. CFHTLenS: the Canada-France-Hawaii Telescope Lensing Survey. , 427(1):146–166, Nov. 2012. doi: 10.1111/j.1365-2966.2012.21952.x.

H. Hildebrandt, T. Erben, K. Kuijken, L. van Waerbeke, C. Heymans, J. Coupon, J. Benjamin, C. Bonnett, L. Fu, H. Hoekstra, T. D. Kitching, Y. Mellier, L. Miller, M. Velander, M. J. Hudson, B. T. P. Rowe, T. Schrabback, E. Semboloni, and N. Benítez. CFHTLenS: improving the quality of photometric redshifts with precision photometry. , 421(3):2355–2367, Apr. 2012. doi: 10.1111/j.1365-2966.2012.20468.x.

M. Hirschmann, G. De Lucia, D. Wilman, S. Weinmann, A. Iovino, O. Cucciati, S. Zibetti, and Á. Villalobos. The influence of the environmental history on quenching star formation in a Λ cold dark matter universe. , 444:2938–2959, Nov. 2014. doi: 10.1093/mnras/stu1609.

M. Hirschmann, G. De Lucia, and F. Fontanot. Galaxy assembly, stellar feedback and metal enrichment: the view from the GAEA model. , 461:1760–1785, Sept. 2016. doi: 10.1093/mnras/stw1318.

H. Hoekstra, Y. Mellier, L. van Waerbeke, E. Semboloni, L. Fu, M. J. Hudson, L. C. Parker, I. Tereno, and K. Benabed. First Cosmic Shear Results from the Canada-France-Hawaii Telescope Wide Synoptic Legacy Survey. , 647(1): 116–127, Aug. 2006. doi: 10.1086/503249.

D. W. Hogg, I. K. Baldry, M. R. Blanton, and D. J. Eisenstein. The K correction. *arXiv e-prints*, art. astro-ph/0210394, Oct. 2002.

E. Hubble. A relation between distance and radial velocity among extra-galactic nebulae. *Proceedings of the National Academy of Sciences*, 15(3):168–173, 1929. ISSN 0027-8424. doi: 10.1073/pnas.15.3.168. URL `https://www.pnas.org/content/15/3/168`.

M. Icaza-Lizaola, R. G. Bower, P. Norberg, S. Cole, M. Schaller, and S. Egan. A sparse regression approach to modelling the relation between galaxy stellar masses and their host haloes. *Monthly Notices of the Royal Astronomical Society*, 507(3):4584–4602, 08 2021. ISSN 0035-8711. doi: 10.1093/mnras/stab2368. URL `https://doi.org/10.1093/mnras/stab2368`.

O. Ilbert, P. Capak, M. Salvato, H. Aussel, H. J. McCracken, D. B. Sanders, N. Scoville, J. Kartaltepe, S. Arnouts, E. Le Floc'h, B. Mobasher, Y. Taniguchi, F. Lamareille, A. Leauthaud, S. Sasaki, D. Thompson, M. Zamojski, G. Zamorani, S. Bardelli, M. Bolzonella, A. Bongiorno, M. Brusa, K. I. Caputi, C. M. Carollo, T. Contini, R. Cook, G. Coppa, O. Cucciati, S. de la Torre, L. de Ravel, P. Franzetti, B. Garilli, G. Hasinger, A. Iovino, P. Kampczyk, J.-P. Kneib, C. Knobel, K. Kovac, J. F. Le Borgne, V. Le Brun, O. Le Fèvre, S. Lilly, D. Looper, C. Maier, V. Mainieri, Y. Mellier, M. Mignoli, T. Murayama, R. Pellò, Y. Peng, E. Pérez-Montero, A. Renzini, E. Ricciardelli, D. Schiminovich, M. Scodeggio, Y. Shioya, J. Silverman, J. Surace, M. Tanaka, L. Tasca, L. Tresse, D. Vergani, and E. Zucca. Cosmos Photometric Redshifts with 30-Bands for 2-deg^2. , 690:1236–1249, Jan. 2009. doi: 10.1088/0004-637X/690/2/1236.

L. Jiang, J. C. Helly, S. Cole, and C. S. Frenk. N-body dark matter haloes with simple hierarchical histories. , 440(3):2115–2135, May 2014. doi: 10.1093/mnras/stu390.

H. Johnston, B. Joachimi, P. Norberg, H. Hoekstra, M. Eriksen, M. C. Fortuna, **Manzoni, Giorgio**, S. Serrano, M. Siudek, L. Tortorelli, L. Cabayol, J. Car-

retero, R. Casas, F. Castander, E. Fernandez, J. García-Bellido, E. Gaztanaga, H. Hildebrandt, R. Miquel, C. Padilla, E. Sanchez, I. Sevilla-Noarbe, and P. Tallada-Crespí. The PAU Survey: Intrinsic alignments and clustering of narrow-band photometric galaxies. *arXiv e-prints*, art. arXiv:2010.09696, Oct. 2020.

S. Juneau, K. Glazebrook, D. Crampton, P. J. McCarthy, S. Savaglio, R. Abraham, R. G. Carlberg, H.-W. Chen, D. Le Borgne, R. O. Marzke, K. Roth, I. Jørgensen, I. Hook, and R. Murowinski. Cosmic Star Formation History and Its Dependence on Galaxy Stellar Mass. , 619:L135–L138, Feb. 2005. doi: 10.1086/427937.

A. Kasparova, I. Chilingarian, S. Borisov, V. Goradzhanov, K. Grishin, I. Katkov, V. Klochkov, E. Rubtsov, and V. Toptun. RCSEDv2: analytic approximations of k-corrections for galaxies out to redshift $z = 1$. *arXiv e-prints*, art. arXiv:2112.04864, Dec. 2021.

G. Kauffman. The Formation and Evolution of Galaxies. In *American Astronomical Society Meeting Abstracts*, volume 195 of *American Astronomical Society Meeting Abstracts*, page 67.01, Dec. 1999.

G. Kauffmann, T. M. Heckman, S. D. M. White, S. Charlot, C. Tremonti, J. Brinchmann, G. Bruzual, E. W. Peng, M. Seibert, M. Bernardi, and . coauthors. Stellar masses and star formation histories for 10^5 galaxies from the Sloan Digital Sky Survey. *MNRAS*, 341:33–53, May 2003. doi: 10.1046/j.1365-8711.2003.06291.x.

S. Kaviraj, L. A. Kirkby, J. Silk, and M. Sarzi. The UV properties of E+A galaxies: constraints on feedback-driven quenching of star formation. , 382:960–970, Dec. 2007. doi: 10.1111/j.1365-2966.2007.12475.x.

J. Kennicutt, R. C. The rate of star formation in normal disk galaxies. , 272:54–67, Sept. 1983. doi: 10.1086/161261.

R. C. Kennicutt, Jr. Star Formation in Galaxies Along the Hubble Sequence. , 36: 189–232, 1998. doi: 10.1146/annurev.astro.36.1.189.

L. J. Kewley, M. A. Dopita, R. S. Sutherland, C. A. Heisler, and J. Trevena. Theoretical Modeling of Starburst Galaxies. , 556:121–140, July 2001. doi: 10.1086/321545.

M. G. Kitzbichler and S. D. M. White. The high-redshift galaxy population in hierarchical galaxy formation models. , 376(1):2–12, Mar. 2007. doi: 10.1111/j. 1365-2966.2007.11458.x.

T. Kodama, I. Tanaka, M. Kajisawa, J. Kurk, B. Venemans, C. De Breuck, J. Vernet, and C. Lidman. The first appearance of the red sequence of galaxies in proto-clusters at $2 <˜ z <˜ 3$. , 377:1717–1725, June 2007. doi: 10.1111/j.1365-2966.2007.11739.x.

P. Kroupa. The Stellar Mass Function (invited review). In R. Rebolo, E. L. Martin, and M. R. Zapatero Osorio, editors, *Brown Dwarfs and Extrasolar Planets*, volume 134 of *Astronomical Society of the Pacific Conference Series*, page 483, Jan 1998.

J. Krywult, L. A. M. Tasca, A. Pollo, D. Vergani, M. Bolzonella, I. Davidzon, A. Iovino, A. Gargiulo, C. P. Haines, M. Scodeggio, L. Guzzo, G. Zamorani, B. Garilli, B. R. Granett, S. de la Torre, U. Abbas, C. Adami, D. Bottini, A. Cappi, O. Cucciati, P. Franzetti, A. Fritz, V. Le Brun, O. Le Fèvre, D. Maccagni, K. Małek, F. Marulli, M. Polletta, R. Tojeiro, A. Zanichelli, S. Arnouts, J. Bel, E. Branchini, J. Coupon, G. De Lucia, O. Ilbert, H. J. McCracken, L. Moscardini, and T. T. Takeuchi. The VIMOS Public Extragalactic Redshift Survey (VIPERS). The coevolution of galaxy morphology and colour to z 1. , 598:A120, Feb 2017. doi: 10.1051/0004-6361/201628953.

M. Kuhlen, M. Vogelsberger, and R. Angulo. Numerical simulations of the dark universe: State of the art and the next decade. *Physics of the Dark Universe*, 1 (1-2):50–93, Nov. 2012. doi: 10.1016/j.dark.2012.10.002.

C. G. Lacey, C. M. Baugh, C. S. Frenk, A. J. Benson, R. G. Bower, S. Cole, V. Gonzalez-Perez, J. C. Helly, C. D. P. Lagos, and P. D. Mitchell. A unified multiwavelength model of galaxy formation. , 462:3854–3911, Nov. 2016. doi: 10.1093/mnras/stw1888.

C. D. P. Lagos, A. S. G. Robotham, J. W. Trayford, R. Tobar, M. Bravo, S. Bellstedt, L. J. M. Davies, S. P. Driver, P. J. Elahi, D. Obreschkow, and C. Power. From the far-ultraviolet to the far-infrared - galaxy emission at 0 ≤ z ≤ 10 in the SHARK semi-analytic model. , page 2096, Sep 2019. doi: 10.1093/mnras/stz2427.

R. Laureijs, J. Amiaux, S. Arduini, J. L. Auguères, J. Brinchmann, R. Cole, M. Cropper, C. Dabin, L. Duvet, A. Ealet, B. Garilli, P. Gondoin, L. Guzzo, J. Hoar, H. Hoekstra, R. Holmes, T. Kitching, T. Maciaszek, Y. Mellier, F. Pasian, W. Percival, J. Rhodes, G. Saavedra Criado, M. Sauvage, R. Scaramella, L. Valenziano, S. Warren, R. Bender, F. Castander, A. Cimatti, O. Le Fèvre, H. Kurki-Suonio, M. Levi, P. Lilje, G. Meylan, R. Nichol, K. Pedersen, V. Popa, R. Rebolo Lopez, H. W. Rix, H. Rottgering, W. Zeilinger, F. Grupp, P. Hudelot, R. Massey, M. Meneghetti, L. Miller, S. Paltani, S. Paulin-Henriksson, S. Pires, C. Saxton, T. Schrabback, G. Seidel, J. Walsh, N. Aghanim, L. Amendola, J. Bartlett, C. Baccigalupi, J. P. Beaulieu, K. Benabed, J. G. Cuby, D. Elbaz, P. Fosalba, G. Gavazzi, A. Helmi, I. Hook, M. Irwin, J. P. Kneib, M. Kunz, F. Mannucci, L. Moscardini, C. Tao, R. Teyssier, J. Weller, G. Zamorani, M. R. Zapatero Osorio, O. Boulade, J. J. Foumond, A. Di Giorgio, P. Guttridge, A. James, M. Kemp, J. Martignac, A. Spencer, D. Walton, T. Blümchen, C. Bonoli, F. Bortoletto, C. Cerna, L. Corcione, C. Fabron, K. Jahnke, S. Ligori, F. Madrid, L. Martin, G. Morgante, T. Pamplona, E. Prieto, M. Riva, R. Toledo, M. Trifoglio, F. Zerbi, F. Abdalla, M. Douspis, C. Grenet, S. Borgani, R. Bouwens, F. Courbin, J. M. Delouis, P. Dubath, A. Fontana, M. Frailis, A. Grazian, J. Koppenhöfer, O. Mansutti, M. Melchior, M. Mignoli, J. Mohr, C. Neissner, K. Noddle, M. Poncet, M. Scodeggio, S. Serrano, N. Shane,

J. L. Starck, C. Surace, A. Taylor, G. Verdoes-Kleijn, C. Vuerli, O. R. Williams, A. Zacchei, B. Altieri, I. Escudero Sanz, R. Kohley, T. Oosterbroek, P. Astier, D. Bacon, S. Bardelli, C. Baugh, F. Bellagamba, C. Benoist, D. Bianchi, A. Biviano, E. Branchini, C. Carbone, V. Cardone, D. Clements, S. Colombi, C. Conselice, G. Cresci, N. Deacon, J. Dunlop, C. Fedeli, F. Fontanot, P. Franzetti, C. Giocoli, J. Garcia-Bellido, J. Gow, A. Heavens, P. Hewett, C. Heymans, A. Holland, Z. Huang, O. Ilbert, B. Joachimi, E. Jennins, E. Kerins, A. Kiessling, D. Kirk, R. Kotak, O. Krause, O. Lahav, F. van Leeuwen, J. Lesgourgues, M. Lombardi, M. Magliocchetti, K. Maguire, E. Majerotto, R. Maoli, F. Marulli, S. Maurogordato, H. McCracken, R. McLure, A. Melchiorri, A. Merson, M. Moresco, M. Nonino, P. Norberg, J. Peacock, R. Pello, M. Penny, V. Pettorino, C. Di Porto, L. Pozzetti, C. Quercellini, M. Radovich, A. Rassat, N. Roche, S. Ronayette, E. Rossetti, B. Sartoris, P. Schneider, E. Semboloni, S. Serjeant, F. Simpson, C. Skordis, G. Smadja, S. Smartt, P. Spano, S. Spiro, M. Sullivan, A. Tilquin, R. Trotta, L. Verde, Y. Wang, G. Williger, G. Zhao, J. Zoubian, and E. Zucca. Euclid Definition Study Report. *arXiv e-prints*, art. arXiv:1110.3193, Oct. 2011.

O. Le Fèvre, G. Vettolani, B. Garilli, L. Tresse, D. Bottini, V. Le Brun, D. Maccagni, J. P. Picat, R. Scaramella, M. Scodeggio, A. Zanichelli, C. Adami, M. Arnaboldi, S. Arnouts, S. Bardelli, M. Bolzonella, A. Cappi, S. Charlot, P. Ciliegi, T. Contini, S. Foucaud, P. Franzetti, I. Gavignaud, L. Guzzo, O. Ilbert, A. Iovino, H. J. McCracken, B. Marano, C. Marinoni, G. Mathez, A. Mazure, B. Meneux, R. Merighi, S. Paltani, R. Pelló, A. Pollo, L. Pozzetti, M. Radovich, G. Zamorani, E. Zucca, M. Bondi, A. Bongiorno, G. Busarello, Y. Mellier, P. Merluzzi, V. Ripepi, and D. Rizzo. The VIMOS VLT Deep Survey: A new window on the distant universe. In F. Casoli, T. Contini, J. M. Hameury, and L. Pagani, editors, *SF2A-2005: Semaine de l'Astrophysique Francaise*, page 19, Dec. 2005.

J. Lian, R. Yan, K. Zhang, and X. Kong. The Quenching Timescale and Quenching Rate of Galaxies. , 832:29, Nov. 2016. doi: 10.3847/0004-637X/832/1/29.

S. J. Lilly, O. Le Fevre, F. Hammer, and D. Crampton. The Canada-France Redshift Survey: The Luminosity Density and Star Formation History of the Universe to Z approximately 1. , 460:L1, Mar. 1996. doi: 10.1086/309975.

S. J. Lilly, O. Le Fèvre, A. Renzini, G. Zamorani, M. Scodeggio, T. Contini, C. M. Carollo, G. Hasinger, J. P. Kneib, A. Iovino, V. Le Brun, C. Maier, V. Mainieri, M. Mignoli, J. Silverman, L. A. M. Tasca, M. Bolzonella, A. Bongiorno, D. Bottini, P. Capak, K. Caputi, A. Cimatti, O. Cucciati, E. Daddi, R. Feldmann, P. Franzetti, B. Garilli, L. Guzzo, O. Ilbert, P. Kampczyk, K. Kovac, F. Lamareille, A. Leauthaud, J. F. Le Borgne, H. J. McCracken, C. Marinoni, R. Pello, E. Ricciardelli, C. Scarlata, D. Vergani, D. B. Sanders, E. Schinnerer, N. Scoville, Y. Taniguchi, S. Arnouts, H. Aussel, S. Bardelli, M. Brusa, A. Cappi, P. Ciliegi, A. Finoguenov, S. Foucaud, A. Franceschini, C. Halliday, C. Impey, C. Knobel, A. Koekemoer, J. Kurk, D. Maccagni, S. Maddox, B. Marano, G. Marconi, B. Meneux, B. Mobasher, C. Moreau, J. A. Peacock, C. Porciani, L. Pozzetti, R. Scaramella, D. Schiminovich, P. Shopbell, I. Smail, D. Thompson, L. Tresse, G. Vettolani, A. Zanichelli, and E. Zucca. zCOSMOS: A Large VLT/VIMOS Redshift Survey Covering $0 < z < 3$ in the COSMOS Field. , 172(1):70–85, Sept. 2007. doi: 10.1086/516589.

S. J. Lilly, V. Le Brun, C. Maier, V. Mainieri, M. Mignoli, M. Scodeggio, G. Zamorani, M. Carollo, T. Contini, J.-P. Kneib, O. Le Fèvre, A. Renzini, S. Bardelli, M. Bolzonella, A. Bongiorno, K. Caputi, G. Coppa, O. Cucciati, S. de la Torre, L. de Ravel, P. Franzetti, B. Garilli, A. Iovino, P. Kampczyk, K. Kovac, C. Knobel, F. Lamareille, J.-F. Le Borgne, R. Pello, Y. Peng, E. Pérez-Montero, E. Ricciardelli, J. D. Silverman, M. Tanaka, L. Tasca, L. Tresse, D. Vergani, E. Zucca, O. Ilbert, M. Salvato, P. Oesch, U. Abbas, D. Bottini, P. Capak, A. Cappi, P. Cassata, A. Cimatti, M. Elvis, M. Fumana, L. Guzzo, G. Hasinger, A. Koekemoer, A. Leauthaud, D. Maccagni, C. Marinoni, H. McCracken, P. Memeo, B. Meneux, C. Porciani, L. Pozzetti, D. Sanders, R. Scaramella, C. Scarlata, N. Scoville,

P. Shopbell, and Y. Taniguchi. The zCOSMOS 10k-Bright Spectroscopic Sample. , 184:218–229, Oct. 2009. doi: 10.1088/0067-0049/184/2/218.

J. Loveday, P. Norberg, I. K. Baldry, J. Bland-Hawthorn, S. Brough, M. J. I. Brown, S. P. Driver, L. S. Kelvin, and S. Phillipps. Galaxy and Mass Assembly (GAMA): maximum-likelihood determination of the luminosity function and its evolution. , 451(2):1540–1552, Aug. 2015. doi: 10.1093/mnras/stv1013.

P. Madau and M. Dickinson. Cosmic Star-Formation History. , 52:415–486, Aug. 2014. doi: 10.1146/annurev-astro-081811-125615.

P. Madau, H. C. Ferguson, M. E. Dickinson, M. Giavalisco, C. C. Steidel, and A. Fruchter. High-redshift galaxies in the Hubble Deep Field: colour selection and star formation history to z~4. , 283:1388–1404, Dec. 1996. doi: 10.1093/mnras/283.4.1388.

R. Maiolino, M. Cirasuolo, J. Afonso, F. E. Bauer, R. Bowler, O. Cucciati, E. Daddi, G. De Lucia, C. Evans, H. Flores, A. Gargiulo, B. Garilli, P. Jablonka, M. Jarvis, J. P. Kneib, S. Lilly, T. Looser, M. Magliocchetti, Z. Man, F. Mannucci, S. Maurogordato, R. J. McLure, P. Norberg, P. Oesch, E. Oliva, S. Paltani, C. Pappalardo, Y. Peng, L. Pentericci, L. Pozzetti, A. Renzini, M. Rodrigues, F. Royer, S. Serjeant, L. Vanzi, V. Wild, and G. Zamorani. MOONRISE: The Main MOONS GTO Extragalactic Survey. *The Messenger*, 180:24–29, June 2020. doi: 10.18727/0722-6691/5197.

G. Manzoni, M. Scodeggio, C. M. Baugh, P. Norberg, G. De Lucia, A. Fritz, C. P. Haines, G. Zamorani, A. Gargiulo, L. Guzzo, A. Iovino, K. Małek, A. Pollo, M. Siudek, and D. Vergani. Modelling the quenching of star formation activity from the evolution of the colour-magnitude relation in VIPERS. , 84:101515, Apr. 2021. doi: 10.1016/j.newast.2020.101515.

D. C. Martin, T. K. Wyder, D. Schiminovich, T. A. Barlow, K. Forster, P. G. Friedman, P. Morrissey, S. G. Neff, M. Seibert, T. Small, B. Y. Welsh, L. Bianchi,

J. Donas, T. M. Heckman, Y.-W. Lee, B. F. Madore, B. Milliard, R. M. Rich, A. S. Szalay, and S. K. Yi. The UV-Optical Galaxy Color-Magnitude Diagram. III. Constraints on Evolution from the Blue to the Red Sequence. , 173:342–356, Dec. 2007. doi: 10.1086/516639.

F. Marulli, A. Veropalumbo, L. Moscardini, A. Cimatti, and K. Dolag. Redshift-space distortions of galaxies, clusters, and AGN. Testing how the accuracy of growth rate measurements depends on scales and sample selections. , 599:A106, Mar. 2017. doi: 10.1051/0004-6361/201526885.

T. McNaught-Roberts, P. Norberg, C. Baugh, C. Lacey, J. Loveday, J. Peacock, I. Baldry, J. Bland-Hawthorn, S. Brough, S. P. Driver, A. S. G. Robotham, and J. A. Vázquez-Mata. Galaxy And Mass Assembly (GAMA): the dependence of the galaxy luminosity function on environment, redshift and colour. *Monthly Notices of the Royal Astronomical Society*, 445(2):2125–2145, Dec 2014. doi: 10.1093/mnras/stu1886.

A. I. Merson, C. M. Baugh, J. C. Helly, V. Gonzalez-Perez, S. Cole, R. Bielby, P. Norberg, C. S. Frenk, A. J. Benson, R. G. Bower, C. G. Lacey, and C. d. P. Lagos. Lightcone mock catalogues from semi-analytic models of galaxy formation - I. Construction and application to the BzK colour selection. , 429(1):556–578, Feb. 2013. doi: 10.1093/mnras/sts355.

L. Miller, T. D. Kitching, C. Heymans, A. F. Heavens, and L. van Waerbeke. Bayesian galaxy shape measurement for weak lensing surveys - I. Methodology and a fast-fitting algorithm. , 382(1):315–324, Nov. 2007. doi: 10.1111/j.1365-2 966.2007.12363.x.

P. D. Mitchell, C. G. Lacey, C. M. Baugh, and S. Cole. How well can we really estimate the stellar masses of galaxies from broad-band photometry? , 435(1): 87–114, Oct 2013. doi: 10.1093/mnras/stt1280.

P. D. Mitchell, C. G. Lacey, C. M. Baugh, and S. Cole. The evolution of the stellar mass versus halo mass relationship. , 456(2):1459–1483, Feb 2016. doi: 10.1093/mnras/stv2741.

J. Moustakas, R. C. Kennicutt, Jr., and C. A. Tremonti. Optical Star Formation Rate Indicators. , 642:775–796, May 2006. doi: 10.1086/500964.

T. Moutard, S. Arnouts, O. Ilbert, J. Coupon, I. Davidzon, L. Guzzo, P. Hudelot, H. J. McCracken, L. Van Werbaeke, G. E. Morrison, O. Le Fèvre, V. Comte, M. Bolzonella, A. Fritz, B. Garilli, and M. Scodeggio. The VIPERS Multi-Lambda Survey. II. Diving with massive galaxies in 22 square degrees since z = 1.5. , 590:A103, May 2016a. doi: 10.1051/0004-6361/201527294.

T. Moutard, S. Arnouts, O. Ilbert, J. Coupon, P. Hudelot, D. Vibert, V. Comte, S. Conseil, I. Davidzon, L. Guzzo, A. Llebaria, C. Martin, H. J. McCracken, B. Milliard, G. Morrison, D. Schiminovich, M. Treyer, and L. Van Werbaeke. The VIPERS Multi-Lambda Survey. I. UV and near-IR observations, multi-colour catalogues, and photometric redshifts. , 590:A102, May 2016b. doi: 10.1 051/0004-6361/201527945.

J. A. Newman, M. C. Cooper, M. Davis, S. M. Faber, A. L. Coil, P. Guhathakurta, D. C. Koo, A. C. Phillips, C. Conroy, A. A. Dutton, D. P. Finkbeiner, B. F. Gerke, D. J. Rosario, B. J. Weiner, C. N. A. Willmer, R. Yan, J. J. Harker, S. A. Kassin, N. P. Konidaris, K. Lai, D. S. Madgwick, K. G. Noeske, G. D. Wirth, A. J. Connolly, N. Kaiser, E. N. Kirby, B. C. Lemaux, L. Lin, J. M. Lotz, G. A. Luppino, C. Marinoni, D. J. Matthews, A. Metevier, and R. P. Schiavon. The deep2 galaxy redshift survey: Design, observations, data reduction, and redshifts. *The Astrophysical Journal Supplement Series*, 208(1):5, Aug 2013. ISSN 1538-4365. doi: 10.1088/0067-0049/208/1/5. URL http://dx.doi.org/10.1088/0 067-0049/208/1/5.

C. Padilla, F. J. Castander, A. Alarcón, J. Aleksic, O. Ballester, L. Cabayol, L. Cardiel-Sas, J. Carretero, R. Casas, J. Castilla, M. Crocce, M. Delfino,

C. Díaz, M. Eriksen, E. Fernández, P. Fosalba, J. García-Bellido, E. Gaztañaga, J. Gaweda, F. Grañena, J. María Ílla, J. Jiménez, L. López, P. Martí, R. Miquel, C. Neissner, C. Pío, E. Sánchez, S. Serrano, I. Sevilla-Noarbe, P. Tallada, N. Tonello, and J. de Vicente. The Physics of the Accelerating Universe Camera. , 157 (6):246, June 2019. doi: 10.3847/1538-3881/ab0412.

Y. Peng, R. Maiolino, and R. Cochrane. Strangulation as the primary mechanism for shutting down star formation in galaxies. , 521:192–195, May 2015. doi: 10.1038/nature14439.

Y.-j. Peng, S. J. Lilly, K. Kovač, M. Bolzonella, L. Pozzetti, A. Renzini, G. Zamorani, O. Ilbert, C. Knobel, A. Iovino, C. Maier, O. Cucciati, L. Tasca, C. M. Carollo, J. Silverman, P. Kampczyk, L. de Ravel, D. Sanders, N. Scoville, T. Contini, V. Mainieri, M. Scodeggio, J.-P. Kneib, O. Le Fèvre, S. Bardelli, A. Bongiorno, K. Caputi, G. Coppa, S. de la Torre, P. Franzetti, B. Garilli, F. Lamareille, J.-F. Le Borgne, V. Le Brun, M. Mignoli, E. Perez Montero, R. Pello, E. Ricciardelli, M. Tanaka, L. Tresse, D. Vergani, N. Welikala, E. Zucca, P. Oesch, U. Abbas, L. Barnes, R. Bordoloi, D. Bottini, A. Cappi, P. Cassata, A. Cimatti, M. Fumana, G. Hasinger, A. Koekemoer, A. Leauthaud, D. Maccagni, C. Marinoni, H. McCracken, P. Memeo, B. Meneux, P. Nair, C. Porciani, V. Presotto, and R. Scaramella. Mass and Environment as Drivers of Galaxy Evolution in SDSS and zCOSMOS and the Origin of the Schechter Function. , 721:193–221, Sept. 2010. doi: 10.1088/0004-637X/721/1/193.

A. Pezzotta, S. de la Torre, J. Bel, B. R. Granett, L. Guzzo, J. A. Peacock, B. Garilli, M. Scodeggio, M. Bolzonella, U. Abbas, C. Adami, D. Bottini, A. Cappi, O. Cucciati, I. Davidzon, P. Franzetti, A. Fritz, A. Iovino, J. Krywult, V. Le Brun, O. Le Fèvre, D. Maccagni, K. Małek, F. Marulli, M. Polletta, A. Pollo, L. A. M. Tasca, R. Tojeiro, D. Vergani, A. Zanichelli, S. Arnouts, E. Branchini, J. Coupon, G. De Lucia, J. Koda, O. Ilbert, F. Mohammad, T. Moutard, and L. Moscardini. The VIMOS Public Extragalactic Redshift

Survey (VIPERS). The growth of structure at 0.5 < z < 1.2 from redshift-space distortions in the clustering of the PDR-2 final sample. , 604:A33, July 2017. doi: 10.1051/0004-6361/201630295.

J. Pforr, C. Maraston, and C. Tonini. Recovering galaxy stellar population properties from broad-band spectral energy distribution fitting. , 422(4):3285–3326, Jun 2012. doi: 10.1111/j.1365-2966.2012.20848.x.

Planck Collaboration, P. A. R. Ade, N. Aghanim, C. Armitage-Caplan, M. Arnaud, M. Ashdown, F. Atrio-Barandela, J. Aumont, C. Baccigalupi, A. J. Banday, R. B. Barreiro, J. G. Bartlett, E. Battaner, K. Benabed, A. Benoît, A. Benoit-Lévy, J. P. Bernard, M. Bersanelli, P. Bielewicz, J. Bobin, J. J. Bock, A. Bonaldi, J. R. Bond, J. Borrill, F. R. Bouchet, M. Bridges, M. Bucher, C. Burigana, R. C. Butler, E. Calabrese, B. Cappellini, J. F. Cardoso, A. Catalano, A. Challinor, A. Chamballu, R. R. Chary, X. Chen, H. C. Chiang, L. Y. Chiang, P. R. Christensen, S. Church, D. L. Clements, S. Colombi, L. P. L. Colombo, F. Couchot, A. Coulais, B. P. Crill, A. Curto, F. Cuttaia, L. Danese, R. D. Davies, R. J. Davis, P. de Bernardis, A. de Rosa, G. de Zotti, J. Delabrouille, J. M. Delouis, F. X. Désert, C. Dickinson, J. M. Diego, K. Dolag, H. Dole, S. Donzelli, O. Doré, M. Douspis, J. Dunkley, X. Dupac, G. Efstathiou, F. Elsner, T. A. Enßlin, H. K. Eriksen, F. Finelli, O. Forni, M. Frailis, A. A. Fraisse, E. Franceschi, T. C. Gaier, S. Galeotta, S. Galli, K. Ganga, M. Giard, G. Giardino, Y. Giraud-Héraud, E. Gjerløw, J. González-Nuevo, K. M. Górski, S. Gratton, A. Gregorio, A. Gruppuso, J. E. Gudmundsson, J. Haissinski, J. Hamann, F. K. Hansen, D. Hanson, D. Harrison, S. Henrot-Versillé, C. Hernández-Monteagudo, D. Herranz, S. R. Hildebrandt, E. Hivon, M. Hobson, W. A. Holmes, A. Hornstrup, Z. Hou, W. Hovest, K. M. Huffenberger, A. H. Jaffe, T. R. Jaffe, J. Jewell, W. C. Jones, M. Juvela, E. Keihänen, R. Keskitalo, T. S. Kisner, R. Kneissl, J. Knoche, L. Knox, M. Kunz, H. Kurki-Suonio, G. Lagache, A. Lähteenmäki, J. M. Lamarre, A. Lasenby, M. Lattanzi, R. J. Laureijs, C. R. Lawrence, S. Leach, J. P. Leahy, R. Leonardi, J. León-Tavares, J. Lesgourgues, A. Lewis, M. Liguori,

P. B. Lilje, M. Linden-Vørnle, M. López-Caniego, P. M. Lubin, J. F. Macías-Pérez, B. Maffei, D. Maino, N. Mandolesi, M. Maris, D. J. Marshall, P. G. Martin, E. Martínez-González, S. Masi, M. Massardi, S. Matarrese, F. Matthai, P. Mazzotta, P. R. Meinhold, A. Melchiorri, J. B. Melin, L. Mendes, E. Menegoni, A. Mennella, M. Migliaccio, M. Millea, S. Mitra, M. A. Miville-Deschênes, A. Moneti, L. Montier, G. Morgante, D. Mortlock, A. Moss, D. Munshi, J. A. Murphy, P. Naselsky, F. Nati, P. Natoli, C. B. Netterfield, H. U. Nørgaard-Nielsen, F. Noviello, D. Novikov, I. Novikov, I. J. O'Dwyer, S. Osborne, C. A. Oxborrow, F. Paci, L. Pagano, F. Pajot, R. Paladini, D. Paoletti, B. Partridge, F. Pasian, G. Patanchon, D. Pearson, T. J. Pearson, H. V. Peiris, O. Perdereau, L. Perotto, F. Perrotta, V. Pettorino, F. Piacentini, M. Piat, E. Pierpaoli, D. Pietrobon, S. Plaszczynski, P. Platania, E. Pointecouteau, G. Polenta, N. Ponthieu, L. Popa, T. Poutanen, G. W. Pratt, G. Prézeau, S. Prunet, J. L. Puget, J. P. Rachen, W. T. Reach, R. Rebolo, M. Reinecke, M. Remazeilles, C. Renault, S. Ricciardi, T. Riller, I. Ristorcelli, G. Rocha, C. Rosset, G. Roudier, M. Rowan-Robinson, J. A. Rubiño-Martín, B. Rusholme, M. Sandri, D. Santos, M. Savelainen, G. Savini, D. Scott, M. D. Seiffert, E. P. S. Shellard, L. D. Spencer, J. L. Starck, V. Stolyarov, R. Stompor, R. Sudiwala, R. Sunyaev, F. Sureau, D. Sutton, A. S. Suur-Uski, J. F. Sygnet, J. A. Tauber, D. Tavagnacco, L. Terenzi, L. Toffolatti, M. Tomasi, M. Tristram, M. Tucci, J. Tuovinen, M. Türler, G. Umana, L. Valenziano, J. Valiviita, B. Van Tent, P. Vielva, F. Villa, N. Vittorio, L. A. Wade, B. D. Wandelt, I. K. Wehus, M. White, S. D. M. White, A. Wilkinson, D. Yvon, A. Zacchei, and A. Zonca. Planck 2013 results. XVI. Cosmological parameters. , 571:A16, Nov. 2014. doi: 10.1051/0004-6361/201321591.

L. Pozzetti, M. Bolzonella, E. Zucca, G. Zamorani, S. Lilly, A. Renzini, M. Moresco, M. Mignoli, P. Cassata, L. Tasca, F. Lamareille, C. Maier, B. Meneux, C. Halliday, P. Oesch, D. Vergani, K. Caputi, K. Kovač, A. Cimatti, O. Cucciati, A. Iovino, Y. Peng, M. Carollo, T. Contini, J.-P. Kneib, O. Le Févre, V. Mainieri, M. Scodeggio, S. Bardelli, A. Bongiorno, G. Coppa, S. de la Torre, L. de

Ravel, P. Franzetti, B. Garilli, P. Kampczyk, C. Knobel, J.-F. Le Borgne, V. Le Brun, R. Pellò, E. Perez Montero, E. Ricciardelli, J. D. Silverman, M. Tanaka, L. Tresse, U. Abbas, D. Bottini, A. Cappi, L. Guzzo, A. M. Koekemoer, A. Leauthaud, D. Maccagni, C. Marinoni, H. J. McCracken, P. Memeo, C. Porciani, R. Scaramella, C. Scarlata, and N. Scoville. zCOSMOS - 10k-bright spectroscopic sample. The bimodality in the galaxy stellar mass function: exploring its evolution with redshift. , 523:A13, Nov. 2010. doi: 10.1051/0004-6361/200913020.

A. S. G. Robotham, S. Bellstedt, C. d. P. Lagos, J. E. Thorne, L. J. Davies, S. P. Driver, and M. Bravo. ProSpect: generating spectral energy distributions with complex star formation and metallicity histories. , 495(1):905–931, June 2020. doi: 10.1093/mnras/staa1116.

S. Rota, B. R. Granett, J. Bel, L. Guzzo, J. A. Peacock, M. J. Wilson, A. Pezzotta, S. de la Torre, B. Garilli, M. Bolzonella, M. Scodeggio, U. Abbas, C. Adami, D. Bottini, A. Cappi, O. Cucciati, I. Davidzon, P. Franzetti, A. Fritz, A. Iovino, J. Krywult, V. Le Brun, O. Le Fèvre, D. Maccagni, K. Małek, F. Marulli, W. J. Percival, M. Polletta, A. Pollo, L. A. M. Tasca, R. Tojeiro, D. Vergani, A. Zanichelli, S. Arnouts, E. Branchini, J. Coupon, G. De Lucia, O. Ilbert, L. Moscardini, and T. Moutard. The VIMOS Public Extragalactic Redshift Survey (VIPERS). The matter density and baryon fraction from the galaxy power spectrum at redshift $0.6 < z < 1.1$. , 601:A144, May 2017. doi: 10.1051/0004-6361/201630116.

G. Rudnick, A. von der Linden, R. Pelló, A. Aragón-Salamanca, D. Marchesini, D. Clowe, G. De Lucia, C. Halliday, P. Jablonka, B. Milvang-Jensen, B. Poggianti, R. Saglia, L. Simard, S. White, and D. Zaritsky. The Rest-frame Optical Luminosity Function of Cluster Galaxies at $z < 0.8$ and the Assembly of the Cluster Red Sequence. , 700:1559–1588, Aug. 2009. doi: 10.1088/0004-637X/700/2/1559.

O. Ruiz-Macias, P. Zarrouk, S. Cole, P. Norberg, C. Baugh, D. Brooks, A. Dey, Y. Duan, S. Eftekharzadeh, D. J. Eisenstein, J. E. Forero-Romero, E. Gaztañaga,

C. Hahn, R. Kehoe, M. Landriau, D. Lang, M. E. Levi, J. Lucey, A. M. Meisner, J. Moustakas, A. D. Myers, N. Palanque-Delabrouille, C. Poppett, F. Prada, A. Raichoor, D. J. Schlegel, M. Schubnell, G. Tarlé, D. H. Weinberg, M. J. Wilson, and C. Yèche. Preliminary Target Selection for the DESI Bright Galaxy Survey (BGS). *Research Notes of the American Astronomical Society*, 4(10):187, Oct. 2020. doi: 10.3847/2515-5172/abc25a.

O. Ruiz-Macias, P. Zarrouk, S. Cole, C. M. Baugh, P. Norberg, J. Lucey, A. Dey, D. J. Eisenstein, P. Doel, E. Gaztañaga, C. Hahn, R. Kehoe, E. Kitanidis, M. Landriau, D. Lang, J. Moustakas, A. D. Myers, F. Prada, M. Schubnell, D. H. Weinberg, and M. J. Wilson. Characterizing the target selection pipeline for the Dark Energy Spectroscopic Instrument Bright Galaxy Survey. , 502(3): 4328–4349, Apr. 2021. doi: 10.1093/mnras/stab292.

B. Ryden. *Introduction to cosmology.* 2003.

S. Salim. Green Valley Galaxies. *Serbian Astronomical Journal*, 189:1–14, Dec. 2014. doi: 10.2298/SAJ1489001S.

A. Sandage. Star formation rates, galaxy morphology, and the Hubble sequence. , 161:89–101, June 1986.

C. Scarlata, C. M. Carollo, S. Lilly, M. T. Sargent, R. Feldmann, P. Kampczyk, C. Porciani, A. Koekemoer, N. Scoville, J.-P. Kneib, A. Leauthaud, R. Massey, J. Rhodes, L. Tasca, P. Capak, C. Maier, H. J. McCracken, B. Mobasher, A. Renzini, Y. Taniguchi, D. Thompson, K. Sheth, M. Ajiki, H. Aussel, T. Murayama, D. B. Sanders, S. Sasaki, Y. Shioya, and M. Takahashi. COSMOS Morphological Classification with the Zurich Estimator of Structural Types (ZEST) and the Evolution Since z = 1 of the Luminosity Function of Early, Disk, and Irregular Galaxies. , 172:406–433, Sept. 2007. doi: 10.1086/516582.

K. Schawinski, C. M. Urry, B. D. Simmons, L. Fortson, S. Kaviraj, W. C. Keel, C. J. Lintott, K. L. Masters, R. C. Nichol, M. Sarzi, R. Skibba, E. Treister, K. W.

Willett, O. I. Wong, and S. K. Yi. The green valley is a red herring: Galaxy Zoo reveals two evolutionary pathways towards quenching of star formation in early- and late-type galaxies. , 440:889–907, May 2014. doi: 10.1093/mnras/stu327.

J. Schaye, R. A. Crain, R. G. Bower, M. Furlong, M. Schaller, T. Theuns, C. Dalla Vecchia, C. S. Frenk, I. G. McCarthy, J. C. Helly, A. Jenkins, Y. M. Rosas-Guevara, S. D. M. White, M. Baes, C. M. Booth, P. Camps, J. F. Navarro, Y. Qu, A. Rahmati, T. Sawala, P. A. Thomas, and J. Trayford. The EAGLE project: simulating the evolution and assembly of galaxies and their environments. , 446 (1):521–554, Jan. 2015. doi: 10.1093/mnras/stu2058.

C. Schreiber, M. Pannella, D. Elbaz, M. Béthermin, H. Inami, M. Dickinson, B. Magnelli, T. Wang, H. Aussel, E. Daddi, S. Juneau, X. Shu, M. T. Sargent, V. Buat, S. M. Faber, H. C. Ferguson, M. Giavalisco, A. M. Koekemoer, G. Magdis, G. E. Morrison, C. Papovich, P. Santini, and D. Scott. The Herschel view of the dominant mode of galaxy growth from z = 4 to the present day. , 575:A74, Mar 2015. doi: 10.1051/0004-6361/201425017.

M. Scodeggio, L. Guzzo, B. Garilli, B. R. Granett, M. Bolzonella, S. de la Torre, U. Abbas, C. Adami, S. Arnouts, D. Bottini, A. Cappi, J. Coupon, O. Cucciati, I. Davidzon, P. Franzetti, A. Fritz, A. Iovino, J. Krywult, V. Le Brun, O. Le Fèvre, D. Maccagni, K. Małek, A. Marchetti, F. Marulli, M. Polletta, A. Pollo, L. A. M. Tasca, R. Tojeiro, D. Vergani, A. Zanichelli, J. Bel, E. Branchini, G. De Lucia, O. Ilbert, H. J. McCracken, T. Moutard, J. A. Peacock, G. Zamorani, A. Burden, M. Fumana, E. Jullo, C. Marinoni, Y. Mellier, L. Moscardini, and W. J. Percival. The VIMOS Public Extragalactic Redshift Survey (VIPERS). Full spectroscopic data and auxiliary information release (PDR-2). , 609:A84, Jan 2018. doi: 10.1051/0004-6361/201630114.

V. Simha, D. H. Weinberg, C. Conroy, R. Dave, M. Fardal, N. Katz, and B. D. Oppenheimer. Parametrising Star Formation Histories. *arXiv e-prints*, art. arXiv:1404.0402, Apr 2014.

M. Siudek, K. Małek, M. Scodeggio, B. Garilli, A. Pollo, C. P. Haines, A. Fritz, M. Bolzonella, S. de la Torre, B. R. Granett, L. Guzzo, U. Abbas, C. Adami, D. Bottini, A. Cappi, O. Cucciati, G. De Lucia, I. Davidzon, P. Franzetti, A. Iovino, J. Krywult, V. Le Brun, O. Le Fèvre, D. Maccagni, A. Marchetti, F. Marulli, M. Polletta, L. A. M. Tasca, R. Tojeiro, D. Vergani, A. Zanichelli, S. Arnouts, J. Bel, E. Branchini, O. Ilbert, A. Gargiulo, L. Moscardini, T. T. Takeuchi, and G. Zamorani. The VIMOS Public Extragalactic Redshift Survey (VIPERS). Star formation history of passive red galaxies. , 597:A107, Jan 2017. doi: 10.1051/0004-6361/201628951.

R. J. Smethurst, C. J. Lintott, B. D. Simmons, K. Schawinski, P. J. Marshall, S. Bamford, L. Fortson, S. Kaviraj, K. L. Masters, T. Melvin, R. C. Nichol, R. A. Skibba, and K. W. Willett. Galaxy Zoo: evidence for diverse star formation histories through the green valley. , 450:435–453, June 2015. doi: 10.1093/mnras/stv161.

A. Smith, S. Cole, C. Baugh, Z. Zheng, R. Angulo, P. Norberg, and I. Zehavi. A lightcone catalogue from the Millennium-XXL simulation. , 470(4):4646–4661, Oct. 2017. doi: 10.1093/mnras/stx1432.

V. Springel, S. D. M. White, G. Tormen, and G. Kauffmann. Populating a cluster of galaxies - I. Results at [formmu2]z=0. , 328(3):726–750, Dec. 2001. doi: 10.1046/j.1365-8711.2001.04912.x.

V. Springel, S. D. M. White, A. Jenkins, C. S. Frenk, N. Yoshida, L. Gao, J. Navarro, R. Thacker, D. Croton, J. Helly, J. A. Peacock, S. Cole, P. Thomas, H. Couchman, A. Evrard, J. Colberg, and F. Pearce. Simulations of the formation, evolution and clustering of galaxies and quasars. , 435(7042):629–636, June 2005. doi: 10.1038/nature03597.

V. Springel, C. S. Frenk, and S. D. M. White. The large-scale structure of the universe. *Nature*, 440(7088):1137–1144, Apr 2006. ISSN 1476-4687. doi: 10.1038/nature04805. URL http://dx.doi.org/10.1038/nature04805.

L. Stothert, P. Norberg, and Baugh. Statistic in large galaxy redshift surveys. *PhD thesis, Durham University*, 1, Dec. 2018a.

L. Stothert, P. Norberg, C. M. Baugh, A. Alarcon, A. Amara, J. Carretero, F. J. Castander, M. Eriksen, E. Fernandez, P. Fosalba, J. Garcia-Bellido, E. Gaztanaga, H. Hoekstra, C. Padilla, A. Refregier, E. Sanchez, and L. Tortorelli. The PAU Survey: spectral features and galaxy clustering using simulated narrow-band photometry. , 481(3):4221–4235, Dec. 2018b. doi: 10.1093/mnras/sty2491.

I. Strateva, Ž. Ivezić, G. R. Knapp, V. K. Narayanan, M. A. Strauss, J. E. Gunn, R. H. Lupton, D. Schlegel, N. A. Bahcall, J. Brinkmann, R. J. Brunner, T. Budavári, I. Csabai, F. J. Castander, M. Doi, M. Fukugita, Z. Győry, M. Hamabe, G. Hennessy, T. Ichikawa, P. Z. Kunszt, D. Q. Lamb, T. A. McKay, S. Okamura, J. Racusin, M. Sekiguchi, D. P. Schneider, K. Shimasaku, and D. York. Color Separation of Galaxy Types in the Sloan Digital Sky Survey Imaging Data. , 122:1861–1874, Oct. 2001a. doi: 10.1086/323301.

I. Strateva, Ž. Ivezić, G. R. Knapp, V. K. Narayanan, M. A. Strauss, J. E. Gunn, R. H. Lupton, D. Schlegel, N. A. Bahcall, J. Brinkmann, R. J. Brunner, T. Budavári, I. Csabai, F. J. Castander, M. Doi, M. Fukugita, Z. Győry, M. Hamabe, G. Hennessy, T. Ichikawa, P. Z. Kunszt, D. Q. Lamb, T. A. McKay, S. Okamura, J. Racusin, M. Sekiguchi, D. P. Schneider, K. Shimasaku, and D. York. Color Separation of Galaxy Types in the Sloan Digital Sky Survey Imaging Data. , 122(4):1861–1874, Oct. 2001b. doi: 10.1086/323301.

E. N. Taylor, A. M. Hopkins, I. K. Baldry, M. J. I. Brown, S. P. Driver, L. S. Kelvin, D. T. Hill, A. S. G. Robotham, J. Bland-Hawthorn, D. H. Jones, R. G. Sharp, D. Thomas, J. Liske, J. Loveday, P. Norberg, J. A. Peacock, S. P. Bamford, S. Brough, M. Colless, E. Cameron, C. J. Conselice, S. M. Croom, C. S. Frenk, M. Gunawardhana, K. Kuijken, R. C. Nichol, H. R. Parkinson, S. Phillipps, K. A. Pimbblet, C. C. Popescu, M. Prescott, W. J. Sutherland, R. J. Tuffs, E. van

Kampen, and D. Wijesinghe. Galaxy And Mass Assembly (GAMA): stellar mass estimates. , 418(3):1587–1620, Dec. 2011. doi: 10.1111/j.1365-2966.2011.19536.x.

P. Taylor and C. Kobayashi. Time evolution of galaxy scaling relations in cosmological simulations. , 463:2465–2479, Dec. 2016. doi: 10.1093/mnras/stw2157.

D. Thomas, C. Maraston, R. Bender, and C. Mendes de Oliveira. The Epochs of Early-Type Galaxy Formation as a Function of Environment. , 621:673–694, Mar. 2005. doi: 10.1086/426932.

R. Thomas, O. Le Fèvre, M. Scodeggio, P. Cassata, B. Garilli, V. Le Brun, B. C. Lemaux, D. Maccagni, J. Pforr, L. A. M. Tasca, G. Zamorani, S. Bardelli, N. P. Hathi, L. Tresse, E. Zucca, and A. M. Koekemoer. The extended epoch of galaxy formation: Age dating of 3600 galaxies with 2 < z < 6.5 in the VIMOS Ultra-Deep Survey. , 602:A35, Jun 2017. doi: 10.1051/0004-6361/201628141.

R. Tibshirani. Regression shrinkage and selection via the lasso. *Journal of the Royal Statistical Society. Series B (Methodological)*, 58(1):267–288, 1996. ISSN 00359246. URL `http://www.jstor.org/stable/2346178`.

A. R. Tomczak, R. F. Quadri, K.-V. H. Tran, I. Labbé, C. M. S. Straatman, C. Papovich, K. Glazebrook, R. Allen, G. B. Brammer, M. Cowley, M. Dickinson, D. Elbaz, H. Inami, G. G. Kacprzak, G. E. Morrison, T. Nanayakkara, S. E. Persson, G. A. Rees, B. Salmon, C. Schreiber, L. R. Spitler, and K. E. Whitaker. The SFR-M* Relation and Empirical Star-Formation Histories from ZFOURGE* at 0.5 < z < 4. , 817:118, Feb. 2016. doi: 10.3847/0004-637X/817/2/118.

T. Treu, R. S. Ellis, T. X. Liao, and P. G. van Dokkum. Keck Spectroscopy of Distant GOODS Spheroidal Galaxies: Downsizing in a Hierarchical Universe. , 622:L5–L8, Mar. 2005. doi: 10.1086/429374.

D. Vergani, B. Garilli, M. Polletta, P. Franzetti, M. Scodeggio, G. Zamorani, C. P. Haines, M. Bolzonella, L. Guzzo, B. R. Granett, S. de la Torre, U. Abbas, C. Adami, D. Bottini, A. Cappi, O. Cucciati, I. Davidzon, G. De Lucia,

A. Fritz, A. Gargiulo, A. J. Hawken, A. Iovino, J. Krywult, V. Le Brun, O. Le Fèvre, D. Maccagni, K. Małek, F. Marulli, A. Pollo, L. A. M. Tasca, R. Tojeiro, A. Zanichelli, S. Arnouts, J. Bel, E. Branchini, J. Coupon, O. Ilbert, T. Moutard, and L. Moscardini. The VIMOS Public Extragalactic Redshift Survey (VIPERS). AGN feedback in [NeV] emitters. , 620:A193, Dec 2018. doi: 10.1051/0004-6361/201732495.

V. Wild, C. J. Walcher, P. H. Johansson, L. Tresse, S. Charlot, A. Pollo, O. Le Fèvre, and L. de Ravel. Post-starburst galaxies: more than just an interesting curiosity. , 395(1):144–159, May 2009. doi: 10.1111/j.1365-2966.2009.14537.x.

V. Wild, O. Almaini, J. Dunlop, C. Simpson, K. Rowlands, R. Bowler, D. Maltby, and R. McLure. The evolution of post-starburst galaxies from z=2 to 0.5. , 463: 832–844, Nov. 2016. doi: 10.1093/mnras/stw1996.

R. J. Wright, C. d. P. Lagos, L. J. M. Davies, C. Power, J. W. Trayford, and O. I. Wong. Quenching time-scales of galaxies in the EAGLE simulations. , 487(3): 3740–3758, Aug 2019. doi: 10.1093/mnras/stz1410.

T. K. Wyder, D. C. Martin, D. Schiminovich, M. Seibert, T. Budavári, M. A. Treyer, T. A. Barlow, K. Forster, P. G. Friedman, P. Morrissey, S. G. Neff, T. Small, L. Bianchi, J. Donas, T. M. Heckman, Y.-W. Lee, B. F. Madore, B. Milliard, R. M. Rich, A. S. Szalay, B. Y. Welsh, and S. K. Yi. The UV-Optical Galaxy Color-Magnitude Diagram. I. Basic Properties. , 173:293–314, Dec. 2007. doi: 10.1086/521402.

H. M. Yesuf, S. M. Faber, J. R. Trump, D. C. Koo, J. J. Fang, F. S. Liu, V. Wild, and C. C. Hayward. From Starburst to Quiescence: Testing Active Galactic Nucleus feedback in Rapidly Quenching Post-starburst Galaxies. , 792:84, Sept. 2014. doi: 10.1088/0004-637X/792/2/84.

D. G. York, J. Adelman, J. E. Anderson, Jr., S. F. Anderson, J. Annis, N. A. Bahcall, J. A. Bakken, R. Barkhouser, S. Bastian, E. Berman, W. N. Boroski,

S. Bracker, C. Briegel, J. W. Briggs, J. Brinkmann, R. Brunner, S. Burles, L. Carey, M. A. Carr, F. J. Castander, B. Chen, P. L. Colestock, A. J. Connolly, J. H. Crocker, I. Csabai, P. C. Czarapata, J. E. Davis, M. Doi, T. Dombeck, D. Eisenstein, N. Ellman, B. R. Elms, M. L. Evans, X. Fan, G. R. Federwitz, L. Fiscelli, S. Friedman, J. A. Frieman, M. Fukugita, B. Gillespie, J. E. Gunn, V. K. Gurbani, E. de Haas, M. Haldeman, F. H. Harris, J. Hayes, T. M. Heckman, G. S. Hennessy, R. B. Hindsley, S. Holm, D. J. Holmgren, C.-h. Huang, C. Hull, D. Husby, S.-I. Ichikawa, T. Ichikawa, Ž. Ivezić, S. Kent, R. S. J. Kim, E. Kinney, M. Klaene, A. N. Kleinman, S. Kleinman, G. R. Knapp, J. Korienek, R. G. Kron, P. Z. Kunszt, D. Q. Lamb, B. Lee, R. F. Leger, S. Limmongkol, C. Lindenmeyer, D. C. Long, C. Loomis, J. Loveday, R. Lucinio, R. H. Lupton, B. MacKinnon, E. J. Mannery, P. M. Mantsch, B. Margon, P. McGehee, T. A. McKay, A. Meiksin, A. Merelli, D. G. Monet, J. A. Munn, V. K. Narayanan, T. Nash, E. Neilsen, R. Neswold, H. J. Newberg, R. C. Nichol, T. Nicinski, M. Nonino, N. Okada, S. Okamura, J. P. Ostriker, R. Owen, A. G. Pauls, J. Peoples, R. L. Peterson, D. Petravick, J. R. Pier, A. Pope, R. Pordes, A. Prosapio, R. Rechenmacher, T. R. Quinn, G. T. Richards, M. W. Richmond, C. H. Rivetta, C. M. Rockosi, K. Ruthmansdorfer, D. Sandford, D. J. Schlegel, D. P. Schneider, M. Sekiguchi, G. Sergey, K. Shimasaku, W. A. Siegmund, S. Smee, J. A. Smith, S. Snedden, R. Stone, C. Stoughton, M. A. Strauss, C. Stubbs, M. SubbaRao, A. S. Szalay, I. Szapudi, G. P. Szokoly, A. R. Thakar, C. Tremonti, D. L. Tucker, A. Uomoto, D. Vanden Berk, M. S. Vogeley, P. Waddell, S.-i. Wang, M. Watanabe, D. H. Weinberg, B. Yanny, N. Yasuda, and SDSS Collaboration. The Sloan Digital Sky Survey: Technical Summary. , 120:1579–1587, Sept. 2000. doi: 10.1086/301513.

P. Zarrouk. The DESI Bright Galaxy Survey: from target selection to preliminary clustering. In *American Astronomical Society Meeting Abstracts*, volume 53 of *American Astronomical Society Meeting Abstracts*, page 303.03, Jan. 2021.

I. Zehavi, Z. Zheng, D. H. Weinberg, M. R. Blanton, N. A. Bahcall, A. A. Berlind,

J. Brinkmann, J. A. Frieman, J. E. Gunn, R. H. Lupton, R. C. Nichol, W. J. Percival, D. P. Schneider, R. A. Skibba, M. A. Strauss, M. Tegmark, and D. G. York. Galaxy Clustering in the Completed SDSS Redshift Survey: The Dependence on Color and Luminosity. , 736(1):59, July 2011. doi: 10.1088/0004-637X/736/1/59.

1. Fleming S, Thompson M, Stevens R, et al. Normal ranges of heart rate and respiratory rate in children from birth to 18 years of age: a systematic review of observational studies. Lancet 2011;377(9770):1011-8. doi: 10.1016/s0140-6736(10)62226-x [published Online First: 2011/03/18]

2. Bjorland PA, Ersdal HL, Eilevstjønn J, et al. Changes in heart rate from 5 s to 5 min after birth in vaginally delivered term newborns with delayed cord clamping. Arch Dis Child Fetal Neonatal Ed 2020 doi: 10.1136/archdischild-2020-320179 [published Online First: 2020/11/12]

3. Dawson JA, Kamlin CO, Wong C, et al. Changes in heart rate in the first minutes after birth. Arch Dis Child Fetal Neonatal Ed 2010;95(3):F177-81. doi: 10.1136/adc.2009.169102 [published Online First: 2010/05/07]

4. Anton O, Fernandez R, Rendon-Morales E, et al. Heart Rate Monitoring in Newborn Babies: A Systematic Review. Neonatology 2019;116(3):199-210. doi: 10.1159/000499675 [published Online First: 2019/06/28]

5. National Institute of Health and Care Excellence. Postnatal care up to 8 weeks after birth. Clinical guidline (CG37). London, UK: NICE [cited 2006. Available from: https://www.nice.org.uk/guidance/CG37/]

6. World Health Organisation. Organizing care of the sick or small newborn baby. Managing newborn problems: a guide for doctors, nurses, and midwives. Geneva: World Health Organization,2003 [updated 2003. Available from: https://www.who.int/maternal_child_adolescent/documents/9241546220/en/]

7. Tveiten L, Diep LM, Halvorsen T, et al. Heart rate during the first 24 hours in term-born infants. Arch Dis Child Fetal Neonatal Ed 2021;106(5):489-93. doi: 10.1136/archdischild-2020-320761 [published Online First: 2021/01/17]

8. British Association of Perinatal Medicine (BAPM). Newborn Early Warning Trigger and Track (NEWTT). A Framework for Practice.April 2015. [Available from: https://www.bapm.org/resources/38-newborn-early-warning-trigger-track-newtt-a-framework-for-practice-2015].

9. National Health services. NHS Improvement. Reducing harm leading to avoidable admission of full-term babies into neonatal units. Findings and resources for improvement, February 2017. `https://www.england.nhs.uk/wp-content/uploads/2021/03/reducing-harm-leading-to-avoidable-admission-of-full-term-babies-into-neonatal-units.pdf`

10. ACoRN Neonatal Society. ACoRN Acute Care of at Risk Newborns 2005 [Available from: http://www.acornprogram.net/2013.

11. Hay WW, Jr., Rodden DJ, Collins SM, et al. Reliability of conventional and new pulse oximetry in neonatal patients. J Perinatol 2002;22(5):360-6. doi: 10.1038/sj.jp.7210740 [published Online First: 2002/06/26]

12. Shah N, Ragaswamy HB, Govindugari K, et al. Performance of three new-generation pulse oximeters during motion and low perfusion in volunteers. J Clin Anesth 2012;24(5):385-91. doi: 10.1016/j.jclinane.2011.10.012 [published Online First: 2012/05/26]

13. Meberg A, Brügmann-Pieper S, Due R, Jr., et al. First day of life pulse oximetry screening to detect congenital heart defects. J Pediatr 2008;152(6):761-5. doi: 10.1016/j.jpeds.2007.12.043 [published Online First: 2008/05/22]

14. Poets CF, Pauls U, Bohnhorst B. Effect of blood transfusion on apnoea, bradycardia and hypoxaemia in preterm infants. Eur J Pediatr 1997;156(4):311-6. doi: 10.1007/s004310050607 [published Online First: 1997/04/01]

15. Harris PA, Taylor R, Thielke R, et al. Research electronic data capture (REDCap)–a metadata-driven methodology and workflow process for providing translational research informatics support. J Biomed Inform 2009;42(2):377-81. doi: 10.1016/j.jbi.2008.08.010 [published Online First: 2008/10/22]

16. Vandenbroucke JP, von Elm E, Altman DG, et al. Strengthening the Reporting of Observational Studies in Epidemiology (STROBE): explanation and elaboration. International journal of surgery (London, England) 2014;12(12):1500-24. doi: 10.1016/j.ijsu.2014.07.014 [published Online First: 2014/07/22]